# New quantitative methods in analyser-based phase contrast X-ray imaging

David John Vine
B. Sc. (Hons)


School of Physics · Monash University

September 2008

PDF EDITION

# Contents

# Abstract

New quantitative methods are developed for analyser-based phase contrast imaging (ABI) with hard X-rays. In the first instance we show that quantitative ABI may be implemented using an extended incoherent source. Next, we outline how complex Green's functions may be reconstructed from phase contrast images and we apply this method to reconstruct the thick perfect crystal Green's function associated with an ABI imaging system.

The use of quantitative ABI with incoherent X-ray sources is not widespread and the first set of results pertains to the feasibility of quantitative ABI imaging and phase retrieval using a rotating anode X-ray source. The necessary conditions for observation of ABI phase contrast are deduced from elementary coherence considerations and numerical simulations. We then focus on the problem of extracting quantitative information from ABI images recorded using an extended incoherent X-ray source. The results of an experiment performed at Friedrich-Schiller University, Germany using a rotating anode X-ray source demonstrate the validity of our approach. It is shown that quantitative information may be extracted from such images under quite general and practicable conditions.

We then develop a new use for phase contrast imaging systems that allows the Green's function associated with a linear shift-invariant imaging system to be deduced from two phase contrast images of a known weak object. This new approach is applied to X-ray crystallography where the development of efficient methods of inferring the phase of rocking curves is an important open problem. We show how the complex Green's function describing Bragg reflection of a coherent scalar X-ray wavefield from a crystal may be recovered from a single image over a wide range of reciprocal space simultaneously. The solution we derive is fast, non-iterative and deterministic. When applied to crystalline structures for which the kinematic scattering approximation is valid, such as thin crystalline films, our technique is shown to solve the famous one-dimensional phase retrieval problem which allows us to directly invert the Green's function to retrieve the depth-dependent interplanar spacing.

Finally we implement our Green's function retrieval method on experimental data collected at the SPring-8 synchrotron in Hyogo, Japan. In the experiment we

recorded analyser-based phase contrast images of a known weak object using a thick perfect silicon analyser crystal. It is then demonstrated that these measurements can be inverted to recover the complex Green's function associated with the analyser crystal Bragg peak. The reconstructed Green's function is found to be in good agreement with the prediction of dynamical diffraction theory.

# Disclosure

I declare this thesis:

(i) contains no material which has been accepted for the award of any other degree or diploma in any university or other institution,

(ii) to the best of my knowledge contains no material previously published or written by another person, except where due reference is made in the text of the thesis,

(iii) includes work which is based on joint research and publications. Where such work is presented a statement declaring the relative contributions of the respective authors has been included.

David Vine: _____ Date: 5 September 2008

# Acknowledgements

I owe a debt of gratitude to my thesis advisors Dr David Paganin and Dr Konstantin Pavlov. Their indefatigable enthusiasm and encouragement, as well as the support that was given whenever required and without exception has been invaluable. Their dedication and diligence to the role of educator/advisor is inspirational. Notwithstanding what I have learnt from them, I have enjoyed our time spent in meetings, long days of beamtime, planes, trains and shinki-buses.

There are many scientists who freely gave their time to help me and I extend them my sincerest thanks: Dr Sergey Podorov, Dr Stuart Midgely, Dr Karen Siu, A/Prof. Imants Svalbe, Dr Brian Usher, Dr Tim Davis, Prof. David Jesson and Dr Tim Gureyev.

The work in this thesis would not have been possible without the support of Prof. Eckhardt Förster. Whilst performing my experiments in Germany I received tremendous support from the staff of the Institute of Optics and Quantum Electronics and the Institute of Applied Physics, Friedrich Schiller University: Dr Jurgen Kräußlich, Dr Ingo Uschmann, Dr Ortrud Wehrhan, Mr Frank Perner, Mr Thomas Kämpfe and Prof. Erst-Bernard Kley. I would like to thank the Federal Republic of Germany and the German Academic Exchange Service (DAAD) for the generous financial support I received whilst in Jena.

I am thankful to our Japanese collaborators from SPring8/ RIKEN for sharing their expertise: Dr Kentaro Uesugi, Dr Akihasa Takeuchi, Dr Yoshio Suzuki and Prof. Naoto Yagi.

I would like to thank the staff of the physics department who ensured all things administrative ran smoothly for me: Jean Pettigrew, Tracey Lawrence, Julia Barnes and James Gibbons.

Thanks to the School of Physics workshop and Alan Holland who somehow managed to turn my sketches into what I actually wanted.

A big thank you to Jenny McCabe and Dr Susan Feteris who gave me the opportunity to teach in the undergraduate physics laboratories.

I have been fortunate during my PhD to have the opportunity to work with and learn from A/ Prof. Michael Morgan about physics and the teaching of physics.

I have been the recipient of a number of scholarships throughout my candidature

and I would like to acknowledge the following funding bodies: the Australian Research Council (ARC), the Access to Major Research Facilities (AMRF) fund, the J. L. William Bequest, the Monash University Faculty of Science and School of Physics.

A special thanks to my friends who made the journey that much more enjoyable: Dr John Daniels, Dr John Gillam and Beth Browne, Dr Ivan Williams, Dr Toby Beveridge, Dr Marcus Kitchen, Dr Karen Siu, Nadia Zatsepin, Sally Irvine, Gary Ruben, Jeff Crosbie, Shakes Chandra, Shane Kennedy, Martin Spencer, Sabeena Sidhu and Kaye Morgan.

A respite from physics was afforded me by the opportunity to share gigs and hangovers with: Mick and Amy Greer, John Jess and Amy Harrison, Jimmy Pote and Jen Templeman, Danny and Amanda Minogue, Pete and Carolyn Glennie, Bern Moran, Andrew Barrie, James Hurley and my fellow Crofters: Scotty Devers and Matty Eastham, thanks.

In between bouts of research I shared the experience of Red Card Special with Jimmy 'James' Pote, Anita 'Neetdawg' Berram, Brendan 'Brock' Merakis and Michael 'Gmac' Greer.

I must single out for thanks: Gary for teaching me about illustration, font selection and lending his encyclopaedic knowledge of LaTeX and programming in general; Nadia for the memorable times spent working back late; John Daniels for sharing an office with me; John Gillam for his enthusiasm for all things science and Ivan Williams for many insightful discussions over coffee.

The presentation of this thesis has been influenced by the theses of Dr Anton Barty and Dr Lincoln Turner, thanks.

My family have been the first to offer their support on the many occasions it has been needed: Melissa, Michelle, Tegan, Hayley, Zac, Luke and Anthony. Special thanks to the nieces and nephews for letting me use their photos in Chapter 4.

Finally, I dedicate this thesis to Mum and Dad who believed in me, encouraged me and supported me throughout my education.

# 1 Introduction

This thesis describes important new analytical and experimental developments to a relatively new mode of imaging with hard X-rays known as crystal analyser-based phase contrast imaging (ABI) (Förster et al., 1980; Somenkov et al., 1991; Ingal and Beliaevskaya, 1995; Davis et al., 1995a,b; Davis, 1996; Chapman et al., 1997).

The availability of bright, coherent beams of X-rays is underpinning a range of new phase sensitive techniques (McNulty et al., 1992; Miao et al., 1999, 2003; Eisebitt et al., 2004; Thibault et al., 2008) and revealing startling discoveries areas as diverse as the dynamics of chemical reactions, spin waves in magnetic materials and X-ray vortices formed during lung imaging (Gaffney and Chapman, 2007; Shpyrko et al., 2007; Kitchen et al., 2004). In this respect the present renaissance in the coherent X-ray research programme is not unlike that which occurred in the years following the availability of lasers in the visible light spectrum. However, the shorter wavelength of X-rays compared with visible-light offers advantages such as higher resolution imaging of optically opaque materials. These results serve to underscore the notion that the availability of coherent X-ray radiation offers the possibility to dramatically improve existing X-ray techniques or, perhaps more enticing, the opportunity to develop entirely new applications which have not heretofore been possible using incoherent radiation.

A smattering of techniques that have benefited from the availability of coherent X-ray sources include X-ray photon correlation spectroscopy (Brauer et al., 1995; Dierker et al., 1995; Thurn-Albrecht et al., 1996) where the dynamics of disordered systems can be observed at high resolution, wavefront engineering (Di Fabrizio et al., 2003) which uses diffractive optical elements to design an incident wavefront and singular X-ray optics (Peele et al., 2002; Peele and Nugent, 2003; Peele et al., 2005; Paganin, 2006) where the observation and dynamics of X-ray vortices are studied.

X-ray phase sensitive imaging has been another beneficiary of the improved coher-

ence at short wavelengths and there has been significant progress made in this area over the past two decades. Phase sensitive imaging with X-rays is well established since the interferometry experiments of Bonse and Hart (1965) however it is the use of synchrotron X-ray sources that has exposed this form of imaging to the mainstream. ABI is an example of just such a phase sensitive technique and has shown significant potential for use in medical diagnostic materials and characterisation applications.

In this thesis we will present two major developments to ABI: the first is to investigate the feasibility of implementing ABI with an extended incoherent X-ray source with a view to performing quantitative phase retrieval. This development fits in with the current drive to adapt quantitative phase contrast imaging for use with laboratory based X-ray sources. Quantitative phase contrast imaging systems have shown their potential usefulness and now to be used on a large scale they must be implemented with the rotating anode X-ray source which is commonly available and affordable.

In the second development we use ABI as a prototype system for reconstructing complex Green's functions associated with shift-invariant coherent linear imaging systems and then implement this technique to demonstrate that it is indeed viable. In the case of ABI we are able to reconstruct the phase and amplitude of the analyser crystal's reflection coefficient but the method has a much wider applicability to reconstructing complex Green's functions.

As an example of the usefulness of such a development, when applied to reconstructing the Green's function for a thin crystalline layer this approach allows the structure of the film to be determined unambiguously from a single two-dimensional intensity measurement. This important application demonstrates a solution to the one-dimensional phase retrieval problem which is the subject of a great deal of study.

In the following section we will introduce the importance of phase sensitive imaging and provide an overview of the current state of the art for phase sensitive imaging techniques involving hard X-rays.

## 1.1 Phase sensitive imaging

The power of X-rays lies in their ability to transmit through optically opaque materials. This property of X-ray wavefields is widely exploited as a medical diagnostic tool (Brant and Clyde, 2007), a means for non-destructive characterisation (Wachtman, 1993) and a preventative security measure (Evans, 2004).

The oldest and most well known form of imaging with X-rays is the radiography pioneered by Röntgen (Röntgen, 1896) in which image intensity is proportional to the

attenuation of X-rays by thickness and/or local compositional variations.

Given that it is the penetrating power of X-rays that makes them useful it is not difficult to imagine a class of materials that are almost perfectly 'X-ray transparent'. A common example is soft biological tissue in the hard X-ray regime. In general any object composed of, or immersed in, materials with approximately the same attenuation coefficients will appear in low contrast in X-ray absorption images.

Concepts such as 'opaque' and 'transparent' are firmly rooted in the paradigm of absorption contrast imaging where the visibility of an object is tied to its ability to attenuate X-rays. But just as the X-ray photon has a wave aspect which complements its corpuscular aspect so we have phase contrast imaging which complements absorption contrast imaging. In the latter the image contrast depends on the transmitted photon flux whereas the former technique uses interference[1] as the contrast mechanism[2].

The rapid temporal oscillation of high energy electromagnetic fields ($10^{18}$Hz) coupled with the limited response time of detectors (seconds) means that any given measurement of the field must necessarily be an average over many oscillations, thus direct measurement of the phase of an x-ray wavefield is not currently possible[3] (Born and Wolf, 1999). Due to our inability to directly measure the phase of the wavefield we must employ an imaging system that renders phase information visible as intensity variations which are directly measurable. It is a concern of coherent X-ray optics to investigate the link between the phase of a wavefield and intensity produced by a phase contrast imaging system and, furthermore, to develop methods for recovering the phase from said intensity measurements. This "phase retrieval problem", which will be reviewed in §1.2, is very closely linked to the inverse problem of making quantitative measurements on the sample which led to these retrieved phase variations.

The methods of rendering phase visible are known as 'phase contrast imaging systems' and it is to this subject that we now turn. The distinct methods we review here are X-ray interferometry (§1.1.1), Talbot interferometry (§1.1.2), Zernike and Schlieren phase contrast (§1.1.3), lensless diffractive imaging (§1.1.4), propagation based imaging (§1.1.5) and crystal analyser based imaging (§1.1.6). The methods have a degree of similarity and we will attempt to describe the link between them.

[1] We note that phase contrast is typically classified as a non-interferometric form of imaging. Traditionally the term 'interferometric phase contrast' refers to the specific phase contrast imaging modality of interferometry (see §1.1.1). Here we use it in the broad sense to mean the contrast that results from the superposition of coherent wavefields.

[2] Trivially of course phase contrast also requires some flux of X-rays.

[3] Quantum mechanical considerations on the ability to measure a well defined phase are discussed in (Mandel and Wolf, 1995).

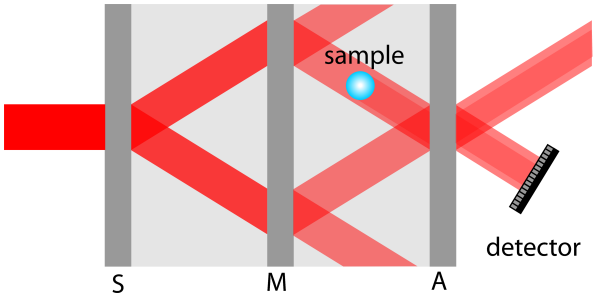


Figure 1.1: **Hard X-ray interferometry.** A typical monolithic hard X-ray interferometer featuring a beam splitter (S), mirror (M) and analyser (A). Adapted from Momose (2003).

### 1.1.1 X-ray interferometry

Interferometry has a long and rich history beginning with visible light where it was famously used by Young to demonstrate the wave nature of light and Michelson to dispel the aether hypothesis (Born and Wolf, 1999). X-ray interferometry uses the division (wavefront, amplitude, polarisation) of a coherent wavefield into two spatially separated beams, the 'object beam' transmitted through the sample being recombined with the 'reference beam' to form an interferogram as in Figure 1.1 (Bonse and Hart, 1965). Interferometric contrast is the result of a coherent superposition of the object and reference beams which gives the characteristic bright/dark fringes as the optical path length between the beams changes through $2\pi$. Interferometry is the most sensitive of phase contrast techniques but as such it is extremely susceptible to aberrations caused by mechanical instability in the optical path length.

Mirrors and beam splitters, the optical elements used in visible light interferometry, have their counterpart in X-ray interferometry as perfect single crystals in Bragg (Bonse and Hart, 1966) or Laue (Bonse and Hart, 1965) geometry. The crystal optics, beam splitters, mirrors and analysers, are fabricated from slabs of near perfect, strain free single crystals. At the expense of a limited field of view it is possible to create an interferometer from a monolithic crystal slab, as in Figure 1.1 (Bonse and Hart, 1965), to limit the problem of mechanical stability between the optical elements.

X-ray interferometry contrast is directly proportional to the phase of the sample. The price to pay for the sensitivity of interferometry is the stringent requirement that the coherence length of the radiation be greater than the maximum optical path difference introduced by the sample (Momose, 2003).

Interferometry has been implemented for X-ray imaging (Bonse and Hart, 1965) and tomography (Momose et al., 1995; Momose, 1995). In the original paper of Bonse and Hart (1965) the interferogram was recorded without a sample so that the

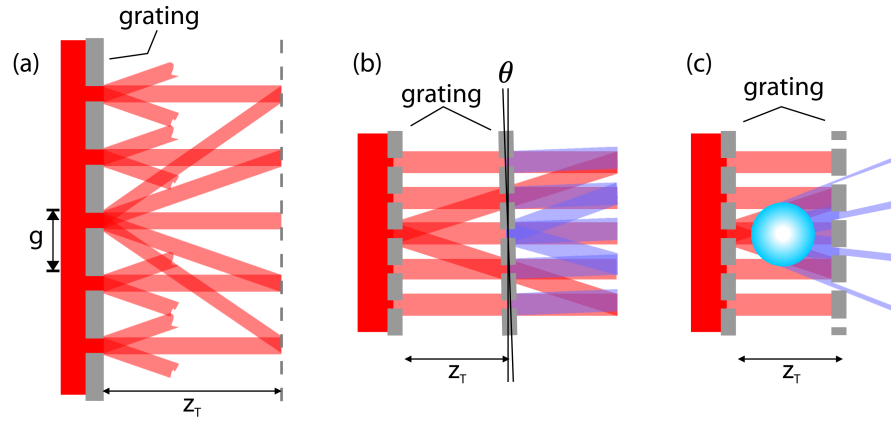


Figure 1.2: **X-ray Talbot interferometry.**(a) the Talbot (self-imaging) effect. A planar X-ray beam illuminates a grating with period g producing a wavefield with discrete diffraction orders. At a distance $z_T = 2g^2/\lambda$ downstream from the grating the diffracted orders recombine to form an image of the grating. (b) The Moire interferometer uses the Talbot effect in conjunction with a second grating a distance $z_T$ and inclined at an angle $\theta$ with respect to the first grating to create a series of Moire fringes. (c) The Talbot interferometer is a dark field imaging technique that uses a second grating at a distance $z_T$ downstream from the first and positioned so that it blocks the wavefield diffracted from the first grating. The refraction of the wavefield introduced by an object placed between the gratings disrupts the balance and allows X-rays to pass through the second grating.

interference fringes revealed information about the very slight strain fields in the perfect crystals. Tomography as performed by Momose et al. (1995) is a more difficult proposition than imaging because one must record many images and rotate the sample between each which has the potential to misalign the interferometer.

It is useful at this point to make a distinction between 'high' coherence and 'low' coherence phase contrast imaging systems. The high-coherence techniques, of which interferometry is an example, require coherence lengths at least as large as the maximum optical path length introduced by the sample to be imaged. Some of the techniques in the following sections can be described as low-coherence in that coherence lengths much smaller than this are acceptable. The distinction is worth making because the high- and low-coherence techniques are usually used to image quite different samples and comparisons between phase contrast techniques are perhaps most meaningfully made within the same 'coherence requirement group'. It should be noted that the coherence length for both high and low coherence cases could be the numerically equal but the important quantity is the relative size of the maximum optical path length introduced by the sample to the coherence length.

### 1.1.2 Talbot interferometry

A different kind of interferometer may be constructed by replacing the perfect crystal beam splitters with one-dimensional gratings with macroscopic periodicity, typically a few micron (Pfeiffer et al., 2008). The effect of the grating on the beam is equivalent to the crystal beam splitter in that each will split the beam into discrete diffraction orders however the macroscopic periodicity of the grating means the beams will be scattered through much smaller angles. Since the beams are scattered through smaller angles they do not become spatially separated as in crystal interferometry. Two common types of grating interferometer are known in the literature as the Moire interferometer (Momose et al., 2003; Weitkamp et al., 2004) and the Talbot interferometer (Clauser, 1998; David et al., 2002; Momose et al., 2003; Pfeiffer et al., 2005, 2006, 2007b; Kottler et al., 2007a,b,c; Pfeiffer et al., 2007a, 2008).

A digression is necessary to introduce the Talbot effect with reference to Figure 1.2(a). If a monochromatic planar X-ray wavefield with wavelength $\lambda$ is incident on a grating with period $g$ then the diffracted wavefield will be composed of a superposition of diffracted plane waves. At a 'Talbot distance' $z_T$,

$$z_T = \frac{2g^2}{\lambda}, \tag{1.1}$$

from the first grating the diffracted wavefield recombines to form an image of the grating, a phenomenon known as the Talbot effect (Talbot, 1836; Rayleigh, 1881). In Moire interferometry (Figure 1.2(b)) two gratings are used in series a Talbot distance apart and with the second slightly rotated by $\theta$ with respect to the first. The inclination of the second grating has the effect of slightly shifting the fringe spacing resulting in a series of Moire fringes (Weitkamp et al., 2004).

In the Talbot interferometer (Figure 1.2(c)) two gratings[4] are placed a Talbot distance apart and shifted half a grating period parallel to its length so that in the absence of a sample the second grating absorbs the field entirely. This configuration is the dark-field mode of operation (Pfeiffer et al., 2008), alternatively the field may not be extinguished entirely which is known as the differential-mode (Pfeiffer et al., 2006). The placement of a sample between the gratings will add a position dependent phase shift to the wavefield so that the second grating is no longer able to extinguish the field. The result is that the wavefield incident on the second grating is partially transmitted proportional to the refraction, and thus phase, of the sample. Another configuration which may result in higher resolution images scans the first and second gratings in parallel (Nesterets and Wilkins, 2008).

[4] A three-grating configuration is possible for use with an incoherent source.

The Talbot interferometer does not require each distinct beam to be mutually coherent and so can be used with low-coherence sources and has been demonstrated with a spectral bandwidth of approximately 10% (Pfeiffer et al., 2006). In this sense it is a low-coherence method and can be used to image samples that introduce maximum optical path lengths much greater than the coherence length of the incident radiation.

It may be difficult to align the grids in a Talbot interferometer and achieve mechanical stability of the two or three grids with an accuracy of much better than a grid period ($\approx 4\mu$m) which provides some practical difficulties to its implementation.

If the second grid of the Talbot interferometer is placed, not at the Talbot distance, but rather in the geometric shadow of the first grid, the method is known as coded aperture phase contrast[5] (Olivo et al., 2001; Olivo and Speller, 2007a,b,c). Two apertures are used in coded aperture phase contrast, analogous to the Talbot interferometer, however the grating period is much larger (factor of $\approx 80$). The second, analyser, grid is not at the Talbot distance of the first, but in its geometric shadow. The second grid is placed in contact with the detector so that the beams from the first grid intersect the edges of the second. When a sample is placed after the first grid a majority of the refraction from the sample in one direction is attenuated, resulting in measurable phase contrast.

The coded aperture and Talbot interferometry imaging (TII) techniques are most sensitive (and least efficient) when the second grid is set to extinguish all X-rays from the first in the absence of the sample. Likewise both methods are able to trade off some sensitivity or contrast for an increased efficiency by moving the second grating from dark-field to differential mode.

Finally, two other phase contrast techniques that use a similar approach to the coded aperture method: the segmented detector (Hornberger et al., 2008) and the array structured detector (Coan and Bravin, 2007). By isolating a segment of the detector in the case of Hornberger et al. (2008) or single pixels in the case of Coan and Bravin (2007) some of the scattered radiation may be excluded, resulting in measurable contrast.

[5]This technique is superficially similar to coded aperture imaging (Dicke, 1968; Fenimore and Cannon, 1978). In that technique an incoherent source is divided into individually coherent but mutually incoherent sources using a coded aperture. Each individual source creates either a projection image or Gabor hologram depending on the aperture-detector distance and the detector records an incoherent sum of the individual holograms. The arrangement of apertures is used to 'decode' the image computationally or optically.

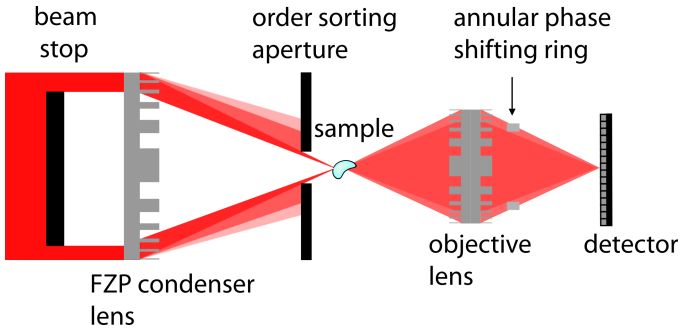


Figure 1.3: **Zernike phase-contrast imaging.** (Adapted from Neuhausler (Neuhausler et al., 2003))

### 1.1.3 Zernike/Schlieren phase contrast

Both Zernike and Schlieren phase contrast methods utilise spatial filtering to achieve phase contrast.

In the Schlieren method an X-ray wavefield is optically Fourier transformed using a lens and half the spatial frequency spectrum is blocked using a thick attenuating 'knife-edge'. The remaining field is made to form an image using another lens and the image will show phase contrast (Ojeda-Castañeda and Berriel-Valdos, 1979).

An improved method devised by Zernike (1934) merely phase shifts the central diffraction order so that it interferes with the scattered radiation. This method is more efficient than the Schlieren method because no radiation is attenuated and has the advantage of producing contrast that is directly proportional to the phase.

Zernike's method has been implemented using hard X-rays for imaging (Hwa Shik and Suk-Won, 2006; Hwa Shik and Tae Joo, 2007), as in Figure 1.3, and tomography (Aoki et al., 2007) but for the lack of efficient lenses at high energy the technique is not widely used. It seems that Schlieren phase contrast (Ojeda-Castañeda and Berriel-Valdos, 1979) has yet to be implemented for hard X-rays[6].

The limitation of Zernike/Schlieren methods in the context of hard X-ray imaging is the reliance on a lens to spatially separate the spatial frequencies for filtering. Of the different optical elements that are available to focus hard X-rays (Erko et al., 1996) we will briefly digress to consider the Fresnel Zone Plate (FZP) (Baez, 1961; Kirz, 1974).

The FZP is a thin circular object whose transmission function is designed in such a way as to attenuate every other Fresnel zone in concentric circles centred on the optical

[6]Analyser-based phase contrast imaging has been called a Schlieren-type method (Förster et al., 1980). As the phase of the rocking curve varies from 0 through $\pi$ over its angular width this is analogous to the conventional Schlieren method except instead of attenuating the field on one side of the knife edge, the crystal phase shifts these spatial frequencies by $\pi$ radians.

axis (Ojeda-Castañeda and Gómez-Reino, 1996). An alternative to the conventional FZP which is based on attenuating every other Fresnel zone is the phase FZP which instead phase shifts every other zone by $\pi$ with a concomitant increase in efficiency. In practice it is difficult to fabricate a continuously varying thickness profile and by way of compromise the FZP can be made as a binary mask which has the effect of producing a series of foci. High-resolution and low-wavelength imaging both require very fine outermost zone widths which are difficult to fabricate and present a serious practical limitation. The efficiency of an FZP is limited to approximately 10% for attenuating FZP's and 40% for phase FZP's at their design wavelength.

The Zernike and Schlieren methods employ two FZP's with a concomitant loss of flux making them feasible only with a brilliant X-ray source. The FZP is more efficient with longer wavelengths and so for soft X-rays it is possible to use FZP's to construct scanning transmission X-ray microscopes (STXM) images from which the phase of the sample can be retrieved (Chapman, 1996; De Jonge et al., 2007, 2008).

As an alternative to using a lens to separate spatial frequencies the same result can be achieved through the introduction of a suitable distance between sample and detector. This method of separating the spatial frequencies is known as far-field or Fraunhofer imaging (Born and Wolf, 1999). An image will be in the far-field if the Fresnel number (Saleh and Teich, 1991; Born and Wolf, 1999),

$$N_F = g^2/\lambda z \tag{1.2}$$

is much less than unity for a feature size $g$, wavelength $\lambda$ and sample-detector distance $z$. For a given $z$ and $\lambda$ only feature sizes smaller than $g$ will be in the far field. Practical values for $z$ are typically a few meters which places an upper limit on $g$ of the order of micrometres for hard X-rays.

### 1.1.4 Lensless Diffractive Imaging

The difficulty of fabricating X-ray lenses is moot for imaging techniques that do not require a lens. If we remove the objective lens of the X-ray microscope (cf. Figure 1.3) and move the detector sufficiently far from the sample such that $N_F \ll 1$ it will record the far field diffraction pattern of the sample. Further, if we recognise that the complex spatial frequency spectrum of a wavefield contains equivalent information to the complex wavefield over the image plane then we may choose to measure the former instead of the latter and simply apply an inverse Fourier transform to recover the image. This idea is the basis for the field of study known as lensless imaging,

diffraction microscopy or coherent diffractive imaging (CDI) (Cederquist et al., 1988; Miao et al., 1999, 2008).

The fundamental difficulty of CDI is that the phase of the Fourier transform (lost upon measurement) must be recovered before the diffraction pattern is inverted to recover the image. In general this is known as the 'phase problem', about which more will be said in §1.2, and describes a class of problems which aim to infer the phase of a complex scalar wavefield from intensity measurements either analytically or iteratively. The problem is well known, most notably in the fields of visible light and electron optics where intensity measurements over one or more planes are used to reconstruct the phase. The phase problem was discussed in relation to quantum mechanics as early as 1933 when Pauli (Pauli, 1980) considered the problem of whether two quantum mechanical wavefunctions linked by a Fourier transform were uniquely specified by their magnitudes only (Orlowski and Paul, 1994).

The phase retrieval encountered in CDI is an important subset of the phase problem where the phase and amplitude of a wavefield are reconstructed from measurements of the magnitude of the Fourier transform, a directly measurable experimental quantity. The problem was investigated in X-ray crystallography (Harker and Kasper, 1948), electrons (Weierstall et al., 2002), coherence theory (Walther, 1963), stellar interferometry (Labeyrie, 1970) and neutron reflectometry (De Haan et al., 1995).

CDI diffraction patterns can, in principle, be measured to diffraction limited resolution using a large enough detection area. The number of photons scattered into the highest spatial frequencies is typically many orders of magnitude lower than the zeroth-order spatial frequency which means diffraction limited imaging requires a very bright beam or a long exposure time. A related practical problem is the need for high dynamic range detectors which do not currently exist. To overcome this problem multiple exposures can be used with either a beam stop for the central order or by creating a composite image (Miao et al., 1999).

Active areas of CDI research include the three-dimensional structural characterisation of nanocrystalline materials and quantitative imaging of nanoparticles (Vartanyants et al., 2005; Miao et al., 2006) and high resolution imaging of non-crystalline materials (Chapman et al., 2006; Bogan et al., 2008).

Variants of the technique include using a scanning aperture with overlapping areas as a phase retrieval constraint (Rodenburg, 2001; Faulkner and Rodenburg, 2004; Rodenburg and Faulkner, 2004; Rodenburg et al., 2007a,b; Johnson et al., 2008), curved beam illumination which guarantees a unique solution (Nugent et al., 2003, 2005; Williams et al., 2006; Quiney et al., 2006; Williams et al., 2007), holographic diffractive

imaging in which a reference object is placed next to the sample to create the hologram (Stadler et al., 2008) and pulsed-beam imaging for dynamic systems (Chapman et al., 2007).

Due to the weak scattering at high spatial frequencies combined with the requirement that the sample resides within a coherent volume, lensless imaging techniques must usually be implemented at synchrotrons. However there has been an effort to develop the technique with compact X-ray sources (Sandberg et al., 2007), waveguide based X-ray sources (De Caro et al., 2008) and incoherent light (Bache et al., 2006; Minghui et al., 2007).

One commonality between the above techniques is that they all attempt to retrieve the phase using variants of a method due to Gerchberg and Saxton (1972) (Fienup et al., 1982; Fienup, 1982; Marchesini, 2007b,a). The details of the algorithm need not concern us save to note the most serious limitations of the Modified-Gerchberg-Saxton algorithm (MGSA). MGSA is unable to select a unique phase distribution from solution space of all phases that possibly satisfy the measured diffraction pattern and that the iterative process it employs may not converge to the correct solution.

The greatest strength of these techniques is that the MGSA method of phase retrieval works under quite general conditions and requires only that the entire sample located inside a coherent volume of the incident radiation.

The Fienup (Fienup et al., 1982) improvement to MGSA works by adding a constraint to the real space which may help the iterative solution to converge. Apart from the Fienup improvement there has been modest progress in the field recently and achieving a solution using MGSA-type methods remains an art and is far from automatic.

The scanning aperture technique (Faulkner and Rodenburg, 2004; Rodenburg and Faulkner, 2004) is not applicable to single image studies such as those that the free electron laser demand because the sample undergoes a Coulomb explosion shortly after being illuminated. The curved beam illumination method (Nugent et al., 2003, 2005) is applicable to soft X-ray energies and is able to uniquely reconstruct the phase if the sample can be placed at the beam focus which may be a practical difficulty. The cost of destroying an FZP for each image formed using curved beam illumination at free electron laser facilities is non-negligible.

Noteworthy progress has been made by Podorov et al. (2007) and Nakajima (2007) who have found unique solutions to the CDI problem using analytic methods. Both methods require an optical element additional to the sample. In the method of (Podorov et al., 2007) the object must reside in less than a quarter of a rectangular

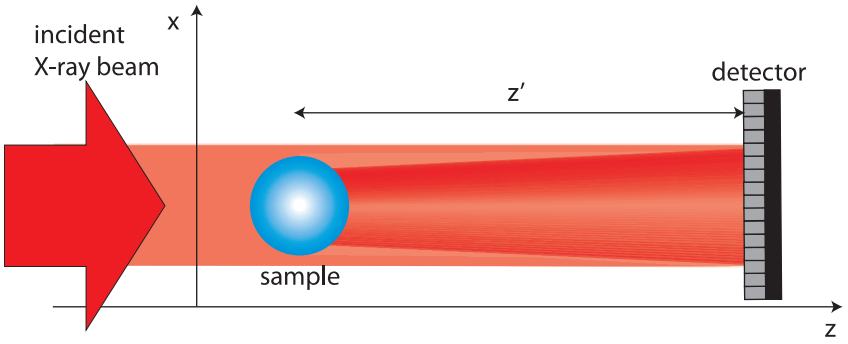


Figure 1.4: **Propagation-based phase contrast imaging.** A planar X-ray beam is incident on a sample which introduces very small phase shifts. Upon propagation a distance $z'$ adjacent rays overlap and interfere to produce phase contrast.

aperture. In the method of Nakajima (2007) a periodic array of apertures is used which have a 2μm side length meaning this technique may be difficult to implement in practice—especially if the algorithm requires sharp edges to the apertures. Quiney *et al.* (Quiney et al., 2008) have developed a method which uses a single image to estimate a longitudinal derivative from which the phase can be retrieved non-iteratively. The method used to estimate the longitudinal derivative is only approximately correct and not valid for the general case of arbitrary illumination and sample and this solution may be best used to seed iterative algorithms.

The comparable coherence requirements of lensless imaging and interferometry mean they can both be used to image thin samples in high-resolution. For interferometry the size of the crystal optics limits the field of view whereas in lensless imaging the far-field requirement of $N_F \ll 1$ (1.2) places an upper limit on sample size. In practice the lensless imaging technique is more popular because it has the potential, when used with the free electron laser X-ray source, to be a high throughput technique whereas the mechanical stability of interferometry makes changing samples difficult.

### 1.1.5 Propagation-based phase contrast imaging

If instead of propagating the wavefield into the far-field as in lensless imaging we propagate only a short distance we are led to the study of near-field, Fresnel or simply propagation-based phase contrast. It is to this subject that we now turn.

As a unit-intensity planar monochromatic X-ray wavefield transmits through a inhomogeneous, non-periodic sample it accumulates a spatially varying phase shift relative to a vacuum. Surfaces of constant phase at the exit surface of the sample are no longer planar and as the wavefield propagates optical energy will flow perpendicular

to this deformed surface (Born and Wolf, 1999), as in Figure 1.4. The distribution of optical energy, which was uniform for the plane wave, now varies in space in a manner governed by the phase variation introduced by the sample. This effect, which converts object induced phase variations into detectable phase variations, is known as propagation based phase contrast imaging (PBI) (Snigirev et al., 1995; Wilkins et al., 1996; Cloetens et al., 1996; Nugent et al., 1996).

The complexity of the relationship between the intensity and the phase increases with propagation distance $z'$ (cf. Figure 1.4). For small propagation distances, PBI contrast is strongest at the boundary between media and the contrast can be explained using geometrical optics—refraction and Snell's law (Born and Wolf, 1999). As the propagation distance increases interference fringes may begin to form and their explanation requires a wave optical theory.

If we assume our sample is illuminated by a monochromatic, paraxial scalar wavefield we may quantitatively explain PBI contrast with reference to the transport-of-intensity equation (TIE) (Teague, 1983),

$$\nabla_\perp \cdot [I(\boldsymbol{\rho}, z')\nabla_\perp \varphi(\boldsymbol{\rho}, z')] \quad = \quad -\frac{2\pi}{\lambda}\frac{\partial I(\boldsymbol{\rho}, z')}{\partial z}. \tag{1.3}$$

where the intensity $I$ is related to the phase gradient $\nabla_\perp \varphi$ transverse to the optical axis $z$ between two planes by the longitudinal intensity derivative $\partial I(\boldsymbol{\rho}, z)/\partial z$. Under the assumption of a phase object the TIE leads to the conclusion that PBI contrast is proportional to the transverse Laplacian of the phase $I \propto z\lambda\nabla_\perp^2 \varphi(\boldsymbol{\rho})$ (Bremmer, 1952; Wilkins et al., 1996). This result says that the contrast increases linearly with propagation distance, for propagation distances that are sufficiently small that $N_F \ll 1$ (cf. (1.2)).

One of the strengths of PBI is its simplicity, it requires no optical elements other than the sample to generate phase contrast. Accordingly it is widely used and is the first X-ray phase contrast technique to be adapted for clinical use as a medical diagnostic tool (Tanaka et al., 2005).

Since the wavelength appears in (1.3) as a multiplicative factor only, PBI can be implemented using polychromatic radiation (Wilkins et al., 1996; Pogany et al., 1997). The use of polychromatic radiation will cause blurring of the image due to a shifting of the fringes for each constituent wavelength which in turn will suppress the interference fringes. Remarkably, one may still obtain string PBI contrast with fully polychromatic radiation, provided the source size is sufficiently small (Wilkins et al., 1996).

PBI requires a large spatial coherence length, which can be achieved in practice using a large source-to-object distance (Snigirev et al., 1995; Cloetens et al., 1996) or

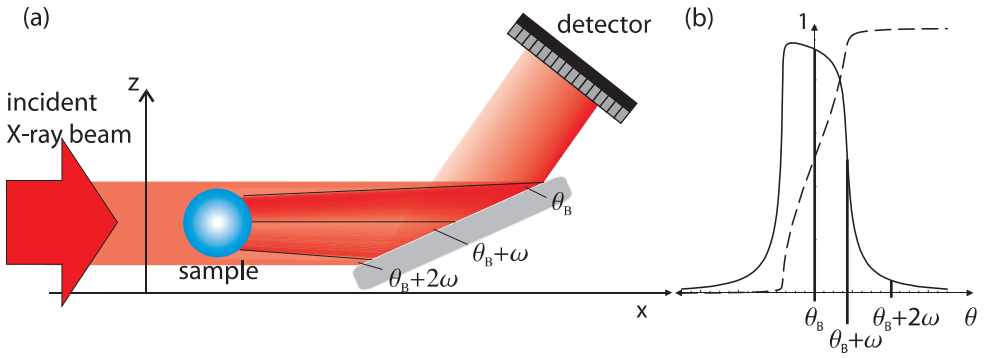


Figure 1.5: **Analyser-based phase contrast imaging.** (a) A hard X-ray beam incident from the left is transmitted through a sample before being diffracted from a thick perfect crystal and detected. (b) The (solid) amplitude and (broken) phase (divided by $\pi$) of the crystal Bragg peak plotted as a function of angle and depicting the reflectivity and phase corresponding the incident angles in (a).

a microfocus source (Pogany et al., 1997; Gureyev et al., 2001; Mayo et al., 2002b). Despite the requirement of a large coherence length PBI is a low coherence method in that it can be used to image samples that introduce optical path length shifts that are much larger than the coherence length.

PBI contrast is well known in electron (Cowley, 1995) and visible light optics (Zernike, 1942) where it is known as defocus contrast. More recently it has demonstrated with neutrons (Allman et al., 2000) and neutral atoms (Fox et al., 2002).

Another significant benefit of PBI imaging is the existence of deterministic phase retrieval algorithms which allow quantitative information to be extracted from one or more images as we shall see further in §1.2.

### 1.1.6 Analyser-based phase contrast imaging

This thesis is primarily concerned with developing new methods for quantitative analyser-based X-ray imaging. In this section we provide an overview of ABI phase contrast and the current the state of the art. We also compare ABI with the other phase contrast imaging techniques which have been covered in the previous sections.

The premise of ABI is to use a Bragg reflection[7] from a perfect crystal to create phase contrast, as shown in Figure 1.5(a). The crystal acts as a band-pass/Schlieren-type filter in Fourier space and accepts only a very narrow range of angles about the exact Bragg condition. In Figure 1.5(b) we see the amplitude and phase of the crystal reflectivity plotted as a function of angle. The undeviated beam is incident on the

[7]The arguments of this section may equivalently be applied to Laue geometry as in (Kitchen et al., 2008).

crystal slightly above the Bragg angle, this is called the working point. The refraction introduced by the sample causes the wavefield to be reflected with an angle dependent reflectivity and phase shift. This figure also makes clear that the amplitude of the Bragg peak is a band pass filter and the phase acts like a $\pi$ phase shifting Schlieren filter. The former is obvious whilst the connection to Schlieren phase contrast can be understood if we note that in Schlieren imaging half of the spatial frequencies are removed with a knife edge whereas for the wavefield incident on the analyser crystal, half of the spatial frequencies are $\pi$ phase shifted. As noted previously, the link between ABI and Schlieren imaging was stated in the paper of Förster et al. (1980).

The choice of analyser crystal and reflection has important ramifications for the contrast and resolution of the ABI image. The sensitivity of ABI contrast to phase gradients is related to the gradient of the Bragg peak, as Figure 1.5(b) makes clear. A crystal reflectivity that changes rapidly with angle is able to convert refraction from the sample through very small angles into large contrast variations. The contrast in ABI images can be increased by slightly detuning the working point from the Bragg angle to the half-reflectivity point or using higher order reflections (Rigon et al., 2002) as the angular gradient increases with reflection order. The resolution of ABI however is related to the crystal point spread function which is the Fourier space dual to the complex reflectivity. A narrow rocking curve corresponds to a wide point spread function which blurs the image detail. For best resolution a Bragg reflection with large angular acceptance should be used and so there is a trade-off between contrast (sensitivity) and resolution (Bushuev et al., 1997; Nesterets et al., 2004; Wilkins et al., 2007).

One possible way to address this tradeoff is to use strained or bent crystals which typically show oscillations in the reflectivity over a wide angular range (Kolpakov et al., 1977). The oscillations should provide contrast while the wide angular acceptance will reflect more spatial frequencies to the detector giving a higher resolution image.

ABI is only sensitive to phase gradients in the diffraction plane of the crystal. This one-directional sensitivity is the biggest limitation for ABI which may be addressed by adding a second reflection (Modregger et al., 2007b,a) or combining ABI with another phase contrast technique such as PBI (Pavlov et al., 2004, 2005; Nesterets et al., 2005b; Coan et al., 2005; Nesterets et al., 2006b) which shows two dimensional phase contrast.

The contrast in ABI images has a simple interpretation in the context of geometrical optics. In the geometrical optics approximation to ABI we perform a Taylor series expansion on the crystal reflectivity and neglect terms higher than first (Chapman et al., 1997) or second order (Pavlov et al., 2004). For objects with feature sizes

larger than a few hundred micron the spatial frequency spectrum is bandlimited to a range smaller than a typical analyser Darwin width[8] and the crystal reflectivity across this band of spatial frequencies is approximately linear. In this regime the contrast is linearly proportional to the refraction angle which in turn is proportional to the derivative of the phase. When the linear approximation to the reflectivity is not valid, such as at the top or tails of the Bragg peak, the contrast is more complicated.

The phase derivative contrast of ABI may be compared with the phase Laplacian contrast of PBI (cf. §1.1.5). The second-derivative contrast will appear most strongly at the boundary between media whereas the first derivative contrast also appears strongly for a smoothly varying phase between boundaries. Ingal and Beliaevskaya (1995) have distinguished between these two cases as boundary and area contrast, respectively.

Practical difficulties to the implementation of ABI are similar to those encountered by X-ray interferometry: mechanical stability and a limited field of view (cf. §1.1.1). Since perfect single crystals are typically used as the analyser it must be possible to grow a large enough crystal to intercept the entire beam. The Bragg peak subtends a very narrow angular range and is susceptible to very slight mechanical and thermal instability. Silicon analysers are often used because they have small thermal expansion coefficients and can be grown in large single crystals.

ABI was first used to characterise targets for laser fusion experiments by Förster et al. (1980). This seminal work contains the kernel of much of the work when ABI was revisited more than a decade later (Somenkov et al., 1991; Ingal and Beliaevskaya, 1995; Davis et al., 1995a,b; Davis, 1996; Chapman et al., 1997) including both wave optical and geometrical explanations of ABI, the increased sensitivity of asymmetric reflections to phase gradients and asymmetric reflection magnification. Asymmetric reflections in ABI can be exploited to magnify the image (Modregger et al., 2006).

The exquisite sensitivity of ABI means it has the potential to be used in a number of areas including medical diagnostics (Arfelli et al., 1998, 2000; Bravin et al., 2002; Bravin, 2003; Lewis et al., 2002; Rigon et al., 2005), materials characterisation and finding historical relics hidden in paintings (Krug et al., 2008).

In ABI the crystal performs an analogous function to the analyser grating in Talbot interferometry and coded aperture phase contrast (cf. §1.1.2). However, owing to the microscopic periodicity of the crystal, and the associated narrow-Darwin-width Bragg peak, it is far more sensitive to phase gradients than macroscopic periodicity grating or aperture-based methods. Continuing further with the analogy suggests another

[8] The differential mode for ABI identified by Gureyev and Wilkins (1997).

form of phase contrast imaging system where one might choose to replace the two gratings of a Talbot interferometer with thin Laue crystals. The result is almost full circle back to X-ray interferometry however in this case we do not recombine the two beams for interference contrast and the first crystal serves only to separate the incident wavefield into discrete diffraction orders.

ABI is sensitive to the spatial and temporal coherence of the illuminating radiation (Nesterets et al., 2005b). In general the contrast and resolution decrease with coherence lengths but we will give a more detailed statement about the coherence requirements of ABI in §3.2. A majority of ABI experiments are performed using synchrotron X-ray sources because of the increased flux and coherence compared to compact bremsstrahlung sources. The crystal rejects a significant proportion of the incident radiation so the increased flux is used to reduce exposure times whilst the large coherence lengths are suitable for ABI imaging. Notwithstanding synchrotron measurements there have been a few measurements of ABI images using anode based sources (Förster et al., 1980; Somenkov et al., 1991; Ingal and Beliaevskaya, 1995; Davis et al., 1995a,b; Bushuev et al., 1997) however the practice is not widespread despite the potential usefulness of ABI as an imaging and characterisation tool.

The phase contrast imaging systems we have been introduced to thus far are useful for making qualitative measurements about samples. In the hard X-ray regime the phase-sensitive measurements are superior to absorption-based measurements for light elements, however absorption measurements may be inverted using Beer's law (Born and Wolf, 1999) to extract quantitative information. We would now like to discuss the quantitative aspect to phase contrast imaging: phase retrieval. Phase retrieval, which allows us to extract quantitative measurements from phase contrast images, has enormous practical importance and so we will give a brief account of the current state of the art.

## 1.2 Phase retrieval

Forward problems, of which imaging is an example, seek to predict the result of a measurement whilst inverse problems (Goncharskii et al., 1992), of which phase retrieval is an example, seek to determine the initial conditions that gave rise to a measurement. So it is to a famous incarnation of the inverse problem we now turn: the phase problem.

Phase retrieval is a generic term describing a class of problems whose aim is to infer the phase of a wavefield from intensity measurements, either analytically or iteratively.

Phase retrieval is the complement of Beer's law (Born and Wolf, 1999) for absorption contrast images in that it allows quantitative measurements to be extracted from phase contrast images. Beer's law states that the projected thickness of an object composed of a single material is linearly proportional to the logarithm of the normalised intensity. Similarly, phase retrieval algorithms attempt to relate the projected thickness (or, more generally, the phase of the wavefield at the exit face of the object) to the measured intensity however their relationship usually has a more complex character than Beer's law because of the wave optical aspect necessary to explain phase effects.

We have already touched on phase retrieval as it applies to the problem of lensless coherent imaging (cf. §1.1.4) and we will now cover some of the important developments of phase retrieval in PBI and ABI.

Phase retrieval in PBI has a long history beginning with the Nobel prize winning work of Gabor (1948). In Gabor's holography the phase and amplitude of a wavefield at the exit surface of a sample are encoded in the propagated intensity by regarding this propagated intensity ('hologram') as resulting from the interference between the unscattered ('reference') and scattered ('object') waves. The intensity can be decoded either optically or computationally after the measurement to recover the incident complex wavefield. We can view a PBI image as a short-propagation-distance in-line hologram which may be inverted to recover the complex wavefield.

Widely used approaches to PBI phase retrieval include those based on the TIE (Teague, 1983), the ambiguity function (Papoulis, 1962) and the Fresnel diffraction integral (Born and Wolf, 1999). Early PBI phase retrieval work lead to a number of methods (Teague, 1983; Gureyev et al., 1995; Gureyev and Nugent, 1996, 1997; Paganin and Nugent, 1998; Gureyev et al., 1999; Paganin and Nugent, 2001; Nugent, 2007) which are able to recover the phase analytically given measurements of the intensity over successive planes separated by a suitable propagation distance. These methods have in common that, unlike the MGSA, they recover the phase uniquely and non-iteratively which is a significant advantage.

To uniquely recover the phase and amplitude of a wavefield requires, in general, either two intensity measurements so that the amount of information input to the reconstruction algorithm is equivalent to the output. The complex wavefield of a pure phase object may, however, be uniquely reconstructed from a single intensity measurement (Gureyev et al., 1999; Bronnikov, 1999, 2002).

Similarly, for objects composed of a single material the phase may be retrieved from a single image (Paganin et al., 2002). Single image phase retrieval paves the way for tomographic (Mayo et al., 2003a; Myers et al., 2007, 2008) and real-time analyses

where it is impractical or impossible to measure two images at different distance from the sample.

A popular approach to ABI phase retrieval uses the geometrical optics approximation (Chapman et al., 1997; Pavlov et al., 2001; Rigon et al., 2003; Nesterets et al., 2006a; Kitchen et al., 2007; Rigon et al., 2007a) to recover quantitative information from images recorded at different angular deviations of the analyser crystal. This simplified approach expands the crystal transfer function as a Taylor series and ignores higher order terms (see e.g. Pavlov et al. (2004)) and can lead to artifacts in the reconstruction but is easy to implement numerically. Variants of the technique use multiple images to improve the quality of the reconstruction (Oltulu et al., 2003; Pagot et al., 2003; Wernick et al., 2003; Rigon et al., 2007b).

In order to extract quantitative information using a more rigorous wave optical approach to ABI (Guigay et al., 2007) requires that approximations are made to the sample transmission function. For samples which interact only very weakly[9] the weak object approximation may be used (Cowley, 1995). The weak object approximation linearises the sample transmission function (Born and Wolf, 1999) so that, to first order, the complex scalar wavefield is proportional to the phase shift and attenuation. The linear relationship between intensity and phase means the phase retrieval problem is tractable in ABI (Nesterets et al., 2004, 2005a) and PBI (Pogany et al., 1997). The weak object approximation is very restrictive and in practice most samples introduce phase shifts that are sufficiently large to render the weak-object approximation inapplicable.

Paganin et al. (2004) and Pavlov et al. (2004) developed generalised phase retrieval algorithms that can be applied to PBI and ABI under the approximation of a linear and slowly varying transfer function respectively. Importantly the algorithm of Paganin et al. (2004) is adaptable to single image phase retrieval for ABI (Briedis et al., 2005).

All of the previously described phase retrieval algorithms have a significant commonality in that, without exception, they assume that the state of the imaging system is known prior to the measurement. In that case the *a priori* knowledge of the imaging system is used to infer information about the sample. One of the core ideas that forms the latter part of this thesis is to investigate methods of measuring the state of the imaging system given knowledge of the sample: in effect we have swapped the roles of what is known and unknown. Thus, rather than viewing a known optical system as a means for studying an unknown object, we may view a known object as a tool for probing an unknown optical system.

This leads to the idea of Green's function reconstruction and we will show that this

[9] Phase shift much less than 1 radian and attenuation of no more than a few percent.

idea has many potential uses, not the least of which is its application to crystallography which we will explore in detail.

## 1.3 Summary

To place the work that follows in context we have reviewed some important results in the field of X-ray phase sensitive imaging.

We have covered six methods for implementing phase contrast imaging; the X-ray interferometer, the Talbot interferometer, Zernike and Schlieren methods, lensless diffractive imaging, propagation-based phase contrast imaging and analyser-based phase contrast imaging. Each of these has subtly different coherence requirements, shows contrast which proportional to the phase directly or through a first or second derivative and have various levels of sensitivity to phase gradients.

There is no preferred, or best, method. The suitability of each must be decided by the use to which it will be applied. Considerations include the coherence of the source, the size of the sample, the required resolution in the image, the number of samples and time available to image them.

PBI is sensitive to the Laplacian of the phase (Bremmer, 1952) and so is useful for so called 'edge-enhancement' applications where strong boundary contrast is all that is required. TII and its variants are sensitive to the derivative of the phase and are thus useful for area- as well as edge-enhancement contrast (Pfeiffer et al., 2006; Olivo and Speller, 2007a). Unlike PBI however both of these techniques require additional optical elements which pose certain experimental difficulties.

Interferometry and lensless imaging as examples of high coherence methods can be grouped together since both require small samples that can fit within a coherent volume.

The remaining techniques (ABI, PBI and TII (and variants)) are low-coherence and there has been a significant push in the past few years, as evidenced by the high impact journals the work relating to TII especially appears in, to develop low coherence methods for imaging biological and light materials samples.

TII and PBI are perhaps the most accepted methods for incoherent-source phase imaging. PBI has been commercialised (Wilkins, 1995) and is being trialled as a diagnostic tool in clinical mammography (Tanaka et al., 2005) and the former methods are a more recent technique which claim to be suitable for use with incoherent sources (Pfeiffer et al., 2006) but the total number of researchers working on it is small. Both of these approaches have been demonstrated with phase retrieval using an

incoherent source (Pfeiffer et al., 2006; Mayo et al., 2002b). However, there have been no studies conducted to show that quantitative phase retrieval is possible using ABI with an incoherent source or to determine the general conditions under which ABI contrast should be measurable.

The phase retrieval algorithms presented in §1.2 are all predicated on the notion that the state of the imaging system is known *a priori*. In cases where the imaging system Green's function is not known or requires validation no general method exists with which to measure or reconstruct it. We will pursue this idea in the latter part of this thesis to develop and implement such a technique we refer to as Green's function reconstruction.

Further, if one pursues this idea we find an entirely new application for Green's function reconstruction beyond phase contrast imaging such as inferring crystalline structure and verifying complex propagators.

A detailed exposition of these ideas will follow in later chapters but first we will, in Chapter 2, formulate the background theory required to place the results in a quantitative context.

# 2 Propagation and scattering

In this chapter we consider image formation in an analyser-based phase contrast imaging system. An electromagnetic wavefield originates at a source and propagates through an imaging system, interacting with the sample and then the analyser crystal before forming an image at the detector. We will review the description of each of these interactions in turn and close the chapter with a quantitative statement of the associated forward problem of image formation in an analyser-based phase contrast imaging system.

We first consider the equation governing the propagation of waves in the classical electric field and how those waves may be detected (§2.1). We then briefly discuss the coherence of X-ray wavefields in relation to phase contrast imaging (§2.2) so that we may discuss partially coherent radiation in Chapter 3. The analysis in the proceeding sections will loosely follow the path of the wavefield as it propagates through a propagation/analyser-based phase contrast imaging system. We consider some properties of electromagnetic waves and their interaction with an inhomogeneous object—the 'sample' we wish to image (§2.3). This section describes the use of the projection approximation which allows the exit plane wavefield to be expressed in terms of the projected linear attenuation coefficient of the sample.

The next two sections describe the diffraction of X-rays through free space (§2.4) and from laterally homogeneous crystals (§2.5). The analysis of free space diffraction uses the angular-spectrum formulation for propagation of a wavefield from plane to parallel plane. The angular spectrum exactly solves the Helmholtz equation for forward-propagating waves, allowing numerical simulations throughout the thesis to be implemented efficiently and accurately. The section on diffraction from crystals with slight deformations is more detailed than the analysis of free space propagation because later chapters will have recourse to determine what the diffracted field tells us about crystal structure. The history of X-ray crystallography is resplendent with

the achievements of many brilliant scientists so it is necessary to cherry pick some relevant results: the dynamical theory of Takagi and its kinematic approximation. Between dynamic and kinematic scattering from slightly strained crystals we have all that is necessary for placing the work of later chapters involving X-ray interaction with crystals into context.

We then introduce the operator formalism for linear shift-invariant optical elements (§2.6) which is useful to expedite the expression of integral equations describing wavefield propagation and scattering and is used extensively in the numerical simulation of the forward problem. This final section brings the results of the chapter together in an operator expression for the forward problem of ABI imaging using an incoherent source.

We conclude these opening remarks with a brief indication of how the background material in the present chapter relates to the remainder of the thesis. (i) The operator expression in leads directly in to the work of Chapter 3 where we demonstrate quantitative ABI phase retrieval using an extended incoherent X-ray source. The forward simulation of this problem uses many of the results of this chapter including the angular spectrum and the dynamical diffraction of an X-ray wavefield from a thick perfect crystal. (ii) In Chapter 4 we consider the problem of Green's function retrieval from a phase contrast image of a weak object. Accordingly the present chapter gives a brief account of Green's function solutions to linear differential equations using the operator formalism and develops the weak object notation for later use. (iii) Chapter 5 presents the result of an experiment in which the Green's function reconstruction approach developed in Chapter 4 is applied to a thick perfect crystal Bragg reflection. We again draw on the result of scalar diffraction and dynamical diffraction developed in the present chapter.

## 2.1 Electromagnetic waves

Maxwell's equations describe the spatio-temporal evolution of electromagnetic waves (Born and Wolf, 1999) and are the starting point for our investigation. We henceforth assume that all materials we encounter are non-magnetic, linear and isotropic. Waves in the electric field $\mathbf{E}$ in a medium with a static electrical permittivity $\epsilon$ and magnetic susceptibility $\mu$ propagate according to (Good, 1999; Attwood, 2000),

$$\nabla^2\mathbf{E} - \epsilon\mu\frac{\partial^2\mathbf{E}}{\partial t^2} = \nabla\left(\frac{\rho}{\epsilon}\right) + \mu\frac{\partial\mathbf{J}}{\partial t} \tag{2.1}$$

where $\mathbf{J} = \mathbf{J}(\mathbf{r}, t)$ is the current density, $\rho = \rho(\mathbf{r}, t)$ is the charge density, $\mathbf{r} = (x, y, z)$ is a position vector in a right-handed Cartesian coordinate system and $t$ is time. In a vacuum $\epsilon = \epsilon_0$ and $\mu = \mu_0$ where $\epsilon_0$ and $\mu_0$ are the vacuum permittivity and permeability respectively.

X-ray detectors respond to the optical energy, or intensity I, of the field (Good, 1999) which is related to the field amplitude by the instantaneous intensity. The instantaneous intensity of the electric field is given by (Mandel and Wolf, 1995)[p. 162][1],

$$I(\mathbf{r}, t) = \mathbf{E}(\mathbf{r}, t) \cdot \mathbf{E}(\mathbf{r}, t). \tag{2.3}$$

The time-dependent fluctuation of the field is unobservably large and as a result the detected intensity is given by the following time average (Mandel and Wolf, 1995),

$$I(\mathbf{r}) = \frac{1}{T}\int_{-T/2}^{T/2} I(\mathbf{r}, t)dt = \langle I(\mathbf{r}, t)\rangle, \tag{2.4}$$

where the time interval $T$ is much greater than the characteristic timescale of the field oscillations. In the averaging of (2.4) we lose direct access to the phase information of the electric field. It is this inability to directly measure the phase that necessitates the indirect phase sensitive imaging techniques of §1.1.

For a majority of the results presented in this thesis the vectorial nature of the electric field may be ignored. The transition from vector to scalar theories is discussed in Nieto-Vesperinas (1991) and Born and Wolf (1999) and we note that we may choose a single scalar component of (2.1) to describe the field. Ignoring the vectorial nature of a paraxial field will, at most, add a multiplicative factor to the intensity which depends on experimental geometry[2] (Cowley, 1995). The proceeding analysis can be simplified by describing the field amplitude in terms of a complex scalar wavefunction $\psi$ (Born and Wolf, 1999; Mandel and Wolf, 1995; Wolf, 2007)[3]. Furthermore, since

[1] The formal definition of the instantaneous intensity of a plane wave is (Born and Wolf, 1999)

$$I(\mathbf{r}, t) = \sqrt{\frac{\epsilon}{\mu}}\mathbf{E}(\mathbf{r}, t) \cdot \mathbf{E}(\mathbf{r}) \tag{2.2}$$

however since we are interested relative measurements of the intensity and not its absolute value the multiplicative constant is irrelevant and can be neglected.

[2] We will revert to a vector theory to discuss the dynamical theory of X-ray diffraction from crystals however we will again find that for the cases in which we are interested the effects of polarisation will result in a multiplicative factor.

[3] In the complex representation the definition of instantaneous intensity (2.3) should be modified

$$I(\mathbf{r}, t) = \mathbf{E}(\mathbf{r}, t) \cdot \mathbf{E}^*(\mathbf{r}, t)$$

where $*$ denotes complex conjugation.

we are interested primarily in coherent scattering we need only consider a single monochromatic component of the field (Born and Wolf, 1999),

$$\psi(\mathbf{r}, t) = \psi(\mathbf{r}, \omega) \exp(-i\omega t). \tag{2.5}$$

It behooves us to drop the functional dependence on $\omega$ with the assumption that henceforth $\psi$ refers to the spatial part $\psi(\mathbf{r}, \omega)$ unless otherwise stated. A polychromatic field can be synthesised where necessary from a weighted sum of monochromatic components considered separately in a Fourier integral. In a vacuum (2.1) in terms of $\psi$ becomes the Helmholtz equation (Born and Wolf, 1999),

$$\nabla^2\psi + k^2\psi = 0, \tag{2.6}$$

where $\nabla = (\partial/\partial x, \partial/\partial y, \partial/\partial z)$, $k = \omega/c = 2\pi/\lambda$ is the wave number and $\lambda$ is the radiation wavelength. For clarity we will define a convention for this thesis that $\Delta$ will be used to represent a small finite change in the quantity it prepends and never the Laplacian. We define for later reference the wave vector $\mathbf{k}$ which has magnitude $|\mathbf{k}| = 2\pi/\lambda$ and Cartesian components $\mathbf{k} = (k_x, k_y, k_z)$, the transverse wave vector $\boldsymbol{\kappa} = (k_x, k_y)$, transverse position vector $\boldsymbol{\rho} = (x, y)$ and transverse gradient operator $\nabla_\perp = (\partial/\partial x, \partial/\partial y)$. Boldface symbols in this thesis will always represent a different quantity than their non-bold versions.

A brief digression is warranted here to set out the convention that will be used for the transverse Fourier transform (Bracewell, 1986),

$$\tilde{\psi}(\boldsymbol{\kappa}) = \frac{1}{2\pi}\iint \psi(\boldsymbol{\rho}) \exp(-i\boldsymbol{\kappa}\cdot\boldsymbol{\rho})\, d\boldsymbol{\rho}, \tag{2.7}$$

$$\psi(\boldsymbol{\rho}) = \frac{1}{2\pi}\iint \tilde{\psi}(\boldsymbol{\kappa}) \exp(i\boldsymbol{\kappa}\cdot\boldsymbol{\rho})\, d\boldsymbol{\kappa}. \tag{2.8}$$

Symbolically the transverse Fourier transform operator may be written,

$$\tilde{\psi}(\boldsymbol{\kappa}) = \mathcal{F}[\psi(\boldsymbol{\rho})], \tag{2.9}$$

$$\psi(\boldsymbol{\rho}) = \mathcal{F}^{-1}[\tilde{\psi}(\boldsymbol{\kappa})]. \tag{2.10}$$

## 2.2 Coherence at X-ray wavelengths

The field of coherent X-ray scattering subsumes a range of science of which phase contrast imaging forms only one part (Lengeler, 2001, 2007; van der Veen and Pfeiffer, 2004). Coherence is at the heart of any phase contrast imaging system as it quantifies the ability of a wavefield to be the carrier of phase information and manifest interference fringes. The coherence requirements of the various types of phase contrast

imaging systems differ and consequently may be used with some X-ray sources only in conjunction with filtering to increase the coherence. In this section we will define some of the basic concepts of coherence for use later in the thesis.

The coherence of a scalar X-ray wavefield with mean wavelength $\bar{\lambda}$ is quantified by the spatial coherence area and temporal (chromatic) coherence length (Mandel and Wolf, 1995; Wolf, 2007),

$$A_S \approx \frac{\bar{\lambda}^2}{\Delta\Omega} \quad ; \quad L_T \approx \frac{\bar{\lambda}^2}{\Delta\lambda} \tag{2.11}$$

where $\Delta\lambda$ is the wavelength spread and $\Delta\Omega \approx d^2/z^2$ is the solid angle subtended by the source, with area $d^2$, from the point of observation at a distance, $z$. We can define a coherent volume $V_c = A_S L_T$ that describes the extent of space around a given point over which there is a persistent relationship in the phase. Quantum mechanically the coherent volume represents the region of space throughout which the photons of the field are intrinsically indistinguishable from each other (Mandel and Wolf, 1995). The bandwidth and apparent size of an X-ray source determines the coherence as defined by (2.11). The spatial coherence area may be increased by moving far from the source thereby decreasing its apparent size.

In Chapter 3 we will have cause to compare the coherence of synchrotron and anode-based X-ray sources. X-ray tubes and synchrotron storage rings radiate incoherently and require filtering to increase the coherence used to measure phase contrast. In contrast to chaotic sources the next generation of X-ray sources will utilise stimulated emission and so have large coherent volumes however these have only recently become available for soft X-rays and are under development for hard X-rays (Rullhusen, 1992; O'Shea and Freund, 2001; Lee and Choi, 2007; Kapteyn et al., 2007).

To quantify the quality of an X-ray source to produce radiation for coherent imaging applications we use the spectral brilliance (Attwood, 2000),

$$B = \frac{\text{power}}{\text{unit phase space}} = \frac{\Delta P}{\Delta A \cdot \Delta\Omega \cdot BW} \tag{2.12}$$

where $\Delta P$ is the power radiated into an area $\Delta A$ subtending an angle $\Delta\Omega$ with spectral bandwidth BW. This relationship implies that the coherent volume can be increased at the expense of photon flux through filtering. Synchrotron radiation, which is strongly peaked in the forward direction (Margaritondo, 2002) has a higher brilliance than an X-ray tube which uses Bremsstrahlung radiation. The characteristic energy of the X-ray tube anode ($\Delta\lambda/\lambda \approx 3.2\times10^{-4}$ for CuK$\alpha$1 radiation (Zaus, 1992)) gives comparable monochromaticity to what can be attained using a synchrotron double crystal monochromator (Si(111) $\Delta\lambda/\lambda \approx 1.3 \times 10^{-4}$ for CuK$\alpha$1 (Stepanov, 2008))

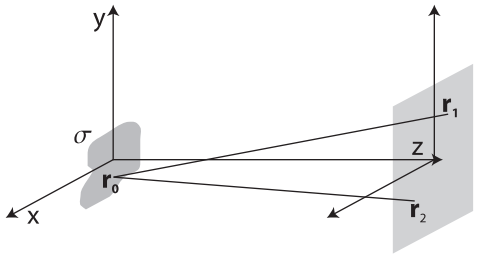


Figure 2.1: **The van Cittert-Zernike theorem.** The two point correlation between the X-ray wavefield detected at $\mathbf{r}_1$ and $\mathbf{r}_2$ due to an incoherent, quasi-monochromatic source $\sigma$ radiating into a vacuum, is given by the van Cittert-Zernike theorem.

whereas the synchrotron is able to deliver a tunable energy. We will often encounter radiation with the property that $\Delta\lambda \ll \bar{\lambda}$ and we will refer to such a field as quasi-monochromatic (Mandel and Wolf, 1995).

A radiation source is considered locally incoherent if there is no correlation in the phase between adjacent radiators (Mandel and Wolf, 1995). Such an extended incoherent source is a useful practical model of X-ray tube sources (and synchrotrons) and as such we would like to briefly describe the van Cittert-Zernike theorem (van Cittert, 1934; Zernike, 1938) which shows how to calculate the intensity recorded over a planar surface a distance $z$ from such a source.

To this end we introduce the mutual intensity $J_I$ for quasi-monochromatic radiation (Mandel and Wolf, 1995; Born and Wolf, 1999; Goodman, 2000; Wolf, 2007),

$$J_I(\mathbf{r}_1, \mathbf{r}_2) = \langle \psi^*(\mathbf{r}_1, t)\psi(\mathbf{r}_2, t)\rangle, \tag{2.13}$$

where angular brackets again denote a time average (cf. (2.4)).

With reference to Figure 2.1 the van Cittert-Zernike theorem is (Born and Wolf, 1999),

$$J_I(\mathbf{r}_1, \mathbf{r}_2) = \int_\sigma I(\mathbf{r}_0) \frac{\exp\left\{i\frac{2\pi}{\bar{\lambda}}\left[|\mathbf{r}_2 - \mathbf{r}_0| - |\mathbf{r}_1 - \mathbf{r}_0|\right]\right\}}{|\mathbf{r}_1 - \mathbf{r}_0||\mathbf{r}_2 - \mathbf{r}_0|} d\mathbf{r}_0 \tag{2.14}$$

where $I(\mathbf{r}_0)$ is the source intensity per unit area This theorem relates the field correlation between points $\mathbf{r}_1$ and $\mathbf{r}_2$ due to a quasi-monochromatic, planar incoherent source of X-rays $\sigma$.

Roughly speaking, the van Cittert-Zernike theorem states that the coherence of a wavefield measured over a plane a perpendicular distance $z$ from an incoherent source will increase as $z$ increases. Physically this means that as the wavefield from disparate, mutually incoherent source points propagates out, these wavefields will superpose and in the region of the superposition there will exist non-negligible correlations (Mandel and Wolf, 1995).

The intensity at $\mathbf{r}_1$ is given by,

$$I(\mathbf{r}_1) = J_1(\mathbf{r}_1, \mathbf{r}_1) = \int_\sigma \frac{I(\mathbf{r}_0)}{|\mathbf{r}_1 - \mathbf{r}_0|^2} d\mathbf{r}_1. \tag{2.15}$$

In the context of incoherent imaging this result tells us that we simply add the contributions of each source point incoherently to find the total field. The result in (2.15) applies to diffraction of X-rays from an incoherent source through free space however its is readily generalisable to an arbitrary linear propagator $G(\mathbf{r}, \mathbf{r}')$ (such as we will encounter later in the form of diffraction from a crystal) (Wolf, 2007),

$$I(\mathbf{r}_1) = \int_\sigma I(\mathbf{r}_0) G^*(\mathbf{r}_1, \mathbf{r}_0) G(\mathbf{r}_1, \mathbf{r}_0) d\mathbf{r}_0. \tag{2.16}$$

## 2.3 Propagation of X-rays through inhomogeneous media

In this section we will consider the problem of describing an X-ray wavefield in a inhomogeneous dielectric material.

The response of a dielectric material to an incident field is described by the dielectric permittivity tensor $\epsilon_{ij}(\mathbf{r})$ which may vary with position through the material and with the frequency of the driving field (Kolpakov et al., 1978). In the X-ray frequency range and far from an absorption edge we may neglect the tensorial aspect of the permittivity, replacing the tensorial field $\epsilon_{ij}(\mathbf{r})$ by the complex scalar field$\epsilon(\mathbf{r})$ (Kolpakov et al., 1978). The complex refractive index is related to the permittivity by (Authier, 2005),

$$n = \sqrt{\frac{\epsilon}{\epsilon_0}} \tag{2.17}$$

and as is customary we introduce the definition

$$n = 1 - \delta + i\beta \tag{2.18}$$

where the real numbers $\delta$ and $\beta$ are the refractive index decrement and attenuation coefficient respectively. In general, both $\delta$ and $\beta$ are functions of the radiation wavelength however we will not explicitly denote the wavelength dependence since we consider monochromatic radiation.

In an inhomogeneous medium waves propagate according to,

$$\nabla^2 \psi + k^2 n^2(\mathbf{r}) \psi = 0. \tag{2.19}$$

which is the inhomogeneous Helmholtz equation (cf. (2.6)).

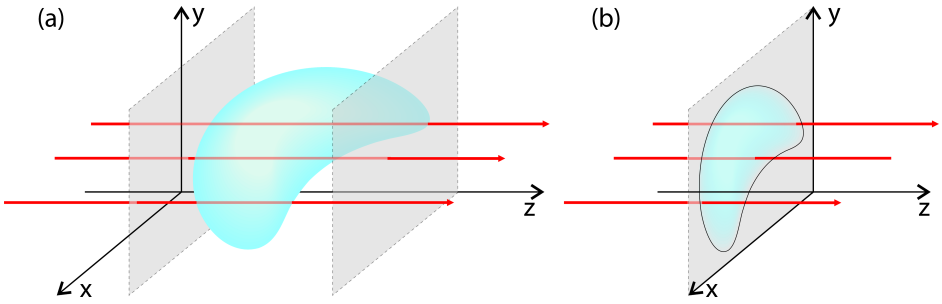


Figure 2.2: **The projection approximation.** (a) An object with complex refractive index $n(\mathbf{r})$ that interacts weakly with hard X-rays lies between two planes. (b) The projection approximation has been used to compress the object along the z-axis to create an equivalent object that can be expressed in terms of a projected refractive index $n(\boldsymbol{\rho}, z)$.

### 2.3.1 The projection approximation for inhomogeneous media

Consider the plane-to-plane propagation of a paraxial scalar beam-like wavefield through an inhomogeneous object wholly residing within the intervening space as in Figure 2.2(a). For a sufficiently thin and weakly interacting object we may assume that the path of the X-rays traversing the object are not significantly different than they would have been in vacuum. In this case the wavefield accumulates phase and attenuation along the ray paths as if the object were compressed along the optic axis. A complete description can be found in Paganin (Paganin, 2006) and here we sketch the main results.

Consider the following ansatz to the inhomogeneous Helmholtz equation for a 'beam-like' wavefield

$$\psi(\boldsymbol{\rho}, z) = \breve{\psi}(\boldsymbol{\rho}, z) \exp ikz \tag{2.20}$$

varying more strongly in $x$ and $y$ than $z$ so that $\partial^2\breve{\psi}/\partial z^2$ is negligible relative to the other terms in (2.21),

$$\left\{2ik\frac{\partial}{\partial z} + \nabla_\perp^2 + k^2[n^2(\mathbf{r}) - 1]\right\}\breve{\psi}(\boldsymbol{\rho}, z) = 0. \tag{2.21}$$

We can uncouple adjacent ray paths in the paraxial equation (2.21) by making the approximation $\nabla_\perp^2\breve{\psi}(\mathbf{r}') \approx 0$. If we integrate (2.21) with respect to $z$ and, in addition, if we note that at X-ray frequencies it is valid to assume $|\delta|, |\beta| \ll 1$ for weakly interacting objects we have what is known as the projection approximation,

$$\breve{\psi}(\boldsymbol{\rho}, z) \approx \exp\left\{-ik\int_0^z [\delta(\boldsymbol{\rho}, z') - i\beta(\boldsymbol{\rho}, z')]dz'\right\}\breve{\psi}(\boldsymbol{\rho}, 0). \tag{2.22}$$

We can make a distinction between the object's effect on the wavefield which traverses and the exit plane wavefield itself by introducing the complex transmission

function (Born and Wolf, 1999), $f$,

$$f(\boldsymbol{\rho}) = \exp\left\{-ik\int_0^z [\delta(\boldsymbol{\rho}, z') - i\beta(\boldsymbol{\rho}, z')]dz'\right\} \tag{2.23}$$

and the wavefield exiting the object becomes (cf. (2.20)),

$$\psi(\boldsymbol{\rho}, z) = f(\boldsymbol{\rho})\exp(ikz). \tag{2.24}$$

For weakly interacting thick objects the Born series (Merzbacher, 1970; Born and Wolf, 1999) provides a method for calculating diffraction from an extended body.

An important special case of (2.22) occurs when a plane wave is incident on a single-material object with projected thickness $t(\boldsymbol{\rho})$ and refractive indices $\delta$, $\beta$,

$$\psi(\boldsymbol{\rho}, z) = \exp[-ik(\delta - i\beta)t(\boldsymbol{\rho})]\exp(ikz) \tag{2.25}$$

where

$$t(\boldsymbol{\rho}, z) = \int_0^z t(\boldsymbol{\rho}, z')dz'. \tag{2.26}$$

We close this section by looking at the weak object approximation to (2.25) which is valid for objects that introduce phase shifts much less than one radian and maximum attenuation of a few percent (cf. §1.2). We adopt the convention defined by Nesterets et al. (2004) and rewrite (2.25) in terms of the phase shift $\varphi$ and attenuation $\mu$,

$$\psi(\boldsymbol{\rho}, 0) = \exp[i\varphi(\boldsymbol{\rho}) - \mu(\boldsymbol{\rho})], \tag{2.27}$$

where,

$$\varphi(\boldsymbol{\rho}) = -k\int_z \delta(\boldsymbol{\rho}, z)dz, \tag{2.28}$$

$$\mu(\boldsymbol{\rho}) = k\int_z \beta(\boldsymbol{\rho}, z)dz. \tag{2.29}$$

Splitting the terms in the exponent into the mean $\overline{\varphi}$, $\overline{\mu}$ and deviation from the mean $\Delta\varphi$, $\Delta\mu$, so that $\overline{\Delta\varphi} = 0$ and $\overline{\Delta\mu} = 0$ we have,

$$\varphi(\boldsymbol{\rho}) = \overline{\varphi} + \Delta\varphi(\boldsymbol{\rho}), \tag{2.30}$$

$$\mu(\boldsymbol{\rho}) = \overline{\mu} + \Delta\mu(\boldsymbol{\rho}), \tag{2.31}$$

gives for $\psi$

$$\psi(\boldsymbol{\rho}) = \exp[i\overline{\varphi} - \overline{\mu}]\exp[i\Delta\varphi(\boldsymbol{\rho}) - \Delta\mu(\boldsymbol{\rho})]. \tag{2.32}$$

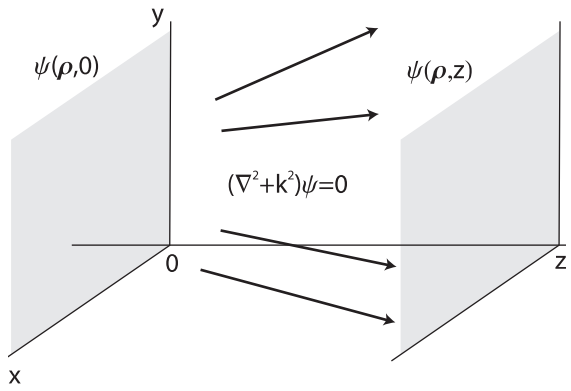


Figure 2.3: **The angular spectrum of plane waves.** The wavefield at $z = 0$ is propagated to $z = z$ using the homogeneous Helmholtz equation (2.6).

If the weak object criteria

$$|\Delta\varphi| \ll 1, \tag{2.33}$$

$$|\Delta\mu| \ll 1, \tag{2.34}$$

are applicable, the second exponent in (2.32) can be expanded as (Cowley, 1995),

$$\psi(\boldsymbol{\rho}) \approx \exp[i\overline{\varphi} - \overline{\mu}][1 + i\Delta\varphi(\boldsymbol{\rho}) - \Delta\mu(\boldsymbol{\rho})] \tag{2.35}$$

which is known as the weak object approximation. As has been previously noted, in practice it can be difficult to create an object that satisfies the weak object criteria for hard X-rays. Eq (2.34) is often easy to satisfy for hard X-rays but (2.33) requires a phase shift of much less than one radian and can be difficult to achieve for all but the weakest objects.

An alternative and less restrictive approximation to (2.33) has been proposed by Guigay (1977). In the context of Fresnel diffraction it was shown that the phase shift need only be much less than 1 radian over the length scale $z\lambda/h$ where $z$ is the propagation distance and $h$ the smallest feature in the object. Since this result was derived for Fresnel diffraction we will use the more restrictive condition (2.33) since we consider object weakness in the case of diffraction from a crystal as well.

## 2.4 Free space diffraction

We now consider the plane-to-plane diffraction of a scalar wavefield when the intervening space is devoid of charges and currents[4]. The solution of this problem will

[4]A plane-to-inclined-plane solution for Fresnel diffraction has been proposed (Modregger et al., 2008).

allow us to propagate an X-ray wavefield between parallel planes of our imaging system and can be used to simulate PBI phase contrast.

The analytical solution to the problem of plane to plane diffraction, known as the angular spectrum of plane waves, links a forward propagating wavefield between planes by requiring that the field obeys the free space Helmholtz equation (2.6) (Lalor, 1968; Goodman, 2000; Mandel and Wolf, 1995). We briefly sketch a particularly transparent formulation (due to Gureyev (Paganin, 2006)) by considering first the propagation of a plane wave,

$$\psi(\boldsymbol{\rho}, z) = \exp \mathrm{i}(\boldsymbol{\kappa} \cdot \boldsymbol{\rho} + k_z z) \tag{2.36}$$

between $z = 0$ and $z$, see Figure 2.3. The Helmholtz equation constrains the wave vector to lie on a sphere of radius $|\mathbf{k}|$, which it will provided that $k_z = \pm\sqrt{k^2 - |\boldsymbol{\kappa}|^2}$. This allows us to express a $+z$-directed plane wave, by choosing the positive sign of the surd, as,

$$\psi(\boldsymbol{\rho}, z) = \exp \mathrm{i} \left( \boldsymbol{\kappa} \cdot \boldsymbol{\rho} + z\sqrt{k^2 - |\boldsymbol{\kappa}|^2} \right). \tag{2.37}$$

This result suggests that a plane wave at $z = 0$ can be propagated through a distance $z$, as in Figure 2.3, by addition of a constant phase $z\sqrt{k^2 - |\boldsymbol{\kappa}|^2}$. Following this logic through we express the field in the plane $z = z$ as a Fourier sum of plane waves in the plane $z = 0$ with multiplicative phase factor,

$$\psi(\boldsymbol{\rho}, z) = \frac{1}{2\pi} \iint \tilde{\psi}(\boldsymbol{\kappa}; z = 0) \exp\left( \mathrm{i}z\sqrt{k^2 - |\boldsymbol{\kappa}|^2} \right) \exp(\mathrm{i}\boldsymbol{\kappa} \cdot \boldsymbol{\rho}) \mathrm{d}\boldsymbol{\kappa}. \tag{2.38}$$

This is the angular spectrum of plane waves and is the main result of this section. It solves the boundary value problem of determining the complex amplitude of a forward propagating scalar wavefield given knowledge of the amplitude over a previous plane.

We can see from the argument of the surd in (2.38) that plane waves corresponding to wavevectors with $|\boldsymbol{\kappa}| \leqslant |\mathbf{k}|$ will propagate and those with $|\boldsymbol{\kappa}| > |\mathbf{k}|$ will be exponentially attenuated. The latter are known as 'evanescent' waves. Thus the propagated field will not contain information smaller than the radiation wavelength $\lambda$, when $z \gg \lambda$ (Nieto-Vesperinas, 1991).

The X-ray wavefields that will be encountered in practice in later chapters all have the common characteristic of being paraxial. Accordingly we seek an approximation to (2.38) which is suitable for X-ray beams and compatible with assumptions made in the projection approximation for paraxial fields (cf. §2.3.1). The paraxial approximation to the angular spectrum assumes that $k_z^2 \gg k_x^2 + k_y^2$ in which case the argument of

the surd in (2.38) becomes,

$$\sqrt{k^2 - |\boldsymbol{\kappa}|^2} \approx k - \frac{|\boldsymbol{\kappa}|^2}{2k}. \tag{2.39}$$

Using this approximation (2.38) becomes,

$$\psi(\boldsymbol{\rho}, z) = \frac{1}{2\pi} \exp(ikz) \iint \tilde{\psi}(\boldsymbol{\kappa}; z = 0) \exp\left(-i\frac{z}{2k}|\boldsymbol{\kappa}|^2\right) \exp(i\boldsymbol{\kappa} \cdot \boldsymbol{\rho}) d\boldsymbol{\kappa}, \tag{2.40}$$

which is a form of the Fresnel diffraction integral. We have now used two approximations to find beam-like results (cf. (2.21) and (2.39)) and it is satisfying to note for consistency that the Fresnel approximation to the angular spectrum is the Fourier representation of the Green's function solution to the homogeneous ($n = 1$) paraxial equation (2.21) (Grella, 1982).

The Fresnel approximation to the angular spectrum is valid for the range of parameter space that gives a Fresnel number $N_F = g^2/\lambda z$ (cf. (1.2)) greater than unity where $g$ is the length scale of the smallest resolvable feature. Physically, the Fresnel number quantifies the curvature of the wavefield a distance $z$ from an object of size $g$ .

Since the Fresnel diffraction regime is quantified by $N_F \geqslant 1$ we distinguish the feature size $g_F = \sqrt{\lambda z}$ below which the Fresnel approximation and theories built thereon are not applicable.

## 2.5 Diffraction from a crystal

The study of crystalline matter and X-ray radiation are inextricably linked. This is principally because the comparable length scales of the crystalline unit cell and hard X-ray wavelengths makes each suitable for investigation of the other. We motivate this section by noting that ABI phase contrast imaging uses a thick perfect crystal as an optical element and understanding ABI presupposes knowledge of how an X-ray wavefield interacts with a crystalline structures. In order to fully understand this interaction we must delve into the dynamical theories of X-ray diffraction. The treatment given here is by no means complete and for a full review of the field see e.g. (Batterman and Cole, 1964; Zachariasen, 1968; Pinsker, 1978; Authier, 2005).

Specifically, we are seeking an expression relating the wavefields incident on and diffracted from the crystal analogous to (2.38) for free space diffraction. We have cause to study interaction with crystals in some detail because we will later investigate what the wavefield scattered from a crystal allows us to infer about its structure (see e.g. §4.4). To this end we will briefly review the well known dynamical theory of Takagi that allows us to calculate the field scattered from crystals with slight distortions.

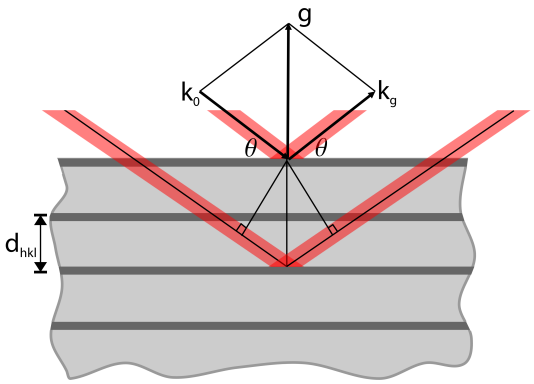


Figure 2.4: **The geometry of Bragg's law.** X-rays are diffracted from planes that satisfy Bragg's law, $2d_{hkl}\sin\theta_B = n\lambda$. The equation $\mathbf{k}_g = \mathbf{k}_0 + \mathbf{g}$ is the vector equivalent of Bragg's law.

Theories describing the diffraction of X-rays by crystals can be divided into three distinct classes; geometric, kinematic and dynamical (Ewald, 1969). The geometric theory embodied by Bragg's law specifies the directions in which reflection from a crystal will occur (Authier, 2005),

$$2d_{hkl}\sin\theta_B = n\lambda \tag{2.41}$$

in terms of the spacing between atomic planes $d_{hkl}$ where $(h, k, l)$ are Miller indices, coordinates of reciprocal lattice points. The kinematic (single scattering) theory specifies the angular spread of radiation for a finite crystal but assumes all atoms in the crystal are subject to the same incident field and is thus applicable to, for example, very thin crystals where the power in the diffracted beam is negligible. The dynamical (multiple scattering) theory accounts for the interaction of incident and reflected waves within the crystal.

### 2.5.1 The dynamical theory of X-ray diffraction

The classical dynamical theory of X-ray diffraction attempts to provide a description for the interaction of the classical electromagnetic field[5] and crystalline structures with a periodic but otherwise arbitrary structure. The problem may be divided into two parts: the description of the crystal and the description of the wavefield that interacts with the crystal.

The utility of X-ray diffraction as an investigative tool in scientific and industrial application has driven the need for an accurate theory that can account for diffraction from the many crystal structures. The effect of naturally occurring defects (such as

[5]For a quantum theory of X-ray diffraction from crystals see e.g. Ashkin and Kuriyama (1966).

dislocations, domain walls, impurities (Authier, 2005)) and structures (multilayer, superlattice (Pietsch et al., 2004)) provide a significant challenge for a unified description of the diffraction process and as such many variants of dynamical theory have been developed.

We now review the most common theories describing crystalline structures and their interaction with electromagnetic fields.

### 2.5.2 Crystalline structures

The early dynamical theories of X-ray diffraction were based on two different approaches pioneered by Darwin and Ewald/ Laue. Darwin's theory (Darwin, 1914b,a) was based on the idea of the crystal being composed of lamellae parallel to the surface and that each of these planes would give one diffracted and one transmitted beam. Plane waves incident on each subsequent crystal plane were diminished in energy due to diffraction from the previous planes and in this way energy was conserved. A set of recurrence relations were formulated and solved for the crystal reflectivity.

The approach of Ewald (Ewald, 1916, 1917, 1979) and von Laue (von Laue, 1931, 1960) was to formulate and solve wave equations inside the crystal. The Ewald/Laue (EL) model of the crystal is fundamentally different to the Darwin description and as such the theories of diffraction from a Darwin crystal and an EL crystal are much different (although they give equivalent results for important systems such as the thick perfect crystal).

Ewald considered crystals to be composed of a periodic distribution of discrete dipoles whereas the von Laue model views the crystal as a continuous periodic charge distribution. In the ideal crystal the charge distribution is periodic so that it may be represented as a Fourier series with the periodicity of the unit cell (Afanas'ev and Kohn, 1971),

$$\chi^{\mathrm{id}}(\mathbf{r}) = \sum_{\mathbf{g}} \chi^{\mathrm{id}}_{\mathbf{g}} \exp(\mathrm{i}\mathbf{g}\cdot\mathbf{r}) \tag{2.42}$$

where $\mathrm{id}$ refers to the ideal crystal, $\mathbf{g}$ is a reciprocal lattice vector and the summation extends over all reciprocal lattice vectors. The reciprocal lattice vectors are related to the (hkl) family of Bragg planes by,

$$d_{hkl} = \frac{2\pi}{|\mathbf{g}_{hkl}|}. \tag{2.43}$$

The polarisability in (2.42) describes an ideal periodic charge distribution and we would like to extend this description to slightly deformed crystals. For example,

coherently strained pseudomorphic layers[6] of semiconductor materials have a strain much less than 1% to avoid relaxation.

We can relate the position of the atoms in the distorted crystal $\mathbf{r}'$ to their position in the ideal crystal $\mathbf{r}$ by the deformation field $\mathbf{u}$,

$$\mathbf{r}' = \mathbf{r} + \mathbf{u}(\mathbf{r}). \tag{2.44}$$

Since the deformation is small we may use the Takagi approximation to (2.44) and write,

$$\mathbf{r} \approx \mathbf{r}' - \mathbf{u}(\mathbf{r}'). \tag{2.45}$$

In this case the deformed crystal polarisability $\chi^{\mathrm{def}}$ is given by (Kato, 1963; Afanas'ev and Kohn, 1971),

$$\begin{aligned} \chi^{\mathrm{def}}(\mathbf{r}) &= \chi^{\mathrm{id}}[\mathbf{r} - \mathbf{u}(\mathbf{r})], & (2.46)\\ &= \sum_{\mathbf{g}} \chi^{\mathrm{id}}_{\mathbf{g}} \exp \mathrm{i}[\mathbf{g}\cdot\mathbf{r} - \mathbf{g}\cdot\mathbf{u}(\mathbf{r})]. & (2.47) \end{aligned}$$

The effect of slight distortion is to shift the charge distribution without affecting its shape (Hartwig, 2001) and the approximation is valid as long as there is no overlap of the core electron wavefunctions (Kuriyama, 1967).

The Takagi approximation has become a standard description for deformed crystals and can be interpreted as a local reciprocal lattice vector $\tilde{\mathbf{g}}$ (Penning, 1966; Authier, 2005),

$$\begin{aligned} \tilde{\mathbf{g}}(\mathbf{r}) &= \nabla\{\mathbf{g}\cdot[\mathbf{r} - \mathbf{u}(\mathbf{r})]\} & (2.48)\\ &= \mathbf{g} - \nabla[\mathbf{g}\cdot\mathbf{u}(\mathbf{r})] & (2.49)\\ &= \frac{2\pi}{\mathrm{d}(\mathbf{r})}\hat{\mathbf{n}}_{\tilde{\mathbf{g}}}(\mathbf{r}), & (2.50) \end{aligned}$$

where $\mathrm{d}$ is the local interplanar spacing at $\mathbf{r}$ and $\hat{\mathbf{n}}$ is the local unit vector normal to the crystal plane. This expression is the gradient of the exponent in (2.47) and so Podorov et al. (2006) proposed the form,

$$\begin{aligned} \mathbf{g}\cdot\mathbf{r} - \mathbf{g}\cdot\mathbf{u}(\mathbf{r}) &= \int_0^{\mathbf{r}} \tilde{\mathbf{g}}(\tilde{\mathbf{r}})\cdot \mathrm{d}\tilde{\mathbf{r}}, & (2.51)\\ &= \int_0^{\mathbf{r}} \left[\frac{2\pi}{\mathrm{d}(\tilde{\mathbf{r}})}\hat{\mathbf{n}}_{\tilde{\mathbf{g}}}(\tilde{\mathbf{r}})\right]\cdot \mathrm{d}\tilde{\mathbf{r}}. & (2.52) \end{aligned}$$

[6] Pseudomorphic layers are formed during epitaxy of semiconductor materials with slightly differing lattice constants (Schuster and Herres, 1994). At the interface, the epitaxial layer strains to fit the lattice of the substrate in the lateral direction resulting in a tetragonal distortion. If the strain is too large the layer will relax. Pseudomorphic layers are commonly used in fields such as bandgap engineering.

This last result has the advantage of conceptual clarity at the expense of computational difficulty as the integral of (2.52) must in general be evaluated numerically.

We now turn to an overview of the of dynamical diffraction theory proposed by Takagi for perfect and slightly deformed crystals.

### 2.5.3 Takagi's dynamical theory of X-ray diffraction

All dynamical theories aim to solve the wave equation (2.1) under the assumption of a periodic charge distribution. The theories differ in how to describe the wavefields inside the crystal and which terms in the governing wave equation can be considered negligible.

In Takagi's dynamical theory, gently perturbed plane waves propagate in the crystal and the envelopes of the waves have a spatial dependence which allows them to satisfy the propagation equation in the case of a deformed crystal.

To begin we rewrite (2.1) [7],

$$\nabla^2 \mathbf{E}(\mathbf{r}) + k^2[1 + \chi(\mathbf{r})]\mathbf{E}(\mathbf{r}) = 0. \tag{2.53}$$

We will first apply the Takagi theory to a perfect crystal and later extend it to crystals with slight distortions. The susceptibility $\chi$ will be as described in the previous section and it remains to choose a form for $\mathbf{E}$. Bloch (Bloch, 1928) showed that the wavefield inside a periodic potential must have the same periodicity as the potential itself. Hence we express the wavefield in the crystal as a Fourier sum,

$$\mathbf{E}(\mathbf{r}) = \sum_{\mathbf{g}} \mathbf{E}_{\mathbf{g}} \exp i[\mathbf{k}_{\mathbf{g}} \cdot \mathbf{r}] \tag{2.54}$$

where $\mathbf{k}_{\mathbf{g}}$ is defined by the Laue equation (cf. Figure 2.4),

$$\mathbf{k}_{\mathbf{g}} = \mathbf{k}_0 + \mathbf{g}, \tag{2.55}$$

the vector equivalent of the Bragg condition. In the case of an infinite triply periodic crystal in which the reciprocal lattice points are $\delta$-functions the sum of plane waves in (2.54) is a good description however we want to generalise this expression to accommodate a description of finite crystals with slight distortions. The plane waves that propagate in the perfect crystal become slowly-varying modulated Bloch waves (Hartwig, 2001; Authier, 2005) in the Takagi theory of distorted crystals by allowing the amplitudes to take on a spatial dependence,

$$\mathbf{E}(\mathbf{r}) = \sum_{\mathbf{g}} \mathbf{E}_{\mathbf{g}}(\mathbf{r}) \exp i[\mathbf{k}_{\mathbf{g}} \cdot \mathbf{r}]. \tag{2.56}$$

[7] Since the wave inside the crystal remains transverse to a good approximation (Afanas'ev and Kohn, 1971) we may assume $\nabla \cdot \mathbf{E} \approx 0$.

The chosen form for $\mathbf{E}$ is substituted into (2.53) yielding a set of differential equations for the $\mathbf{E_g}$ which must vanish. The relative size of each of the terms means that some contribute negligibly and the decision of which terms are negligible is one of the discriminants between the variants of dynamical theories (Hartwig, 2001). Takagi theory assumes that the amplitudes $\mathbf{E_g}$ will have a macroscopic variation so that their second derivative can be considered negligible relative to the first derivative and that the wave is approximately transverse within the crystal (Afanas'ev and Kohn, 1971). When only two reciprocal points intersect the Ewald sphere we may use the two-beam approximation which allows for two strong beams, the incident $\psi_0$ and reflected $\psi_g$, within the crystal. Under these conditions we have the Takagi equations (Afanas'ev and Kohn, 1971),

$$2i(\mathbf{k}_0 \cdot \nabla)\psi_0 + k^2\chi_0\psi_0 + Ck^2\chi_{\bar{g}} \exp[i\mathbf{g} \cdot \mathbf{u}(\mathbf{r})]\psi_{\mathbf{g}} = 0, \tag{2.57}$$

$$2i(\mathbf{k}_g \cdot \nabla)\psi_g + k^2(\chi_0 - \alpha_g)\psi_g + Ck^2\chi_g \exp[-i\mathbf{g} \cdot \mathbf{u}(\mathbf{r})]\psi_0 = 0. \tag{2.58}$$

where $\mathbf{k}_0$ and $\mathbf{k}_g$ are the incident and diffracted wavevectors (see Figure 2.5), $\alpha_g = (|\mathbf{k_g}|^2 - k^2)/k^2$ is the resonant error and we have changed back to a scalar amplitude with the addition of a polarisation factor $C = 1, \sin 2\theta$ for sigma and pi polarisation states respectively.

The two equations (2.57) and (2.58) are the fundamental description of dynamical diffraction in the Takagi theory. The linearised resonant error has a geometrical interpretation in which it can be associated with the deviation of the wavevector from the Bragg condition. The linearisation of the resonant error strongly limits the Takagi theory to describing the angular range immediately adjacent to the Bragg reflection such that $|\theta - \theta_B| \ll 1$.

This limitation has spawned considerable effort (e.g. (Caticha, 1993; De Caro et al., 1997; Holy and Fewster, 2003; Podorov et al., 2006)) to develop a wide angle diffraction theory capable of describing diffraction between reciprocal lattice vectors as well as at the Bragg position. Recent progress has been made in this field (Pavlov et al., 2007; Kaganer, 2007, 2008). Kaganer, in particular, has shown that the reflection between reciprocal lattice points along the crystal truncation rod is given exactly by the sum of the two-beam solutions for all Bragg reflections along the crystal truncation rod.

### 2.5.4 The amplitude reflection coefficient

We now have the basis of the dynamical theory of X-ray diffraction that can describe the scattering of X-rays for crystals with slight deformation. We would like to preempt

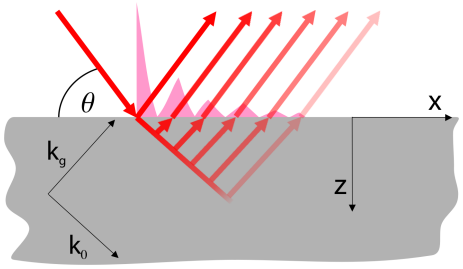


Figure 2.5: **Diffraction geometry for the Takagi equations.** The X-ray wavefield penetrates the crystal to the extinction depth resulting in a spread of reflected rays.

some of the later work of this thesis by presenting the solution to the dynamical equations for some cases of interest; the semi-infinite perfect crystal and the laterally homogeneous thin crystal with depth-dependent deformation.

The solution of the coupled partial differential equations (2.57) and (2.58) gives the complex amplitude reflection coefficient (ARC), $r(\theta)$, which describes the spatial frequency response of the crystal to the incident field and for future reference we define the rocking curve $R(\theta) = |r(\theta)|^2$.

A brief comment on the argument of $r$: principally we will use three arguments in the ARC function, $\theta$, $\omega$ and $k_x$. The parameter $\theta$ will describe $r$ over an unspecified angular range whereas $\omega$ will usually be taken to be a small deviation from the Bragg condition as is usual in the literature. Finally, for beam like wavefields we may make the approximation $\omega \approx k_x/k$ which is useful for Fourier transformations. Importantly, henceforth $\omega$ will not refer to angular frequency and where there is chance of confusion we will denote $\omega_C$ to be the crystal angular deviation from the Bragg angle.

If the ARC is known we may express an arbitrary field diffracted from the crystal as a Fourier integral in which the spatial frequencies have been modulated according to the crystal response. The diffracted field $\Psi$ is related to the incident field via the crystal ARC by,

$$\Psi\left(-\frac{x}{\gamma}, y, z; \omega_C\right) = \frac{1}{2\pi}\iint_{-\infty}^{\infty} \tilde{\psi}(\boldsymbol{\kappa}; z) r\left(\omega_C - \frac{k_x}{\gamma k}\right) \exp(i\boldsymbol{\kappa}\cdot\boldsymbol{\rho}) d\boldsymbol{\kappa}, \qquad (2.59)$$

where $\gamma = \sin\theta_0/\sin\theta_g$ is the asymmetry factor of the crystal, namely the ratio of the sines of the angles that the incident and diffracted X-ray beams make with the crystal surface.

The solution of the Takagi equations for a semi-infinite perfect crystal is well known (see for example (Afanas'ev and Kohn, 1971; Authier, 2005))

$$r(\eta) = -\frac{1}{2\chi_{\bar{g}} C}\left(\eta - \sqrt{\eta^2 + \zeta^2}\right) \qquad (2.60)$$

where $\eta = \alpha_g\gamma + \chi_0(1-\gamma)$, $\zeta = 2C\sqrt{\gamma\chi_g\chi_{\bar{g}}}$, and the sign of the surd is chosen to be opposite to the sign of Re[$\eta$].

The function $r(\eta)$ describes the Bragg peak of the reflection at $\mathbf{g}_{hkl}$ and its structure can be used to determine macroscopic characteristics of the crystal. The inverse Fourier transform of (2.60), the crystal point spread function, is derived in Appendix A and the result given here (Afanas'ev and Kohn, 1971),

$$G(x) = i\frac{kC\chi_g\gamma_0}{2\sin 2\theta_B}\left(J_0(Bx) + J_2(Bx)\right)H(x)\exp(iAx) \tag{2.61}$$

where $J_n(x)$ is a Bessel function of the first kind of order n and

$$A = k\chi_0\frac{\gamma_0 + |\gamma_g|}{2\sin 2\theta_B} - k\alpha_g\frac{\gamma_0}{2\sin 2\theta_B}, \tag{2.62}$$

$$B = \frac{kC\sqrt{\chi_g\chi_{\bar{g}}\gamma_0|\gamma_1|}}{\sin 2\theta_B}. \tag{2.63}$$

Measurement of the kinematic ARC will later in §4.4 be used to infer crystal structure and so we will briefly overview the salient details of kinematic scattering here. The penetration depth of the X-ray wavefield in the crystal is given by (Authier, 2005),

$$\Lambda = \frac{\lambda\sqrt{\gamma_0|\gamma_g|}}{C\sqrt{\chi_g\chi_{\bar{g}}}}. \tag{2.64}$$

There are a number of cases in which we can assume the power in the diffracted beam is negligible: crystals which have either a total thickness much smaller than the penetration depth, $t \ll \Lambda$, or large deformations, or a very high defect density or being far from the Bragg condition. In any of these situations we may assume that the entire depth of the crystal is subject to the same incident field and that the diffraction is kinematic.

We can approximate kinematic scattering from by thin deformed layers by letting the Fourier coefficient of the susceptibility $\chi_{\bar{g}} \approx 0$. If we assume that the crystal is laterally infinite, that the chemical composition of the thin layer does not vary with depth and that we can neglect refraction and absorption within the layer we have, for a symmetric reflection, (Petrashen', 1974),

$$r(\eta) = \frac{i\pi\chi_g}{\lambda\sin\theta_B}\int_{-\infty}^{\infty}\Omega(z)\exp\left[-i\eta z - i\mathbf{g}\cdot\mathbf{u}(z)\right]dz. \tag{2.65}$$

Here $\Omega(z)$ is the crystal shape function, which is equal to unity within the film and zero elsewhere and $\eta = (4\pi/\lambda)\omega\cos\theta_B$.

This important result tells us that the ARC of the thin layer is just the Fourier transform of its shape function multiplied by a phase factor that describes the crystal deformation.

Up to this point we have covered the requisite background that allows quantitative analysis of the free space diffraction of X-rays and their diffraction from thick perfect crystals and thin crystalline films. We will now join these results in a description of the analyser-based imaging system. To avoid the unnecessary complexity of convolution integrals we will describe the ABI system using the operator formalism for linear, shift-invariant optical elements. It is to this topic that we now turn.

## 2.6 Green's functions and linear shift invariant imaging systems

The operator formalism we will encounter in this section lends itself particularly well to numerical implementation. Each section (e.g. propagation from sample to crystal) of the ABI system may be written as a term in a cascaded optical system (Develis and Parrent, 1967) and the transfer function of the entire system is simply a multiplication of the distinct component transfer functions in real or reciprocal space.

First we will introduce the operator formalism and then we revisit the main results of Section 2.4 and 2.5 so that we can place them in the context of operators for linear shift-invariant systems.

The linear partial differential equations that we have encountered in describing diffracted wavefield (such as the Helmholtz equation cf. (2.6)) have had a general form like,

$$O_{\mathbf{r}}\Psi(\mathbf{r}) = s(\mathbf{r}) \tag{2.66}$$

where $O_{\mathbf{r}}$ is a linear differential operator that acts on $\mathbf{r}$ and $s$ is a source term describing the incident field, distribution of electric charge or current. We outline one method of solving such equations whose solution is useful for its physical clarity. To this end let us rewrite (2.66) as,

$$O_{\mathbf{r}}G(\mathbf{r},\mathbf{r}') = \delta(\mathbf{r}-\mathbf{r}') \tag{2.67}$$

where we have introduced the Green's function $G$ and replaced the source term with a Dirac delta. The (outgoing) Green's function, defined as a solution to (2.67) that is outgoing at infinity, describes the characteristic response of the system that results from an impulse-like unit input. Eq. (2.67) describes how the field must vary at $\mathbf{r}$ in order to accommodate a Dirac delta source at $\mathbf{r}'$ (for some specified boundary conditions) but we would prefer to have a description that was explicit in $G$. Trivially,

$$G(\mathbf{r},\mathbf{r}') = O_{\mathbf{r}}^{-1}\delta(\mathbf{r}-\mathbf{r}') \tag{2.68}$$

which allows us to write (2.66)

$$\begin{aligned}\Psi(\mathbf{r}) &= O_{\mathbf{r}}^{-1}\int s(\mathbf{r}')\delta(\mathbf{r}-\mathbf{r}')d\mathbf{r}',\\ &= \int s(\mathbf{r}')O_{\mathbf{r}}^{-1}\delta(\mathbf{r}-\mathbf{r}')d\mathbf{r}',\\ &= \int s(\mathbf{r}')G(\mathbf{r},\mathbf{r}')d\mathbf{r}'. \end{aligned} \tag{2.69}$$

Furthermore, if we presuppose that the Green's function is shift-invariant so that $G(\mathbf{r},\mathbf{r}') \rightarrow G(\mathbf{r}-\mathbf{r}')$. Physically, this means the properties of the Green's function are independent of the absolute coordinates and shifting the input will result in an equivalent shift of the corresponding output. Under the assumption of shift-invariance (2.69) becomes a convolution,

$$\Psi(\mathbf{r}) = \int G(\mathbf{r}-\mathbf{r}')\psi(\mathbf{r}')d\mathbf{r}' \tag{2.70}$$

and in this case the source $s(\mathbf{r}) = \psi(\mathbf{r})$, i.e. the scalar wavefield. The convolution representation has the significant advantage that it can be evaluated using the Fourier convolution theorem (Bracewell, 1986) which allows us to write (2.70) as

$$\Psi(\mathbf{r}) = G(\mathbf{r}) \star \psi(\mathbf{r}), \tag{2.71}$$

$$= \mathcal{F}_3^{-1}\left[\mathcal{F}_3[G(\mathbf{r})]\mathcal{F}_3[\psi(\mathbf{r})]\right] \tag{2.72}$$

where $\mathcal{F}_3$ denotes a three dimensional Fourier transform and $\star$ denotes convolution. The result tells us that the imaging system takes an input wavefield, acts on it with Green's function G which re-weights the spatial frequencies, and outputs a new wavefield.

With this new notation we can recast some previous results in terms of convolutions and operator equations. Take for example the angular spectrum (cf. (2.38)),

$$\Psi(\boldsymbol{\rho},z) = \frac{1}{2\pi}\int\int_{-\infty}^{\infty}\tilde{\psi}(\boldsymbol{\kappa},0)\exp\left(iz\sqrt{k^2-|\boldsymbol{\kappa}|^2}\right)\exp(i\boldsymbol{\kappa}\cdot\boldsymbol{\rho})d\boldsymbol{\kappa} \tag{2.73}$$

$$= \mathcal{F}^{-1}\left[\exp\left(iz\sqrt{k^2-|\boldsymbol{\kappa}|^2}\right)\times\mathcal{F}[\psi(\boldsymbol{\rho})]\right] \tag{2.74}$$

$$= \psi(\boldsymbol{\rho},0)\star G_{AS}(\boldsymbol{\rho},z) \tag{2.75}$$

where

$$G_{AS}(\mathbf{r}) = \frac{1}{2\pi}\frac{\partial}{\partial z}\frac{\exp[ik(\mathbf{r})]}{|\mathbf{r}|}, \tag{2.76}$$

is the angular spectrum Green's function (Lalor, 1968). Eq. (2.75) is the Rayleigh-Sommerfeld diffraction integral of the first kind (Born and Wolf, 1999).

Similarly, we can use the semi infinite perfect crystal Green's function (2.61) to rewrite (2.59),

$$\Psi(\mathbf{r};\omega_C) = \mathcal{F}^{-1}\left[r(\omega_C - k_x/\gamma k)\mathcal{F}[\psi(\boldsymbol{\rho})]\right], \tag{2.77}$$

$$= i\frac{kC\chi_g\gamma_0}{2\sin 2\theta_B}\psi(\mathbf{r}) \star \{J_0(Bx) + J_2(Bx)\}H(x) \times \exp[iAx], \tag{2.78}$$

where $r(\omega)$ is the perfect crystal ARC and here $\omega_C$ is the small deviation from the Bragg angle to avoid confusion with angular frequency.

We have seen how to propagate an X-ray wavefield through inhomogeneous media, homogeneous media and periodic media and we have now developed the compact operator formalism to describe those results. Together with an understanding of the coherence properties of X-ray wavefields we have met the theoretical requirement for understanding the forward problem of image formation that is required for the developments to be reported later in this thesis.

### 2.6.1 Modelling the forward problem in analyser-based imaging

In this section we will bring the results we have described thus far together in a description of an ABI phase contrast imaging system in terms of operator theory (Paganin, 2006).

The diffraction operators with which we will describe the theory have the form of $D = \mathcal{F}^{-1}\tilde{D}_b\tilde{D}_a\mathcal{F}[\cdot]$. This operator equation is read from right to left as acting on some scalar wavefunction (where the "$\cdot$" indicates the placeholder for the wavefield), applying a Fourier transform, then two linear, shift-invariant propagators sequentially $\tilde{D}_a$ then $\tilde{D}_b$[8] before applying an inverse transform.

In this way we can build up a description of the entire imaging system in terms of cascaded operators. First we will give the expression for monochromatic radiation from a point-source and then we will extend this to quasi-monochromatic radiation from an extended incoherent source.

We note that a similar statement regarding the forward problem of image formation in ABI has been made in Nesterets et al. (2005b) however that formulation, equivalent in nearly all respects to the one presented here, was expressed in terms of convolution integrals whereas the operator description given here lends itself more readily to numerical implementation.

[8]The propagators commute and so can be applied in any order but reading from right to left aids clarity of understanding.

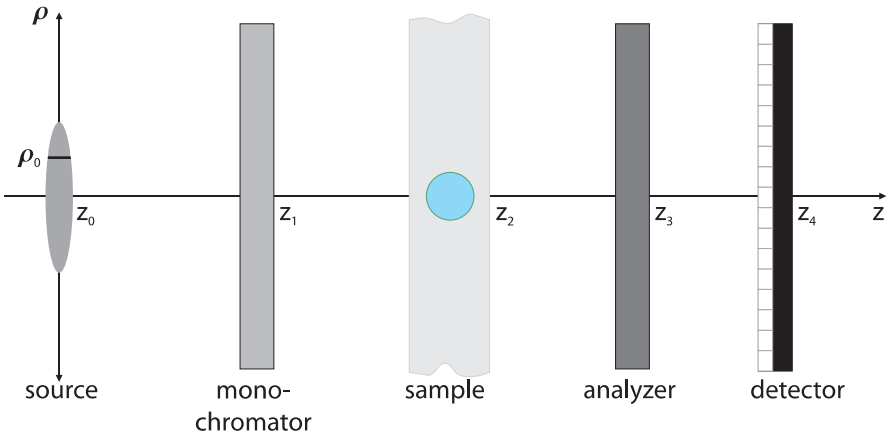


Figure 2.6: **Model analyser-based imaging system.** This block diagram shows the layout of an idealised analyser-based imaging system used to model the forward problem of image formation in ABI.

A note on a convention which expedites the following description of the ABI imaging system. The monochromator and analyser crystal ARC's are one-dimensional functions and any magnification they impart due to asymmetric reflection acts on only one spatial variable. We would like simplify the proceeding description by introducing the convention that when dividing by the asymmetry ratio $\tilde{\gamma}$ with the tilde, the division applies only to the $x$-component of $\boldsymbol{\rho}$ or $k_x$-component of $\boldsymbol{\kappa}$.

Consider the analyser-based imaging system of Figure 2.6 comprising an X-ray source, monochromator, sample, analyser crystal and detector. Between each of these elements there is a propagation distance and at the end the detector will record the intensity of the field integrated over a function $S(\boldsymbol{\rho}, \lambda)$ describing the intensity per unit area and spectral bandwidth of the source.

We may write the field on the detector $\Psi$ due to a monochromatic point-source at $\boldsymbol{\rho}_0$ in operational terms as,

$$\begin{aligned}\Psi\left(\frac{\boldsymbol{\rho}}{\tilde{\gamma}_T}, z_4, \lambda, \boldsymbol{\rho}_0, \omega_C, N, \lambda_0\right) &= D_2(\boldsymbol{\rho}, \lambda, z_4 - z_2, \omega_C, \lambda_0) f(\boldsymbol{\rho}, \lambda) \\ &\times D_1(\boldsymbol{\rho}, \lambda, z_2 - z_0, N, \lambda_0)\delta(\boldsymbol{\rho} - \boldsymbol{\rho}_0). \quad (2.79)\end{aligned}$$

Here, the operators $D_{1,2}$ are field propagators which take the field from the source to the sample, with transmission function $f$, and from the sample to the detector respectively. The variables in (2.79) will be defined in the following text as they are introduced.

The first propagator $D_1$ describes the propagation of the field from a point in the planar source at $z = z_0$ and propagation through a distance $z_1 - z_0$ to the monochro-

mator and then onto the sample at $z = z_2$. The source to sample propagator

$$\begin{aligned} D_1(\boldsymbol{\rho}, \lambda, z_2 - z_0, N, \lambda_0) &= \mathcal{F}^{-1}\tilde{D}_{AS}(\boldsymbol{\kappa}, \lambda, z_2 - z_1, \breve{\gamma}_N)\tilde{D}_M(\boldsymbol{\kappa}, \lambda, N, \lambda_0) \\ &\times \tilde{D}_S(\boldsymbol{\kappa}, \lambda, z_1 - z_0)\mathcal{F}[\cdot] \end{aligned} \tag{2.80}$$

is defined in terms of the source-to-monochromator propagator $\tilde{D}_S$ (Mandel and Wolf, 1995),

$$\tilde{D}_S(\boldsymbol{\kappa}, \lambda, z) = \frac{i}{\lambda}\frac{\exp\left(iz\sqrt{k^2 - |\boldsymbol{\kappa}|^2}\right)}{\sqrt{k^2 - |\boldsymbol{\kappa}|^2}}, \tag{2.81}$$

and N-reflection monochromator in terms of the monochromator crystal ARCs, $r_i$ (cf. §2.5.4) (Slusky and Macrander, 1987; Moller, 1994),

$$\tilde{D}_M(\boldsymbol{\kappa}, \lambda, N, \lambda_0) = \prod_{i=1}^{N} r_i\left(\pm\left[\omega_i - \frac{k_x}{\breve{\gamma}_i k}\right] - \frac{\lambda - \lambda_0}{\lambda_0}\tan\theta_{B_i}\right), \tag{2.82}$$

$$\breve{\gamma}_i = \prod_{j=1}^{i}\tilde{\gamma}_j \tag{2.83}$$

and finally, the angular spectrum propagator (cf. (2.38)),

$$\tilde{D}_{AS}(\boldsymbol{\kappa}, \lambda, z, \breve{\gamma}_N) = \exp\left[iz\sqrt{k^2 - \left(\frac{|\boldsymbol{\kappa}|}{\breve{\gamma}_N}\right)^2}\right]. \tag{2.84}$$

The first propagator $\tilde{D}_S$ describes a spherical wave originating from a point source at $\mathbf{r} = (\boldsymbol{\rho}, z_0)$ and propagating to $z_1$. We assume that $z_1$ is large enough that the field incident on the monochromator is paraxial and we can approximate the angular deviations in the argument of r as $\omega \approx k_x/k$. The second propagator, $\tilde{D}_M$, represents an N-reflection monochromator where each crystal of the monochromator is described by an $r_i$ with Bragg angle $\theta_{B_i}$. The bandwidth of the incident quasi-monochromatic radiation is expanded about the mean wavelength $\lambda_0$. The functional dependence on each crystal's rocking angle $\omega_i$ is suppressed for clarity, however we will later explicitly include the analyser crystal rocking angle as $\omega_C$. The $\gamma_i$ is the asymmetry ratio for the i-th crystal. The sign of the term in square brackets in (2.82) is chosen depending on the monochromator geometry so that consecutive non-dispersive reflections share the same sign and dispersive reflections have opposite signs.

For example the propagator for a non-dispersive two reflection monochromator would be,

$$\begin{aligned} \tilde{D}_M(\boldsymbol{\kappa}, \lambda, N = 2) &= r_1\left(\omega_1 - \frac{k_x}{\tilde{\gamma}_1 k} - \frac{\lambda - \lambda_0}{\lambda_0}\tan\theta_{B_1}\right) \\ &\times r_2\left(\omega_2 - \frac{k_x}{\tilde{\gamma}_1\tilde{\gamma}_2 k} - \frac{\lambda - \lambda_0}{\lambda_0}\tan\theta_{B_2}\right). \end{aligned} \tag{2.85}$$

The angular spectrum propagator $\tilde{D}_{AS}$ is as defined in (2.38) with an extra functional dependence on $\gamma$ to allow for possibility of asymmetric reflections. For each successive element past the monochromator we must scale the spatial frequency by the asymmetry factor of the N crystal reflections of the monochromator, $\check{\gamma}_N$.

The sample to detector propagator is composed similarly,

$$\begin{aligned} D_2(\boldsymbol{\rho}, \lambda, z_4 - z_2, \omega_C, \lambda_0) &= \mathcal{F}^{-1}\tilde{D}_{AS}(\boldsymbol{\kappa}, \lambda, z_4 - z_3, \tilde{\gamma}_C\check{\gamma}_N)\tilde{D}_C(\boldsymbol{\kappa}, \lambda, \omega_C, \check{\gamma}_N, \lambda_0) \\ &\times \tilde{D}_{AS}(\boldsymbol{\kappa}, \lambda, z_3 - z_2, \check{\gamma}_N)\mathcal{F}[\cdot] \end{aligned} \tag{2.86}$$

where, again, $\mathcal{F}[\cdot]$ represents the Fourier transform of the function that takes the position of the placeholder, "$\cdot$". All other propagators are as defined except for the analyser crystal,

$$\tilde{D}_C(\boldsymbol{\kappa}, \lambda, \omega_C, \check{\gamma}_N, \lambda_0) = r\left(\omega_C - \frac{k_x}{\check{\gamma}_N\tilde{\gamma}_C k} - \frac{\lambda - \lambda_0}{\lambda_0}\tan\theta_{B_C}\right) \tag{2.87}$$

and $\gamma_C$ is the analyser asymmetry and we define the total asymmetry factor $\tilde{\gamma}_T = \check{\gamma}_N\tilde{\gamma}_C$. The final intensity recorded by the detector is,

$$\begin{aligned} I\left(\frac{\boldsymbol{\rho}}{\tilde{\gamma}_T}, z_4, N, \omega_C, \lambda_0\right) &= \int_{\lambda_0-\Delta\lambda}^{\lambda_0+\Delta\lambda} d\lambda \int_\sigma d\boldsymbol{\rho}_0 S(\boldsymbol{\rho}_0, \lambda) \\ &\times \left|\Psi\left(\frac{\boldsymbol{\rho}}{\tilde{\gamma}_T}, z_4, \lambda, \boldsymbol{\rho}_0, N, \omega_C, \lambda_0\right)\right|^2 \end{aligned} \tag{2.88}$$

The wavelength dependence in $\tilde{D}_M$ limits the validity to quasi-monochromatic radiation since we have assumed a linear expansion of $\lambda$ about the mean wavelength in the argument of r (Slusky and Macrander, 1987; Moller, 1994). The assumption of quasi-monochromatic radiation is acceptable for the applications considered in this thesis. A general expression for the wavelength dependence in the argument of r is given in (Nesterets et al., 2005b).

The full propagator (2.88) is rarely used in practice as the essential components of an experiment can often be adequately described using such idealisations as the planar incident wavefield and monochromatic radiation. In addition, approximations must be made to (2.88) in order to make the associated inverse problem tractable.

## 2.7 Summary

In the proceeding chapters we will be concerned with describing analyser-based phase contrast imaging systems using the idealisations of coherent and incoherent radiation. Accordingly this chapter introduced the subject of coherence as it applied to rapidly

oscillating electromagnetic fields and showed how the field from an incoherent planar source may be calculated using the van Cittert-Zernike theorem.

We began by elucidating the basic properties of the electromagnetic field from the vector wave equation which follows from Maxwell's equations. The interaction of the complex X-ray wavefield with inhomogeneous media was described and the projection approximation was derived. This was followed by a description of the angular spectrum of plane waves which allows us to propagate a wavefield between parallel planes.

The interaction of the X-ray wavefield with crystalline matter is of central importance to this thesis and so we introduced the dynamical theory of X-ray diffraction. Using the Takagi formalism we can calculate the field diffracted from a crystal with slight distortions in the limit of dynamic and kinematic scattering.

The chapter concluded with the operator theory for linear shift-invariant systems applied to analyser-based phase contrast imaging. We summarised the main results by developing an operational description for ABI using an extended, incoherent and polychromatic planar source.

In the next chapter we will utilise these results to simulate ABI imaging using an incoherent source. A thorough understanding of the forward problem of image formation also provides an entry point to the study of the inverse problem and in the major claim of the next chapter we will demonstrate that it is possible to perform quantitative phase on ABI images recorded using an extended, incoherent, quasi-monochromatic source.

In Chapter 4 we again use the key results of this chapter to develop a new use for phase contrast imaging, namely Green's function retrieval and show that in the case of ABI it is possible to recover the complex Green's function of the analyser crystal. In this chapter we developed the relationship between the ARC and crystal's structure so that we can profitably utilise this connection once the Green's function has been recovered.

Chapter 5 demonstrates the implementation of our Green's function retrieval technique to experimental ABI data we recorded using a thick silicon analyser crystal. In this chapter we have given the prediction of dynamical diffraction theory for the same Green's function so that we may later compare the reconstruction to the theoretical result.

We now turn to the problem of phase contrast imaging and quantitative phase retrieval using a rotating anode X-ray source.

# 3 Analyser-based phase contrast imaging and phase retrieval using an extended incoherent X-ray source

This chapter investigates the problem of recording crystal analyser-based phase contrast images using an extended incoherent source, culminating in a quantitative analysis of the image thereby obtained[1]. In §3.1 we review the current state of the art for phase contrast imaging using laboratory X-ray sources. We follow this in §3.2 by considering the minimal coherence requirements that enable ABI contrast to be observed. We then discuss the possibility of achieving the minimum requirements using X-ray tube sources. In this section it will be shown that it is possible to measure ABI images using a standard X-ray diffractometer (XRD) with a crystal monochromator. Section 3.3 presents the results of an experiment in which an XRD with copper rotating-anode source was used to measure ABI images of a plastic test phantom.

The key result of this chapter is in §3.4 where we show that quantitative information may be extracted from images recorded using a rotating anode X-ray source under quite general conditions. ABI has immense potential as a characterisation tool and the ability to obtain quantitative information is an important practical consideration. As of yet no studies have been conducted which perform phase retrieval on ABI images recorded using an incoherent source and in §3.4 we perform phase retrieval on the data of §3.3 to demonstrate that this application is possible. The retrieved projected thickness is compared with an optical microscopy cross-section and the two are found to be in excellent quantitative agreement.

[1] This chapter is based on the publication "*Analyzer-based phase contrast imaging and phase retrieval*", D. J. Vine, D. M. Paganin, K. M. Pavlov, J. Kräußlich, O. Wehrhan, I. Uschmann and E. Förster, *Appl. Phys. Lett.*, **91** 254110 (2007) (Vine et al., 2007a)

## 3.1 Phase contrast and phase retrieval using conventional X-ray sources

A majority of the experimental research on X-ray phase contrast imaging to date uses synchrotron X-ray sources because they offer high brightness and coherence. Whilst this research is ongoing we now know that phase contrast imaging has an important role to play in areas such as medical diagnostic imaging (Arfelli et al., 1998; Bravin et al., 2002; Lewis, 2004) and materials characterisation (Schenk et al., 2005; Mayo et al., 2002a). The usage of these techniques however will be limited if they cannot be adapted for use with commonly available sources of X-rays. The use of laboratory based X-ray sources offers convenience, lower cost, higher volume and a quicker turnaround time than comparable synchrotron experiments. The usage of laboratory X-ray sources can be contrasted with the typical synchrotron experiment which can be difficult to win and usually requires expensive long distance travel.

Synchrotron sources have several advantages over laboratory based X-ray sources including increased flux and coherence and tunable energy (Attwood, 2000). Whilst the primacy of synchrotron facilities is not in doubt there remains a real need to develop phase contrast for widespread use, which realistically means using a fixed- or rotating-anode X-ray tube.

There are two notable compact alternatives to the anode based X-ray sources; namely the 'table-top' synchrotron and the laser plasma X-ray sources. For example, the Mirrorcle brand 'tabletop' synchrotrons are a commercially available product which combines the technology of synchrotrons and anode X-ray sources (Yamada et al., 2001; Yamada, 2003; Hirai et al., 2006). In the Mirrorcle synchrotron, electrons are accelerated through megavoltage potentials and injected into a storage ring where they are incident on a thin target anode to radiate Bremsstrahlung X-rays. The brilliance of the 6MeV model Bremsstrahlung is nearly an order of magnitude above the rotating anode Bremsstrahlung (Photon Production Laboratory, Ltd., 2008). The characteristic peaks of the rotating anode spectrum are, however, more brilliant than the Mirrorcle. The X-rays are not 'synchrotron X-rays', since they are not generated from the tangential acceleration of relativistic electrons, and therefore do not benefit from the increased brilliance of being emitted into a small opening angle (as is the case for insertion devices (Attwood, 2000)).

The laser plasma source uses a powerful pulsed laser to create a plasma which then radiates X-rays. Whilst the pulses have high peak brilliance the total flux is small as is the repetition rate, typically 10Hz (Toth et al., 2005, 2007). The X-ray emission

spectrum is peaked around atomic transition energies in the anode which can be filtered to achieve a monochromatic beam. The ability to focus the laser beam onto the anode limits the smallest achievable source size. A related device is the X-pinch which vaporises wires to create a plasma which radiates X-rays that can be used for imaging (Pikuz et al., 2001).

Whilst both of these sources have been demonstrated for phase contrast imaging they are not widely used and so we will focus our discussion on the X-ray tube source.

We are primarily interested in implementing ABI with such conventional X-ray sources however it is worth briefly to recapitulate the two alternative phase contrast methods that are commonly used with X-ray tube sources: propagation-based phase contrast imaging (PBI)(cf. §1.1.5) and Talbot interferometry imaging (TII)(§1.1.2).

Both of these have been introduced previously and so we will restrict the discussion to the pertinent aspects of these techniques as they relate to imaging with an X-ray tube source. The simplicity of PBI is a significant advantage over other techniques since it requires no optical elements beside a suitable propagation distance between sample and detector (Wilkins et al., 1996; Pogany et al., 1997; Stevenson et al., 1999; Mayo et al., 2003a,b). It is sensitive to the Laplacian of the phase in both transverse directions to the optical axis (Bremmer, 1952) (cf. §1.1.5) however it is very sensitive to spatial coherence and so must use either a microfocus tube source (Mayo et al., 2003a,b; Wilkins et al., 1996) or a collimator (crystal optics or mechanical). TII relies on precisely fabricated gratings which are designed to work with a specific wavelength and so the X-ray energy in this scheme is not easily tunable (Clauser, 1998; David et al., 2002; Weitkamp et al., 2004; Pfeiffer et al., 2006, 2008). An additional grating close to the X-ray source provides the field with the requisite coherence properties so crystal optics and small source sizes are not necessary

Analyser-based imaging (cf. 1.1.6) has been implemented using conventional X-ray tubes by a number of researchers (Förster et al., 1980; Somenkov et al., 1991; Ingal and Beliaevskaya, 1995; Davis et al., 1995b; Bushuev et al., 1997; Keyrilainen et al., 2002). In all of these cases the imaging was qualitative and general conditions under which ABI could be observed were not investigated.

The central aim of this chapter is to fill this gap and demonstrate the conditions under which ABI can be implemented using a rotating anode source and furthermore to show that quantitative measurements can be extracted from the results. To that end we now turn to a discussion of the feasibility of implementing ABI on a standard X-ray diffractometer using an extended incoherent source.

## 3.2 Considerations on the feasibility of implementing ABI using an extended incoherent X-ray source

We will break our discussion of the feasibility of implementing ABI using an incoherent source into two parts; the coherence requirements and the possibility of achieving the coherence requirements in terms of source and monochromator.

We will find that the biggest challenge to the practical implementation of ABI is the limited photon flux at the detector which results in a typical acquisition time of tens of minutes to several hours depending on the method of image acquisition.

### 3.2.1 Coherence requirements for analyser-based imaging

We would like to consider the coherence requirements for ABI with a view to determining some general conditions under which those requirements are met. A simple model of an ABI imaging system will be used that allows the state of coherence of the incident radiation to be varied and its effect on the detected intensity observed.

The effect of temporal coherence on ABI contrast was studied in Nesterets et al. (2005b) who found that the monochromator played a crucial role in ABI contrast formation. In that article a plane, polychromatic X-ray beam was incident on a sample, followed by analyser crystal and then detected with or without a monochromator. The effect of polychromaticity can be explained with reference to the crystal ARC function (Slusky and Macrander, 1987; Moller, 1994),

$$r = r\left(\omega - \frac{k_x}{k} - \frac{\lambda - \lambda_0}{\lambda_0}\tan\theta_B\right) \tag{3.1}$$

where $\omega$ is the small deviation from the Bragg angle and $\lambda_0$ is the mean wavelength. From (3.1) we can see that a variation in wavelength is equivalent to a slight change in the incident angle of the radiation. Nesterets et al. (2005b) found that in the absence of the monochromator the contribution of symmetric points on either side of the rocking, due to the incident polychromatic radiation, produced equal and opposite contrast which tended to cancel out. The introduction of a monochromator re-weighted the contributions to the contrast from each side of the analyser ARC which removed the contrast cancellation.

We find that ABI contrast could be observed in the absence of a monochromator if either the incident radiation bandwidth (for polychromatic plane waves) or the incident divergence (for paraxial monochromatic waves) are smaller than analyser crystal Darwin width, $\Delta\theta_D$, where the conversion between polychromaticity and

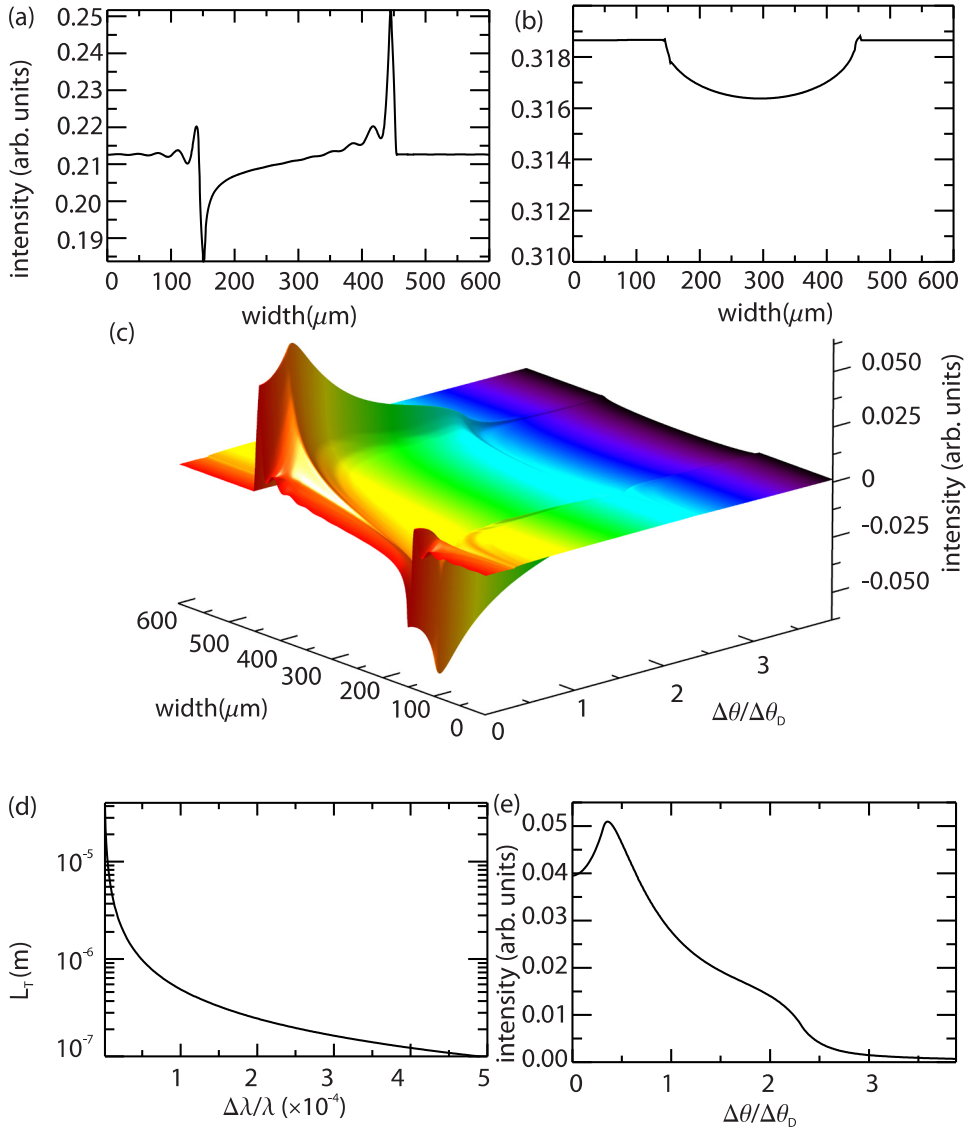


Figure 3.1: **The effect of temporal incoherence on ABI contrast formation.** For simulation details see text. Line profiles through the measured intensity as a function of incident beam polychromaticity for (a) $\Delta\lambda/\lambda = 1.2 \times 10^{-6}$ and (b) $\Delta\lambda/\lambda = 5 \times 10^{-4}$. (c) The transition between (a) and (b) plotted as a function of the ratio of beam divergence $\Delta\theta$ to analyser Darwin width $\Delta\theta_D$ ($\Delta\theta_D = 10.3\mu$rad for Si(111) sigma polarisation (Stepanov, 2008)). (d) The temporal coherence length, $L_T$, as a function of incident beam polychromaticity. (a) A line profile through the surface of (c) beginning with the highest contrast point and plotted as a function of beam divergence.

divergence comes from (3.2). In this case the symmetric points of the rocking curve are not illuminated simultaneously and the contrast cancellation cannot occur.

To demonstrate that ABI can be measured without a monochromator for suitably quasi-monochromatic plane wave illumination or monochromatic paraxial wave illumination we performed the following simulation. Plane polychromatic X-ray

radiation with mean energy 25keV ($\lambda_0 = 0.49$Å) was made incident on a water-filled cylindrical hole of diameter 300μm in a slab of polypropylene. The complex refractive indices of the water and polypropylene are ($\delta$,$\beta$)=($3.4 \times 10^{-7}$, $9.7 \times 10^{-11}$) and ($3.7 \times 10^{-7}$, $1.7 \times 10^{-10}$) respectively (Gullikson, 2008). The wavefield exiting the sample was Bragg reflected from the symmetric (111) reflection of a semi-infinite, perfect silicon analyser crystal detuned from the exact Bragg condition by 1.4" and then detected. The effect of propagation between the sample, analyser and detector has been neglected in this idealised experiment. The wavelength dependence of the sample complex refractive index has been neglected which is a good approximation for small bandwidths such as those we will be considering.

The coherence of the radiation is varied by increasing or decreasing its bandwidth (cf. (2.11)) and we note that since divergence in the incident beam is equivalent to a wavelength spread,

$$\frac{\Delta\lambda}{\lambda} = -\Delta\theta \cot\theta_B \tag{3.2}$$

meaning we can discuss the effect of spatial incoherence from temporal coherence considerations. The simulations were performed by dividing the bandwidth of the incident radiation (a top hat function) into discrete steps and incoherently adding the intensity formed by the monochromatic ABI imaging system for each discrete wavelength step.

The results of the simulations are presented in Figure 3.1 where we have depicted line profiles through the intensity recorded as the bandwidth of the incident radiation is varied. In Figure 3.1(a) and (b) we have a $\Delta\lambda/\lambda = 1.2 \times 10^{-6}$ ($\Delta\theta/\Delta\theta_D \approx 1\%$) and $\Delta\lambda/\lambda = 5 \times 10^{-4}$ ($\Delta\theta/\Delta\theta_D \approx 388\%$). In the former case we can see quite strong ABI contrast whereas for the larger bandwidth the ABI contrast has all but disappeared leaving only the absorption contrast profile. The transition from Figure 3.1(a) to (b) is given as the surface plot in Figure 3.1(c) which has been normalised by subtracting the mean of each line profile for ease of visualisation. Also plotted is the temporal coherence length as a function of bandwidth in Figure 3.1(d) and a line profile through the surface of Figure 3.1(c) at the point with maximum contrast as a function of bandwidth.

The decrease in contrast with increasing bandwidth is due to the mechanism identified by Nesterets et al. (2005b) in that symmetric points on the ARC when illuminated simultaneously cause a cancellation of the ABI contrast. The contrast initially increases and then begins to decrease when the divergence of the incident radiation approaches half the Darwin width, see Figure 3.1(e). The initial increase in

contrast is due to the adjacent points on the rocking curve being illuminated and the similar contrast of these points superposing to increase the overall contrast. After the slight increase, the contrast effectively drops until it reaches the absorption contrast profile. The contrast does not disappear as the beam divergence reaches one Darwin width because the analyser is slightly detuned from the Bragg condition.

The results of this simulation lead us to make the claim that in order to observe optimal ABI contrast the radiation incident on the analyser crystal should have a divergence less than the analyser's Darwin width.

### 3.2.2 Source/ Monochromator Requirements for ABI

In this section we ascertain the source-monochromator coupling (Slusky and Macrander, 1987; Moller, 1994; Caciuffo et al., 1987; Robinson and Tweet, 1992; Schuster and Herres, 1994) that will provide sufficient coherence for ABI phase contrast to be measured. It is well known that the X-ray tube requires monochromatisation in order to produce radiation with a usable coherence length. We will first describe that radiation from an X-ray tube with a macroscopic focal size is incoherent which necessitates monochromatisation. Several monochromator geometries are briefly discussed and the resulting coherence properties of the radiation they produce. The coherence requirements of ABI deduced in §3.2.1, namely that the incident beam divergence should be smaller than the analyser Darwin width for optimal ABI contrast, are compared with the coherence lengths of radiation from commonly used monochromators.

Whilst the fixed- and rotating-tube source are both commonly used in XRD experiments we will concentrate on the latter source because it produces a more brilliant beam. The relevant source parameters for the purposes of ABI are the flux and focal spot size. The focal spot size is the footprint of the electron beam on the anode and is the effective X-ray source size. The flux is limited by the maximum heat load of the anode, the focal spot and power of the electron beam.

Whilst decreasing the source size is one method of increasing the spatial coherence the resulting increase in image acquisition time due to a diminished flux is prohibitive. A better method may be to have a large focal spot for maximum flux and increase the coherence of the field using crystal optics. We make a distinction between monochromators and analysers as the function of the former is to reduce the energy bandwidth and the latter to reduce the angular acceptance.

A monochromator uses the finite width of a Bragg reflection peak to select an energy band from a continuous spectrum. The Darwin width of a Bragg peak is

| Crystal | hkl | $\Delta\alpha$ (μrad) | $\Delta\lambda/\lambda$ $(\times 10^{-6})$ | $L_T$ (μm) | $L_S$ (μm) | $\Lambda$ (μm) |
|---|---|---|---|---|---|---|
| Silicon | 111 | 33.2 | 131.0 | 1.9 | 4.6 | 1.5 |
| | 220 | 24.9 | 56.9 | 2.7 | 6.2 | 2.1 |
| | 311 | 10.5 | 13.35 | 11.5 | 14.7 | 3.8 |
| | 440 | 12.0 | 8.9 | 17.3 | 12.8 | 6.9 |
| Germanium | 111 | 74.81 | 308.3 | 0.5 | 2.1 | 0.67 |
| | 220 | 57.8 | 138.6 | 1.1 | 2.7 | 0.92 |
| | 311 | 23.7 | 32.1 | 4.8 | 6.5 | 1.64 |
| | 440 | 25.5 | 20.9 | 7.4 | 6.05 | 3.02 |

Table 3.1: **Properties of commonly used monochromator crystals** Darwin width ($\Delta\alpha$) (Stepanov, 2008), bandwidth, temporal coherence length $L_T = \lambda^2/\Delta\lambda$, spatial coherence length $L_S = \lambda/\Delta\alpha$ and extinction length $\Lambda$ (Stepanov, 2008) for some reflections from silicon and germanium at $\lambda = 1.54$ (CuK$\alpha$1).

proportional to a number of factors including the asymmetry of the reflection and the Fourier coefficient of its susceptibility and so a judicious choice of these parameters is required when designing an experiment. Commonly used materials for X-ray monochromators are silicon and germanium and Table 3.1 lists the salient properties of these crystals.

For ABI with a tube source we would like to create a bandpass that selects the characteristic line width of the K$\alpha_1$ peak and also provides sufficient spatial coherence by collimating the beam. Common monochromator configurations are the double-crystal and four-crystal setups and we briefly turn to a discussion of the properties of these for ABI.

Double-crystals configured in a parallel (+-) arrangement will be non-dispersive if they are made of the same element and use the same reflection. This arrangement is called non-dispersive because it does not increase the wavefield divergence. The parallel crystal setup is used for beam collimation because it is good for suppressing the tails of the rocking curve however it requires a slit to provide energy band discrimination.

The anti-parallel (++), or dispersive, two crystal arrangement provides excellent energy band discrimination but produces a beam with greater divergence than the comparable non-dispersive reflection (Caciuffo et al., 1987). This problem is alleviated somewhat with the four-crystal Bartels monochromator which combines two non-dispersive reflections with a dispersive reflection between the innermost crystals. This setup has the advantage of combining the best features of both dispersive and non-dispersive geometries. If the pass band is made to select the characteristic transition of the anode then a beam with excellent collimation and monochromaticity can be attained. The disadvantage of this monochromator is significant loss of flux from the

four reflections.

The angular acceptance of a crystal can be used to calculate the temporal and spatial coherence lengths of the exiting radiation (Pietsch et al., 2004),

$$L_T = \frac{\lambda^2}{\Delta\lambda}, \tag{3.3}$$

$$L_S = \frac{\lambda}{\Delta\alpha} \tag{3.4}$$

and these are shown in Table 3.1 for some common crystal reflections.

To maximise the flux at the detector the analyser crystal should be chosen to match the monochromator crystal in a (+n,-n) non-dispersive setting.

We are now in a position to compare the coherence requirements of ABI with the coherence of the radiation from the monochromator. In section 3.2.1 we made the claim that the divergence of the beam falling on the analyser crystal should be no greater than its Darwin width to achieve an acceptable level of phase contrast. In Figure 3.2 we have calculated the full-width at half-maximum of the effective reflectivity of the Ge(220) four-crystal Bartels monochromator as a function of the angle between dispersive reflections (Slusky and Macrander, 1987; Moller, 1994)

$$r(\omega) = r\left(\omega - \theta_B - \frac{\lambda - \lambda_0}{\lambda_0}\tan\theta_B\right)^2 r\left(-\omega + \theta_B - \frac{\lambda - \lambda_0}{\lambda_0}\tan\theta_B\right)^2. \tag{3.5}$$

The Darwin width of a Ge(220) analyser crystal is 57.8μrad (11.9 arcseconds) and we can see from Figure 3.2(b) that the range of angles shown all the FWHM satisfy the condition of providing a beam divergence smaller than the Ge(220) Darwin width. This is not unexpected since we are using the same crystal and reflection for monochromator and analyser however the same methodology could be applied to monochromator/analyser pairs using different crystals or reflections to determine the range of angles that will give optimal ABI contrast.

The final choice of ω is a tradeoff between energy band discrimination and flux and we can see in Figure 3.2(b) the shaded area represents the normalised area of the combined four reflection Bartels monochromator. A larger area correlates with a greater transmitted flux and so this plot depicts the cost of increased energy discrimination in terms of transmitted flux.

### 3.2.3 Stability requirements for analyser based imaging

The thermal stability of the crystal optics and the mechanical stability of the equipment in general must be controlled to achieve optimum imaging conditions.

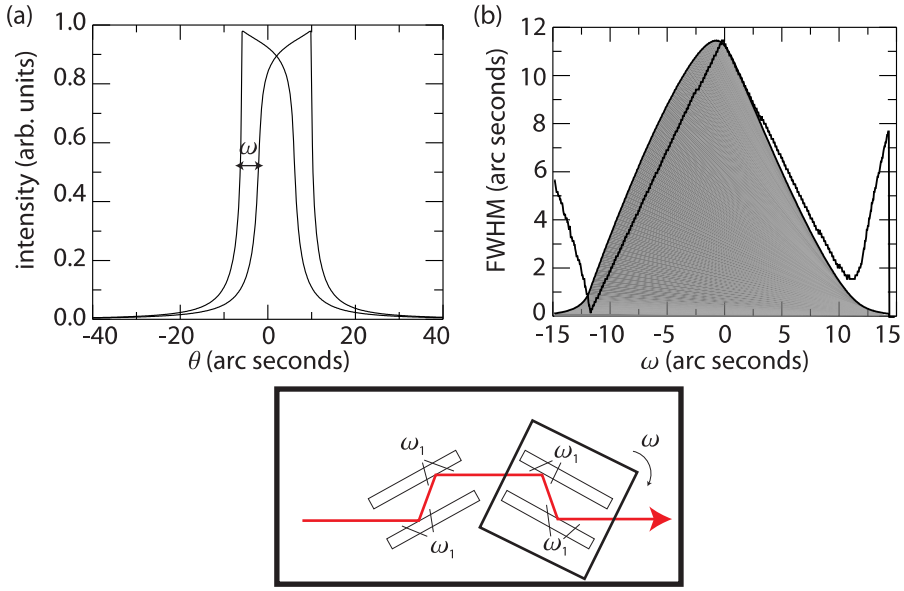


Figure 3.2: **FWHM of the Bartels monochromator.** (a) each peak represents the two non-dispersive reflections of the Ge(220) four crystal Bartels monochromator are plotted with an angle ω between the dispersive reflections as in the inset. (b) the full-width at half-maximum (FWHM) of the combined Bartels monochromator transfer function is plotted against ω (Fig 2 in Möller (Moller, 1994) shows an equivalent surface to the one from which these FWHM are calculated). The shaded area is the normalised area of the transfer function and can be associated with the transmitted flux.

The mechanical stability is perhaps easier to control because the ABI requirements are no more stringent than those of HRXRD. Since any motion during the exposures will appear as a blurring of the image we simply require a mechanical stability better than the smallest resolvable feature.

Thermal stability plays a far more important role in ABI image contrast formation. The thermal expansion of the analyser crystal during the measurement changes the interplanar spacing and thus shifts the Bragg angle. Shifting the Bragg angle varies the working point of the direct beam during the exposure and will cause artifacts in the image.

We can estimate the shift of the Bragg peak, for monochromatic radiation, due to thermal variation by considering,

$$\frac{\Delta d}{d} = -\cot\theta_B \Delta\theta, \tag{3.6}$$

where d is the lattice spacing. The linear expansion factors α of silicon and germanium at room temperature are $\alpha_{Si} = 2.6 \times 10^{-6}K^{-1}$ (Roberts, 1981) and $\alpha_{Ge} = 5.8 \times 10^{-6}K^{-1}$ (Feder and Light, 1972). Equating these results gives for a temperature

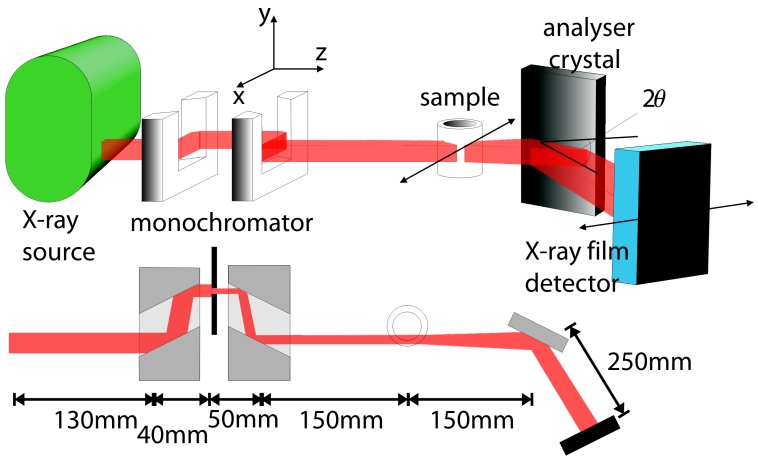


Figure 3.3: **Experimental apparatus used to record an ABI image using an incoherent source.** A rotating anode, Ge(220) four-crystal monochromator and analyser crystal were used to image a plastic test phantom.

variation $\Delta T$ gives,

$$\frac{\Delta d}{d} = \alpha \Delta T = -\cot\theta_B \Delta\theta. \tag{3.7}$$

We can see that a temperature change of $1^\circ$K results in a shift of the Ge rocking curve $\Delta\theta = 0.5''$ which is approximately 5% of the Darwin width—a non-negligible amount.

This suggests that special care should be taken in controlling the ambient temperature of the experiment and indeed temperature is a concern in the experiment we will describe in the following section. The temperature control we require is no more onerous than should be done in a careful HRXRD measurement however.

## 3.3 Experimental setup for quantitative ABI

In the preceding section we have shown that it should be possible to measure ABI phase contrast images using an X-ray diffractometer. In particular, we showed that the requirement to observe ABI contrast is an incident beam divergence smaller than the angular acceptance of the analyser crystal and if possible a coherence length longer than the extinction length of the analyser. We then presented some characteristics of monochromators that spoke to their ability to meet the minimum requirement.

Further to the possibility of measuring phase contrast, with some additional measurements involving the linearity of the X-ray film detector with exposure, we will show that we can now perform quantitative phase retrieval from images measured using an extended incoherent source. This key step paves the way for quantitative

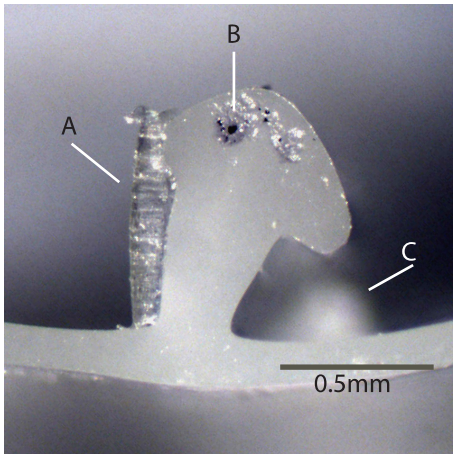


Figure 3.4: **Cross sectional optical microscopy image of the sample.** The sample is the interlocking strip from a resealable plastic bag. The sample shown here was sectioned following the X-ray measurement. Three artifacts in the image have been labelled: A is a sliver of plastic which resulted from the cross-sectioning the sample for optical measurement, B is some dirt that could not be removed before imaging but again is a result of the cross-sectioning and C is an out of focus artifact not present in the sample.

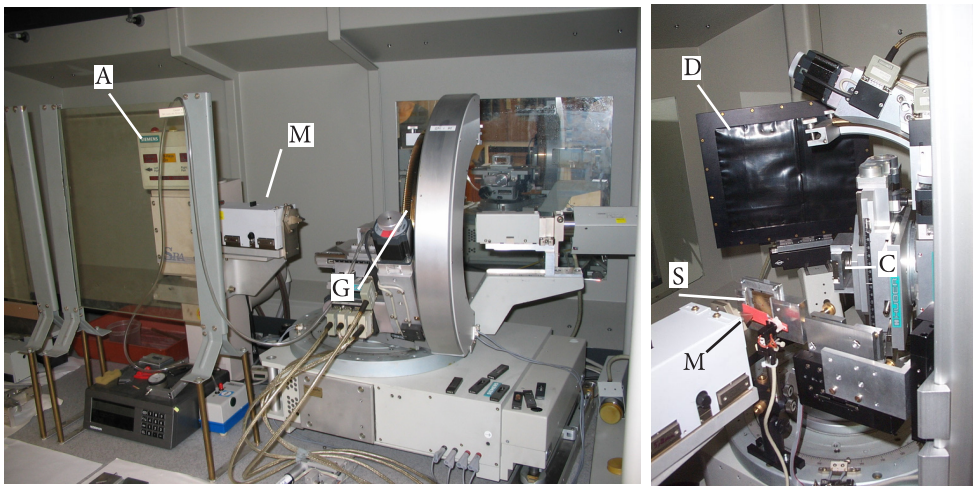


Figure 3.5: **Diffractometer used to record analyser-based phase contrast image**. A—Rotating anode X-ray source, M—the 4-bounce Ge(220) Bartels monochromator, G—the 4-circle goniometer, S—the sample stage, C—the Ge(220) analyser crystal and D—the high resolution photographic film detector.

characterisation using ABI to be implemented in X-ray laboratories and may obviate the need for synchrotron sources for some applications.

We chose as our sample a thin plastic interlocking strip from a resealable bag (see Fig 3.4). This sample was chosen because it was rigid enough to not move during the measurement and could be sectioned for optical measurement at the conclusion of the ABI experiment.

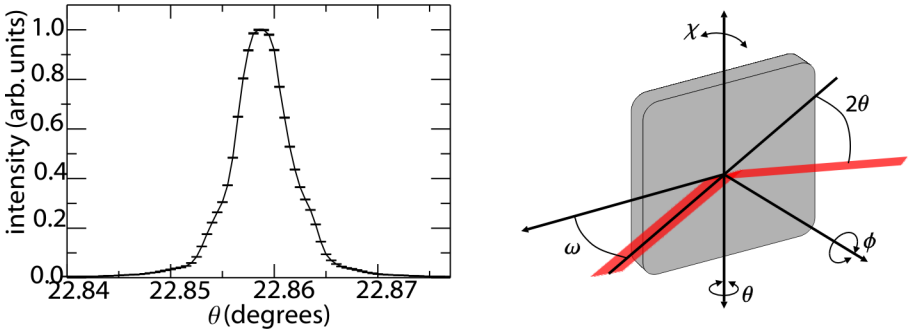


Figure 3.6: **Ge(220) rocking curve measurement and goniometer axis.** (a) A $\theta - 2\theta$ scan of the GaAs(220) rocking curve. (b) Axis of the four-circle goniometer.

The diffractometer (see Figure 3.5), a Siemens D-5000, includes a copper rotating anode X-ray source, 4-circle goniometer and scintillation detector. The diffractometer was modified to include a sample stage with two-dimensional transverse translation and beam shutter mounted between the monochromator and analyser crystal and a high resolution film detector stage mounted in front of the scintillation detector with one-dimensional transverse translation capability. All experiments were performed at the Institute of Optics and Quantum Electronics at Friedrich-Schiller University in Jena, Germany[2].

The rotating-anode source was operated at 30kV and 100mA with a focal spot of 0.5× 1mm and a primary slit size of 2mm. A four-bounce germanium (220) Bartels monochromator was used with a secondary slit of 0.2mm between the innermost reflections. The K$\alpha$1 line was selected from the copper anode to give a mean wavelength $\lambda = 1.5406$Å. The spatial and temporal coherence were calculated to be $L_S = 2.5\mu$m and $L_T = 1\mu$m respectively. The beam size exiting the monochromator was approximately 0.2mm (hor)× 1mm (ver) and the distances are as given in Figure 3.3. Due to the small beam size relative to the sample the image was acquired as a number of discrete exposures and overlaid in a post-measurement processing step.

The analyser crystal was mounted in the goniometer as in a normal HRXRD experiment. A rocking curve was measured prior to recording each image and a typical scan is shown in Figure 3.6(a). To provide the highest contrast for ABI the analyser crystal was detuned from the exact Bragg condition to the 50% reflectivity point—either side of the Bragg angle is equivalent and for these measurements the low-angle side was chosen arbitrarily. The goniometer rotation axis adhered to the

[2]I performed these experiments in October-December 2006 at the Institute of Optics and Quantum Electronics at Friedrich-Schiller University, Jena with help from staff at the Institute. A complete summary of my contribution is given prior to the reprint describing this work in Appendix B.

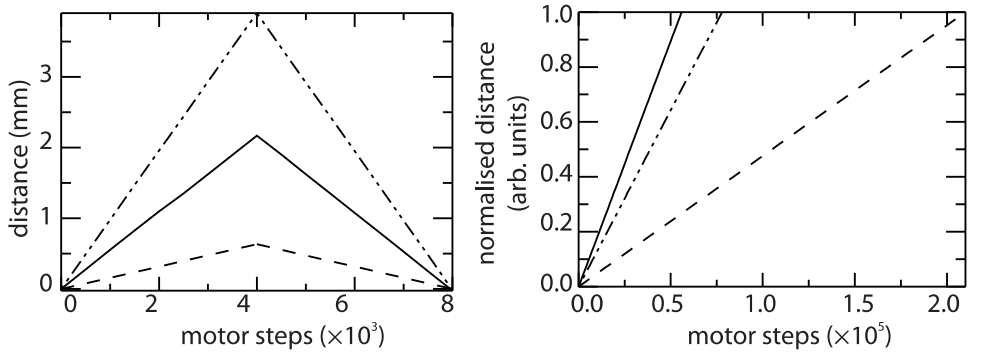


Figure 3.7: **Sample and detector stage translation linearity and backlash** (a) stepper motor backlash for (solid) sample horizontal, (broken) sample vertical and (broken/ dash) detector horizontal. (b) linearity of motor drivers. Normalised distance versus step across the range of the motors.

standard as given in Figure 3.6(b) with the relevant parameter for ABI imaging being the θ rotation which has a reproducible accuracy of 0.001°.

An Agfa high resolution X-ray film detector was used to record the images. The use of film increased the post image processing considerably but has the advantage of micrometric resolution. The film was digitally scanned using an Epson Perfection 4990 at 16-bit greyscale with a maximum interpolated resolution of 12800dpi (natural resolution 6400dpi) or 1.98μm.

The vertical and horizontal sample stage and detector horizontal translation stepper motors were controlled by Labview (National Instruments Corporation, USA). As the image processing required a large number of distinct exposures to be overlaid we require a high degree of accuracy in the hand-made translation stages. Correspondingly, the motors were checked for backlash and linearity and the results are in Figure 3.7. In Figure 3.7(a) the motors were checked for backlash by translating them in one direction by 20 motor steps for a total of 500 steps and then reversing them in the same manner. The initial and final positions differed by (solid) 24μm, (broken) 15μm and (broken/dash) 1 μm respectively. In Figure 3.7(b) the motors were checked for linearity over by stepping them 50 steps and recording their position over the entire travel of the motors.

The X-ray film exposure response was tested by recording the direct beam (analyser, no sample) over a range of exposure times. The results are presented in Figure 3.8 whose top panel shows the line profile through the exposures and below is the mean pixel value as a function of exposure time. The film response is approximately linear over the range 0 to 80 seconds. This result is particularly important in the context of quantitative imaging where we will assume that greyscale level is linearly proportional

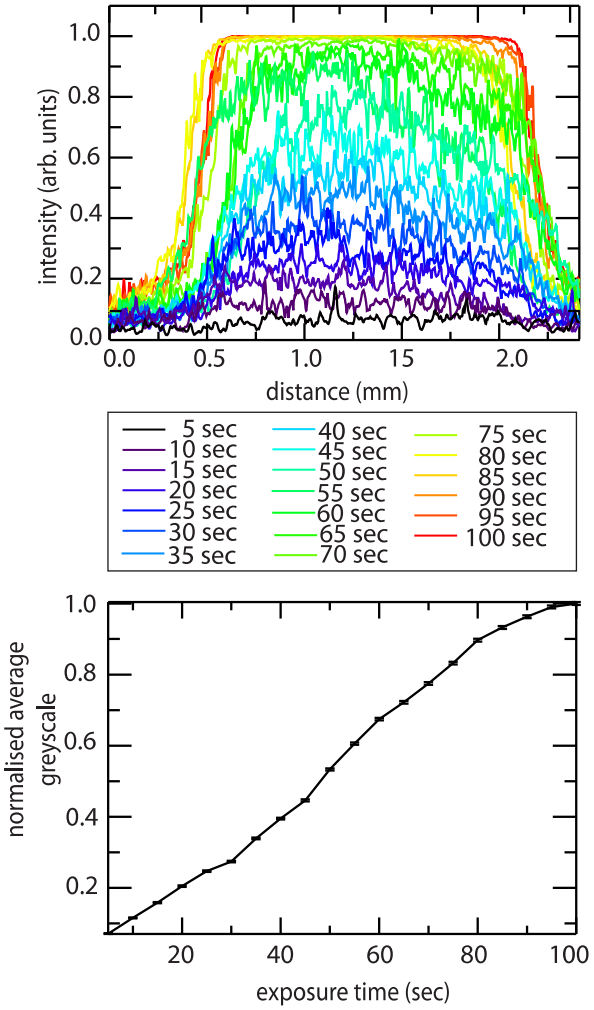


Figure 3.8: **Calibration of the high resolution X-ray film.** (a) line profiles as a function of exposure time. (b) the normalised average greyscale value as a function of exposure time.

to the number of absorbed photons.

The image measurements were recorded by sequentially scanning the sample through the beam and recording a number of discrete exposures; a typical exposure set is shown in Figure 3.9. In the figure a series of ten direct beam exposures are present on the left followed by a gap, then 105 different sample positions and each sample image recorded twice, followed by a further ten direct beam measurements. The image was stitched together digitally in a post-measurement processing step. The sample was translated 27.5μm between exposures, equivalent to 13% of the beam width, and the large overlap between adjacent exposures was used to match features for assembling the final image and to further improve the signal-to-noise. The beam size at the sample was approximately 0.2 × 1.5mm and at the detector approximately

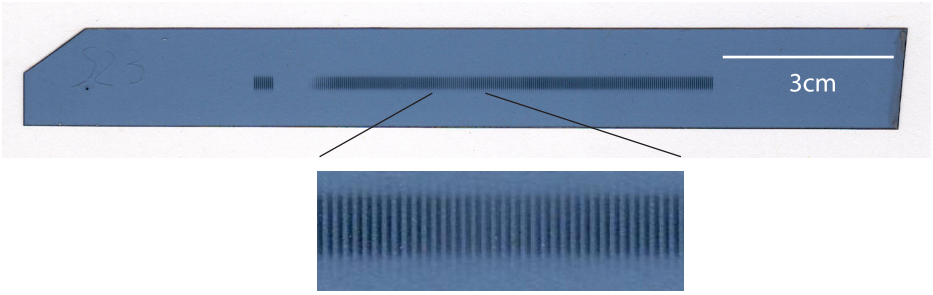


Figure 3.9: **A single 'image' recorded on high resolution X-ray film.** The resultant image is assembled from 105 discrete exposures as the sample is scanned through the beam. To the left are the 10 initial direct beam measurements (final direct beam images are also present however there is no gap between them and the images).

$0.2 \times 2.1$mm corresponding to a geometrical magnification of 2.1. To acquire an acceptable signal to noise ratio each sample position was imaged twice and averaged. Each measurement was exposed for 47 seconds and the data set took approximately four hours to measure. The ambient temperature during the experiments fluctuated by no more than 3° as measured on a digital thermometer in the diffractometer enclosure.

The film was developed and digitally scanned and individual exposures were cut from the scan using IDL 6.4 (ITT Visual Information Solutions, Boulder, CO). After averaging the exposures, direct beams and dark field (no exposure), a flatted exposure was created according to,

$$\text{flat exposure} = \frac{\text{average exposure} - \text{average dark}}{\text{average direct} - \text{average dark}} \tag{3.8}$$

where the average direct beam exposures are a linear interpolation between the initial and final direct exposures.

Assembling the final image was performed using PCDetpak32 software v6.0 (R. Lewis, Monash Centre for Synchrotron Science) by identifying a feature in two adjacent exposures and measuring the shift in pixels between them. This shift was then used to overlay the common region between each of the exposures and the final image was the sum of each overlaid adjacent.

The sample was oriented vertically (refraction parallel to the analyser crystal diffraction plane) and horizontally (perpendicular to the analyser diffraction plane) and these results are shown in Figure 3.10 and Figure 3.11 respectively. The phase contrast is clearly evident in Figure 3.10 as is the varying background level due to thermal expansion of the analyser crystal which caused a shift in the working point (angle of incidence of direct beam) of the rocking curve. Clearly the linear interpolation of

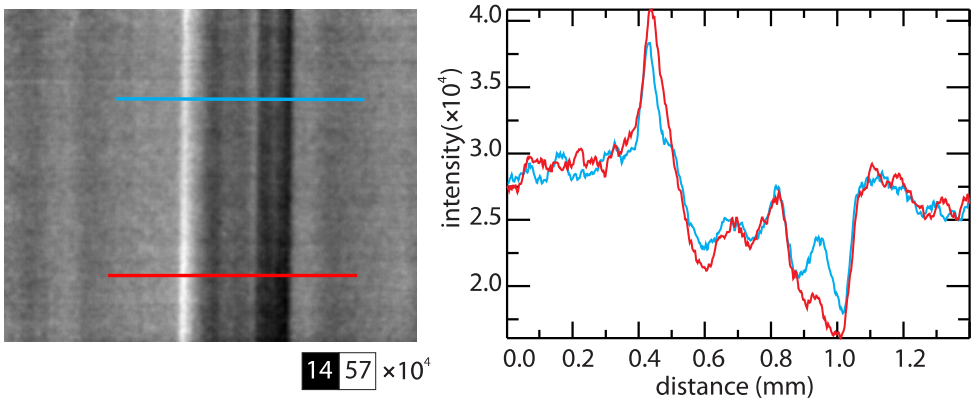


Figure 3.10: **Analyser-based phase contrast image using a rotating anode source.** A pseudo-one-dimensional plastic test phantom (cf. Figure 3.4) oriented so that refraction is perpendicular to the analyser crystal diffraction plane. Coloured line profiles are presented to the right.

direct beam exposures used in flatting the image was inadequate given the apparently non-linear variation in background. The blurring in the image has contributions from the finite source size, analyser crystal and detector.

Figure 3.11 shows virtually no contrast due to the sample as the diffraction from the plastic phantom was perpendicular to the diffraction plane of the analyser crystal. The oscillating contrast evident in this image is again due to the thermal instability of the analyser crystal.

The X-ray beam in the vertical direction is mechanically collimated using slits only. This results in a non-negligible divergence which gives a magnification of 2.1 in the vertical direction. The crystal is insensitive to this divergence and so it does not affect ABI contrast formation.

The time taken to record the image, as stated previously, was approximately four hours. This sort of time scale is prohibitive for many applications and must be reduced to the order of minutes for ABI to be practicable as characterisation tool. The attenuation of the copper K$\alpha$1 X-rays in air is approximately 2% (Hubbell, 1982) and negligible for our purposes. The predominant sink of flux in our experiment is the monochromator and so we are left with a trade-off between flux and coherence which affect the exposure time and ABI contrast visibility respectively.

## 3.4 Phase retrieval using an extended incoherent source

The ability to perform quantitative phase retrieval on phase contrast images is enormously important for many applications. Extracting quantitative information from

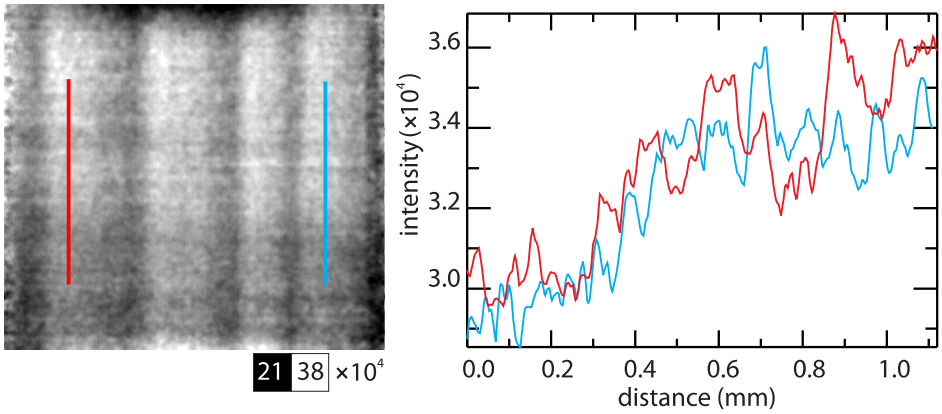


Figure 3.11: **The plastic test phantom of Fig. 3.10 rotated by** 90°**.** Refraction from the sample is parallel to the diffraction plane of the analyser crystal resulting in little or no contrast due to the sample. The vertical oscillations are due to the thermal expansion of the analyser crystal over the course of the measurement.

phase contrast images is a useful tool which may make the use of ABI attractive to a wider range of scientists than those currently using the technique (predominantly at synchrotrons). We would like to now show that quantitative phase retrieval may be performed on the image measured in §3.3, Figure 3.10.

In ABI phase retrieval there are a number of common approximations such as the weak object (Nesterets et al., 2004)(cf. §2.3), linear transfer function[3] (Paganin et al., 2004) and slowly varying transfer function[4](Pavlov et al., 2004). These approximations limit the range of validity of their application meaning phase retrieval is not possible in a wide variety of cases. The linear transfer function approximation has been used for synchrotron ABI data however here we face the significant complication that the working point of the direct beam on the analyser crystal rocking curve is not constant. Since the gradient of the rocking curve is calculated at this point and assumed constant this will lead to significant artifacts if not compensated for.

For these conditions we have chosen to employ a phase retrieval algorithm due to Paganin et al. (2004) which enables the phase to be retrieved from a single image given that the object is composed of a single material. This phase retrieval algorithm, the details of which will be outlined in the next paragraph, has the advantage of not assuming knowledge of the sample's complex refractive index or the working point of the incident beam on the rocking curve. Instead, it uses a single real parameter to optimise the phase retrieval by tuning the parameter to give the best feature visibility.

[3]This approximation linearises the imaging system transfer function with respect to spatial frequency, which greatly aids analytic phase retrieval solutions however it is quite a restrictive approximation.

[4]In this approximation the second and higher-order derivatives of the transfer function with respect to spatial frequency are neglected.

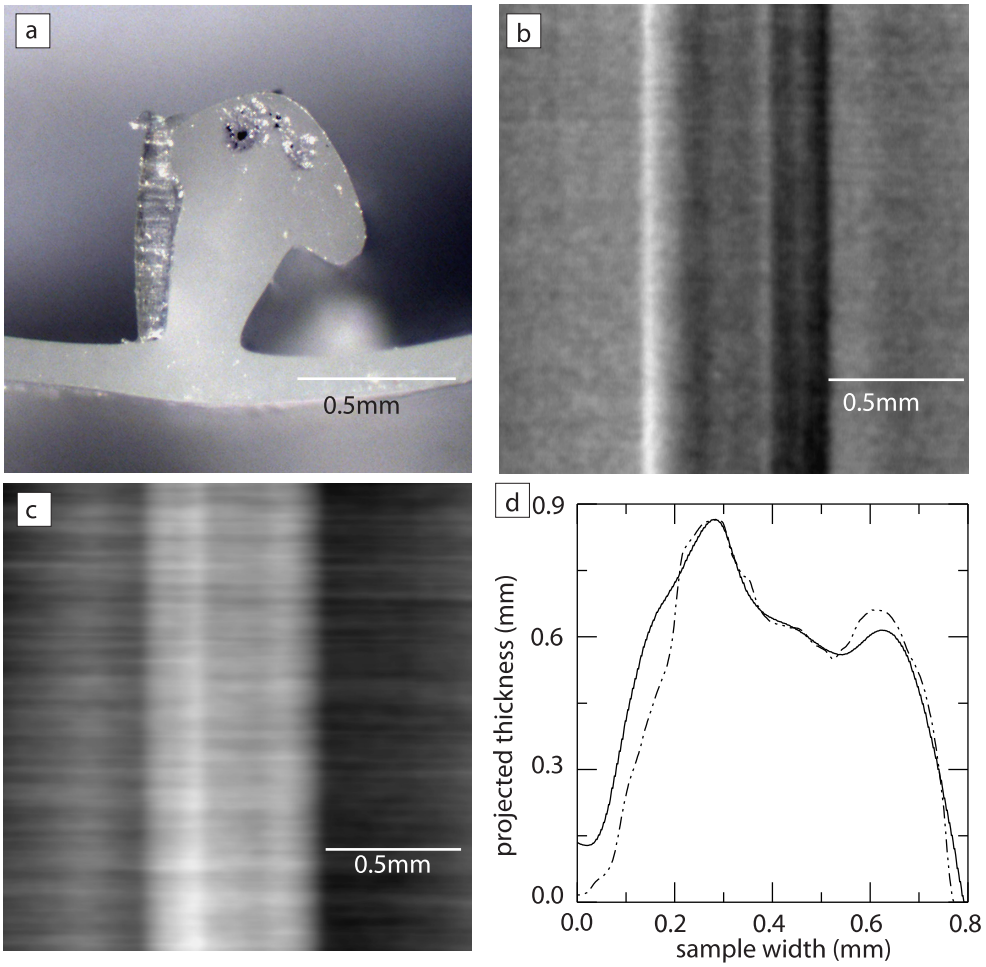


Figure 3.12: **Phase retrieval performed on ABI image data.** (a) and (b) are the optical microscopy cross section and ABI image of the plastic test phantom. (c) is the phase retrieved from (b), (d) is a comparison of the average projected thickness retrieved from the ABI image (solid line) with the reference optical microscopy image (broken line).

The use of a tunable parameter in the phase retrieval algorithm is analogous to the focus knob on a microscope which can be adjusted until an image is in focus. Similarly here the tunable parameter is varied until a precondition is met, namely the disappearance of the characteristic linear transfer function contrast. The use of a tunable parameter instead of knowledge of the sample's complex refractive index and the direct beam reflectivity considerably simplifies what would otherwise be a complicated multi-dimensional optimisation problem. The ability to perform phase retrieval on a single image saves time and effort by obviating the need to record a second image which is more common for ABI phase retrieval (see for example (Chapman et al., 1997)).

We assume that we have a normally incident plane wave with unit intensity illu-

minating the sample which is thin enough for the projection approximation to be valid (cf. §2.3). The sample is composed of a single material and so the phase, $\varphi$, and attenuation, $\mu$, of the transmission function are related by,

$$\varphi = -\frac{\delta}{\beta}\mu \tag{3.9}$$

where $\delta$, $\beta$ and $\lambda$ have their usual meaning (cf. (2.18)). The single-material approximation is the key to one-image phase retrieval because the phase and attenuation are linearly proportional to each other, so that a single image contains enough information to uniquely specify the phase and amplitude.

We assume that the input phase and intensity are slowly varying functions so that their spatial frequency spectrum is bandlimited to low spatial frequencies. This allows us to expand the crystal rocking curve, $R$, as a first order Taylor series with respect to spatial frequency about a (static) working point of the rocking curve $k_x^0$,

$$R(k_x) \approx R(k_x^0) + (k_x - k_x^0)R'(k_x^0) \tag{3.10}$$

where $R(k_x^0)$ is the reflectivity of the unscattered X-rays and $R'(k_x^0)$ is the gradient at that point. The linearisation of the analyser crystal ARC is equivalent to assuming that the rays incident on the crystal will be reflected with an intensity linearly proportional to their refraction angle. This will be a good approximation if the sample introduces refraction through angles smaller than the Darwin width of the crystal.

Under these approximations the projected thickness of the sample is related to the measured intensity, I, by (Paganin et al., 2004),

$$\begin{aligned} t(x,y) = &-\frac{1}{2k\beta} \\ &\times \ln\left(\mathcal{F}^{-1}\left[\frac{1}{|A|^2 + ik_x\{\frac{\delta}{\beta}\mathrm{Re}[AB^*] - \mathrm{Im}[AB^*]\}}\mathcal{F}\{I(x,y)\}\right]\right) \end{aligned} \tag{3.11}$$

where $A = R(k_x^0) - k_x^0 R'(k_x^0)$ and $B = R'(k_x^0)$. Noting that the output will be in the form of a greyscale image we can make some significant simplifications to (3.11). If a greyscale image's contrast is scaled to cover the entire bit-depth of its digital representation then it will be insensitive to multiplication by, and addition of a constant. We can use this information to rewrite (3.11) as a function of a single parameter $\tau$,

$$t_S(x,y) = -\ln\mathcal{F}^{-1}\left(\frac{\mathcal{F}I(x,y)}{1 + ik_x\tau}\right) \tag{3.12}$$

where

$$\tau = \frac{\delta}{\beta|A|^2}\left(\mathrm{Re}[AB^*] - \mathrm{Im}[AB^*]\right), \tag{3.13}$$

$$t_S = 2k\beta t(x,y) - \ln|A|^2 \tag{3.14}$$

and $t_s$ is the scaled projected thickness. The projected thickness retrieved in this manner will not be scaled correctly. If some feature size of the sample is known *a priori* then the greyscale map can be scaled against it for a quantitative measurement. This is a significant limitation for this technique as it requires detailed knowledge about the sample that cannot be extracted from the phase retrieval process as given above. The reference measurement would be unnecessary if the complex refractive index, $R(k_x^0)$ and $R'(k_x^0)$ were known.

The parameter $\tau$ is varied until it is judged that the features in the reconstructed image are easiest to see. Imaging systems with linear transfer functions of spatial frequency give contrast proportional to the first derivative of the phase (Paganin et al., 2004). As $\tau$ increases from zero this 'first derivative' contrast begins to disappear and the optimal visibility is achieved when it has disappeared completely. Increasing $\tau$ further results in streaking artifacts that are characteristic of this method and we shall explain their origin. In moving from the sample to its ABI image the crystal amplifies the spatial frequencies in the $x$-direction and so in the inverse problem these same frequencies are suppressed. The suppression of frequency in the $x$-direction leads to strongly varying contrast in the perpendicular $y$-direction (Paganin et al., 2004).

The 'correct' choice for $\tau$ balances the removal of first derivative contrast with the introduction of streaking artifacts.

The phase retrieval algorithm outlined above was applied to the data in Figure 3.10 and the results are presented in Figure 3.12(c), in the same Figure (a) and (b) are reproductions of the sample cross section and ABI image for convenience. In Figure 3.12(d) the retrieved projected thickness is compared with a reference optical microscopy measurement.

We note that the middle section of the test phantom is clearly visible despite the significant blurring observable at its outer edges. The background shows a linear increase in thickness from right to left which is also present in the ABI image but exaggerated upon reconstruction.

The line profile of the phase retrieval data in Figure 3.12(d) was calculated by taking an average over the vertical direction of the test phantom after the phase retrieval was performed. Importantly, the maximum thickness of this measurement was calibrated against the *a priori* known maximum thickness of the sample. The assumption of some *a priori* information regarding the sample thickness is particularly restrictive and can be removed if the refractive index of the sample and gradient of the rocking curve at the working point are known.

In performing the phase retrieval we made use of two strong assumptions: that

the crystal transfer function varies linearly with spatial frequency and that the working point of the direct beam on the analyser crystal was static throughout the experiment. Despite these approximations we have made a quantitative measurement which compares favourably to the reference measurement. This suggests our approach is quite robust to practical experimental limitations. This is most obvious when we consider that the working point varied considerably during the experiment which could introduce significant artifacts given that our approach is based on a static working point with static gradient associated with that point.

Our approach is particularly suitable for ABI when the working point of the direct beam on the rocking curve is not static. If the thermal stability problem was resolved we could use (3.11) which would remove the requirement for a reference measurement to scale our reconstructed projected thickness.

## 3.5 Summary

Analyser-based phase contrast imaging is a potentially useful tool for medical diagnostic and materials characterisation purposes but is not widely used outside of synchrotron X-ray sources. The ability to perform ABI with conventional sources offers a more cost effective, high volume and quicker turn around than the current method of using synchrotron X-ray sources. We have shown that when used in conjunction with commonly available rotating anode sources it is possible to record ABI phase contrast images and extract quantitative information from them.

We began this chapter with a discussion of the coherence requirements of ABI and it was found that for maximum ABI visibility the beam incident on the analyser crystal should have a divergence smaller than the analyser's Darwin width. To achieve these minimum standards using an X-ray tube it is necessary to monochromate and collimate the beam and we then discussed the feasibility of achieving the minimum coherence standards using common monochromator crystals and the Bartels four-reflection monochromator geometry. It was found that, at the expense of incident flux, it is possible to achieve the necessary beam coherence.

The extreme sensitivity of ABI requires that fluctuations in the ambient temperature during the experiment should be kept to a minimum.

Having shown that it should be possible to measure ABI images using a rotating anode and Bartels monochromator we then presented the results of an experiment where an ABI image of a plastic phantom was recorded and the projected thickness retrieved. The retrieved projected thickness was shown to quantitatively agree with an

independent optical microscopy measurement.

The most significant problem that must be overcome for this method to become a practicable characterisation tool is a reduction in the exposure time. The available flux in the experiment presented in this chapter was reduced by the Bartels monochromator which allowed excellent ABI contrast to be obtained however if one was willing to sacrifice some visibility it should be possible, using the conditions set out earlier, to use a double-crystal monochromator to observe ABI contrast with an increased flux.

The results we have presented demonstrate that it is indeed possible to extract quantitative information from ABI images recorded using an extended incoherent source. Given the potential of ABI to serve as a characterisation tool for light elements we believe that some of the problems we have addressed pave the way to ABI becoming a more mainstream technique with incoherent X-ray sources.

# 4 Quantitative reconstruction of shift-invariant Green's functions

In this chapter we present an entirely new application of phase contrast imaging, to quantitative retrieval of the complex Green's function characterising a shift-invariant linear optical system[1].

We have seen that phase contrast images may be inverted to reconstruct complex wavefields (cf. §1.2) and from them we may infer some properties of the sample from its transmission function. What is less appreciated is that the image output by the phase contrast imaging system contains information about the complex Green's function of the imaging system which created it. If instead of assuming that the imaging system is well characterised and then investigating a sample, we instead assume knowledge of the sample, it is possible, in some circumstances, to recover the Green's function associated with the imaging system.

Other than imaging system Green's functions, we now have a method to reconstruct Green's functions describing a range of different physical situations such as electromagnetism and quantum mechanics. The work in this chapter specifically applies to Green's functions which are linear and shift-invariant and whilst this is restrictive we note that there are a great many systems of practical interest that fall within this category.

In §4.1 we will review the field of Green's function retrieval, that is reconstructing Green's functions from intensity measurements, and formally state the inverse problem that will be solved. Section 4.2 describes how two phase contrast intensity images of a known input may be inverted to recover the complex Green's function of an arbitrary linear, shift-invariant imaging system. We follow this in §4.3 by applying the solution to the famous one-dimensional phase problem in crystallography by recovering the

[1]This chapter is based on the publication *"Unambiguous reconstruction of the complex reflection coefficient of a laterally homogeneous crystal using analyser-based phase contrast imaging"*,Vine, D. J., Paganin, D. M., Pavlov, K. M. and Podorov, S. G., *J. Appl. Cryst.*, **40** 650-657 (Vine et al., 2007b)

complex amplitude reflection coefficient associated with Bragg reflection from a single phase contrast image. Numerical simulations are then presented which demonstrate the validity and viability of the solution. Having shown that the complex Green's function can indeed be retrieved we then show in §4.4 how it may be used to unambiguously infer crystalline structures for which the kinematic scattering approximation is valid.

We close the chapter with some experimental considerations on the applicability of this technique to real data and then follow in Chapter 5 with the implementation of this technique to experimental data we collected at the SPring-8 synchrotron in Hyogo, Japan.

## 4.1 Green's function retrieval

Cowley's classic text on diffraction physics seeks to provide "an appreciation of how ... physical observations using different radiations and different types of sample may be knit together with a common thread of theory" (Cowley, 1995). One such example of a unifying principle is the Green's function method for solving linear differential equations, which forms a cornerstone of many wave-phenomenological analyses.

Indeed, the formal equivalence between the inhomogeneous Helmholtz equation (cf. (2.6)) and the time-independent Schrödinger equation, together with their associated Green's functions, sets up a fruitful parallel between these theories that may be employed in a variety of contexts.

The diverse fields of scientific endeavour that commonly employ Green's function methods are too numerous to list here, given the almost ubiquitous presence of linear differential equations in physics. We will narrow our consideration to the field of coherent optics, which is undergoing a renaissance due to the availability of brighter sources at ever decreasing wavelengths and across a greater range of radiations than ever before. Key examples include the burgeoning field of atom lasers (Kasevich, 2002), together with recent developments in coherent X-ray science (Chapman et al., 2006; Gahl et al., 2008) promised by free electron laser facilities being built around the world (Patel, 2002).

The Green's function is used in coherent optics in modelling the forward problem of wavefield scattering, and in solution of the associated inverse problem of wavefield reconstruction from a series of one or more measurements of the scattered intensity. The inverse problem is particularly important in coherent optics because of the ubiquity of the phase retrieval problem—the inability to directly measure the phase of a

wavefield at short wavelengths.

In all of these techniques one presupposes knowledge of the Green's function for the system in question and in many cases, such as the Helmholtz/Schrödinger propagator for free space propagation of a photon or massive particle, the solution is well known. For systems in which the propagator is unknown, or for which one would like to verify an assumed form of the complex propagator, there is no general technique for measuring the said propagators. This neatly defines the research question posed in this chapter: How does one measure the complex Green's function of an optical system?

For fields other than optics the idea of Green's function retrieval has been applied using elastodynamic waves to investigate the Green's function of the earth itself (Campillo and Paul, 2003; van Tiggelen, 2003; Wapenaar, 2004; Wapenaar et al., 2006). However, seismic waves do not oscillate near optical frequencies and thus do not have the phase problem making this a simpler problem to investigate.

To place the question in more formal terms consider the classic time-independent Green's function description of wavefield evolution (Jackson, 1998),

$$\Psi(\mathbf{r}) = \int G(\mathbf{r}, \mathbf{r}')\psi(\mathbf{r}')d\mathbf{r}', \tag{4.1}$$

where $\Psi$, $\psi$ describe coherent complex scalar wavefields and $\mathbf{r}$ is the usual three-dimensional position vector. The problem is to solve (4.1) for G given knowledge of $|\Psi|$ and $\psi$; in general this is a highly non-linear inverse problem.

The problem can be linearised without compromising the generality of G by choosing $\psi$ to have the property that $\psi(\mathbf{r}) \propto 1 + \Delta\psi(\mathbf{r})$ where $|\Delta\psi| \ll 1$ - the 'weak object' approximation (WOA) (Cowley, 1995) of §2.3.1. Using this condition it is possible to solve (4.1) for G in a manner which is non-iterative, unambiguous and useful for a wide class of complex Green's functions.

Evidently this method of reconstructing the Green's function is applicable to systems in which an object that obeys the WOA ascribed to $\psi$ can be readily fabricated. This is an important practical consideration that is dependent on the type of radiation used and we will defer the question to §4.2. Before proceeding we will illustrate the essence of our idea by way of a simple example. We will takes as our archetypal system the diffraction of X-rays from an analyser crystal to determine the amplitude reflection coefficient (ARC) (cf. §2.5.4). We have chosen to exemplify our technique on a system involving X-rays and Bragg reflection from a crystal however it is worth noting that it could be replaced by any radiation/ optical system satisfying (4.1). With reference to Figure 4.1(a) consider an idealised standard XRD scenario in which a plane wave A is

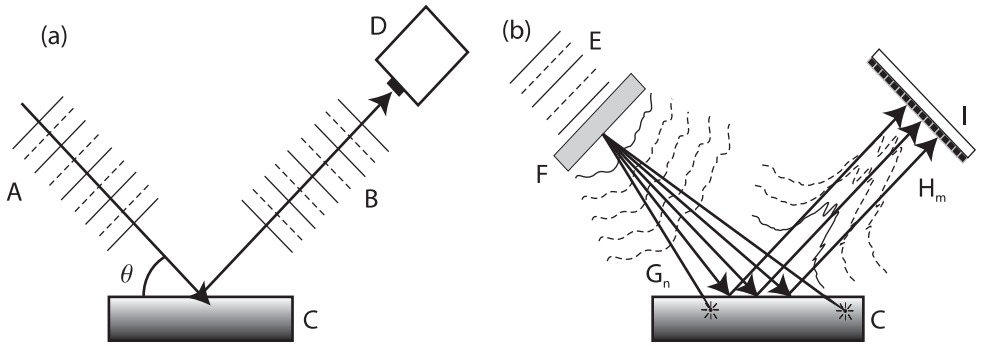


Figure 4.1: **Overview of Green's function retrieval.** (a) In an idealised X-ray diffraction experiment a plane wave is diffracted from a crystal and is incident on a point-like detector. The crystal reflectivity as a function of angle is built up by serially scanning the crystal through θ. (b) Our method illuminates the crystal with a known coherent superposition of plane waves. After diffraction from the crystal an area detector records an interference pattern, effectively interrogating many angles θ in parallel.

incident at an angle θ upon the surface of a crystal C. The intensity of the reflected plane wave B is then registered using a detector D, which need not be position sensitive. The phase of the reflected plane wave is lost and one performs a series of measurements of angles θ so as to build up a rocking curve of the crystal reflection. Compare this with the 'parallelised' scenario in Figure 4.1(b), where an incident plane wave E passes through a known weak object F, to yield a known coherent superposition of plane waves $G_n$ for $n = 1, 2$ *etc.* This coherent superposition of plane waves is then reflected from the surface of the same crystal C, the reflected waves $H_m$ (for $m = 1, 2$ *etc.*) then mutually interfering to form a two dimensional analyser-based phase contrast image at the detector I. The phase contrast image evidently contains information regarding both the phase and amplitude of the complex ARC of the crystal since (i) the mutual interference of the reflected plane waves governs both of these quantities, and (ii) a continuum of angles θ is contained within the field at the exit surface of F. The solution we have developed shows how one may solve the inverse problem of determining the complex ARC of the crystal, given a known weak object F, together with the phase contrast image of this object registered by the detector.

In the following section we will present the detailed solution to the problem of reconstructing the complex Green's function from a phase contrast image of a known weak object.

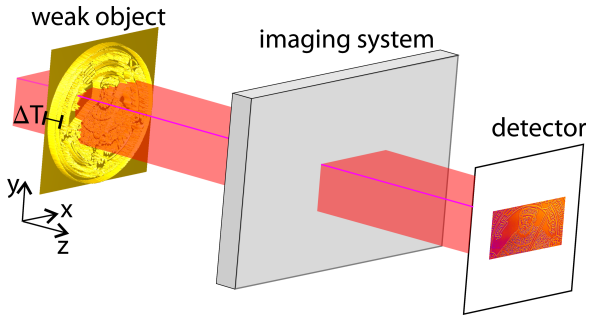


Figure 4.2: **Reconstructing a generic complex Green's function.** Planar, monochromatic X-rays illuminate a known weak object and are then incident on a generic imaging system. The field exits the imaging system and is detected on a two-dimensional position sensitive detector.

## 4.2 Quantitative Green's function retrieval from phase contrast X-ray images

We begin the solution of the inverse problem of Green's function retrieval with a statement of the associated forward problem, namely the recording of a phase contrast image of weak object.

Consider the experimental arrangement of Figure 4.2 where a two-dimensional planar, monochromatic hard X-ray bean is incident on a weak object, with known projected thickness, before interacting with the generic imaging system (e.g. diffraction through free space, reflection from an analyser crystal). The wavefield is then incident on a position sensitive detector which records the field intensity.

Since we will use the transfer-function formalism to describe the problem we are limited to Green's functions which are shift-invariant (Goodman, 2004) (cf. §2.6). Important examples of such systems include the Helmholtz and Schrödinger propagators and laterally homogeneous crystalline structures.

The *a priori* knowledge of the weak object projected thickness and chemical composition allows the complex transmission function, $f$, to be calculated (cf. (2.23)). We assume that a z-directed plane wave, $\exp(ikz)$, is incident on the weak object so that the transmitted wavefield is given by,

$$\psi(\boldsymbol{\rho}, z) = f(\boldsymbol{\rho}) \exp(ik_z z). \tag{4.2}$$

The transverse spatial frequency spectrum of $\psi$ represents exactly those frequencies which will probe $G$ and from which information about $G$ can be recovered. Since $G$ is a complex function we will in general require two independent measurements for its reconstruction however there are cases of practical interest where the Green's function can be recovered from a single measurement provided it can be reduced

to a one-dimensional function. In such a case the two dimensional measurement represents a set of one dimensional measurements that can be used for averaging against noise.

Assuming the propagation distances between sample, imaging system and detector to be negligible, the wavefield incident on the detector, $\Psi$, is given by,

$$\Psi(\boldsymbol{\rho},\tau) = \iint_{-\infty}^{\infty} G(\boldsymbol{\rho}-\boldsymbol{\rho}',\tau)\psi(\boldsymbol{\rho}')\,d\boldsymbol{\rho}' \tag{4.3}$$

where $\tau$ is a parameter describing the state of the imaging system. Typically, $\tau$ will consist of a set of real numbers. For example, the $\tau$ could describe the level of defocus or spherical aberration.

Using the projection approximation (cf. §2.3.1), the complex amplitude $\psi$ is linearly related to the projected phase $\varphi$ and attenuation $\mu$ by (Nesterets et al., 2004),

$$\begin{aligned}
\psi(\boldsymbol{\rho}) &\equiv \exp[i\varphi(\boldsymbol{\rho}) - \mu(\boldsymbol{\rho})], && (4.4)\\
&= \exp(i\overline{\varphi} - \overline{\mu})\exp[i\Delta\varphi(\boldsymbol{\rho}) - \Delta\mu(\boldsymbol{\rho})], && (4.5)\\
&\approx \overline{\psi}[1 + \Delta\psi(\boldsymbol{\rho})]. && (4.6)
\end{aligned}$$

The overline indicates an average value (cf. 2.3.1),

$$\begin{aligned}
\overline{\psi} &= \exp(i\overline{\varphi} - \overline{\mu}), && (4.7)\\
\Delta\psi(\boldsymbol{\rho}) &= i\Delta\varphi(\boldsymbol{\rho}) - \Delta\mu(\boldsymbol{\rho}), && (4.8)\\
\overline{\Delta\varphi} &= 0, && (4.9)\\
\overline{\Delta\mu} &= 0, && (4.10)\\
|\Delta\varphi| &\ll 1, && (4.11)\\
|\Delta\mu| &\ll 1. && (4.12)
\end{aligned}$$

The utility of our method depends critically on whether an object that satisfies the above mentioned criteria can be fabricated and to that end we now state explicitly the physical parameters demanded of such an object. The weak object described here is with reference to the objects shown in Figure 4.3 that are used in the numerical simulations. Two remarks about the weak object (i) the greyscale level is proportional to the projected thickness and (ii) the weak phase and weak attenuation objects are physically distinct. We have chosen to use greyscale photographs for our weak object projected thicknesses because the spatial frequency spectrum is non-negligible up to the Nyquist frequency. Our algorithm will reconstruct over the band of spatial frequencies introduced by the weak object and so it is preferable to simulate as wide a range of frequencies as possible, which we achieved using the greyscale photographs.

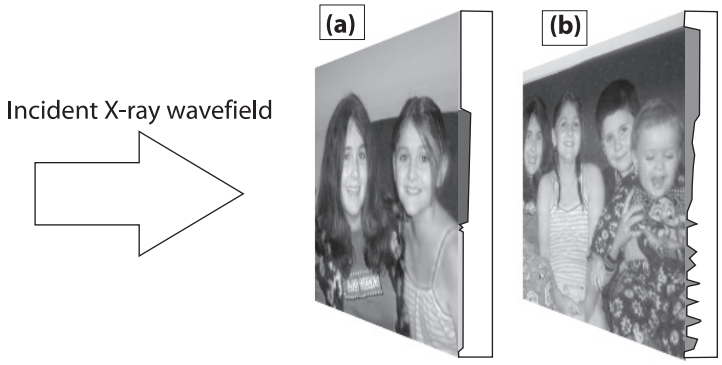


Figure 4.3: **Simulated weak object.** The weak phase (a) and amplitude (b) objects used in the numerical simulations. The greyscale level corresponds to the etching depth in the physical realisation of the object. The object is 0.5mm×0.5mm (256×256 pixels).

Specifically the object we now describe has the following four properties: (i) it is well characterised, (ii) weakly phase shifting ($\Delta\varphi \approx 0.1$) with a depth profile as in Figure 4.3(a), (iii) weakly attenuating ($\Delta\mu \approx 0.1$) with a depth profile as is given in Figure 4.3(b) and (iv) the weak phase variations and weak attenuation are linearly independent. The first requirement of being well characterised can be addressed using advanced lithography techniques where a critical dimension tolerance of tens of nanometres is standard (Anderson, 2006) and continuous depth profiling (or greyscaling) such as is shown in Figure 4.3 is possible (Kley, 1997; Daschner et al., 1997; Geissler, 2004). We also note that the more common binary lithography object can be used for this application.

The surface topography can be precisely measured using X-ray diffraction (Paganin et al., 2002; Pavlov et al., 2004) or atomic force microscopy (Foster and Hofer, 2006) given that the object is homogeneous and we need only know the surface profile.

Linear independence of $\Delta\varphi$ and $\Delta\mu$ is assured through the use of separate objects to provide the weak phase shift (the weak phase object) and weak attenuation (weak amplitude object). The weak phase object introduces a maximum 0.1 radian phase shift and no absorption. The weak amplitude object has a maximum ten percent attenuation and a $2\pi$ phase shift. The requirement that the weakly attenuating object introduce an exact $2\pi$ phase shift may seem difficult to realise but the use of refraction matching techniques makes it quite rudimentary (Hasnah et al., 2005) using the following methodology. The object etching pattern must be binary so that the thickness variation corresponds to a 0 or $2\pi$ phase shift for a particular refractive index and wavelength. Any measurable deviation from this phase shift is compensated for by immersing the object in a refractive index matching fluid whose composition is

varied[2] until the position sensitive detector, which captures an X-ray contrast image of the index-matched sample, records no phase contrast due to that object. Whilst a continuously etched depth profile has been used for the weak amplitude object in the numerical simulations, a binary level object will not degrade the quality of the reconstructions.

Finally, an example weak phase object whose physical realisation corresponds to the inset photograph of Figure 4.3(a) is an amorphous Silicon Oxide (a-SiO2) substrate continuously etched so that the maximum thickness variation is 0.4μm and the lateral pixel size is 20nm for a 20:1 aspect ratio. For 10keV X-rays this corresponds to a phase shift of 0.1 and maximum $|\Delta\mu| \approx 0.001$. The weak amplitude object may be realised, for example, using an amorphous Silicon (a-Si) substrate with a binary pattern similar to Figure 4.3(b) etched into it with a thickness variation of 25.4μm and a pixel size of 0.8μm. At 10keV this corresponds to $\approx 2\pi$ phase shift and $\Delta\mu \approx 0.1$ which clearly satisfies the weak object criteria.

Upon substitution of (4.6) into (4.1) we have the following relationship (Nesterets et al., 2004),

$$\Psi(\boldsymbol{\rho},\tau) \approx \overline{\psi}\tilde{G}_\tau + \overline{\psi}\iint_{-\infty}^{\infty} G(\boldsymbol{\rho}-\boldsymbol{\rho}',\tau)\Delta\psi(\boldsymbol{\rho}')\mathrm{d}\boldsymbol{\rho}', \tag{4.13}$$

$$I_\Psi(\boldsymbol{\rho},\tau) = I_{\overline{\psi}}\left\{|\tilde{G}_\tau|^2 + 2\mathrm{Re}\left[\tilde{G}_\tau^*\iint_{-\infty}^{\infty} G(\boldsymbol{\rho}-\boldsymbol{\rho}',\tau)\Delta\psi(\boldsymbol{\rho}')\mathrm{d}\boldsymbol{\rho}'\right]\right\}, \tag{4.14}$$

where the superscript $*$ denotes complex conjugation, $I_\Psi = |\Psi|^2$ and $I_{\overline{\psi}} = |\overline{\psi}|^2$, $\tilde{G}_\tau = \iint_{-\infty}^{\infty} G(\boldsymbol{\rho},\tau)\mathrm{d}\boldsymbol{\rho}$ is a known complex number and terms quadratic in $\Delta\psi$ are assumed to be negligible. The magnitude of $\tilde{G}_\tau$ is known since it represents the ratio of the zeroth spatial frequencies of $|\Psi|$ and $|\psi|$, a directly measurable quantity. The phase of $\tilde{G}_\tau$ adds an arbitrary, constant phase shift to the recovered Green's function and can be neglected.

We now show how the expression in (4.14) may be inverted to obtain a closed-form expression for the complex Green's function, using two phase contrast images. We begin by introducing the (known) contrast transfer function,

$$C(\boldsymbol{\rho},\tau) = \frac{I_\Psi(\boldsymbol{\rho},\tau)}{I_{\overline{\psi}}} - |\tilde{G}_\tau|^2, \tag{4.15}$$

together with the unknown function,

$$h(\boldsymbol{\rho},\tau) = \tilde{G}_\tau^* G(\boldsymbol{\rho},\tau). \tag{4.16}$$

[2]Typically the refractive index of the fluid is varied by adding drops of a concentrated solution then recording an image and repeating the process until the desired lack of contrast is achieved.

This last expression is the unknown function G scaled by a known complex number. Combining (4.15) and (4.16) into (4.14) yields,

$$\begin{aligned} C(\boldsymbol{\rho},\tau) &= -2\left[\iint_{-\infty}^{\infty} h_I(\boldsymbol{\rho}-\boldsymbol{\rho}',\tau)\Delta\varphi(\boldsymbol{\rho}')d\boldsymbol{\rho}'\right. \\ &+ \left.\iint_{-\infty}^{\infty} h_R(\boldsymbol{\rho}-\boldsymbol{\rho}',\tau)\Delta\mu(\boldsymbol{\rho}')d\boldsymbol{\rho}'\right]. \end{aligned} \tag{4.17}$$

The subscripts R and I refer to the real and imaginary parts of $h(\boldsymbol{\rho})$ respectively, so that

$$h_R(\boldsymbol{\rho},\tau) = \frac{1}{2}\left[\tilde{G}_\tau^* G(\boldsymbol{\rho},\tau) + \tilde{G}_\tau G^*(\boldsymbol{\rho},\tau)\right], \tag{4.18}$$

$$h_I(\boldsymbol{\rho},\tau) = \frac{i}{2}\left[\tilde{G}_\tau G^*(\boldsymbol{\rho},\tau) - \tilde{G}_\tau^* G(\boldsymbol{\rho},\tau)\right]. \tag{4.19}$$

Taking the Fourier transform of (4.17) gives

$$-\tilde{C}(\boldsymbol{\kappa},\tau) = [\tilde{\Delta\mu}(\boldsymbol{\kappa}) - i\tilde{\Delta\varphi}(\boldsymbol{\kappa})]\tilde{h}(\boldsymbol{\kappa},\tau) + [\tilde{\Delta\mu}(\boldsymbol{\kappa}) + i\tilde{\Delta\varphi}(\boldsymbol{\kappa})]\tilde{h}^*(-\boldsymbol{\kappa},\tau), \tag{4.20}$$

where the tilde indicates a reciprocal space quantity. Eq. (4.20) may be solved using two linearly independent phase contrast images (for example, images of different objects). In general this requires that there are two sets of weak objects, $\Delta\mu_1$, $\Delta\varphi_1$ and $\Delta\mu_2$, $\Delta\varphi_2$ resulting in two intensity measurements $I_{\Psi,1}$ and $I_{\Psi,2}$. The solution of (4.20), with functional dependence on $\boldsymbol{\kappa}$ suppressed for clarity, is given by

$$\begin{pmatrix} \tilde{h}_R^e \\ \tilde{h}_R^o \\ \tilde{h}_I^e \\ \tilde{h}_I^o \end{pmatrix} = -\frac{1}{2}\begin{pmatrix} \tilde{\Delta\mu}_{R,1} & \tilde{\Delta\varphi}_{I,1} & \tilde{\Delta\varphi}_{R,1} & -\tilde{\Delta\mu}_{I,1} \\ \tilde{\Delta\mu}_{I,1} & -\tilde{\Delta\varphi}_{R,1} & \tilde{\Delta\varphi}_{I,1} & \tilde{\Delta\mu}_{R,1} \\ \tilde{\Delta\mu}_{R,2} & \tilde{\Delta\varphi}_{I,2} & \tilde{\Delta\varphi}_{R,2} & -\tilde{\Delta\mu}_{I,2} \\ \tilde{\Delta\mu}_{I,2} & -\tilde{\Delta\varphi}_{R,2} & \tilde{\Delta\varphi}_{I,2} & \tilde{\Delta\mu}_{R,2} \end{pmatrix}^{-1} \begin{pmatrix} \tilde{C}_{R,1} \\ \tilde{C}_{I,1} \\ \tilde{C}_{R,2} \\ \tilde{C}_{I,2} \end{pmatrix}. \tag{4.21}$$

The subscripts R, I refer to the real and imaginary part of the function, superscripts $e$ and $o$ refer to the even and odd part of the function and subscripts 1, 2 refer to the first and second set of weak objects and the corresponding phase contrast image respectively.

Given that $h$ is directly proportional to the desired function G (cf. (4.16)) then (4.21) is the solution we require. We have simply to solve (4.21) for each pixel and we obtain for G

$$G(\boldsymbol{\rho},\tau) = \mathcal{F}^{-1}\left[\frac{\tilde{h}(\boldsymbol{\kappa},\tau)}{\tilde{G}_\tau}\right]. \tag{4.22}$$

Eq. 4.22 leaves the possibility of a division by zero problem if $|\tilde{G}_\tau| = 0$ however this quantity represents the ratio of the average detected to incident intensity (cf. (4.14))

and as such as this quantity tends toward zero so does the contrast function C—in essence there is no detected intensity image.

The determinant of (4.21) will be non-zero if $\Delta\varphi_1$, $\Delta\varphi_2$, $\Delta\mu_1$ and $\Delta\mu_2$ are linearly independent.

Having shown the possibility of reconstructing the complex Green's function of an arbitrary linear, shift-invariant Green's function we now turn to a practical example: Reconstructing the ARC of a laterally homogeneous crystal.

## 4.3 Reconstruction of complex amplitude reflection coefficients

The problem of unambiguously determining the deformation field and chemical composition of layered crystals and thin films from diffraction data is of significant practical importance (Pietsch et al., 2004; Fewster, 2003; Birkholz et al., 2006). X-ray diffraction (XRD) is a standard tool for investigating crystals to determine these properties but in general both the intensity and phase variations imparted by the crystal on the diffracted X-ray wavefield must be known to arrive at an unambiguous solution.

In §4.2 we proposed an analytical solution to the problem of recovering an arbitrary linear, shift invariant Green's function. We will now show how that formalism may be adapted to recover the complex amplitude reflection coefficient (ARC) using a single analyser-based X-ray phase contrast image (Förster et al., 1980; Somenkov et al., 1991; Ingal and Beliaevskaya, 1995; Davis et al., 1995a,b; Paganin, 2006) (cf. §1.1.6). The recovery from a single image is possible because the ARC is a one dimensional function and so a two-dimensional $N \times N$ image contains $N/2$ independent ARC measurements. We follow this in §4.4 by demonstrating (within the kinematic scattering approximation) an unambiguous, analytic solution to the problem of determining the interplanar spacing of a layered crystal from a single two dimensional intensity measurement using the recovered complex ARC.

We now give a brief overview of what has been achieved to solve the problem of determining the interplanar spacing of layered crystals from X-ray diffraction measurements (Goncharskii et al., 1992). The deformation profile of such crystals can be obtained directly from the rocking curve using fitting procedures (Speriosu et al., 1979; Petrashen', 1975; Kyutt et al., 1980). This method cannot guarantee a unique solution due to the existence of so-called 'crystal analogues', namely crystals of differing structure that have the same reflectivity (Afanas'ev and Fanchenko, 1986, 1988;

Afanas'ev et al., 1990). The method of integral characteristics gives the average strain for thin layers (Afanas'ev et al., 1977; Kohn et al., 1981; Afanas'ev et al., 1990). The strain profile may be obtained directly from the rocking curve using a discrete form of the kinematic ARC (Stepanov, 1994). Iterative schemes using Fourier analysis of the rocking curve have been proposed for the kinematic (Podorov et al., 1994, 1999), semi-dynamical (Podorov et al., 1998) and dynamical diffraction regimes (Podorov and Punegov, 1999). These schemes are often computationally intensive, slow and prone to stagnation without necessarily achieving the correct solution. Phase retrieval can be implemented using the Hilbert transform (Petrashen' and Chukhovskii, 1989) but the solution is ambiguous and an appropriate algorithm is required to choose the unique solution (Nikulin, 1998; Dilanian et al., 2006). Measuring the distribution of photoemission electrons due to X-ray standing waves in dynamical diffraction may be used to infer the phase (Afanas'ev and Kon, 1978; Koval'chuk and Kohn, 1986; Koval'chuk et al., 1986). The reliance of standing wave methods on the detection of photoelectrons means they are limited to investigating near-surface layers where there is an appreciable probability of an electron escaping the crystal. A variant of the standing wave approach measures both the distribution of secondary photoelectrons and the scattered X-rays to find the deformation field in surface layers much smaller than the extinction length (Vartanyants et al., 1989). Alternatively, the phase can be retrieved in multiple-beam diffraction by considering the interference of the diffracted waves in a crystal (Hart and Lang, 1961; Authier, 2005). Neutron reflectometry can recover phase information if the sample is mounted on a known reference layer (Majkrzak and Berk, 1995; Majkrzak et al., 2000).

In contrast to the limitations of the techniques just outlined the method we propose gives a single-shot, non-iterative, analytic solution for the ARC that requires no special sample preparation, is valid for both kinematic and dynamical diffraction regimes, works with any reflection, symmetric and asymmetric, Bragg and Laue diffraction geometries. Our method also determines the ARC over a wide range of angular space simultaneously, is not susceptible to the problem of crystal analogues and the inversion algorithm is fast and robust in the presence of realistic levels of experimental noise.

We require only that: (i) the sample crystal be locally laterally homogeneous over the area of X-ray illumination, and (ii) the action of the crystal on the incident X-rays may be modelled using the transfer-function formalism (Goodman, 2004). Notwithstanding the X-ray illumination coherence requirements our experimental setup is very similar to standard XRD, the only differences are the use of an area detector and the addition of the weak object between monochromator and analyser

crystal.

We would like to emphasize the importance of being able to reconstruct the ARC from a single image. Standard XRD works by probing each reciprocal space point in a serial manner and the resolution is set by the precision of the goniometer stepper motors. Compare this to the method we propose which uses a single two-dimensional measurement that is capable of a massively parallelised measurement of a range of rocking angles simultaneously. If this were the only advantage of our method it is already more efficient than XRD however our method also reconstructs the phase of the rocking curve. The phase of the X-ray rocking curve is not easily measured and the techniques that attempt to address this problem do not all have the advantages of: parallelised measurement, no special sample preparation, non-iterative and an angular resolution comparable to high resolution X-ray diffraction techniques.

Using this method one can verify the phase predicted by the dynamical theory of X-ray diffraction. Whilst the magnitude of the ARC, a directly measurable quantity, has been verified innumerable times, experiments which investigate the phase of the ARC are less frequently addressed. An efficient method for accessing this fundamental quantity is an important and useful goal.

The range and resolution of reciprocal space that can be examined with this technique is Nyquist limited by the detector characteristics and is comparable to high resolution XRD. The serial nature of the data acquisition at all reciprocal space points simultaneously makes the technique suitable for high-speed measurements. Methods for single-exposure measurement of an entire rocking curve exist (Fewster, 2005) however our method is capable of measuring the ARC modulus and phase at a spatial resolution that is at least equal to those methods.

### 4.3.1 Inverse problem of reconstructing the complex ARC. I. The weak-object approximation

We now present an adaptation of the formalism of §4.2 to the problem ARC retrieval. A planar, monochromatic hard X-ray beam of unit intensity is transmitted through the known weak object before being Bragg diffracted and detected as in Figure 4.4. In the following we consider the case of symmetrical Bragg reflection, although we note the theory is applicable to asymmetric reflection and Laue diffraction geometry. Asymmetric reflections can be used to magnify the image but this idea has limited applicability in Green's function reconstruction because the reconstruction algorithm requires the division of two images and the images must be the same size so a magnified image must be rescaled in the post-measurement processing. The most efficient

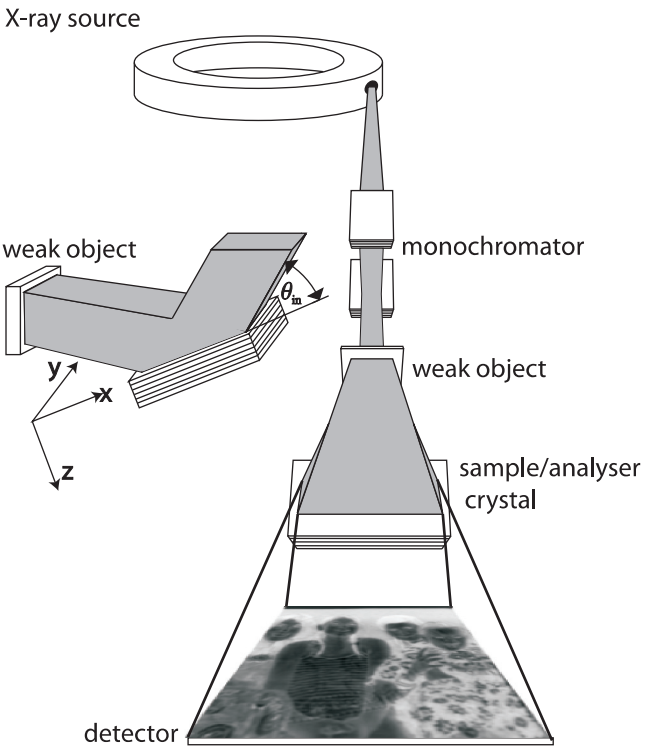


Figure 4.4: **Reconstructing the complex ARC.** X-rays are produced at source and monochromated/collimated before illuminating an *a priori* characterised weak object. The wavefield diffracted from the weak object is Bragg reflected from the sample/analyser crystal before being registered using a two-dimensional position-sensitive detector.

situation occurs when the measured ABI phase contrast image has the same spatial resolution as the *a priori* characterised weak object and this may be achieved with either an appropriate detector or magnification by asymmetric reflection.

Let the xy plane be coincident with the planar crystal surface and the positive z-axis be directed normally into the crystal. The wavefields incident, $\psi(x, y)$, and diffracted, $\Psi(x, y, \omega_C)$ from the crystal surface are given by

$$\Psi(-x, y; \omega_C) = \int_{-\infty}^{\infty} G[x - x'; \omega_C]\psi(x', y)dx' \tag{4.23}$$

where $G(x; \omega)$ is the crystal point spread function (the ARC's real space dual) and $\omega_C$ is the deviation from $\theta_B$. The point spread function is related to the ARC by

$$r(\theta_B + \omega_C - k_x/k) = \mathcal{F}[G(x; \omega_C)] \tag{4.24}$$

and $\omega_C$ stays constant throughout the experiment.

The analysis proceeds along the same lines as §4.2 beginning with

$$\begin{aligned} I_\psi(-x,y;\omega_C) &= \bar{I}_{\overline{\psi}}(R_\omega \\ &+ 2\mathrm{Re}\left\{ r^*_\omega \int_{-\infty}^{+\infty} G[x-x';\omega_C]\Delta\psi(x',y)dx' \right\}\Big) \end{aligned} \tag{4.25}$$

where $r_\omega = \int_{-\infty}^{\infty} G(x;\omega_C)dx$ and $R_\omega = |r_\omega|^2$. The contrast function, (4.15) should be transformed according to $x \to -x$ to account for the image inversion and finally we have the comparable solution adapted to ARC reconstruction (cf. (4.21)),

$$\begin{pmatrix} \tilde{h}^e_R \\ \tilde{h}^o_R \\ \tilde{h}^e_I \\ \tilde{h}^o_I \end{pmatrix} = -\frac{1}{2} \begin{pmatrix} \tilde{\Delta\mu}^i_R & \tilde{\Delta\varphi}^i_I & \tilde{\Delta\varphi}^i_R & -\tilde{\Delta\mu}^i_I \\ \tilde{\Delta\mu}^i_I & -\tilde{\Delta\varphi}^i_R & \tilde{\Delta\varphi}^i_I & \tilde{\Delta\mu}^i_R \\ \tilde{\Delta\mu}^j_R & \tilde{\Delta\varphi}^j_I & \tilde{\Delta\varphi}^j_R & -\tilde{\Delta\mu}^j_I \\ \tilde{\Delta\mu}^j_I & -\tilde{\Delta\varphi}^j_R & \tilde{\Delta\varphi}^j_I & \tilde{\Delta\mu}^j_R \end{pmatrix}^{-1} \begin{pmatrix} \tilde{C}^i_R \\ \tilde{C}^i_I \\ \tilde{C}^j_R \\ \tilde{C}^j_I \end{pmatrix} \tag{4.26}$$

where $i, j$ now refer to individual rows in the same image, the functional dependence on $k_x$ has been suppressed for clarity and $h(x;\omega_C) = r^*_\omega G(x;\omega_C)$, $\tilde{h} = \mathcal{F}_1[h]$ and $\mathcal{F}_1$ is a one-dimensional Fourier transform.

The ARC we seek to reconstruct is a one-dimensional function and we require two independent one-dimensional measurements to reconstruct both its real and imaginary parts. The ABI image we have recorded however contains many more independent measurements than the two that are required and so by a suitable averaging process we can use the redundant data in the overdetermined solution to galvanise our reconstruction against experimental noise. We propose to do this in the following manner.

Let our functions $C$, $\Delta\mu$ and $\Delta\varphi$ be square arrays of side length $N$, then according to our reconstruction algorithm it contains $N/2$ sets of independent measurements. The matrix inversion in (4.26) will amplify noise when the magnitude of the denominator becomes small. To ameliorate this effect as much as possible we averaged our results prior to the matrix division, which can be understood with reference to the following example.

Consider the matrix equation $\mathbf{A}(k_x)\mathbf{x}(k_x) = \mathbf{B}(k_x)$ then the averaging was performed in the following way,

$$\mathbf{x}(k_x) = \frac{1}{N}\sum_{i=1}^{N} \mathbf{A}_i^{-1}(k_x)\mathbf{B}_i(k_x), \tag{4.27}$$

$$= \frac{1}{\sum_{i=1}^{N} |\mathbf{A}_i(k_x)|^2} \sum_{i=1}^{N} \mathbf{B}_i(k_x)\mathbf{A}_i^*(k_x). \tag{4.28}$$

Summing over the independent measurements before the division increases the signal to noise and reduces exposure to amplification of noise caused by division by small numbers.

The weak-object approximation allowed us to derive a closed-form expression for the complex ARC in terms of the detected intensity and known weak object. Under the weak-object approximation all non-linear terms, which would otherwise be present in (4.25), can be legitimately neglected. In practice this approximation has two consequences that it is desirable to overcome. Firstly, the ability to compensate for larger phase shifts and attenuations provides some practical leeway to use weak objects with larger thickness variations than would otherwise be acceptable. Secondly, there is an optimisation problem between satisfying the weak-object criteria and the signal-to-noise in an image. A larger phase shift will result in greater contrast at the cost of invalidating the weak-object criteria. Ideally we would like to use a more strongly scattering object and to that end we present a modification of the formalism above to allow for an order of magnitude increase in the object's scattering strength ($|\Delta\varphi|, |\Delta\mu| < 1$, rather than $|\Delta\varphi|, |\Delta\mu| \ll 1$). We refer to this as the 'relaxed weak-object approximation'.

### 4.3.2 Inverse problem of reconstructing the complex ARC. II. The relaxed weak-object approximation

To incorporate a relaxed weak-object approximation we must include the nonlinear terms previously neglected from (4.25). This can be done using an iterative procedure analogous to the Born series (Merzbacher, 1970; Born and Wolf, 1999). To this end, rewrite (4.26) schematically as

$$\tilde{\mathbf{h}}_1 = -\frac{1}{2}\tilde{\mathbf{\Delta}}^{-1}\tilde{\mathbf{C}}_0. \tag{4.29}$$

Here, boldface letters denote matrices, obtained from(4.26) as follows: $\tilde{\mathbf{h}}$ corresponds the column matrix on the left side, $\tilde{\mathbf{\Delta}}$ is the square matrix on the right side, and $\tilde{\mathbf{C}}$ is the column vector on the right side. Subscripts 0, 1 indicate the iteration order. As suggested by this notation, we will use (4.26) as the first order step in an iterative procedure.

Up to second order in the known function $\Delta\psi(\boldsymbol{\rho})$ the squared modulus of (4.23)

becomes:

$$\begin{aligned} I_\psi(-x,y;\omega_C)/I_{\overline{\psi}} &= R_\omega \\ &+ 2\mathrm{Re}\left\{ r_\omega^* \int_{-\infty}^{+\infty} G(x-x';\omega_C)\Delta\psi(x',y)dx' \right\} \\ &+ \mathrm{Re}\left\{ r_\omega^* \int_{-\infty}^{+\infty} G(x-x';\omega_C)\Delta\psi^2(x',y)dx' \right\} \\ &+ \left| \int_{-\infty}^{+\infty} G(x-x';\omega_C)\Delta\psi(x',y)dx' \right|^2 \\ &+ \frac{1}{4}\left| \int_{-\infty}^{+\infty} G(x-x';\omega_C)\Delta\psi^2(x',y)dx' \right| \\ &+ \mathrm{Re}\left\{ \left[ \int_{-\infty}^{+\infty} G(x-x';\omega_C)\Delta\psi(x',y)dx' \right]^* \right. \\ &\times \left. \int_{-\infty}^{+\infty} G(x-x';\omega_C)\Delta\psi^2(x',y)dx' \right\}. \end{aligned} \tag{4.30}$$

All quantities are as previously defined. We define a functional $I_n(x,y,G_n(x;\omega_C))$ containing all nonlinear terms in the right-hand side of (4.30) (i.e. it contains all the terms that were previously neglected in (4.25). The explicit dependence in I on the unknown function $G_n(x;\omega_C)$ is used to clarify the iterative scheme.

Successive iterations now include the nonlinear terms, $I_n(x,y,G_n(x;\omega_C))$, using the recursive formula:

$$\tilde{\mathbf{h}}_{n+1} = -\frac{1}{2}\tilde{\mathbf{\Delta}}^{-1}(\tilde{\mathbf{C}}_n). \tag{4.31}$$

Here $\tilde{\mathbf{h}}_{n+1}$ is the $n+1^{\text{th}}$ iterative solution for the complex ARC, $\tilde{\mathbf{\Delta}}$ is as previously defined and, to define $\tilde{\mathbf{C}}_n$, we redefine (4.15) as follows,

$$\tilde{C}_n(k_x,\omega_C;y) = \mathcal{F}\left\{ \left( \frac{I_\psi(x,y)}{I_{\overline{\psi}}} - R_\omega - I_n(x,y,G_n(x;\omega_C)) \right) \right\} \tag{4.32}$$

and

$$\mathbf{C_n} = \begin{pmatrix} \mathrm{Re}\{\tilde{C}_n(k_x,\omega;y_i)\} \\ \mathrm{Im}\{\tilde{C}_n(k_x,\omega;y_i)\} \\ \mathrm{Re}\{\tilde{C}_n(k_x,\omega;y_j)\} \\ \mathrm{Im}\{\tilde{C}_n(k_x,\omega;y_j)\} \end{pmatrix}. \tag{4.33}$$

Note the dependence of $I_n(x,y,G_n(x;\omega_C))$ on $G_n$, the current iteration of $G(x;\omega_C)$. Eq. 4.31 together with (4.33) defines the iterative scheme which allows the relaxed weak-object approximation $|\Delta\varphi|, |\Delta\mu| < 1$.

We now present a numerical simulation which demonstrates the validity of the reconstruction algorithms defined thus far for the complex ARC. We have chosen to reconstruct the well known ARC of the semi-infinite perfect crystal.

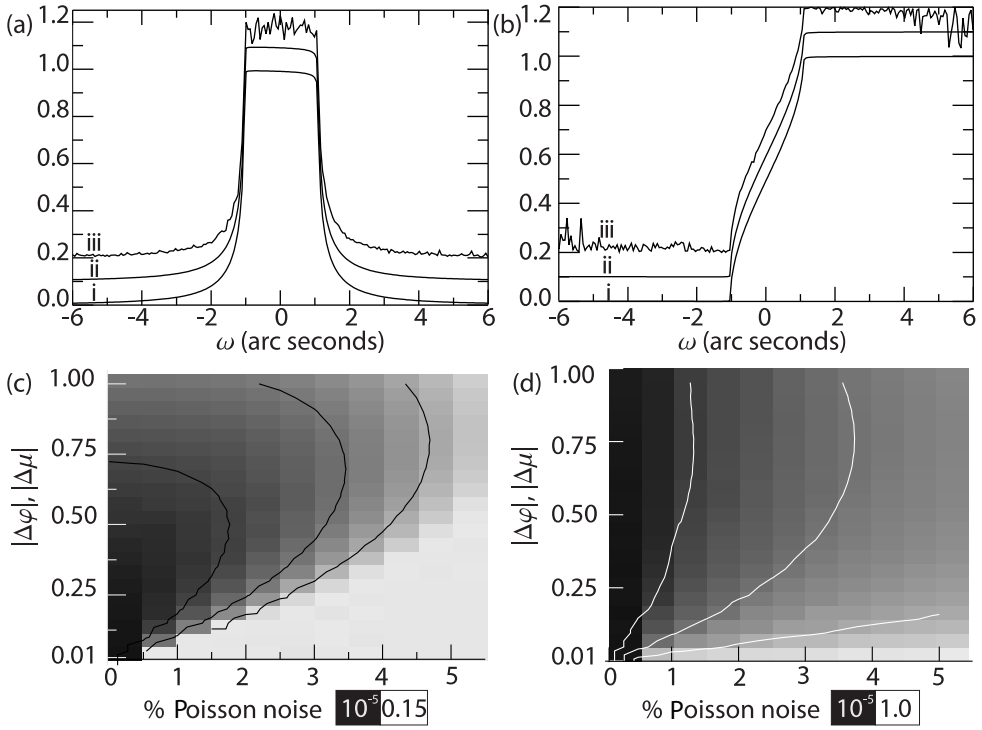


Figure 4.5: **Semi-infinite, perfect crystal ARC reconstruction.** (a) and (b) show the amplitude and phase (divided by $\pi$) with three traces (offset for clarity) representing (i) input, reconstructed with (ii) $|\Delta\varphi|, |\Delta\mu| \leqslant 0.1$, no noise (RMS error negligible) and (iii) $|\Delta\varphi|, |\Delta\mu| \leqslant 0.78$ with 1% Poisson noise (RMS error: 4% amplitude, 20% phase, 4% detected intensity). (c) and (d) present the RMS error in the amplitude and phase respectively for $|\Delta\varphi|, |\Delta\mu|$ against noise. RMS errors in (c) have been capped at 15% to facilitate visualisation of the contour details.

The reconstruction quality of $r(k_x)$ is quantified by calculating the RMS reconstruction error (RMS error between reconstruction and input functions divided by the RMS error between the input and its mean (Herman, 1980; Nesterets et al., 2004)) against the input function.

The known weak object was simulated using the phase and amplitude maps of Figure 4.3(a) and (b) respectively. The 'weakness' of the weak object was varied by changing the maximum values of $|\Delta\varphi|$ and $|\Delta\mu|$. Poisson noise was simulated in the detected intensity by adding Poisson-distributed random numbers whose standard deviation is a specified percentage of the maximum intensity registered in the 2D image. Thus, for example, 1% Poisson noise means the noise varies locally in the image from 1% at the highest signal-to-noise regions, to much larger values at the lowest signal-to-noise regions. As a result of this noise model a 1% Poisson noise level will not, in general, correspond to 1% RMS error in the image. To allow for this we will quote the reconstruction error in the ARC's phase and amplitude with the error

introduced into the detected intensity by the addition of noise.

The amplitude and phase (divided by $\pi$) of $r(k_x)$ for a symmetric Bragg reflection from Si(111) at 25keV are shown in Figure 4.5(a) and (b). Three traces are shown offset from each other for clarity and the roman numerals refer to (i) input, reconstructed with (ii) $|\Delta\varphi|, |\Delta\mu| \leqslant 0.1$, no noise and (iii) $|\Delta\varphi|, |\Delta\mu| \leqslant 0.78$ with 1% Poisson noise (RMS error: 4% amplitude, 20% phase, 4% detected intensity).

To gauge the success of the iterative algorithm in §4.3.2 consider the top left corner of Figure 4.5 (c) and (d) for $|\Delta\varphi|, |\Delta\mu| = 1$ and no noise. Clearly, the weak object approximation is not valid but with iteration the reconstruction shows RMS error of only 4% and 2% in the amplitude and phase respectively.

All simulations used 15 iterations and a single iteration took less than 1 second using a 2GHz Pentium M machine. One important consideration for the practical utility of this method is its robustness with respect to experimental noise. To some extent a smaller signal-to-noise can be compensated by using a more strongly scattering object at the expense of invalidating the weak object approximation. The tradeoff between those two quantities is plotted in Figure 4.5(c) and (d) which show that there exists an optimum level of object weakness for a given noise level.

## 4.4 Unambiguous determination of thin crystalline structure information from a single intensity measurement

To demonstrate the utility of our method of ARC reconstruction we will show how it may be used to unambiguously determine the structure of a thin and laterally homogeneous crystal structure. Specifically, we present numerical simulations which demonstrate the reconstruction of an arbitrary, depth dependent strain profile in a crystal for which a kinematic scattering approximation is valid.

The kinematic scattering approximation to the ARC for a symmetrical Bragg geometry in the limit of small deformation takes the form (Petrashen', 1974) (cf. §2.5)

$$r(\eta) = \frac{i\pi\chi_g}{\lambda \sin\theta_B} \int_{-\infty}^{\infty} \Omega(z) \exp i\,(-\eta z - \mathbf{g}\cdot\mathbf{u})\, dz. \tag{4.34}$$

Here $\omega$ is the angular deviation from the exact Bragg angle, $\eta = \frac{4\pi\omega}{\lambda}\cos\theta_B$ and $\chi_0 \approx 0$, $\chi_g$ is the Fourier component of the susceptibility in the direction of a Bragg reflection from the substrate and is assumed to be constant throughout the layer, $\Omega(z)$ is the shape function equal to unity inside the crystal and zero elsewhere, $\mathbf{g}$ and $\mathbf{u}$ are the diffraction vector and displacement of atoms from their position in the 'ideal'

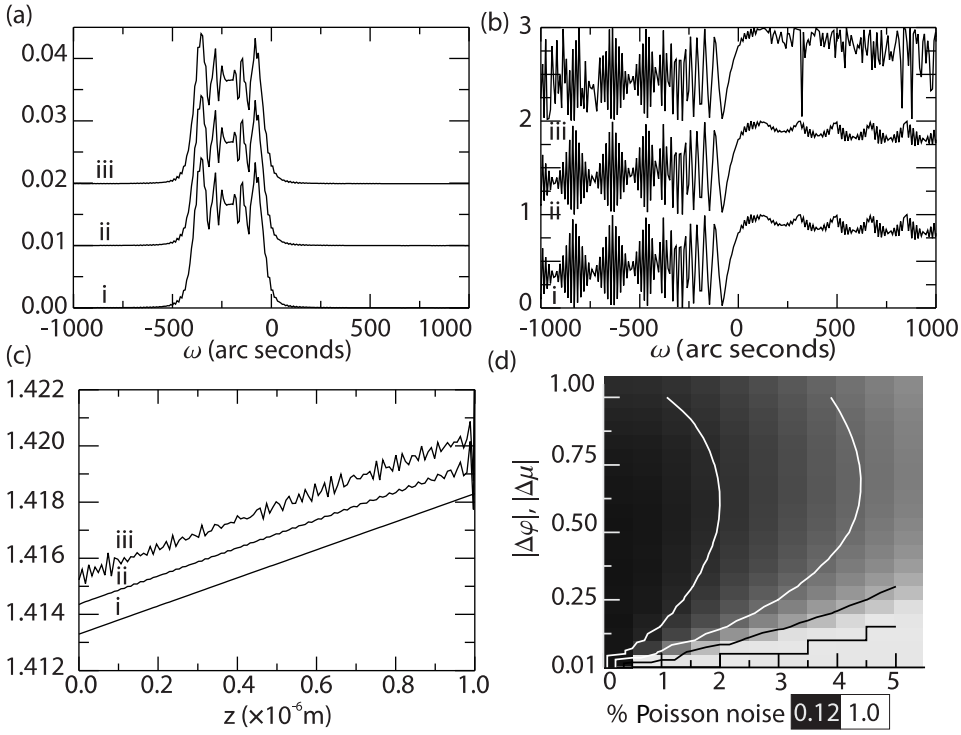


Figure 4.6: **Unambiguous reconstruction of crystal strain profile.** Input and reconstructed ARC and variation in the interplanar lattice spacing for a thin GaAs(004) film with 0.5% strain. (a) and (b) show the ARC's amplitude and phase (divided by $\pi$) and (c) the interplanar spacing variation and $d_0 = 1.413$Å with traces (offset by a constant) showing (i) input, and reconstruction using (ii) $|\Delta\varphi|, |\Delta\mu| \leqslant 0.01$, no noise (RMS error: negligible) and (iii) $|\Delta\varphi|, |\Delta\mu| \leqslant 0.5$, 1% Poisson noise (RMS error: 0.2% amplitude, 41% phase, 6% detected intensity). (d) shows the RMS error in the reconstructed lattice spacing for $|\Delta\varphi|$, $|\Delta\mu|$ against noise.

lattice, respectively. Setting $\chi_0 = 0$ amounts to ignoring attenuation and refraction within the thin layer.

Here we investigate the case of a linear variation in the lattice parameter (Kolpakov et al., 1977). The linearly strained crystal is an example of a simple crystal analogue because the sign of the strain gradient cannot be determined unambiguously from the reflectivity within the framework of the kinematic approximation (Afanas'ev and Fanchenko, 1988). The interplanar spacing can be solved explicitly when the complex ARC is known, in that case the solution is given by (Podorov et al., 1994)

$$\frac{2\pi\Delta d(z)}{d_0^2} = -\mathrm{Re}\left(\frac{\int_{-\infty}^{\infty}\eta r(\eta)\exp(i\eta z)d\eta}{\int_{-\infty}^{\infty} r(\eta)\exp(i\eta z)d\eta}\right) \tag{4.35}$$

where $\Delta d(z)$ is the variation in the interplanar spacing of the film, $d_0$ is the substrate interplanar spacing. We have used a logarithmic derivative to solve for the interplanar spacing because it is more stable numerically than the alternative of taking the

logarithm of the inverse Fourier transform of $r(\eta)$ directly.

As an example consider diffraction from a 1 micron thickness film of GaAs(004) with a 0.5% strain and 8.74keV X-rays (CuK$\alpha$1) as in Figure 4.6(a) and (b) trace (i). We note briefly that the characteristically asymmetric reflectivity of a thin strained layer is not observed here because absorption has been neglected and scattering from the thin layer is kinematic (Kolpakov and Punegov, 1985). The amplitude and phase maps of the known weak object are as in Figure 4.3(a) and (b) ( $3.6\mu m \times 3.6\mu m$). The ARC's amplitude and phase (divided by $\pi$) is shown in Figure 4.6(a) and (b) respectively and (c) shows the variation in the interplanar spacing. The three traces refer to (i) input, reconstruction using (ii) $|\Delta\varphi|,|\Delta\mu| \leqslant 0.1$, no noise (RMS error negligible) and (iii) $|\Delta\varphi|,|\Delta\mu| \leqslant 0.5$ with 1% Poisson noise (RMS error: 0.2% amplitude, 41% phase, 7% detected intensity). The oscillation in the reconstructed lattice variation Figure 4.6(c)(ii) is due to the step-function-like model for the film thickness and was responsible for the error not dropping below 10%. The RMS error increased to 16% in Figure 4.6(c)(iii) but the lattice parameter's linearity variation is still evident.

## 4.5 Summary

In summary we have developed an entirely new method for reconstructing complex Green's functions from phase contrast images of known weak objects.

The method is applicable to linear shift-invariant Green's functions, able to probe a wide range of spatial frequencies simultaneously and provides an unambiguous and non-iterative solution. The most restrictive approximation used relates to the weak object and does not limit the generality of the reconstruction algorithm.

We have shown that the complex ARC of a crystal reflection can be reconstructed from a single phase contrast image and when applied to kinematic diffraction from thin layers we are able to unambiguously reconstruct the depth-dependent interplanar spacing. We must assume that refraction and attenuation in the layer are negligible however this is usually a good approximation for kinematic diffraction.

Numerical simulations demonstrated the theory's validity and its robustness in the presence of experimental noise. This method unambiguously determines the crystal layer structure and is not susceptible to the problem of crystal analogues. Our technique enables experimental determination of the ARC phase, as predicted by X-ray dynamical diffraction theory for ideal crystals (Authier, 2005).

The most significant practical impediment to the implementation of our method lies in the fabrication of an object satisfying the weak object requirements. To demon-

strate that such an object can be made and that our method does indeed work with experimental data we now turn to an experimental implementation of the method.

# 5 Quantitative reconstruction of the thick perfect crystal Green's function

In this chapter we apply Green's function retrieval to experimental data and reconstruct the Green's function associated with X-ray diffraction from a thick perfect silicon (111) Bragg plane[1].

In the previous chapter we developed a theoretical approach which allows the complex Green's function of an imaging system to be reconstructed from two phase contrast images. This work represents a significant advance in the use of phase contrast imaging by expanding its ambit from sample characterisation to investigating imaging systems. Linear, shift-invariant Green's functions arise most notably in quantum mechanics, light, electron, neutron and neutral atom optics and all of these systems may be profitably studied using the technique we proposed in Chapter 4.

X-ray crystallography is an active area of research, with well over a century having elapsed since research efforts began in earnest. Indeed this statement can be quantified using a modern metric; "Google Scholar" returned over five thousand hits for the search term "X-ray crystallography" in 2008 alone (Google, 2008). In Chapter 4 we applied our technique to the reconstruction of crystal Green's functions, or equivalently the amplitude reflection coefficient, using simulated data. In this chapter we go one step further and apply the technique to experimental data we collected and demonstrate that it is a viable method.

The reconstructed amplitude reflection coefficient for the thick perfect crystal presented in this chapter allows direct verification of the ARC phase predicted by the theory of dynamical diffraction. The phase of the rocking curve is difficult to measure experimentally and our technique is able to reconstruct it using only the approximation of linearity and shift-invariance which demonstrates the power and

[1]This chapter is based on the manuscript *'Deterministic Green's function retrieval using hard X-rays'*, D. J. Vine, D. M. Paganin, K. M. Pavlov, K. Uesugi, A. Takeuchi, Y. Suzuki, N. Yagi, T. Kämpfe, E.-B. Kley and E. Förster, (submitted)

generality of this approach.

The Green's function associated with X-ray diffraction from a thick perfect crystal is retrieved by recording a single analyser-based phase contrast image of a known weak object using the experimental setup of Figure 4.4. Given that the weak object phase and amplitude illuminating the crystal surface are known, we can invert the ABI intensity image to reconstruct the spatial frequency spectrum of the analyser crystal. Whilst we have chosen the thick perfect crystal for our pilot study the real usefulness of this technique would be in characterising more exotic, laterally homogeneous, layered crystalline structures which could be unambiguously characterised with this method. The requirement of lateral homogeneity is restrictive but we note that the class of structures for which this technique is applicable includes some kinds of light emitting diodes and laser diodes which are fabricated from thin semiconductor films (Birkholz et al., 2006).

The first stage of our experiment in §5.1 involves the design and characterisation of the weak object that is paramount to the success of the Green's function retrieval technique. After recapitulating the reconstruction algorithm of §4.2, we outline the necessary experimental setup for Green's function reconstruction and present the experimental data. Finally in §5.3 we present the results of the reconstruction and compare it with the theoretical prediction of dynamical diffraction theory.

It will be found that there are a number of practical difficulties in fabricating a weak object that truly satisfies the weakness criteria (cf. §2.3.1) and in aligning the two dimensional images which serve as the inputs to our algorithm.

We close the chapter by presenting the results of applying our single-shot, deterministic reconstruction algorithm to the experimental ABI data. The reconstructed phase of the rocking curve is shown to be in excellent agreement with the result predicted by the theory of dynamical diffraction almost a century ago.

## 5.1 Weak object design and characterisation

The first step in reconstructing the Green's function associated with the silicon crystal Bragg reflection is the fabrication of the weak object (cf. §4.3). The crucial weak object imparts weak phase shift and attenuation to the incident beam such that its transmission function can be expressed as a linear function of phase and attenuation (cf. (2.35)). The linearisation of the transmission function results in an expression for the ABI intensity which is easily inverted to recover the Green's function.

The weak object need only be characterised once and can then be used for re-

construction of an arbitrary Green's function satisfying the requirements outlined in Chapter 4.

We would like to consider separately the two equally crucial components of this section: weak object design and characterisation. It is to the former we turn to first.

When designing the weak object we must take into account that it should satisfy (i) the 'weakness' criteria (cf. (2.33) and (2.34)),

$$|\Delta\varphi(\boldsymbol{\rho})| \ll 1, \tag{5.1}$$

$$|\Delta\mu(\boldsymbol{\rho})| \ll 1, \tag{5.2}$$

(ii) $\Delta\varphi$, $\Delta\mu$ must be linearly independent and (iii) each of $\Delta\varphi$ and $\Delta\mu$ should be aperiodic. These constraints are required to satisfy the reconstruction algorithm and it was also determined from ARC reconstruction simulations that $|\Delta\varphi|$ and $|\Delta\mu|$ must also be approximately the same order of magnitude numerically. This last constraint on the approximate equality of magnitude between phase shift and attenuation is difficult to achieve in practice because it implies equality of the real and imaginary parts of the complex refractive index and the author is unaware of the existence of such a material.

The most obvious solution which we considered was outlined in the previous chapter (see text above (4.13)) and involves using a separate object for the weak phase and weak attenuation. The weak phase object has negligible absorption and the weak attenuation object has an exactly $2\pi$ phase shift (achieved through design and immersion in refraction matching fluid (Hasnah et al., 2002)). This approach imposes a number of practical problems and requires high precision components.

An alternative approach is to use a weak phase object (negligible absorption) only and introduce the requisite weak 'attenuation' by propagating the wavefield a distance $z_0$ prior to impinging on the crystal surface. Propagation through a distance $z_0$ will endow the field with propagation based phase contrast, proportional to the Laplacian of the phase (cf. §1.1.5), which can be considered as an 'effective attenuation' of some equivalent object.

With this approach in mind a weak phase object that satisfied the weakness and aperiodicity requirements was fabricated using electron-beam lithography of a binary pattern a depth of 0.8μm into a 0.8mm thickness slab of $SiO_2$ with lateral resolution of 400nm, see Figure 5.1(a). The etching pattern was selected to be aperiodic and contain multiscale feature sizes. The former ensures that there will be no discrete diffraction peaks while the latter condition attempts to ensure that the power in the diffracted wavefield is distributed through the spatial frequency spectrum. The reader will recall

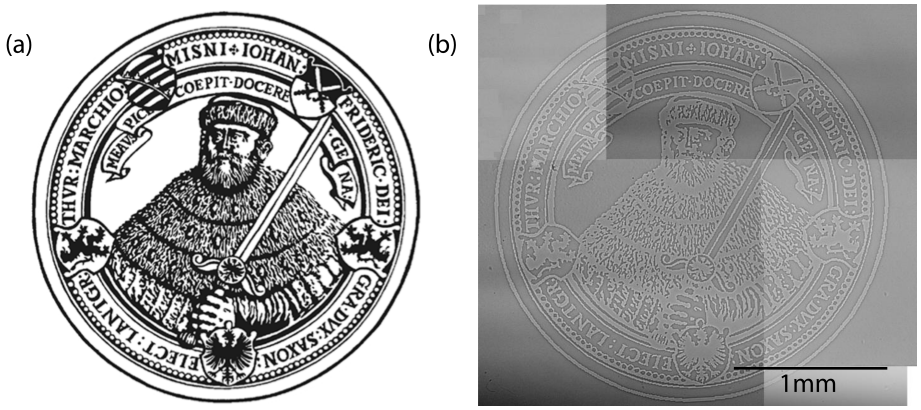


Figure 5.1: **Weak object etching pattern.** (a) the seal of Friedrich-Schiller University was used as the aperiodic etching pattern of the weak object. (b) a composite propagation-based phase contrast image of the weak object showing the accuracy of the etching (SPring-8 BL20XU, double Si(111) mono, 20keV X-rays, 245m source-sample distance, 1.2m sample-detector distance).

from Chapter 4 (cf. §4.2 especially the text after (4.6)) that we can reconstruct the spatial frequencies for which there is an appreciable power in the wavefields incident and diffracted from the crystal. Other than the requirements just listed the pattern is arbitrary[2].

Let $t(\boldsymbol{\rho})$ be the projected thickness of the binary mask then its transmission function, $f$, is (cf. (2.25))

$$f(\boldsymbol{\rho}) = \exp[-ik(\delta - i\beta)t(\boldsymbol{\rho})] \tag{5.3}$$

$$\approx \exp[-ik(\delta - i\beta)\bar{t}]\{1 - ik(\delta - i\beta)\Delta t(\boldsymbol{\rho})\} \tag{5.4}$$

where we have split $t$ in to the mean thickness $\bar{t}$ and deviation from the mean $\Delta t(\boldsymbol{\rho})$. From (5.3) we can see $\varphi = i(\delta/\beta)\mu$ and this object does not satisfy the requirement of linear independence (condition (ii) following (5.2)). $SiO_2$ was chosen because it has an amorphous crystal structure to eliminate diffraction and because it is possible to create high aspect ratio (20:1) binary masks.

With a view to satisfying the approximate equality between $\Delta\varphi$ and $\Delta\mu$ we present Figure 5.2(a) which is a plot of the real and imaginary parts of the complex refractive index of $SiO_2$ over a range of hard X-ray wavelengths. The phase shift and attenuation for 800nm of $SiO_2$ is shown in Figure 5.2(b) over the same range. The difference between $\delta$ and $\beta$ increases with X-ray energy which suggests we should low energy X-rays to achieve equivalence between $\Delta\varphi$ and $\Delta\mu$ however as Figure 5.2(b) shows

[2]The object was fabricated by T. Kämpfe and E.-B. Kley at the Institute of Applied Physics, Friedrich-Schiller University (Germany) and as such we took the university seal, Johann Frederick (der Grossmuetige), founder of Friedrich-Schiller University, as the pattern.

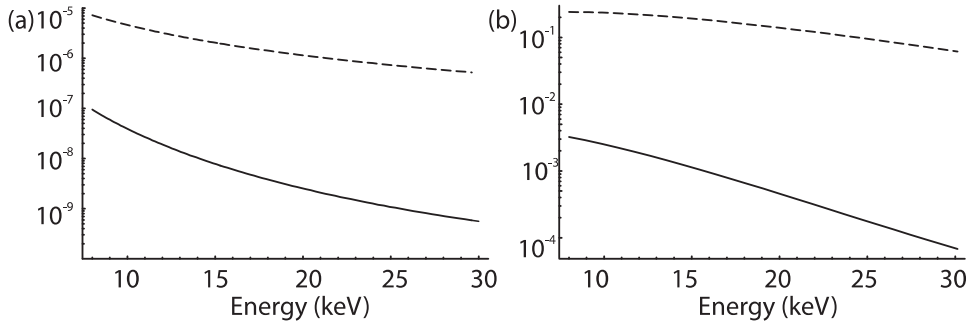


Figure 5.2: **Weak object characteristics of $SiO_2$.** (a) Log-linear plot of (broken) $\delta$ and (solid) $\beta$ against energy. (b) Log-linear plot of (broken) phase shift $[= (2\pi/\lambda)\delta(\lambda)t]$ and (solid) attenuation $[= (2\pi/\lambda)\beta(\lambda)t]$ for thickness t= 800nm, an etching depth readily achievable using electron-beam lithography.

the difference between $\varphi$ and $\mu$ is still approximately two orders of magnitude at low energies. This difference is too large for successful implementation of our algorithm and it is necessary to bolster the effective attenuation with PBI.

By introducing a propagation distance between the sample and the analyser crystal, the field at the entrance plane of the crystal will show PBI phase contrast which, as mentioned earlier, we will consider to be the effective attenuation of some equivalent object.

The complex scalar wavefield, $\psi$, exiting the weak object is the product of a plane wave and the transmission function (cf. (2.24)),

$$\psi(\boldsymbol{\rho}, z) = f(\boldsymbol{\rho}) \exp(ik_z z) \tag{5.5}$$

which can be related to the field a distance $z_0$ away (see Figure 5.6) by the angular spectrum of plane waves (cf. §2.4)

$$\psi(\boldsymbol{\rho}, z_0) = \frac{1}{(2\pi)^2} \iint_{-\infty}^{\infty} \psi(\boldsymbol{\rho}', 0) \exp\left(iz_0\sqrt{k^2 - |\boldsymbol{\kappa}|^2}\right) \exp[i\boldsymbol{\kappa} \cdot (\boldsymbol{\rho} - \boldsymbol{\rho}')] d\boldsymbol{\rho}' d\boldsymbol{\kappa}. \tag{5.6}$$

By adjusting $z_0$ we can tune the magnitude of $\Delta\mu$. The PBI contrast for a weak object is proportional to the Laplacian of the phase (Bremmer, 1952) which cannot be expressed as a linear algebraic function of the phase, satisfying the requirement of linear independence. Figure 5.3 shows $\Delta\varphi$ and $\Delta\mu$ plotted against $z_0$ for 20keV hard X-rays. It can be seen that the 'attenuation' increases much more rapidly than the phase for the first metre of propagation and we conclude to use a sample-to-analyser distance of 1.2m.

In summary, we have used a weak phase object with negligible absorption in conjunction with wavefield propagation to create a weak phase-amplitude object. This method has allowed us to satisfy the four requirements: weakness, aperiodicity, linear

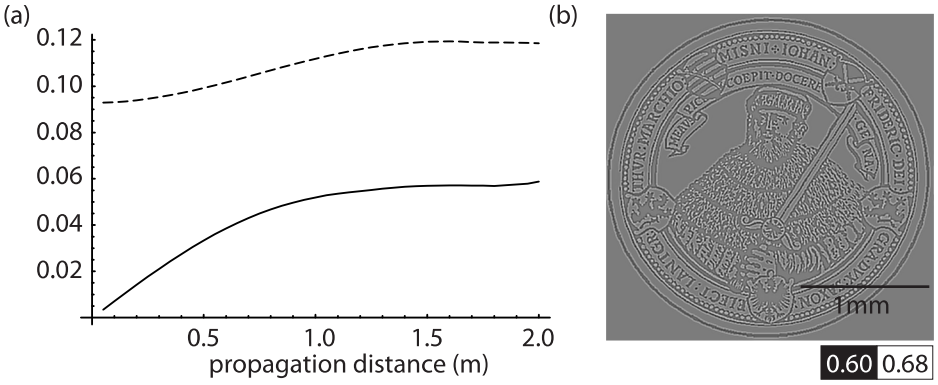


Figure 5.3: **Weak object phase and attenuation against propagation distance.** (a) (broken) $|\Delta\varphi|$ and (solid) $|\Delta\mu|$ against propagation distance for 20keV X-rays and the phase object described in the text. (b) a simulated PBI image ($z$=1.2m) from which the measurements in (a) were taken.

independence of $\Delta\varphi$ and $\Delta\mu$ and an approximate order-of-magnitude equivalence between phase shift and attenuation.

We now turn to the characterisation of the weak object which was performed using propagation-based phase contrast imaging (§1.1.5). The problem of quantitative phase retrieval (equivalently, projected thickness retrieval for objects composed of a single material whose complex refractive index is known) from a single propagation-based phase contrast image was solved by Paganin (Paganin et al., 2002; Paganin, 2006). We now give a brief account of this solution.

We assume monochromatic $z$-directed plane waves illuminate a single material object with projected thickness $t(\boldsymbol{\rho})$ (cf. (2.25))

$$\psi(\boldsymbol{\rho}, z=0) = \exp[-ik\{\delta - i\beta\}t(\boldsymbol{\rho})] \tag{5.7}$$

and would like to retrieve the projected thickness. We will use the TIE (cf. (1.3)) to relate the phase and intensity in the exit-surface plane of the sample (contact plane) to the intensity a distance $z_0$ away. We begin with the TIE (1.3),

$$\nabla_\perp \cdot [I(\boldsymbol{\rho},0)\nabla_\perp \varphi(\boldsymbol{\rho},0)] = -k\frac{\partial I(\boldsymbol{\rho},0)}{\partial z} \tag{5.8}$$

where

$$I(\boldsymbol{\rho},0) = \exp[-2k\beta t(\boldsymbol{\rho})], \tag{5.9}$$

$$\varphi(\boldsymbol{\rho},0) = -k\delta t(\boldsymbol{\rho}). \tag{5.10}$$

The left-hand side of (5.8) may be rewritten as,

$$-\delta\nabla_\perp \cdot [\exp\{-2k\beta t(\boldsymbol{\rho})\}\nabla_\perp t(\boldsymbol{\rho})] = \frac{\delta}{2k\beta}\nabla_\perp^2 \exp[-2k\beta t(\boldsymbol{\rho})]. \tag{5.11}$$

The longitudinal derivative on the right-hand side of (5.8) can be approximated as a first-order finite difference equation,

$$\frac{\partial I(\boldsymbol{\rho},0)}{\partial z} = \frac{I(\boldsymbol{\rho},z_0) - I(\boldsymbol{\rho},0)}{z_0}. \tag{5.12}$$

Combining (5.11) and (5.12) with (5.8) gives for the projected thickness,

$$\left[1 - \frac{z_0\delta}{2k\beta}\nabla_\perp^2\right] \exp[-2k\beta t(\boldsymbol{\rho})] = I(\boldsymbol{\rho},z_0). \tag{5.13}$$

Eq. 5.13 is easily solved using the Fourier derivative theorem to give the following expression which is explicit in the projected thickness,

$$t(\boldsymbol{\rho}) = -\frac{1}{2k\beta}\ln \mathcal{F}^{-1}\left[\frac{1}{1-\frac{z_0\delta}{2k\beta}|\boldsymbol{\kappa}|^2}\mathcal{F}[I(\boldsymbol{\rho},z_0)]\right]. \tag{5.14}$$

From (5.14) we may retrieve the projected thickness of a single material objected using a single propagation based intensity image and so we now turn the measurement of these images.

The experimental measurement of the PBI images were performed at SPring-8 beamline BL20XU using a non-dispersive double crystal Si(111) monochromator and 245m source to sample propagation distance, see Figure 5.6. The images were recorded using a CCD camera with an effective pixel size of 0.9μm. A sequence of 500 images, direct beam and dark current were recorded using an exposure time of 100ms and the corrected images are shown in Figure 5.4.

The top two images of the figure clearly show a pair of horizontal stripes which is due to either a variation in thickness of the $SiO_2$ substrate or a warping of the beryllium window that separated the vacuum beam pipe with the experimental hutch. This low frequency background variation, which is also present in the lower images of Figure 5.4, will be seen to significantly compromise the weak object criteria.

Phase retrieval was performed on the images in Figure 5.4 by selecting the matching 1024×1024 pixel subimage area from the 0.7m and 1.2m images which was chosen by inspection to have the least artifacts. Quantitative comparison of the retrieved phase required that sub-images matched to the same area of the weak object to single pixel accuracy.

At this point a two (or more) image phase retrieval algorithm (Paganin and Nugent, 1998) could be applied to the data however this was found to be impractical. Two image PBI phase retrieval is extremely sensitive to misalignment of the image centroids and requires that they are aligned with sub-pixel accuracy. Shifting the centroid of an image can be achieved through zero-padding the image array and transversely

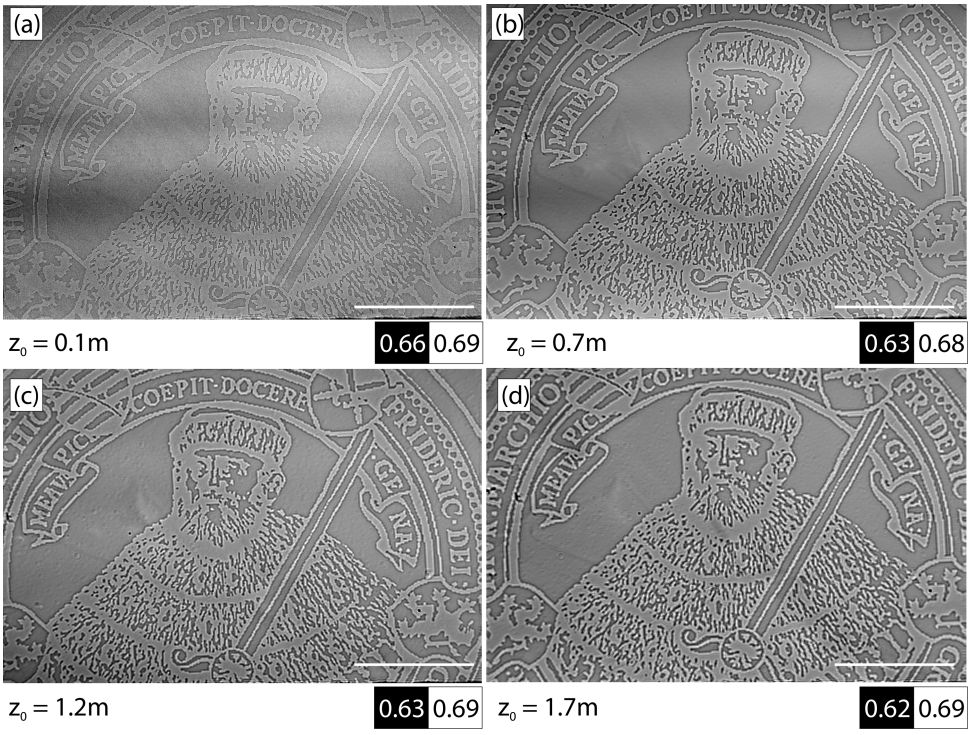


Figure 5.4: **Propagation-based phase contrast images for characterisation of the weak object.** Images measured at 20keV with (a) 0.13m, (b) 0.7m, (c) 1.2m, (d) 1.7m sample to detector propagation distance. All scale bars are 0.5mm.

shifting it until the centroid is in the desired location. The impracticality occurs when attempting to Fourier transform a zero-padded low-contrast image, such as the one we are using, which introduces ringing artifacts, known as Gibbs phenomenon (Gibbs, 1898), which are greater than the signal we are trying to reconstruct. Since we cannot avoid using Fourier transforms, as the ARC that we are trying to reconstruct exists in reciprocal space, we are forced to conclude that centroid shifting is not possible. As a corollary it is worth mentioning that Fourier transforms performed on data in this chapter was achieved by 'reflection padding' the array to be transformed. Reflection padding consists of mirroring a square array of side length N across its boundary such that in the padded array, the original array sits in the centre of a $3N \times 3N$ padded array (Volkov et al., 2002). Padding the image in this manner ensures the image is continuous, but not necessarily smooth, at the boundary, thereby minimising ringing artifacts.

The recovered projected thicknesses is presented in the middle panels of Figure 5.5 with their corresponding measured intensity images on the left. The retrieved thickness shows significant low frequency background variation over which the weak object

thickness variation is imprinted. The background variation corresponds to either an approximately 10μm variation in the thickness of the $SiO_2$ substrate or a distortion in the beryllium window producing PBI aberrations. This will prove to be a serious limitation to the accuracy with which the ARC can be reconstructed because the deviation of the projected thickness from its mean value is no longer small. Strategies to ameliorate this problem will be discussed in §5.3. We note that appropriate filtering could possibly remove this background however we require that the phase incident on the crystal actually be weak.

The power spectra of the retrieved projected thickness are presented on the right of Figure 5.5 to illustrate the core weakness of using PBI to characterise the weak object. The Fresnel rings in the power spectrum constitute a loss of information at these spatial frequencies. The information loss was compensated by averaging the projected thicknesses recovered from the 0.7m and 1.2m PBI images separately. We can estimate the spatial resolution of the recovered phase using the Fresnel criterion, $N_F = g^2/\lambda z$. If we choose a Fresnel number of 1 then PBI phase retrieval can recover the projected thickness with a resolution not better than 9μm or approximately 10 pixels which, by inspection, is approximately correct.

Now that we have recovered the projected thickness of the weak object we have concluded the characterisation process and we are in a position to be able to infer the complex wavefield incident on the surface of the crystal.

## 5.2 Experimental design for Green's function retrieval

Having characterised the weak object we now describe the experimental setup that was used to record the images that will be used to reconstruct the Green's function associated with the ABI analyser crystal.

With reference to Figure 5.6 a planar, monochromatic hard X-ray wavefield illuminates the weak object and propagates through a distance $z_0 = 1.2$m before being incident on the crystal surface. As described earlier the introduction of a 1.2m propagation distance gives the field at the entrance plane of the crystal an effective attenuation. The wavefield is then reflected from the analyser crystal and propagates a distance $z_1$ to the detector. In practice we would like the crystal-detector distance to be as small as practicable which in our experiment was $z_1 = 0.06$m.

The wavefield incident on the crystal surface is given by $\psi(x, y, z_0)$. The top and bottom of the beam intersect the crystal at different distances from the sample and the resulting propagation difference will result in marginally greater PBI phase contrast

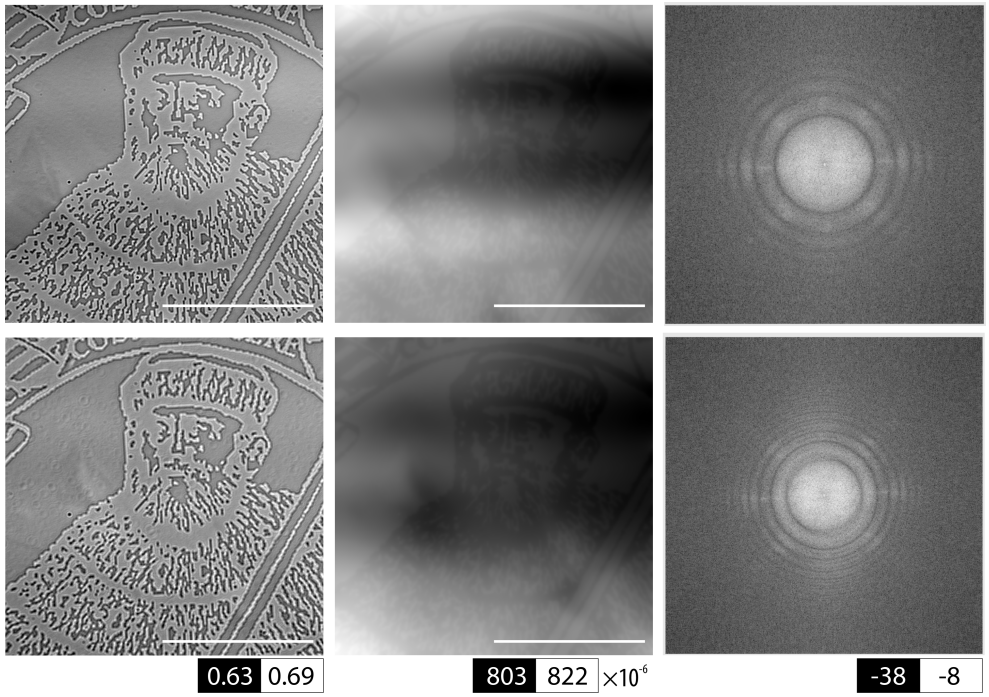


Figure 5.5: **Phase retrieval for weak object characterisation.** The left most panels show measured PBI images at a propagation distance of (top) 0.7m and (bottom) 1.2m that will be used for phase retrieval. The middle panels show the single image phase retrieval algorithm applied to the left panels to recover the projected thickness. These images are difficult to see in print due to the low contrast and we recommend looking at the electronic copy in the PDF version of the thesis. The right panels show the power spectrum of the projected thickness on a log scale. All scale bars are 0.5mm.

for the longer propagation distance. With a 1mm beam height this amounts to a centimetre and was considered negligible.

As discussed in the previous section the wavefield incident at the entrance plane of the crystal is given by (5.6) and we now define this wavefield to be our weak object (cf. (4.6)),

$$\psi(\boldsymbol{\rho}, z_0) = \exp[\mathrm{i}\overline{\varphi} - \overline{\mu}]\{1 + \mathrm{i}\Delta\varphi(\boldsymbol{\rho}) - \Delta\mu(\boldsymbol{\rho})\}. \tag{5.15}$$

We note that (5.15) makes clear the connection of this approach to in-line holography: the field transmitted through the weak object, $\psi(\boldsymbol{\rho}, z_0)$, is the sum of the direct beam and a known weak perturbation. Reflection from the crystal will modulate the amplitude and phase of the field and the detector records the hologram. The hologram evidently contains the response of the imaging system to all spatial frequencies present in $\psi$ which allows a massively parallel interrogation of a wide range of reciprocal space simultaneously.

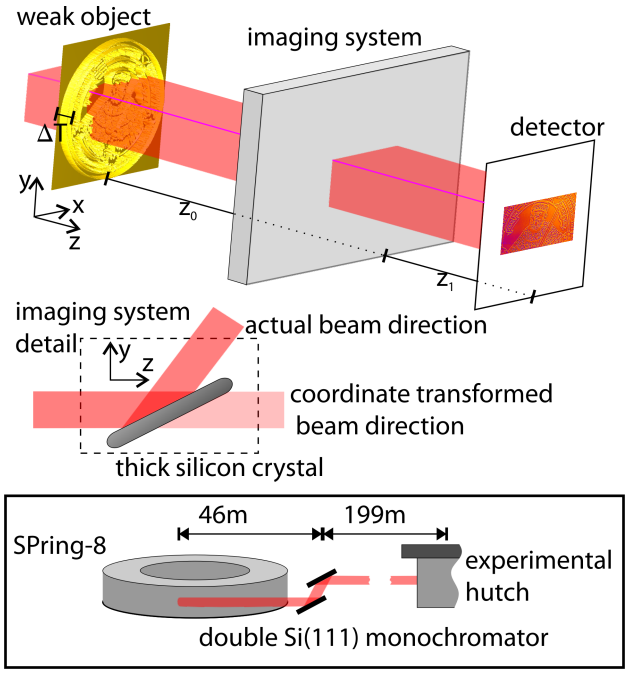


Figure 5.6: **Schematic experimental setup for ARC reconstruction.** 20keV X-rays from SPring-8 BL20XU illuminate an *a priori* characterised weak object. The weakly perturbed field is then Bragg reflected (see inset) from a thick perfect silicon crystal (111) and recorded on a detector. This single image may be deterministically inverted to recover the complex ARC.

The experiments were conducted at the BL20XU undulator beamline at SPring-8 using 20keV X-rays from a double Si (111) monochromator. The X-ray beam size was approximately 4(hor) $\times$ 2(ver) mm at 245 m from the source. Images were recorded using a Hamamatsu CCD detector coupled to an optical lens and phosphor screen with a 0.9 μm effective pixel size and 2(hor) $\times$ 1.3(ver) mm field of view.

The range and resolution of the reconstruction are Nyquist limited by the detector so that for N pixels of size $\Delta x$ the maximum frequency is $\lambda/2\Delta x$ with a resolution of $\lambda/N\Delta x$. Whilst these represent an upper limit they are dependent on the scattering power from the weak object's smallest features being detectable. As noted earlier the phase retrieval step put a lower limit of 9μm on the retrievable feature size which combined with factors including the non-plane wave illumination will serve to limit the reconstruction to some smaller angular range.

The measured ABI images are presented in Figure 5.7 at various points on the rocking curve. The range of images were recorded because the algorithm requires both phase and attenuation contrast to work and the amount of phase contrast can be tuned by changing the rocking angle. These images could then be used to determine, by trial and error, which rocking angle gave the best results. The images recorded at

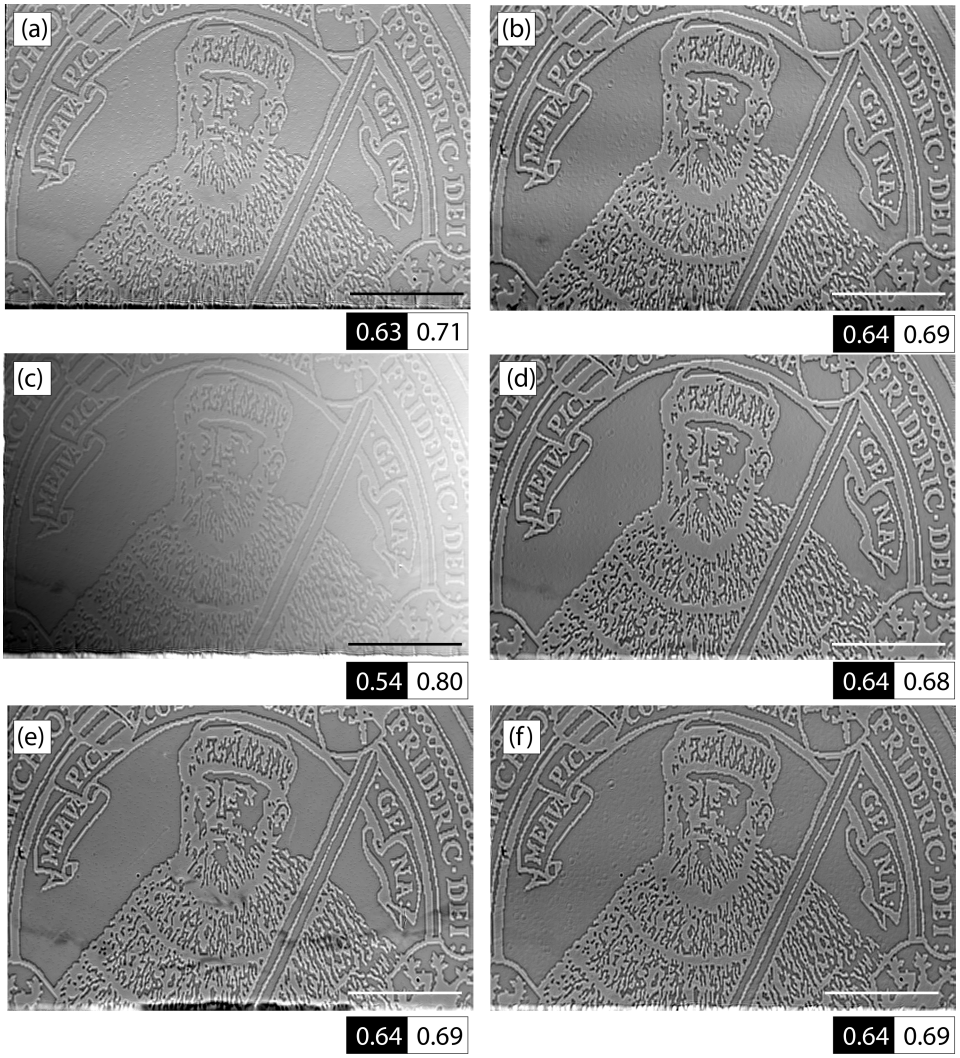


Figure 5.7: **ABI images for ARC reconstruction.** Analyser-based phase contrast images of the known weak object recorded at different values of crystal angular deviation from the Bragg angle. The left column are measured above the Bragg angle and the right column below it. (a,b) 50% reflectivity, (c,d) 70% reflectivity and (e,f) 100% reflectivity. All scale bars are 0.5mm.

rocking angles above the Bragg angle (left column of Figure 5.7) show a significant lack of contrast compared to the low angle images and for this reason these images were not used for reconstructions.

In comparing the ABI images of Figure 5.7 with the PBI images of Figure 5.4 we can see a magnification in the y-direction of the ABI images. This implies that the analyser crystal reflection was not symmetric but rather the crystal surface was miscut by approximately 0.8° to the (111) plane. The asymmetric reflection was compensated for in the post-processing phase by re-scaling the input images to match the output. A simplex was chosen in each image and then registered using an affine transfor-

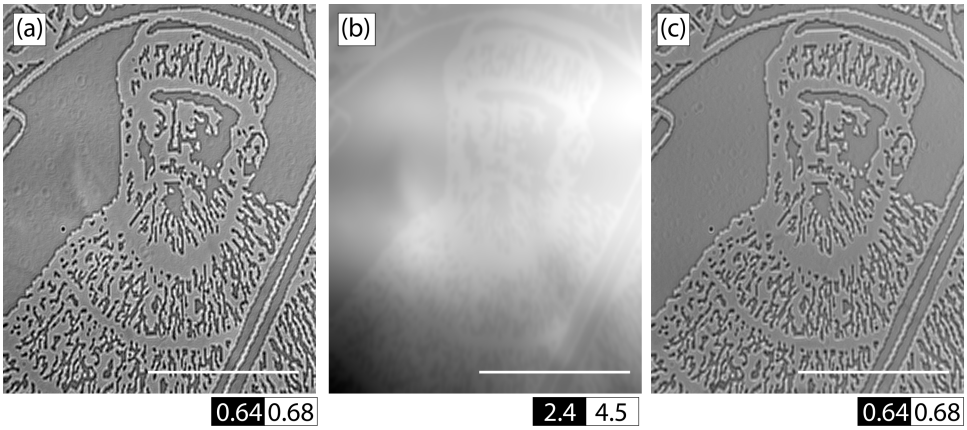


Figure 5.8: **Input images for the reconstruction algorithm.** (a) the input intensity $|\psi(\boldsymbol{\rho}, z_0)|$, (b) the input phase $\mathrm{Arg}[\psi(\boldsymbol{\rho}, z_0)]$, (c) the output intensity $|\Psi(\boldsymbol{\rho}, z_0 + z_1)|$. All scale bars are 0.5mm.

mation (Yale, 1988) implemented in ImageJ (v1.37) plugin TurboReg (Biomedical Imaging Group, École Polytechnique Fédérale de Lausaunne) function for affine transformations. The affine transformation rotates and scales images to a match a simplex in the two images whilst preserving co-linearity.

We now have the requisite data for ARC reconstruction and we turn to implementation of the reconstruction algorithm.

## 5.3 Semi-infinite perfect crystal ARC reconstruction

The problem, as stated previously and solved by (4.26), is to reconstruct the ARC of the thick silicon crystal, $\mathfrak{r}$, given complex wavefield over the entrance plane of the crystal $\psi(\boldsymbol{\rho}, z_0)$ and measured intensity at the detector $|\Psi(\boldsymbol{\rho}, z_0 + z_1)|$. We have now seen how the quantities $\psi$ and $|\Psi|$ have been measured. In §5.1 we have described how the weak object was characterised so that its transmission function $\mathfrak{f}$ is known and the wavefield $\psi(\boldsymbol{\rho}, z_0)$ is given by (5.6). $|\Psi|$ was measured directly in the manner described in §5.2.

The three inputs to the reconstruction algorithm are presented in Figure 5.8. Figure 5.8(a) and (b) are the measured PBI intensity over the entrance plane of the crystal and the simulated phase over the same plane from the recovered projected thickness. The measured PBI intensity was used in Figure 5.8(a) in preference to the simulated intensity over the same plane from the reconstructed projected thickness because it did not suffer from the blurring inherent in the phase retrieval process. Through trial and error it was determined that the 70% reflectivity ABI image (Figure 5.7(d)) gave

the best reconstruction and so Figure 5.8(c) is taken from that image.

The inputs in Figure 5.8 have been processed to ensure they are aligned to sub-pixel level using a number of steps which we outline now. The biggest practical problem was the magnification of the ABI images caused by the asymmetric reflection which meant the inclusion of an image registration step in the processing. From raw data the images were flat- and dark-field corrected according to (3.8) and then corrected for geometrical magnification. A $1024\times1024$ sub-image was selected by inspection to have the least artifacts that would deleteriously affect the reconstruction. The use of sub-images also minimises the effects of the low frequency background variation in the recovered phase because the deviation from the mean is reduced. The intensity and phase images (Figure 5.8(a) and (b)) were then registered to the ABI image using the ImageJ TurboReg plugin. The algorithm is sensitive to image misalignment however the quality of the match was judged by eye only and this proved sufficient to achieve acceptable results.

In principle the three inputs to the algorithm, Figure 5.8, are simply fed into the algorithm and the ARC is output. In practice there are two other constraints which can be applied to the image data to reduce artifacts. The first of these was to divide the inputs in Figure 5.8 into smaller sub-images, each of which was run through the algorithm and averaged for the final result. The sub-images were taken to be $256\times256$ pixels and the final result is the average of 100 sub-images. The second constraint enforces the requirement of even- and odd-ness of the reconstructed solution. The solution given in (4.26) is in terms of even and odd functions which when reconstructed using experimental data are in general not purely even or odd so this constraint is imposed upon them.

The average reconstructed ARC for the thick perfect crystal is presented in Figure 5.9. This plot is the main result of this chapter and shows the comparison between the reconstructed and theoretical ARC magnitude and phase for the thick silicon crystal. This experimental result is the culmination of much of the work presented in the last chapter on Green's function retrieval and conclusively demonstrates that Green's functions associated with reflection from a perfect crystal can be quantitatively reconstructed from phase contrast images. Further, this is a beautiful validation of the classic prediction of the dynamical theory of X-ray diffraction for the phase of the rocking curve.

We can see that the match between experiment and theory is overall quite good however there are some clear artifacts in the reconstructions. There are a number of possible reasons for the discrepancy between the reconstruction and theoretical

measurement. The input phase variation is of the order of 1 radian (see Figure 5.8(b)) and it is likely that this was a major contributor to the artifacts in the reconstruction. The weak object with 1 radian phase shift is problematic because it violates the weak phase criteria but also because, numerically, it is so much bigger than the weak attenuation (about 0.1). The cause of the unwanted large phase shifts in the weak object were most likely due to a non-uniform $SiO_2$ substrate or distortions in the beryllium window. This serves to highlight the difficulty of creating and using a weak object.

Another likely reason for the discrepancy is the sensitivity of the algorithm to sub-pixel alignment which, having been done by inspection, may not have been optimal. It is possible the results could be improved by employing a parameter-search algorithm that minimises the difference between the reconstruction and the theoretical prediction however it was felt that this would destroy the objectivity of the reconstructions.

The grey shaded regions show the condition number of the inverse matrix in (4.26) and represents the region of validity of the reconstruction. A large condition number indicates that the output of (4.26) varies significantly upon a small change in the input and so at this point the solution is numerically unstable. At high spatial frequencies the large condition number is due to the low power scattered into these frequencies. The large condition number in the vicinity of the DC frequency is due to the increased susceptibility to noise at this point because the odd components in (4.26) must necessarily be zero at this point meaning that all information is carried in only the two even components.

The angular range of the reconstruction is limited by the experimental conditions. The power spectrum of the input images drops rapidly from the central order indicating that the power scattered into the highest spatial frequencies was equivalent to that introduced by noise in the CCD detector. These frequencies are not recoverable using our technique effectively limiting the reconstruction range and have been excluded from Figure 5.9. This problem could be addressed with a weak object with finer feature scales than the estimated 9μm of the object we have used.

Interestingly we have been able to separate instrumental effects which are due to the monochromator crystals from the reconstructed ARC. This is because the algorithm simply sees the effects of the crystal because the effects of the monochromator and source are included in the input field, and so we reconstruct only the effect of the crystal.

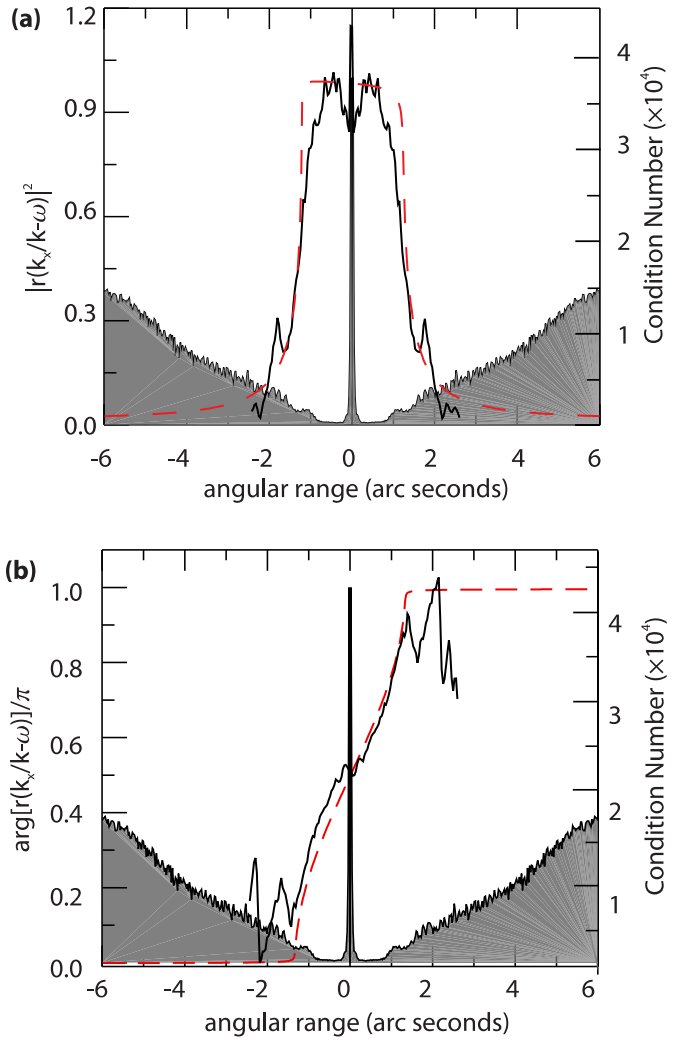


Figure 5.9: **Reconstruction of thick perfect silicon(111) complex ARC.** The (solid) reconstructed and (broken) theoretical (a) magnitude and (b) phase of the ARC. The condition number is shaded in grey beneath the plots and quantified in the right axis.

## 5.4 Discussion

In this chapter we presented the result of our Green's function reconstruction technique to the Green's function associated with reflection from the thick perfect silicon (111) Bragg plane. Our reconstruction was shown to be in quantitative agreement with classic prediction of dynamical diffraction theory.

This result is a new method for solving the one-dimensional phase retrieval problem of crystallography. In many cases of practical interest where one is concerned with inferring crystal structure from diffraction data, the phase of the ARC must be recovered for an unambiguous solution. A number of solutions have been developed to

address this problem including (cf. §4.3) Fourier analysis of the rocking curve, methods which utilise the Hilbert transform and standing-wave electron photo-emission based techniques. In contrast to these techniques, the method we have demonstrated is deterministic and non-iterative, is able to reconstruct a wide range of angular space simultaneously and is sensitive to both amplitude and phase of the ARC.

We emphasise that our method, which can be used to reconstruct the entire rocking curve from a single two-dimensional measurement, is already more efficient than methods which measure the rocking curve in a serial manner however we reconstruct the phase as well.

The phase that we reconstructed in Figure 5.9(b) is a beautiful validation of the classic prediction of the phase of the rocking curve of dynamical diffraction theory (Authier, 2005). This result paves the way for the possibility of reconstructing the complex ARC for thick perfect crystal analyser and monochromator crystals as opposed to measuring the rocking curve and associating with it the theoretical phase. This last point is particularly important for ABI imaging where both the rocking curve and its phase must be known for a wave-optical analysis of the forward and inverse problems.

The positive result of the reconstruction for the perfect crystal suggests an immediate extension to reconstructing the ARC of thin crystalline films and it is in this area that this result may have the largest impact. For thin crystalline films we can use this technique to infer crystal structure directly and unambiguously using a single two-dimensional intensity measurement.

## 5.5 Summary

In conclusion, we have demonstrated the reconstruction of the complex Green's function associated with reflection from a perfect silicon single crystal Bragg plane.

We have developed a method for Green's function reconstruction in Chapter 4 and the results of this chapter are a culmination of that work which shows that the technique is viable. The Green's function we have reconstructed is in excellent agreement with the prediction of classical dynamical diffraction theory and provides a validation of the phase predicted by that theory.

We began with the design and characterisation of the weak object that is the crucial optical element of this technique. The characterisation of the weak object yields the projected thickness, which is considered *a priori* information for the reconstruction algorithm, and allows the complex wavefield at the entrance surface to the crystal to

be calculated.

Following the characterisation of the weak object we recorded ABI images of the weak object and these were used to recover the imaging system Green's function. Whilst the reconstruction was shown to be in good agreement with the prediction of dynamical diffraction theory there were a number of limitations imposed by the experimental conditions. Primarily these were the violation of the weak object criteria, asymmetric Bragg reflection and complications arising from using PBI phase retrieval as the characterisation method.

The reconstruction shows that we developed a viable new method for solving the one dimensional phase problem in crystallography. The technique has wider application than crystallography and it can be applied to reconstructing the Green's function associated with any one- or two-dimensional linear and shift-invariant imaging system.

# 6 Conclusions

## 6.1 Overview

Extensions to analyser-based phase contrast imaging (ABI) have been demonstrated which allow quantitative measurements to be extracted from images recorded using an extended incoherent source and that allow the Green's function associated with an imaging system to be quantitatively reconstructed. We supplemented the theoretical and numerical results with numerical simulations and rigorous experiments which in both cases validated our results.

ABI is predominantly performed at synchrotrons because of the outstanding brilliance and coherence of those sources. There is a demand however for phase contrast imaging systems that can be implemented using incoherent X-ray sources. ABI is a useful tool for quantitative characterisation and its use could be more widespread if it could be used in conjunction with widely available rotating anode-X-ray sources. These sources offer a number of advantages over the synchrotron, not in terms of the quality of the radiation, but rather in practical aspects such as volume of samples investigated, cost to use and convenience of having an 'in-house' characterisation technique.

In Chapter 3 we studied ABI imaging and phase retrieval using an extended incoherent source. We found that ABI contrast depends critically on the spatial coherence of the incident radiation and degrades decreasing coherence. Using numerical simulations of an idealised ABI imaging system we showed that the divergence of the wavefield incident on the analyser crystal should be kept to less than the Darwin width of the analyser crystal to achieve the best image contrast. There are a number of common monochromator crystal and configurations and these were considered for their ability to provide the requisite spatial coherence. We also considered the stability requirements of the diffractometer and it was found that whilst mechanical

stability would degrade the ABI image, the susceptibility of analyser crystals to thermal instability was a greater concern. The ambient temperature during a measurement should be carefully controlled to limit artifacts in the measured image.

We then presented results of an experiment in which quantitative information was extracted from images recorded using a rotating anode X-ray source with four-reflection Bartels monochromator. In order to perform quantitative phase retrieval we demonstrated that the X-ray film has a linear response against exposure time for the range of exposures that were used for our ABI measurement. Images of a plastic test phantom were recorded and the projected thickness recovered using a single-image phase retrieval algorithm which assumed the crystal had a linear transfer function. The retrieved projected thickness was scaled against an *a priori* known feature size in the object and the resulting calibrated projected thickness was compared to a reference optical microscopy measurement and the two were found to be in excellent agreement.

The conventional utility of phase contrast imaging systems is in visualising samples that are not easily seen using absorption contrast techniques. In Chapter 4 of this thesis we investigated an entirely new application of phase contrast imaging systems by swapping the roles of sample and imaging system. We were able to show that by imaging a known weak object we could reconstruct the complex linear, shift-invariant Green's function associated with the imaging system.

We introduced the weak object and showed that intensity images of the weak object are linearly proportional to the phase and attenuation of the weak object. This was exploited to develop a method for reconstructing a linear and shift-invariant, but otherwise arbitrary, complex Green's function from two intensity images. This approach was applied to ABI and it was shown using numerical simulations that the semi-infinite Green's function associated with Bragg reflection could be reconstructed unambiguously from a single measurement. Further simulations showed that when applied to thin crystalline films our method unambiguously determines the crystalline structure. In the context of crystallography the Green's function we seek to reconstruct is one-dimensional and so can be reconstructed from a single phase contrast image.

The ability to use a single measurement to interrogate a wide range of reciprocal space simultaneously is enormously advantageous over current serial measurement techniques which probe reciprocal space points individually. In addition, we reconstruct the complex function which is not currently possible using standard X-ray diffractometry.

Amongst the other possible uses for Green's function reconstruction, we stress the applicability of this work to the characterisation of thin layered crystalline films which

are enormously important to the semiconductor industry.

The Green's function reconstruction approach developed in chapter 4 depends crucially on whether an optical element with the properties ascribed to the weak object in Chapter 4 can be realised in practice. In Chapter 5 we addressed this problem by giving the results of an experiment in which the Green's function associated with Bragg reflection from a thick perfect crystal was reconstructed.

We began Chapter 5 by presenting the design and characterisation of the weak object. The weak object consists of a binary pattern etched into amorphous $SiO_2$ and was characterised using phase retrieval from propagation based phase contrast images. The characterised weak object along with the measured ABI image were then used as inputs to the reconstruction algorithm given in Chapter 4.

The reconstructed ARC, the Fourier space dual to the Green's function, associated with Bragg reflection from the thick silicon 111 Bragg plane was found to be in excellent agreement with the prediction of classical dynamical diffraction. The reconstruction validates our approach and shows that it is able to work in practice.

The work of Chapter 5 is the culmination of the theory presented in Chapter 4. The success of this technique applied to crystallography suggests that the other applications hinted at in that chapter such as reconstructing Schrödinger or Helmholtz propagators could profitably be studied using this technique.

## 6.2 Limitations of this study and suggestions for future work

The ABI phase imaging and quantitative phase retrieval reported in Chapter 3 represents a significant step forward for this technique and the prospects of it becoming a standard quantitative characterisation tool with extended incoherent sources.

A number of challenges persist that require improvement. The biggest practical impediment to the viability of incoherent source ABI is the long measurement time. In the experiment presented in Chapter 3 the measurements were recorded over approximately four hours. The main reason for this is the use of a four reflection monochromator which rejects a significant proportion of the flux from the rotating-anode tube. The Bartels monochromator was chosen because it provides the lowest incident beam divergence and thus the highest ABI contrast. If one was willing to sacrifice some sensitivity to phase gradients then it would be possible to reduce the exposure time by using a monochromator with larger band-pass. Further study is required of this problem to determine the optimum source/monochromator configuration for a given analyser crystal and sample size.

The phase retrieval performed on the ABI data of Chapter 3 used a tunable parameter to expedite the process because the refractive indices of the sample were not determined experimentally (although these could be estimated without a significant loss of accuracy) and because the working point of the incident beam on the analyser crystal rocking curve was not constant. The use of the tunable parameter significantly simplifies the phase retrieval process but necessitates the use of *a priori* information about the sample, such as its maximum thickness, in order to extract a quantitative measurement. Clearly it is undesirable from the point of view of sample characterisation to require information about the sample that is to be measured. We suggest two ways to address the necessity of using the tunable parameter phase retrieval algorithm. The first and easiest is to provide better control of the ambient temperature in conjunction with reducing the measurement time so that the impact any temperature fluctuations is minimised. The second is the development of a dynamic phase retrieval algorithm where the crystal transfer function is expanded as a Taylor series in time as well as reciprocal-space. Provided that the temperature fluctuation could be approximated as a linear or quadratic function of time the associated inverse problem may be tractable.

We have demonstrated that the Green's function retrieval technique can be applied to crystallographic data. The technique can be applied immediately to other linear, shift-invariant complex Green's functions such as the Helmholtz and Schrödinger propagators, the reconstruction of which would be of fundamental interest given their importance in optics, diffraction and quantum mechanics.

Continuing with the technique in crystallography, it is immediately applicable to the characterisation of thin layered films and superior to currently used techniques which involving fitting functions to the measured rocking curve. As the rocking curve represents only half the data the reconstructed crystal structure cannot be determined uniquely without a prior information, a problem which the approach of Chapters 4 and 5 does not suffer from.

The Green's function reconstruction method would significantly benefit by addressing the following two issues. First, extending the theory to remove the requirement of linearity and shift-invariance would significantly increase the range of applicability of this technique. The generalisation to arbitrary Green's functions would allow the investigation of, for example, lenses and arbitrary crystalline structures. Removing the requirement of linearity and shift-invariance would be a formidable theoretical accomplishment however.

From a practical standpoint the weak-object design could be improved so that

there was significantly more refraction through large angles. This would allow the reconstruction to probe a wider range of reciprocal space in a single measurement further maximising a significant advantage this approach has over conventional serial measurement processes such as X-ray diffractometry. The characterisation of the weak object would be best carried out using a method other than propagation based phase contrast phase retrieval because the Fresnel rings in the power spectrum of the wavefield incident on the crystal represent regions where the spatial frequency of the Green's function cannot be reconstructed.

The registration of the images that serve as the inputs to the Green's function reconstruction algorithm must be aligned with sub-pixel accuracy. The process of aligning these images is labour intensive and time consuming. Future reconstructions would be expedited by attaching fiducial markers with feature sizes the same as the detector pixel size to the weak object in the form of a simplex. Image registration could, under those circumstances, be automated which would massively increase the rate at which reconstructions could be processed.

## 6.3 Summary

This thesis reported the development of two quantitative extensions to analyser-based phase contrast imaging with hard X-rays. In particular, we have shown that it is possible to perform quantitative phase retrieval on ABI images measured using an extended incoherent source and developed a new approach which allows complex Green's functions associated with linear, shift-invariant imaging systems to be reconstructed. For both of these applications experiments were conducted to demonstrate the validity of the approach.

The work that is presented in this thesis is immediately applicable to the problem of characterising the crystalline structure of thin layered films. The Green's function reconstruction technique is generalisable to other linear, shift-invariant Green's functions such as the Schrödinger and Helmholtz propagators. Improvements to the technique could focus on removing the requirement of linear, shift-invariance although this is a formidable problem.

Whilst ABI has been implemented using incoherent sources the practice is not widespread. Our research shows the most significant impediment to widespread use of ABI as a quantitative characterisation tool for use with a rotating anode source is the prohibitive exposure time. Further investigation of the optimal tradeoff between contrast and exposure time for given source-monochromator configurations is required

to make ABI practicable with extended incoherent X-ray sources.

# Bibliography


Afanas'ev, A. M. and Fanchenko, S. S. (1986). Recovery of profiles of damaged regions of discontinuity in thin subsurface layers from X-ray diffraction data. *Sov. Phys. Dokl.*, 31(4):280–2. (Cited on page 82.)

Afanas'ev, A. M. and Fanchenko, S. S. (1988). On the X-ray analysis of thin subsurface layers. Bicrystal diffraction analogues. *Acta Cryst. A*, A44:25–33. doi:10.1107/S0108767387008158. (Cited on pages 82 and 91.)

Afanas'ev, A. M., Fanchenko, S. S., and Maslov, A. V. (1990). On the equivalent strain and damage distributions of thin subsurface layers in the triple-crystal X-ray diffractometry. *Phys. Stat. Sol. A*, 117(2):341–50. doi:10.1002/pssa.2211170203. (Cited on page 83.)

Afanas'ev, A. M. and Kohn, V. G. (1971). Dynamical theory of X-ray diffraction in crystals with defects. *Acta Cryst. A*, A27(pt.5):421–30. doi:10.1107/S0567739471000962. (Cited on pages 36, 37, 38, 39, 40, 41, 147 and 150.)

Afanas'ev, A. M. and Kon, V. G. (1978). External photoeffect in the diffraction of X-rays in a crystal with a perturbed layer. *Sov. Phys. JETP*, 47(1):154–161. (Cited on page 83.)

Afanas'ev, A. M., Kovalchuk, M. V., Kovev, E. K., and Kohn, V. G. (1977). X-ray diffraction in a perfect crystal with disturbed surface layer. *Phys. Stat. Sol. A*, 42(1):415–22. doi:10.1002/pssa.2210420148. (Cited on page 83.)

Allman, B. E., McMahon, P. J., Nugent, K. A., Paganin, D., Jacobson, D. L., Arif, M., and Werner, S. A. (2000). Phase radiography with neutrons. *Nature*, 408:158–159. doi:10.1038/35041626. (Cited on page 14.)

Anderson, E. H. (2006). Specialized electron beam nanolithography for EUV and X-ray diffractive optics. *Quantum Electron.*, 42(1):27–35. (Cited on page 79.)

Aoki, S., Hoshino, M., and Watanabe, N. (2007). Application of a Zernike-type phase contrast hard X-ray microscope to microtomography. *J. X-ray Sci. Tech.*, 15(2):65–72. Available from: http://iospress.metapress.com/content/e315t076k8320103/. (Cited on page 8.)

Arfelli, F., Assante, M., Bonvicini, V., Bravin, A., Cantatore, G., Castelli, E., dalla Palma,

L., di Michiel, M., Longo, R., Olivo, A., Pani, S., Pontoni, D., Poropat, P., Prest, M., Rashevsky, A., Tromba, G., Vacchi, A., Vallazza, E., and Zanconati, F. (1998). Low-dose phase contrast X-ray medical imaging. *Phys. Med. Biol.*, 43(10):2845–52. doi:10.1088/0031-9155/43/10/013. (Cited on pages 16 and 50.)

Arfelli, F., Bonvicini, V., Bravin, A., Cantatore, G., Castelli, E., Dalla Palma, L., Di Michiel, M., Fabrizioli, M., Longo, R., Menk, R., Olivo, A., Pani, S., Pontoni, D., Poropat, P., Prest, M., Rashevsky, A., Ratti, M., Rigon, L., Tromba, G., Vacchi, A., Vallazza, E., and Zanconati, F. (2000). Mammography with synchrotron radiation: phase-detection techniques. *Rad.*, 215(1):286–93. Available from: http://radiology.rsnajnls.org/cgi/content/abstract/215/1/286. (Cited on page 16.)

Ashkin, M. and Kuriyama, M. (1966). Quantum theory of X-rays diffraction by a crystal. *J. Phys. Soc. Jap.*, 21(8):1549–1558. doi:10.1143/JPSJ.21.1549. (Cited on page 35.)

Attwood, D. (2000). *Soft X-rays and Extreme Ultraviolet Radiation: Principles and Application*. University Press, Cambridge. (Cited on pages 24, 27 and 50.)

Authier, A. (2005). *Dynamical Theory of X-Ray Diffraction*. Oxford University Press, Oxford, revised edition. (Cited on pages 29, 34, 35, 36, 37, 38, 40, 41, 83, 92 and 111.)

Bache, M., Magatti, D., Ferri, F., Gatti, A., Brambilla, E., and Lugiato, L. A. (2006). Coherent imaging of a pure phase object with classical incoherent light. *Phys. Rev. A*, 73(5):053802. doi:10.1103/PhysRevA.73.053802. (Cited on page 11.)

Baez, A. V. (1961). Fresnel zone plate for optical image formation using extreme ultraviolet and soft X radiation. *J. Opt. Soc. Am.*, 51(4):405–412. Available from: http://www.opticsinfobase.org/abstract.cfm?URI=josa-51-4-405. (Cited on page 8.)

Batterman, B. W. and Cole, H. (1964). Dynamical diffraction of X-rays by perfect crystals. *Rev. Mod. Phys.*, 36(3):681–717. doi:10.1103/RevModPhys.36.681. (Cited on page 34.)

Birkholz, M., Fewster, P. F., and Genzel, C. (2006). *Thin Film Analysis by X-ray Scattering*. Wiley, Weinheim. (Cited on pages 82 and 96.)

Bloch, F. (1928). Quantum mechanics of electrons in crystal lattices. *Zeitschrift fur Physik*, 52(7-8):555–600. (Cited on page 38.)

Bogan, M. J., Benner, W. H., Boulet, S., Rohner, U., Frank, M., Barty, A., Seibert, M. M.,

Maia, F., Marchesini, S., Bajt, S., Woods, B., Riot, V., Hau-Riege, S. P., Svenda, M., Marklund, E., Spiller, E., Hajdu, J., and Chapman, H. N. (2008). Single particle X-ray diffractive imaging. *Nano Lett.*, 8(1):310–316. doi:10.1021/nl072728k. (Cited on page 10.)

Bonse, U. and Hart, M. (1965). An X-ray interferometer. *Appl. Phys. Lett.*, 6(8):155–156. doi:10.1063/1.1754212. (Cited on pages 2 and 4.)

Bonse, U. and Hart, M. (1966). An x-ray interferometer with bragg case beam splitting and beam recombination. *Zeitschrift fur Physik*, 194(1):1–17. doi:10.1007/BF01326517. (Cited on page 4.)

Born, M. and Wolf, E. (1999). *Principles of Optics*. Cambridge University Press, Cambridge, seventh (expanded) edition. (Cited on pages 3, 4, 9, 13, 17, 18, 19, 24, 25, 26, 28, 31, 43 and 87.)

Bracewell, R. N. (1986). *The Fourier Transform and Its Applications*. McGraw-Hill, New York. (Cited on pages 26, 43 and 148.)

Brant, W. and Clyde, A. H. (2007). *Fundamentals of Diagnostic Radiology*. Lippicourt, Williams and Wilkins, Philadelphia, 3rd edition. (Cited on page 2.)

Brauer, S., Stephenson, G. B., Sutton, M., Bruning, R., Dufresne, E., Mochrie, S. G. J., Grubel, G., Als-Nielsen, J., and Abernathy, D. L. (1995). X-ray intensity fluctuation spectroscopy observation of critical dynamics in $Fe_3Al$. *Phys. Rev. Lett.*, 74(11):2010–13. doi:10.1103/PhysRevLett.74.2010. (Cited on page 1.)

Bravin, A. (2003). Exploiting the X-ray refraction contrast with an analyser: the state of the art. *J. Phys. D*, 36(10A):24–9. doi:10.1088/0022-3727/36/10A/306. (Cited on page 16.)

Bravin, A., Fiedler, S., and Thomlinson, W. C. (2002). Very-low-dose mammography: new perspectives in diffraction enhanced imaging (DEI) mammography. *Proc. SPIE*, 4682:167–73. doi:10.1117/12.465555. (Cited on pages 16 and 50.)

Bremmer, H. (1952). On the asymptotic evaluation of diffraction integrals with a special view to the theory of defocusing and optical contrast. *Physica*, 18:469–485. doi:10.1016/S0031-8914(52)80079-5. (Cited on pages 13, 20, 51 and 99.)

Briedis, D., Siu, K. K. W., Paganin, D. M., Pavlov, K. M., and Lewis, R. A. (2005). Analyser-based mammography using single-image reconstruction. *Phys. Med. Biol.*, 50(15):3599–611. doi:10.1088/0031-9155/50/15/008. (Cited on page 19.)

Bronnikov, A. V. (1999). Reconstruction formulas in phase-contrast tomography. *Opt. Commun.*, 171(4-6):239–44. doi:10.1016/S0030-4018(99)00575-1. (Cited on

page 18.)

Bronnikov, A. V. (2002). Theory of quantitative phase-contrast computed tomography. *J. Opt. Soc. Am. A*, 19(3):472–480. doi:10.1364/JOSAA.19.000472. (Cited on page 18.)

Bushuev, V. A., Beliaevskaya, E. A., and Ingal, V. N. (1997). Wave-optical description of X-ray phase contrast images of weakly absorbing non-crystalline objects. *Nuovo Cimento D*, 19D(2-4):513–20. (Cited on pages 15, 17 and 51.)

Caciuffo, R., Melone, S., Rustichelli, F., and Boeuf, A. (1987). Monochromators for X-ray synchrotron radiation. *Phys. Rep.*, 152(1):1–71. doi:10.1016/0370-1573(87)90080-9. (Cited on pages 55 and 56.)

Campillo, M. and Paul, A. (2003). Long-range correlations in the diffuse seismic coda. *Science*, 299(5606):547–9. doi:10.1126/science.1078551. (Cited on page 75.)

Caticha, A. (1993). Diffraction of X-rays at the far tails of the Bragg peaks. *Phys. Rev. B*, 47(1):76. doi:10.1103/PhysRevB.47.76. (Cited on page 39.)

Cederquist, J. N., Fienup, J. R., Marron, J. C., and Paxman, R. G. (1988). Phase retrieval from experimental far-field speckle data. *Opt. Lett.*, 13(8):619–21. Available from: http://www.opticsinfobase.org/abstract.cfm?URI=ol-13-8-619. (Cited on page 10.)

Chapman, D., Thomlinson, W., Johnston, R. E., Washburn, D., Pisano, E., Gmur, N., Zhong, Z., Menk, R., Arfelli, F., and Sayers, D. (1997). Diffraction enhanced X-ray imaging. *Phys. Med. Biol.*, 42(11):2015–25. doi:10.1088/0031-9155/42/11/001. (Cited on pages 1, 15, 16, 19 and 67.)

Chapman, H., Barty, A., Bogan, M. J., Boutet, S., Frank, M., Hau-Riege, S. P., Marchesini, S., Woods, B. W., Bajt, S., Benner, W. H., London, R. A., Plonjes, E., Kuhlmann, M., Treusch, R., Dusterer, S., Tschentscher, T., Schneider, J. R., Spiller, E., Moller, T., Bostedt, C., Hoener, M., Shapiro, D. A., Hodgson, K. O., Van Der Spoel, D., Burmeister, F., Bergh, M., Caleman, C., Huldt, G., Seibert, M. M., Maia, F. R. N. C., Lee, R. W., Szoke, A., Timneanu, N., and Hajdu, J. (2006). Femtosecond diffractive imaging with a soft-X-ray free-electron laser. *Nature Phys.*, 2(12):839–43. doi:10.1038/nphys461. (Cited on pages 10 and 74.)

Chapman, H. N. (1996). Phase-retrieval X-ray microscopy by Wigner-distribution deconvolution. *Ultramicroscopy*, 66(3-4):153–172. doi:10.1016/S0304-3991(96)00084-8. (Cited on page 9.)

Chapman, H. N., Hau-Riege, S. P., Bogan, M. J., Bajt, S., Barty, A., Boutet, S., March-

esini, S., Frank, M., Woods, B. W., Benner, W. H., London, R. A., Rohner, U., Szoke, A., Spiller, E., Moller, T., Bostedt, C., Shapiro, D. A., Kuhlmann, M., Treusch, R., Plonjes, E., Burmeister, F., Bergh, M., Caleman, C., Huldt, G., Seibert, M. M., and Hajdu, J. (2007). Femtosecond time-delay X-ray holography. *Nature*, 448(7154):676–9. doi:10.1038/nature06049. (Cited on page 11.)

Clauser, J. F. U. S. (1998). Ultrahigh resolution interferometric X-ray imaging. US Patent 5812629. (Cited on pages 6 and 51.)

Cloetens, P., Barrett, R., Baruchel, J., Guigay, J.-P., and Schlenker, M. (1996). Phase objects in synchrotron radiation hard X-ray imaging. *J. Phys. D*, 29(1):133–46. doi:10.1088/0022-3727/29/1/023. (Cited on page 13.)

Coan, P. and Bravin, A. (2007). Analysis of the X-ray refraction using an array-structured detector. *Appl. Phys. Lett.*, 90(18):184106–1. doi:10.1063/1.2736275. (Cited on page 7.)

Coan, P., Pagot, E., Fiedler, S., Cloetens, P., Baruchel, J., and Bravin, A. (2005). Phase-contrast X-ray imaging combining free space propagation and Bragg diffraction. *J. Synchrotron Radiat.*, 12:241–5. doi:10.1107/S0909049504028444. (Cited on page 15.)

Cowley, J. M. (1995). *Diffraction Physics*. North-Holland Publishing Company, Amsterdam, third edition. (Cited on pages 14, 19, 25, 32, 74 and 75.)

Darwin, C. G. (1914a). Roentgen-ray reflection. *Philos. Mag.*, 27:315. (Cited on page 36.)

Darwin, C. G. (1914b). Roentgen-ray reflection. II. *Philos. Mag.*, 27:675. (Cited on page 36.)

Daschner, W., Long, P., Stein, R., Wu, C., and Lee, S. H. (1997). Cost-effective mass fabrication of multilevel diffractive optical elements by use of a single optical exposure with a gray-scale mask on high-energy beam-sensitive glass. *Appl. Opt.*, 36(20):4675–4680. doi:10.1364/AO.36.004675. (Cited on page 79.)

David, C., Nohammer, B., Solak, H. H., and Ziegler, E. (2002). Differential X-ray phase contrast imaging using a shearing interferometer. *Appl. Phys. Lett.*, 81(17):3287–9. doi:10.1063/1.1516611. (Cited on pages 6 and 51.)

Davis, T. J. (1996). X-ray diffraction imaging using perfect crystals. *J. X-ray Sci. Tech.*, 6(4):317–42. doi:10.1006/jxra.1996.0021. (Cited on pages 1 and 16.)

Davis, T. J., Gao, D., Gureyev, T. E., Stevenson, A. W., and Wilkins, S. W. (1995a). Phase-contrast imaging of weakly absorbing materials using hard X-rays. *Nature*,

373(6515):595–8. doi:10.1038/373595a0. (Cited on pages 1, 16, 17 and 82.)

Davis, T. J., Gureyev, T. E., Gao, D., Stevenson, A. W., and Wilkins, S. W. (1995b). X-ray image contrast from a simple phase object. *Phys. Rev. Lett.*, 74(16):3173–6. doi:10.1103/PhysRevLett.74.3173. (Cited on pages 1, 16, 17, 51 and 82.)

De Caro, L., Giannini, C., Pelliccia, D., Mocuta, C., Metzger, T. H., Guagliardi, A., Cedola, A., Burkeeva, I., and Lagomarsino, S. (2008). In-line holography and coherent diffractive imaging with X-ray waveguides. *Phys. Rev. B*, 77(8):081408–1. doi:10.1103/PhysRevB.77.081408. (Cited on page 11.)

De Caro, L., Giannini, C., and Tapfer, L. (1997). Generalized Laue dynamical theory for X-ray reflectivity at low and high incidence angles on strained multilayers. *Phys. Rev. B*, 56(15):9744. doi:10.1103/PhysRevB.56.9744. (Cited on page 39.)

De Haan, V. O., Van Well, A. A., Adenwalla, S., and Felcher, G. P. (1995). Retrieval of phase information in neutron reflectometry. *Phys. Rev. B*, 52(15):10831–3. doi:10.1103/PhysRevB.52.10831. (Cited on page 10.)

De Jonge, M. D., Hornberger, B., Holzner, C., Legnini, D., Paterson, D., McNulty, I., Jacobsen, C., and Vogt, S. (2008). Quantitative phase imaging with a scanning transmission X-ray microscope. *Phys. Rev. Lett.*, 100(16):163902. doi:10.1103/PhysRevLett.100.163902. (Cited on page 9.)

De Jonge, M. D., Vogt, S., Legnini, D., McNulty, I., Rau, C., Paterson, D., Hornberger, B., Holzner, C., and Jacobsen, C. (2007). A method for phase reconstruction from measurements obtained using a configured detector with a scanning transmission X-ray microscope. *Nucl. Inst. Meth. Phys. A*, 582(1):218–220. doi:10.1016/j.nima.2007.08.111. (Cited on page 9.)

Develis, J. B. and Parrent, G. B., J. (1967). Transfer function for cascaded optical systems. *J. Opt. Soc. Am.*, 57(12):1486–1490. Available from: http://www.opticsinfobase.org/abstract.cfm?URI=josa-57-12-1486. (Cited on page 42.)

Di Fabrizio, E., Cojoc, D., Cabrini, S., Kaulich, B., Susini, J., Facci, P., and Wilhein, T. (2003). Diffractive optical elements for differential interference contrast X-ray microscopy. *Opt. Express*, 11(19):2278–2288. Available from: http://www.opticsexpress.org/abstract.cfm?URI=oe-11-19-2278. (Cited on page 1.)

Dicke, R. H. (1968). Scatter-hole camera for X-rays and $\gamma$-rays. *Astrophys. J*, 153:L101. (Cited on page 7.)

Dierker, S. B., Pindak, R., Fleming, R. M., Robinson, I. K., and Berman, L. (1995).

X-ray photon correlation spectroscopy study of Brownian motion of gold colloids in glycerol. *Phys. Rev. Lett.*, 75(3):449. doi:10.1103/PhysRevLett.75.449. (Cited on page 1.)

Dilanian, R. A., Nikulin, A. Yu., Darahanau, A. V., Hester, J., and Zaumseil, P. (2006). Application of phase-retrieval X-ray diffractometry to carbon doped SiGe(C)/Si(C) superlattice structures. II. High resolution reconstruction using neural network root finder technique. *J. Appl. Phys.*, 99(11):113526–1. doi:10.1063/1.2201447. (Cited on page 83.)

Eisebitt, S., Luning, J., Schlotter, W. F., Lorgen, M., Hellwig, O., Eberhardt, W., and Stohr, J. (2004). Lensless imaging of magnetic nanostructures by X-ray spectroholography. *Nature*, 432(7019):885–888. doi:10.1038/nature03139. (Cited on page 1.)

Erko, A. I., Aristov, V. V., and Vidal, B. (1996). *Diffraction X-ray Optics*. Institute of Physics, London. (Cited on page 8.)

Evans, J. P. (2004). X-ray imaging for security applications. *Proc. SPIE*, 5199:26–36. doi:10.1117/12.515134. (Cited on page 2.)

Ewald, P. P. (1916). Optics of crystals. *Ann. Phys.-Berlin*, 354(1):1–38. doi:10.1002/andp.19163540102. (Cited on page 36.)

Ewald, P. P. (1917). Zur begründung der kristalloptik. III. Röntgenstrahlen. *Ann. Phys.-Berlin*, 359(24):519. doi:10.1002/andp.19173592402. (Cited on page 36.)

Ewald, P. P. (1969). Introduction to the dynamical theory of X-ray diffraction. *Acta Cryst. A*, A25(1):103–8. doi:10.1107/S0567739469000155. (Cited on page 35.)

Ewald, P. P. (1979). A review of my papers on crystal optics 1912 to 1968. *Acta Cryst. A*, A35(1):1–9. doi:10.1107/S0567739479000024. (Cited on page 36.)

Faulkner, H. M. L. and Rodenburg, J. M. (2004). Movable aperture lensless transmission microscopy: a novel phase retrieval algorithm. *Phys. Rev. Lett.*, 93(2):023903–1. doi:10.1103/PhysRevLett.93.023903. (Cited on pages 10 and 11.)

Feder, R. and Light, T. B. (1972). A determination of the thermal expansion of pure Ge and a measurement of the differential thermal expansion of a Ge-GaAs thin layer couple. *J. Appl. Phys.*, 43(7):3114. doi:10.1063/1.1661668. (Cited on page 58.)

Fenimore, E. E. and Cannon, T. M. (1978). Coded aperture imaging with uniformly redundant arrays. *Appl. Opt.*, 17(3):337–347. Available from: http://ao.osa.org/abstract.cfm?URI=ao-17-3-337. (Cited on page 7.)

Fewster, P. F. (2003). *X-ray Scattering from Semiconductors*. Imperial College Press,

London, 2nd rev. edition. (Cited on page 82.)

Fewster, P. F. (2005). A 'static' high-resolution X-ray diffractometer. *J. Appl. Cryst.*, 38:62–8. doi:10.1107/S0021889804026822. (Cited on page 84.)

Fienup, J. R. (1982). Phase retrieval algorithms: a comparison. *Appl. Opt.*, 21(15):2758–69. Available from: http://www.opticsinfobase.org/abstract.cfm?URI=ao-21-15-2758. (Cited on page 11.)

Fienup, J. R., Crimmins, T. R., and Holsztynski, W. (1982). Reconstruction of the support of an object from the support of its autocorrelation. *J. Opt. Soc. Am.*, 72(5):610–624. Available from: http://www.opticsinfobase.org/abstract.cfm?URI=josa-72-5-610. (Cited on page 11.)

Förster, E., Goetz, K., and Zaumseil, P. (1980). Double crystal diffractometry for the characterization of targets for laser fusion experiments. *Krist. Tech.*, 15(8):937–945. doi:10.1002/crat.19800150812. (Cited on pages 1, 8, 15, 16, 17, 51 and 82.)

Foster, A. S. and Hofer, W. A. (2006). *Scanning Probe Microscopy*. Springer, New York. (Cited on page 79.)

Fox, P. J., Mackin, T. R., Turner, L. D., Colton, I., Nugent, K. A., and Scholten, R. E. (2002). Noninterferometric phase imaging of a neutral atomic beam. *J. Opt. Soc. Am. B*, 19(8):1773–6. doi:10.1364/JOSAB.19.001773. (Cited on page 14.)

Gabor, D. (1948). A new microscopic principle. *Nature*, 161:777–778. doi:10.1038/161777a0. (Cited on page 18.)

Gaffney, K. J. and Chapman, H. N. (2007). Imaging atomic structure and dynamics with ultrafast X-ray scattering. *Science*, 316(5830):1444–8. doi:10.1126/science.1135923. (Cited on page 1.)

Gahl, C., Azima, A., Beye, M., Deppe, M., Dobrich, K., Hasslinger, U., Hennies, F., Melnikov, A., Nagasono, M., Pietzsch, A., Wolf, M., Wurth, W., and Fohlisch, A. (2008). A femtosecond X-ray optical cross-correlator. *Nat. Photon.*, 2(3):165–169. doi:10.1038/nphoton.2007.298. (Cited on page 74.)

Geissler, M. S. (2004). Patterning: Principles and some new developments. *Adv. Mater.*, 16(15):1249–1269. doi:10.1002/adma.200400835. (Cited on page 79.)

Gerchberg, R. W. and Saxton, W. O. (1972). A practical algorithm for the determination of phase from image and diffraction plane pictures. *Optik*, 35(2):237–46. (Cited on page 11.)

Gibbs, J. W. (1898). Fourier series. *Nature*, 59(1522):200. doi:10.1038/059200b0. (Cited on page 102.)

Goncharskii, A. V., Kolpakov, A. V., and Stepanov, A. A. (1992). *Inverse Problems in X-Ray Diffraction*. Latvian University, Riga. (Cited on pages 17 and 82.)

Good, R. H. (1999). *Classical Electromagnetism*. Saunders College Publishing, Orlando. (Cited on pages 24 and 25.)

Goodman, J. W. (2000). *Statistical Optics*. Wiley-Interscience, New York. (Cited on pages 28 and 33.)

Goodman, J. W. (2004). *Introduction to Fourier Optics*. Roberts & Company, Denver, 3rd edition. (Cited on pages 77 and 83.)

Google (2008). Google scholar - advanced search. Available from: http://scholar.google.com.au/advanced_scholar_search?hl=en&lr=. (Cited on page 95.)

Grella, R. (1982). Fresnel propagation and diffraction and paraxial wave equation. *J. Opt.*, 13(6):367–74. doi:10.1088/0150-536X/13/6/006. (Cited on page 34.)

Guigay, J. P. (1977). Fourier transform analysis of Fresnel diffraction patterns and in-line holograms. *Optik*, 49(1):121–125. (Cited on page 32.)

Guigay, J. P., Pagot, E., and Cloetens, P. (2007). Fourier optics approach to X-ray analyser-based imaging. *Opt. Commun.*, 270(2):180–8. doi:10.1016/j.optcom.2006.09.072. (Cited on page 19.)

Gullikson, E. (2008). Index of refraction. Available from: http://henke.lbl.gov/optical_constants/getdb2.html. (Cited on page 54.)

Gureyev, T. E., Mayo, S., Wilkins, S. W., Paganin, D., and Stevenson, A. W. (2001). Quantitative in-line phase-contrast imaging with multienergy X-rays. *Phys. Rev. Lett.*, 86(25):5827. doi:10.1103/PhysRevLett.86.5827. (Cited on page 14.)

Gureyev, T. E. and Nugent, K. A. (1996). Phase retrieval with the transport-of-intensity equation. II. Orthogonal series solution for nonuniform illumination. *J. Opt. Soc. Am. A*, 13(8):1670. Available from: http://www.opticsinfobase.org/abstract.cfm?URI=josaa-13-8-1670. (Cited on page 18.)

Gureyev, T. E. and Nugent, K. A. (1997). Rapid quantitative phase imaging using the transport of intensity equation. *Opt. Commun.*, 133(1-6):339–46. doi:10.1016/S0030-4018(96)00454-3. (Cited on page 18.)

Gureyev, T. E., Raven, C., Snigirev, A., Snigireva, I., and Wilkins, S. W. (1999). Hard x-ray quantitative non-interferometric phase-contrast imaging. *Proc. SPIE*, 3659(I):356–364. doi:10.1117/12.349510. (Cited on page 18.)

Gureyev, T. E., Roberts, A., and Nugent, K. A. (1995). Phase retrieval with the transport-of-intensity equation: matrix solution with use of Zernike polynomials. *J.*

*Opt. Soc. Am. A*, 12(9):1932–41. Available from: http://www.opticsinfobase.org/abstract.cfm?URI=josaa-12-9-1932. (Cited on page 18.)

Gureyev, T. E. and Wilkins, S. W. (1997). Regimes of X-ray phase-contrast imaging with perfect crystals. *Nuovo Cimento D*, 19D(2-4):545–52. (Cited on pages 16 and 148.)

Harker, D. and Kasper, J. S. (1948). Phases of Fourier coefficients directly from crystal diffraction data. *Acta Cryst.*, 1:70–75. doi:10.1107/S0365110X4800020X. (Cited on page 10.)

Hart, M. and Lang, A. R. (1961). Direct determination of X-ray phase relationships through simultaneous reflections. *Phys. Rev. Lett.*, 7:120–121. doi:10.1103/PhysRevLett.7.120. (Cited on page 83.)

Hartwig, J. (2001). Hierarchy of dynamical theories of X-ray diffraction for deformed and perfect crystals. *J. Phys. D*, 34:70–7. doi:10.1088/0022-3727/34/10A/315. (Cited on pages 37, 38 and 39.)

Hasnah, M., Oltulu, O., Zhong, Z., and Chapman, D. (2002). Application of absorption and refraction matching techniques for diffraction enhanced imaging. *Rev. Sci. Instrum.*, 73:1657. doi:10.1063/1.1445831. (Cited on page 97.)

Hasnah, M. O., Parham, C., Pisano, E. D., Zhong, Z., Oltulu, O., and Chapman, D. (2005). Mass density images from the diffraction enhanced imaging technique. *Med. Phys.*, 32(2):549–52. doi:10.1118/1.1852794. (Cited on page 79.)

Herman, G. T. (1980). *Image Reconstruction from Projections*. Academic Press. (Cited on page 89.)

Hirai, T., Yamada, H., Sasaki, M., Hasegawa, D., Morita, M., Oda, Y., Takaku, J., Hanashima, T., Nitta, N., Takahashi, M., and Murata, K. (2006). Refraction contrast 11 ×-magnified X-ray imaging of large objects by MIRRORCLE-type table-top synchrotron. *J. Synchrotron Radiat.*, 13:397–402. doi:10.1107/S0909049506027026. (Cited on page 50.)

Holy, V. and Fewster, P. F. (2003). Dynamical diffraction in layered systems - a quest for the final formula. *J. Phys. D*, 36(10A):A5–A8. doi:10.1088/0022-3727/36/10A/302. (Cited on page 39.)

Hornberger, B., De Jonge, M. D., Feser, M., Holl, P., Holzner, C., Jacobsen, C., Legnini, D., Paterson, D., Rehak, P., Struder, L., and Vogt, S. (2008). Differential phase contrast with a segmented detector in a scanning X-ray microprobe. *J. Synchrotron Radiat.*, 15(4):355–362. doi:10.1107/S0909049508008509. (Cited on page 7.)

Hubbell, J. H. (1982). Photon mass attenuation and energy-absorption coefficients from 1 kev to 20 MeV. *Int. J. Appl. Radiat. Isot.*, 33:1269–1290. (Cited on page 65.)

Hwa Shik, Y. and Suk-Won, J. (2006). Hard X-ray microscopy with Zernike phase contrast. *J. Microsc.*, 223:53–6. doi:10.1111/j.1365-2818.2006.01592.x. (Cited on page 8.)

Hwa Shik, Y. and Tae Joo, S. (2007). A study of the human hair structure with a Zernike phase contrast X-ray microscope. *J. Microsc.*, 223(1):107–9. doi:10.1111/j.1365-2818.2007.01833.x. (Cited on page 8.)

Ingal, V. N. and Beliaevskaya, E. A. (1995). X-ray plane-wave topography observation of the phase contrast from a non-crystalline object. *J. Phys. D*, 28(11):2314–17. doi:10.1088/0022-3727/28/11/012. (Cited on pages 1, 16, 17, 51 and 82.)

Jackson, J. D. (1998). *Classical Electrodynamics*. Wiley, New York, third edition. (Cited on page 75.)

Johnson, I., Jefimovs, K., Bunk, O., David, C., Dierolf, M., Gray, J., Renker, D., and Pfeiffer, F. (2008). Coherent diffractive imaging using phase front modifications. *Phys. Rev. Lett.*, 100(15):155503–1. doi:10.1103/PhysRevLett.100.155503. (Cited on page 10.)

Kaganer, V. M. (2007). Crystal truncation rods in kinematical and dynamical X-ray diffraction theories. *Phys. Rev. B*, 75(24):245425–1. doi:10.1103/PhysRevB.75.245425. (Cited on page 39.)

Kaganer, V. M. (2008). Structure of $Fe_3Si$ /GaAs(001) epitaxial films from X-ray crystal truncation rods. *Phys. Rev. B*, 75:125325. doi:10.1103/PhysRevB.77.125325. (Cited on page 39.)

Kapteyn, H., Cohen, O., Christov, I., and Murnane, M. (2007). Harnessing attosecond science in the quest for coherent X-rays. *Science*, 317(5839):775–778. doi:10.1126/science.1143679. (Cited on page 27.)

Kasevich, M. A. (2002). Coherence with atoms. *Science*, 298(5597):1363–1368. doi:10.1126/science.1079430. (Cited on page 74.)

Kato, N. (1963). Dynamical diffraction theory of waves in distorted crystals. II. Perturbation theory. *Acta Cryst.*, 16(L2):282–290. doi:10.1107/S0365110X6300075X. (Cited on page 37.)

Keyrilainen, J., Fernandez, M., and Suortti, P. (2002). Refraction contrast in X-ray imaging. *Nucl. Inst. Meth. Phys. A*, 488(1-2):419–27. doi:10.1016/S0168-9002(02)00442-4. (Cited on page 51.)

Kirz, J. (1974). Phase zone plates for X-rays and the extreme UV. *J. Opt. Soc. Am. A*, 64(3):301–9. Available from: http://www.opticsinfobase.org/abstract.cfm?URI=josa-64-3-301. (Cited on page 8.)

Kitchen, M. J., Paganin, D., Lewis, R. A., Yagi, N., Uesugi, K., and Mudie, S. T. (2004). On the origin of speckle in X-ray phase contrast images of lung tissue. *Phys. Med. Biol.*, 49(18):4335–48. Available from: http://dx.doi.org/10.1088/0031-9155/49/18/010. (Cited on page 1.)

Kitchen, M. J., Pavlov, K. M., Hooper, S. B., Vine, D. J., Siu, K. K. W., Wallace, M. J., Siew, M. L. L., Yagi, N., Uesugi, K., and Lewis, R. A. (2008). Simultaneous acquisition of dual analyser-based phase contrast X-ray images for small animal imaging. *Euro. J. Radiol.*, In Press, Corrected Proof. doi:10.1016/j.ejrad.2008.04.028. (Cited on page 14.)

Kitchen, M. J., Pavlov, K. M., Siu, K. K. W., Menk, R. H., Tromba, G., and Lewis, R. A. (2007). Analyser-based phase contrast image reconstruction using geometrical optics. *Phys. Med. Biol.*, 52(14):4171–87. doi:10.1088/0031-9155/52/14/010. (Cited on page 19.)

Kley, E.-B. (1997). Continuous profile writing by electron and optical lithography. *Microelectron. Eng.*, 34(3-4):261–298. doi:10.1016/S0167-9317(97)00186-X. (Cited on page 79.)

Kohn, V. G., Kovalchuk, M. V., Imamov, R. M., and Lobanovich, E. F. (1981). The method of integral characteristics in X-ray diffraction studies of the structure of the surface layers of single crystals. *Phys. Stat. Sol. A*, 64(2):435–42. doi:10.1002/pssa.2210640203. (Cited on page 83.)

Kolpakov, A. V., Bushuev, V. A., and Kuz'min, R. N. (1978). Dielectric permittivity in the X-ray region. *Soviet Physics Uspekhi*, 21(11):959. doi:10.1070/PU1978v021n11ABEH005717. (Cited on page 29.)

Kolpakov, A. V., Khapachev, Y., Kuznetsov, G. F., and Kuz'min, R. N. (1977). X-ray diffraction in a thin crystal with a linear variation of lattice period. *Kristall.*, 22(3):473–80. (Cited on pages 15 and 91.)

Kolpakov, A. V. and Punegov, V. I. (1985). X-ray diffraction in a crystal with a linear lattice parameter variation. *Sol. Stat. Comm.*, 54(7):573–8. doi:10.1016/0038-1098(85)90080-8. (Cited on page 92.)

Kottler, C., David, C., Pfeiffer, F., and Bunk, O. (2007a). A two-directional approach for grating based differential phase contrast imaging using hard X-rays. *Opt. Exp.*,

15(3):1175–1181. doi:10.1364/OE.15.001175. (Cited on page 6.)

Kottler, C., Pfeiffer, F., Bunk, O., Grunzweig, C., Bruder, J., Kaufmann, R., Tlustos, L., Walt, H., Briod, I., Weitkamp, T., and David, C. (2007b). Phase contrast X-ray imaging of large samples using an incoherent laboratory source. *Phys. Stat. Sol. A*, 204(8):2728–33. doi:10.1002/pssa.200675659. (Cited on page 6.)

Kottler, C., Pfeiffer, F., Bunk, O., Grunzweig, C., and David, C. (2007c). Grating interferometer based scanning setup for hard X-ray phase contrast imaging. *Rev. Sci. Instrum.*, 78(4):43710–1. doi:10.1063/1.2723064. (Cited on page 6.)

Koval'chuk, M. V. and Kohn, V. G. (1986). X-ray standing waves, a new method of studying the structure of crystals. *Sov. Phys. - Uspekhi*, 29(5):426–46. (Cited on page 83.)

Koval'chuk, M. V., Liljequist, D., and Kon, V. G. (1986). Electron transport problem in the analysis of photoemission results from experiments with X-ray standing waves. *Sov. Phys. Solid State*, 28(11):1918–22. (Cited on page 83.)

Krug, K., Porra, L., Coan, P., Wallert, A., Dik, J., Coerdt, A., Bravin, A., Elyyan, M., Reischig, P., Helfen, L., and Baumbach, T. (2008). Relics in medieval altarpieces? Combining X-ray tomographic, laminographic and phase-contrast imaging to visualise thin organic objects in paintings. *J. Synchrotron Radiat.*, 15:55–61. doi:10.1107/S0909049507045438. (Cited on page 16.)

Kuriyama, M. (1967). Theory of X-ray diffraction by a distorted crystal. *J. Phys. Soc. Jap.*, 23(6):1369. doi:10.1143/JPSJ.23.1369. (Cited on page 37.)

Kyutt, R. N., Petrashen', P. V., and Sorokin, L. M. (1980). Strain profiles in ion-doped silicon obtained from X-ray rocking curves. *Phys. Stat. Sol. A*, 60(2):381–389. doi:10.1002/pssa.2210600207. (Cited on page 82.)

Labeyrie, A. (1970). Attainment of diffraction limited resolution in large telescopes by Fourier analysing speckle patterns in star images. *Astron. Astrophys.*, 6:85–87. Available from: http://adsabs.harvard.edu/full/1970A&A.....6...85L. (Cited on page 10.)

Lalor, E. (1968). Conditions of validity of the angular spectum of plane waves. *J. Opt. Soc. Am. A*, 58(9):1235–1237. Available from: http://www.opticsinfobase.org/abstract.cfm?URI=josa-58-9-1235. (Cited on pages 33 and 43.)

Lee, T.-Y. and Choi, J. (2007). Feasibility of a low-energy X-ray free-electron laser. *J. Synchrotron Radiat.*, 14(6):522–526. doi:10.1107/S0909049507037296. (Cited on page 27.)

Lengeler, B. (2001). Coherence in X-ray physics. *Naturwissenschaften*, 88:249–260. doi:10.1007/s001140100221. (Cited on page 26.)

Lengeler, B. (2007). Coherence. *Appl. Phys. A - Mater.*, A87(3):585–92. doi:10.1007/s00339-007-3974-0. (Cited on page 26.)

Lewis, R. A. (2004). Medical phase contrast X-ray imaging: current status and future prospects. *Phys. Med. Biol.*, 49(16):3573–83. doi:10.1088/0031-9155/49/16/005. (Cited on page 50.)

Lewis, R. A., Rogers, K. D., Hall, C. J., Hufton, A. P., Evans, S., Menk, R., Tromba, G., Arfelli, F., Rigon, L., Olivo, A., Evans, A., Pinder, S. E., Jacobs, E., Ellis, I. O., and Dance, D. R. (2002). Diffraction-enhanced imaging: improved contrast and lower dose X-ray imaging. *Proc. SPIE*, 4682:286–97. doi:10.1117/12.465570. (Cited on page 16.)

Majkrzak, C. F. and Berk, N. F. (1995). Exact determination of the phase in neutron reflectometry. *Phys. Rev. B*, 52(15):10827–30. doi:10.1103/PhysRevB.52.10827. (Cited on page 83.)

Majkrzak, C. F., Berk, N. F., Silin, V., and Meuse, C. W. (2000). Experimental demonstration of phase determination in neutron reflectometry by variation of the surrounding media. *Physica B*, 283:248–52. doi:10.1016/S0921-4526(99)01985-7. (Cited on page 83.)

Mandel, L. and Wolf, E. (1995). *Optical Coherence and Quantum Optics*. Cambridge University Press, Cambridge. (Cited on pages 3, 25, 27, 28, 33 and 46.)

Marchesini, S. (2007a). Erratum: A unified evaluation of iterative projection algorithms for phase retrieval. *Rev. Sci. Instrum.*, 78(4):049901. doi:10.1063/1.2736942. (Cited on page 11.)

Marchesini, S. (2007b). A unified evaluation of iterative projection algorithms for phase retrieval. *Rev. Sci. Instrum.*, 78(1):011301. doi:10.1063/1.2403783. (Cited on page 11.)

Margaritondo, G. (2002). *Elements of Synchrotron Light: for Biology, Chemistry and Medical Research*. Oxford University Press, New York. (Cited on page 27.)

Mayo, S. C., Davis, T. J., Gureyev, T. E., Miller, P. R., Paganin, D., Pogany, A., Stevenson, A. W., and Wilkins, S. W. (2003a). X-ray phase-contrast microscopy and microtomography. *Opt. Exp.*, 11(19):2289–2302. Available from: http://www.opticsinfobase.org/abstract.cfm?URI=oe-11-19-2289. (Cited on pages 18 and 51.)

Mayo, S. C., Miller, P. R., Wilkins, S. W., Davis, T. J., Gao, D., Gureyev, T. E., Paganin, D., Parry, D. J., Pogany, A., Robb, T., and Stevenson, A. W. (2002a). Phase-contrast X-ray projection microscopy for materials characterisation. *Materials Forum*, 26:15–19. (Cited on page 50.)

Mayo, S. C., Miller, P. R., Wilkins, S. W., Davis, T. J., Gao, D., Gureyev, T. E., Paganin, D., Parry, D. J., Pogany, A., and Stevenson, A. W. (2002b). Quantitative X-ray projection microscopy: phase-contrast and multi-spectral imaging [in SEM]. *J. Microsc.*, 207:79–96. doi:10.1046/j.1365-2818.2002.01046.x. (Cited on pages 14 and 21.)

Mayo, S. C., Miller, P. R., Wilkins, S. W., Davis, T. J., Gao, D., Gureyev, T. E., Paganin, D., Parry, D. J., Pogany, A., and Stevenson, A. W. (2003b). Applications of phase-contrast X-ray microscopy in an SEM. *J. Phys. IV, Proc.*, 104:543–6. doi:10.1051/jp4:20030140. (Cited on page 51.)

McNulty, I., Kirz, J., Jacobsen, C., Anderson, E. H., Howells, M. R., and Kern, D. P. (1992). High-resolution imaging by Fourier transform X-ray holography. *Science*, 256(5059):1009–12. doi:10.1126/science.256.5059.1009. (Cited on page 1.)

Merzbacher, E. (1970). *Quantum Mechanics*. John Wiley & Sons, New York, 2nd edition. (Cited on pages 31 and 87.)

Miao, J., Charalambous, P., Kirz, J., and Sayre, D. (1999). Extending the methodology of X-ray crystallography to allow imaging of micrometre-sized non-crystalline specimens. *Nature*, 400(6742):342–344. doi:10.1038/22498. (Cited on pages 1 and 10.)

Miao, J., Chen, C.-C., Song, C., Nishino, Y., Kohmura, Y., Ishikawa, T., Ramunno-Johnson, D., Lee, T.-K., and Risbud, S. H. (2006). Three-dimensional GaN-$Ga_2O_3$ core shell structure revealed by X-ray diffraction microscopy. *Phys. Rev. Lett.*, 97(21):215503. doi:10.1103/PhysRevLett.97.215503. (Cited on page 10.)

Miao, J., Ishikawa, T., Anderson, E. H., and Hodgson, K. O. (2003). Phase retrieval of diffraction patterns from noncrystalline samples using the oversampling method. *Phys. Rev. B*, 67(17):174104. doi:10.1103/PhysRevB.67.174104. (Cited on page 1.)

Miao, J., Ishikawa, T., Shen, Q., and Earnest, T. (2008). Extending X-ray crystallography to allow the imaging of noncrystalline materials, cells, and single protein complexes. *Ann. Rev. Phys. Chem.*, 59:387–410. doi:10.1146/annurev.physchem.59.032607.093642. (Cited on page 10.)

Minghui, Z., Qing, W., Xia, S., Yongfeng, L., Honglin, L., Jing, C., and Shensheng, H. (2007). Lensless Fourier-transform ghost imaging with classical incoherent light. *Phys. Rev. A*, 75(2):21803–1. doi:10.1103/PhysRevA.75.021803. (Cited on page 11.)

Modregger, P., Lubbert, D., Schafer, P., and Kohler, R. (2006). Magnified X-ray phase imaging using asymmetric Bragg reflection: experiment and theory. *Phys. Rev. B*, 74(5):54107–1. doi:10.1103/PhysRevB.74.054107. (Cited on page 16.)

Modregger, P., Lubbert, D., Schafer, P., and Kohler, R. (2007a). Spatial resolution in Bragg-magnified X-ray images as determined by Fourier analysis. *Phys. Stat. Sol. A*, 204(8):2746–52. doi:10.1002/pssa.200675685. (Cited on page 15.)

Modregger, P., Lubbert, D., Schafer, P., and Kohler, R. (2007b). Two dimensional diffraction enhanced imaging algorithm. *Appl. Phys. Lett.*, 90(19):193501–1. doi:10.1063/1.2737344. (Cited on page 15.)

Modregger, P., Lubbert, D., Schafer, P., Kohler, R., Weitkamp, T., Hanke, M., and Baumbach, T. (2008). Fresnel diffraction in the case of an inclined image plane. *Opt. Exp.*, 16(7):5141–5149. doi:10.1364/OE.16.005141. (Cited on page 32.)

Moller, M. O. (1994). Apparatus function of a five-crystal X-ray diffractometer with a four-reflection monochromator. *J. Appl. Cryst.*, 27(pt 3):369–378. doi:10.1107/S0021889893011069. (Cited on pages 46, 47, 52, 55, 57 and 58.)

Momose, A. (1995). Demonstration of phase-contrast X-ray computed tomography using an X-ray interferometer. *Nucl. Inst. Meth. Phys. A*, 352(3):622–8. doi:10.1016/0168-9002(95)90017-9. (Cited on page 4.)

Momose, A. (2003). Phase-sensitive imaging and phase tomography using X-ray interferometers. *Opt. Exp.*, 11(19):2303–2314. Available from: http://www.opticsinfobase.org/abstract.cfm?URI=oe-11-19-2303. (Cited on page 4.)

Momose, A., Kawamoto, S., Koyama, I., Hamaishi, Y., Takai, H., and Suzuki, Y. (2003). Demonstration of X-ray Talbot interferometry. *Jpn. J. Appl. Phys. 2*, 42(7B):866–8. doi:10.1143/JJAP.42.L866. (Cited on page 6.)

Momose, A., Takeda, T., and Itai, Y. (1995). Phase-contrast X-ray computed tomography for observing biological specimens and organic materials. *Rev. Sci. Instrum.*, 66:1434–6. doi:10.1063/1.1145931. (Cited on pages 4 and 5.)

Myers, G. R., Mayo, S. C., Gureyev, T. E., Paganin, D. M., and Wilkins, S. W. (2007). Polychromatic cone-beam phase-contrast tomography. *Phys. Rev. A*, 76(4):045804–

1. Available from: http://dx.doi.org/10.1103/PhysRevA.76.045804. (Cited on page 18.)

Myers, G. R., Paganin, D. M., Gureyev, T. E., and Mayo, S. C. (2008). Phase-contrast tomography of single-material objects from few projections. *Opt. Exp.*, 16(2):908–919. Available from: http://dx.doi.org/10.1364/OE.16.000908. (Cited on page 18.)

Nakajima, N. (2007). Noniterative phase retrieval from a single diffraction intensity pattern by use of an aperture array. *Phys. Rev. Lett.*, 98(22):223901. doi:10.1103/PhysRevLett.98.223901. (Cited on pages 11 and 12.)

Nesterets, Y. I., Coan, P., Gureyev, T. E., Braving, A., Cloetens, P., and Wilkins, S. W. (2006a). On qualitative and quantitative analysis in analyser-based imaging. *Acta Cryst. A*, 62:296–308. doi:10.1107/S0108767306017843. (Cited on page 19.)

Nesterets, Y. I., Gureev, T. E., Pavlov, K. M., Paganin, D. M., Lewis, R. A., and Wilkins, S. W. (2005a). Comparison of three theoretical approaches to quantitative analyzer-based imaging. *B. Russ. Acad. Sci. Phys.*, 69(2):246–252. (Cited on page 19.)

Nesterets, Y. I. and Wilkins, S. W. (2008). Phase-contrast imaging using a scanning-double-grating configuration. *Opt. Exp.*, 16(8):5849–5867. doi:10.1364/OE.16.005849. (Cited on page 6.)

Nesterets, Ya. I., Gureyev, T. E., Paganin, D., Pavlov, K. M., and Wilkins, S. W. (2004). Quantitative diffraction-enhanced X-ray imaging of weak objects. *J. Phys. D*, 37(8):1262–74. doi:10.1088/0022-3727/37/8/016. (Cited on pages 15, 19, 31, 66, 78, 80, 89 and 155.)

Nesterets, Ya. I., Gureyev, T.E., and Wilkins, S.W. (2005b). Polychromaticity in the combined propagation-based/analyser-based phase-contrast imaging. *J. Phys. D*, 38:4259–4271. doi:10.1088/0022-3727/38/24/001. (Cited on pages 15, 17, 44, 47, 52 and 54.)

Nesterets, Ya. I., Pavlov, K., Paganin, D., and Wilkins, S. W. (2006b). Combined analyser-based and propagation-based phase-contrast imaging of weak objects. *Opt. Commun.*, 259(1):19–31. doi:10.1016/j.optcom.2005.08.055. (Cited on page 15.)

Neuhausler, U., Schneider, G., Ludwig, W., and Hambach, D. (2003). Phase contrast X-ray microscopy at 4 kev photon energy with 60 nm resolution. *J. Phys. D*, 36:A79–A82. doi:10.1088/0022-3727/36/10A/316. (Cited on page 8.)

Nieto-Vesperinas, M. (1991). *Scattering and Diffraction in Physical Optics*. John Wiley

& Sons, New York. (Cited on pages 25 and 33.)

Nikulin, A. Yu. (1998). Uniqueness of the complex diffraction amplitude in X-ray Bragg diffraction. *Phys. Rev. B*, 57(18):11178–83. doi:10.1103/PhysRevB.57.11178. (Cited on page 83.)

Nugent, K. A. (2007). X-ray noninterferometric phase imaging: A unified picture. *J. Opt. Soc. Am. A*, 24(2):536–547. Available from: http://www.opticsinfobase.org/abstract.cfm?URI=josaa-24-2-536. (Cited on page 18.)

Nugent, K. A., Gureyev, T. E., Cookson, D. F., Paganin, D., and Barnea, Z. (1996). Quantitative phase imaging using hard X-rays. *Phys. Rev. Lett.*, 77(14):2961. doi:10.1103/PhysRevLett.77.2961. (Cited on page 13.)

Nugent, K. A., Peele, A. G., Chapman, H. N., and Mancuso, A. P. (2003). Unique phase recovery for nonperiodic objects. *Phys. Rev. Lett.*, 91(20):203902–1. doi:10.1103/PhysRevLett.91.203902. (Cited on pages 10 and 11.)

Nugent, K. A., Peele, A. G., Quiney, H. M., and Chapman, H. N. (2005). Diffraction with wavefront curvature: a path to unique phase recovery. *Acta Cryst. A*, A61:373–81. doi:10.1107/S010876730501055X. (Cited on pages 10 and 11.)

Ojeda-Castañeda, J. and Berriel-Valdos, L. R. (1979). Classification scheme and properties of Schlieren techniques. *Appl. Opt.*, 18(19):3338–3341. Available from: http://www.opticsinfobase.org/abstract.cfm?URI=ao-18-19-3338. (Cited on page 8.)

Ojeda-Castañeda, J. and Gómez-Reino, C., editors (1996). *Selected Papers on Zone Plates*. SPIE Milestone Series. SPIE, Washington. (Cited on page 9.)

Olivo, A., Arfelli, F., Cantatore, G., Longo, R., Menk, R. H., Pani, S., Prest, M., Poropat, P., Rigon, L., Tromba, G., Vallazza, E., and Castelli, E. (2001). An innovative digital imaging set-up allowing a low-dose approach to phase contrast applications in the medical field. *Med. Phys.*, 28(8):1610–19. doi:10.1118/1.1388219. (Cited on page 7.)

Olivo, A. and Speller, R. (2007a). A coded-aperture technique allowing X-ray phase contrast imaging with conventional sources. *Appl. Phys. Lett.*, 91(7):074106–1. doi:10.1063/1.2772193. (Cited on pages 7 and 20.)

Olivo, A. and Speller, R. (2007b). Modelling of a novel x-ray phase contrast imaging technique based on coded apertures. *Phys. Med. Biol.*, 52(22):6555–73. doi:10.1088/0031-9155/52/22/001. (Cited on page 7.)

Olivo, A. and Speller, R. (2007c). Polychromatic phase contrast imaging as a basic

step towards a widespread application of the technique. *Nucl. Inst. Meth. Phys. A*, 580(2):1079–82. doi:10.1016/j.nima.2007.06.066. (Cited on page 7.)

Oltulu, O., Zhong, Z., Hasnah, M., Wernick, M. N., and Chapman, D. (2003). Extraction of extinction, refraction and absorption properties in diffraction enhanced imaging. *J. Phys. D*, 36(17):2152–6. doi:10.1088/0022-3727/36/17/320. (Cited on page 19.)

Orlowski, A. and Paul, H. (1994). Phase retrieval in quantum mechanics. *Phys. Rev. A*, 50(2):921–4. doi:10.1103/PhysRevA.50.R921. (Cited on page 10.)

O'Shea, P. G. and Freund, H. P. (2001). Free-electron lasers: status and applications. *Science*, 292(5523):1853–8. doi:10.1126/science.1055718. (Cited on page 27.)

Paganin, D., Gureyev, T. E., Pavlov, K. M., Lewis, R. A., and Kitchen, M. (2004). Phase retrieval using coherent imaging systems with linear transfer functions. *Opt. Commun.*, 234(1-6):87–105. doi:10.1016/j.optcom.2004.02.015. (Cited on pages 19, 66, 68 and 69.)

Paganin, D. and Nugent, K. A. (1998). Noninterferometric phase imaging with partially coherent light. *Phys. Rev. Lett.*, 80(12):2586–9. doi:10.1103/PhysRevLett.80.2586. (Cited on pages 18 and 101.)

Paganin, D. and Nugent, K. A. (2001). Noninterferometric phase determination. In Hawkes, P. W., Kazan, B., and Mulvey, T., editors, *Advances in Imaging and Electron Physics*, volume 118, pages 86–123. Academic Press, San Diego. (Cited on page 18.)

Paganin, D. M. (2006). *Coherent X-Ray Optics*. Oxford University Press, New York. (Cited on pages 1, 30, 33, 44, 82 and 100.)

Paganin, D. M., Mayo, S. C., Gureyev, T. E., Miller, P. R., and Wilkins, S. W. (2002). Simultaneous phase and amplitude extraction from a single defocused image of a homogeneous object. *J. Microsc.*, 206:33–40. doi:10.1046/j.1365-2818.2002.01010.x. (Cited on pages 18, 79 and 100.)

Pagot, E., Cloetens, P., Fiedler, S., Bravin, A., Coan, P., Baruchel, J., Hartwig, J., and Thomlinson, W. (2003). A method to extract quantitative information in analyzer-based X-ray phase contrast imaging. *Appl. Phys. Lett.*, 82(20):3421–3. doi:10.1063/1.1575508. (Cited on page 19.)

Papoulis, A. (1962). *The Fourier Integral and its Applications*. McGraw-Hill, New York. (Cited on page 18.)

Patel, N. (2002). Shorter, brighter, better. *Nature*, 415(6868):110–111. doi:10.1038/415110a. (Cited on page 74.)

Pauli, W. (1980). *General Principles of Quantum Mechanics*. Springer, Berlin. (Cited on page 10.)

Pavlov, K. M., Gureyev, T. E., Paganin, D., Nesterets, Ya.I., Kitchen, M., Siu, K. K. W., Gillam, J. E., Uesugi, K., Yagi, N., Morgan, M. J., and Lewis, R. A. (2005). Unification of analyser-based and propagation-based X-ray phase-contrast imaging. *Nucl. Instrum. Meth. Phys. Res. A*, 548:163–168. doi:10.1016/j.nima.2005.03.084. (Cited on page 15.)

Pavlov, K. M., Gureyev, T. E., Paganin, D., Nesterets, Ya. I., Morgan, M. J., and Lewis, R. A. (2004). Linear systems with slowly varying transfer functions and their application to X-ray phase-contrast imaging. *J. Phys. D*, 37(19):2746–50. doi:10.1088/0022-3727/37/19/021. (Cited on pages 15, 19, 66 and 79.)

Pavlov, K. M., Kewish, C. M., Davis, J. R., and Morgan, M. J. (2001). A variant on the geometrical optics approximation in diffraction enhanced tomography. *J. Phys. D*, 34(10A):168–72. doi:10.1088/0022-3727/34/24/701. (Cited on page 19.)

Pavlov, K. M., Paganin, D. M., Vine, D. J., and Kirste, L. (2007). Wide angle X-ray dynamical diffraction by deformed crystals: Recurrence relations. *Phys. Stat. Sol. A*, 204(8):2613–2619. doi:10.1002/pssa.200675663. (Cited on page 39.)

Peele, A. and Nugent, K. (2003). X-ray vortex beams: A theoretical analysis. *Opt. Exp.*, 11(19):2315–2322. Available from: http://www.opticsexpress.org/abstract.cfm?URI=oe-11-19-2315. (Cited on page 1.)

Peele, A. G., Mancuso, A. P., Tran, C. Q., Paterson, D., McNulty, I., Hayes, J. P., and Nugent, K. A. (2005). Phase retrieval from coherent soft X-ray optics. *J. Electron. Spectrosc.*, 144-147:1171–1173. doi:10.1016/j.elspec.2005.01.065. (Cited on page 1.)

Peele, A. G., McMahon, P. J., Paterson, D., Tran, C. Q., Mancuso, A. P., Nugent, K. A., Hayes, J. P., Harvey, E., Lai, B., and McNulty, I. (2002). Observation of an X-ray vortex. *Opt. Lett.*, 27(20):1752–1754. doi:10.1364/OL.27.001752. (Cited on page 1.)

Penning, P. (1966). Theory of X-ray diffraction in unstrained and lightly strained perfect crystals. *Phil. Res. Rep. Supl.*, 5:102 pp. (Cited on page 37.)

Petrashen', P. V. (1974). Application of the Riemann method to the calculation of the diffraction of X-rays in a crystal with a quadratic displacement field. *Sov. Phys. Solid State*, 15(10):2096–2097. (Cited on pages 41 and 90.)

Petrashen', P. V. (1975). Determination of deformation of a doped thin film by

diffraction methods. *Sov. Phys. Solid State*, 17(9):1882–1883. (Cited on page 82.)

Petrashen', P. V. and Chukhovskii, F. N. (1989). Restoration of the phase of an X-ray wave diffracted in a single-crystal layered structure. *Sov. Phys. Dokl.*, 34(11):957–959. (Cited on page 83.)

Pfeiffer, F., Bech, M., Bunk, O., Kraft, P., Eikenberry, E. F., Bronnimann, C., Grunzweig, C., and David, C. (2008). Hard X-ray dark-field imaging using a grating interferometer. *Nature Mat.*, 7(2):134–137. doi:10.1038/nmat2096. (Cited on pages 6 and 51.)

Pfeiffer, F., Bunk, O., David, C., Bech, M., Le Duc, G., Bravin, A., and Cloetens, P. (2007a). High-resolution brain tumor visualization using three-dimensional X-ray phase contrast tomography. *Phys. Med. Biol.*, 52(23):6923–6930. doi:10.1088/0031-9155/52/23/010. (Cited on page 6.)

Pfeiffer, F., Bunk, O., Schulze-Briese, C., Diaz, A., Weitkamp, T., David, C., Van Der Veen, J. F., Vartanyants, I., and Robinson, I. K. (2005). Shearing interferometer for quantifying the coherence of hard X-ray beams. *Phys. Rev. Lett.*, 94(16):164801. doi:10.1103/PhysRevLett.94.164801. (Cited on page 6.)

Pfeiffer, F., Kottler, C., Bunk, O., and David, C. (2007b). Hard X-ray phase tomography with low-brilliance sources. *Phys. Rev. Lett.*, 98(10):108105–1. doi:10.1103/PhysRevLett.98.108105. (Cited on page 6.)

Pfeiffer, F., Weitkamp, T., Bunk, O., and David, C. (2006). Phase retrieval and differential phase-contrast imaging with low-brilliance X-ray sources. *Nature Phys.*, 2(4):258–261. doi:10.1038/nphys265. (Cited on pages 6, 7, 20, 21 and 51.)

Photon Production Laboratory, Ltd. (2008). Operational theory (http://www.photon-production.co.jp/e/ppl-introduction.html). Available from: http://www.photon-production.co.jp/e/PPL-Introduction.html. (Cited on page 50.)

Pietsch, U., Holý, V., and Baumbach, T. (2004). *High-Resolution X-ray Scattering*. Springer-Verlag, New York, 2nd edition. (Cited on pages 36, 57 and 82.)

Pikuz, S. A., Shelkovenko, T. A., Sinars, D. B., Chandler, K. M., and Hammer, D. A. (2001). Phase-contrast X-ray radiography using X pinch radiation. *Proc. SPIE*, 4504:234–239. doi:10.1117/12.448471. (Cited on page 51.)

Pinsker, Z. G. (1978). *Dynamical Scattering of X-rays in Crystals*, volume 3 of *Springer series in Solid-State Physics*. Springer-Verlag, Berlin. (Cited on page 34.)

Podorov, S. G., Faleev, N. N., Pavlov, K. M., Paganin, D. M., Stepanov, S. A., and Förster, E. (2006). A new approach to wide-angle dynamical X-ray diffraction by deformed

crystals. *J. Appl. Cryst.*, 39:652–655. doi:10.1107/S0021889806025696. (Cited on pages 37 and 39.)

Podorov, S. G., Holzer, G., Forster, E., and Faleev, N. N. (1998). Semidynamical solution of the inverse problem of X-ray Bragg diffraction on multilayered crystals. *Phys. Stat. Sol. A*, 169(1):9–16. doi:10.1002/(SICI)1521-396X(199809)169:1<9::AID-PSSA9>3.0.CO;2-U. (Cited on page 83.)

Podorov, S. G., Holzer, G., Forster, E., and Faleev, N. N. (1999). Fourier analysis of X-ray rocking curves from superlattices. *Phys. Stat. Sol. B*, 213(2):317–24. doi:10.1002/(SICI)1521-3951(199906)213:2<317::AID-PSSB317>3.3.CO;2-J. (Cited on page 83.)

Podorov, S. G., Pavlov, K. M., and Paganin, D. M. (2007). A non-iterative reconstruction method for direct and unambiguous coherent diffractive imaging. *Opt. Express*, 15(16):9954–9962. doi:10.1364/OE.15.009954. (Cited on page 11.)

Podorov, S. G. and Punegov, V. I. (1999). Iterative solution of the inverse problem of dynamic diffraction in inhomogeneous crystals. *Tech. Phys.*, 44(3):257–60. (Cited on page 83.)

Podorov, S. G., Punegov, V. I., and Kusikov, V. A. (1994). Solution of the inverse problem of kinematic X-ray diffraction by nonuniform crystal structures. *Phys. Solid State*, 36(3):454–8. (Cited on pages 83 and 91.)

Pogany, A., Gao, D., and Wilkins, S. W. (1997). Contrast and resolution in imaging with a microfocus X-ray source. *Rev. Sci. Instrum.*, 68(7):2774–82. doi:10.1063/1.1148194. (Cited on pages 13, 14, 19 and 51.)

Quiney, H. M., Peele, A. G., Cai, Z., Paterson, D., and Nugent, K. A. (2006). Diffractive imaging of highly focused X-ray fields. *Nature Phys.*, 2(2):101–4. doi:10.1038/nphys218. (Cited on page 10.)

Quiney, H. M., Williams, G. J., and Nugent, K. A. (2008). Non-iterative solution of the phase retrieval problem using a single diffraction measurement. *Opt. Exp.*, 16(10):6896–6903. doi:10.1364/OE.16.006896. (Cited on page 12.)

Rayleigh, L. (1881). On copying diffraction gratings and some phenomena connected therewith. *Philos. Mag.*, 11:196–205. (Cited on page 6.)

Rigon, L., Abrami, A., Arfelli, F., Barroso, R. C., Bergamaschi, A., Bille, F., Bregant, P., Brizzi, F., Casarin, K., Castelli, E., Chenda, V., Palma, L. D., Dreossi, D., Fava, C., Longo, R., Mancini, L., Menk, R. H., Montanari, F., Olivo, A., Pani, S., Pillon, A., Quai, E., Kaiser, S. R., Rokvic, T., Tonutti, M., Tromba, G., Vascotto, A., Venanzi, C.,

Zanconati, F., Zanetti, A., and Zanini, F. (2005). Medical applications of synchrotron radiation at the SYRMEP beamline of ELETTRA. *Nucl. Inst. Meth. Phys. A*, 548(1-2):221–7. doi:10.1016/j.nima.2005.03.093. (Cited on page 16.)

Rigon, L., Arfelli, F., and Menk, R.-H. (2007a). Generalized diffraction enhanced imaging to retrieve absorption, refraction and scattering effects. *J. Phys. D*, 40(10):3077–3089. doi:10.1088/0022-3727/40/10/011. (Cited on page 19.)

Rigon, L., Arfelli, F., and Menk, R. H. (2007b). Three-image diffraction enhanced imaging algorithm to extract absorption, refraction, and ultrasmall-angle scattering. *Appl. Phys. Lett.*, 90(11):114102–1. doi:10.1063/1.2713147. (Cited on page 19.)

Rigon, L., Besch, H.-J., Arfelli, F., Menk, R.-H., Heitner, G., and Plothow-Besch, H. (2003). A new DEI algorithm capable of investigating sub-pixel structures. *J. Phys. D*, 36(10A):107–12. doi:10.1088/0022-3727/36/10A/322. (Cited on page 19.)

Rigon, L., Zhong, Z., Arfelli, F., Menk, R.-H., and Pillon, A. (2002). Diffraction enhanced imaging utilizing different crystal reflections at ELETTRA and NSLS. *Proc. SPIE*, 4682:255–266. doi:10.1117/12.465567. (Cited on page 15.)

Roberts, R. B. (1981). Thermal expansion reference data: silicon 300 - 850 k. *J. Phys. D*, 14:L163–6. doi:10.1088/0022-3727/14/10/003. (Cited on page 58.)

Robinson, I. K. and Tweet, D. J. (1992). Surface X-ray diffraction. *Rep. Prog. Phys.*, 55(5):599–651. doi:10.1088/0034-4885/55/5/002. (Cited on page 55.)

Rodenburg, J. M. (2001). A simple model of holography and some enhanced resolution methods in electron microscopy. *Ultramicroscopy*, 87(3):105–121. doi:10.1016/S0304-3991(00)00097-8. (Cited on page 10.)

Rodenburg, J. M. and Faulkner, H. M. L. (2004). A phase retrieval algorithm for shifting illumination. *Appl. Phys. Lett.*, 85(20):4795–4797. doi:10.1063/1.1823034. (Cited on pages 10 and 11.)

Rodenburg, J. M., Hurst, A. C., and Cullis, A. G. (2007a). Transmission microscopy without lenses for objects of unlimited size. *Ultramicroscopy*, 107(2-3):227–31. doi:10.1016/j.ultramic.2006.07.007. (Cited on page 10.)

Rodenburg, J. M., Hurst, A. C., Cullis, A. G., Dobson, B. R., Pfeiffer, F., Bunk, O., David, C., Jefimovs, K., and Johnson, I. (2007b). Hard X-ray lensless imaging of extended objects. *Phys. Rev. Lett.*, 98(3):034801. doi:10.1103/PhysRevLett.98.034801. (Cited on page 10.)

Röntgen, W. C. (1896). On a new kind of rays. *Nature*, 53:274–276. (Cited on page 2.)

Rullhusen, P. (1992). Novel X-ray sources produced by electron beams. *EPAC92*.

*Third European Particle Accelerator Conference*, pages 240–4. Available from: http://epaper.kek.jp/e92/PDF/EPAC1992_0240.PDF. (Cited on page 27.)

Saleh, B. E. A. and Teich, M. C. (1991). *Fundamentals of Photonics.* John WIley & Sons, New York. (Cited on page 9.)

Sandberg, R. L., Paul, A., Raymondson, D. A., Hadrich, S., Gaudiosi, D. M., Holtsnider, J., Tobey, R. I., Cohen, O., Murnane, M. M., Kapteyn, H. C., Song, C., Miao, J., Liu, Y., and Salmassi, F. (2007). Lensless diffractive imaging using tabletop coherent high-harmonic soft X-ray beams. *Phys. Rev. Lett.*, 99(9):098103. doi:10.1103/PhysRevLett.99.098103. (Cited on page 11.)

Schenk, T., Thi, H. N., Gastaldi, J., Reinhart, G., Cristiglio, V., Mangelinck-Noel, N., Klein, H., Hartwig, J., Grushko, B., Billia, B., and Baruchel, J. (2005). Application of synchrotron X-ray imaging to the study of directional solidification of aluminium-based alloys. *J. Cryst. Growth*, 275(1-2):201–8. doi:10.1016/j.jcrysgro.2004.10.081. (Cited on page 50.)

Schuster, M. and Herres, N. (1994). An introduction to high-resolution X-ray diffractometry. (Cited on pages 37 and 55.)

Shpyrko, O. G., Isaacs, E. D., Logan, J. M., Feng, Y., Aeppli, G., Jaramillo, R., Kim, H. C., Rosenbaum, T. F., Zschack, P., Sprung, M., Narayanan, S., and Sandy, A. R. (2007). Direct measurement of antiferromagnetic domain fluctuations. *Nature*, 447(7140):68–71. doi:10.1038/nature05776. (Cited on page 1.)

Slusky, S. E. G. and Macrander, A. T. (1987). X-ray diffraction with a four-reflection monochromator. *J. Appl. Cryst.*, 20:522–8. doi:10.1107/S0021889887086096. (Cited on pages 46, 47, 52, 55 and 57.)

Snigirev, A. A., Snigireva, I. I., Kohn, V. G., Kuznetsov, S., and Schelokov, I. A. (1995). On the possibilities of X-ray phase contrast microimaging by coherent high-energy synchrotron radiation. *Rev. Sci. Instrum.*, 66(12):5486–92. doi:10.1063/1.1146073. (Cited on page 13.)

Somenkov, V. A., Tkalich, A. K., and Shil'stein, S. S. (1991). Refraction contrast in X-ray introscopy. *Sov. Phys. Tech. Phys.*, 36(11):1309–11. (Cited on pages 1, 16, 17, 51 and 82.)

Speriosu, V. S., Glass, H. L., and Kobayashi, T. (1979). X-ray determination of strain and damage distributions in ion-implanted layers. *Appl. Phys. Lett.*, 34(9):539–42. doi:10.1063/1.90879. (Cited on page 82.)

Stadler, L.-M., Gutt, C., Autenrieth, T., Leupold, O., Rehbein, S., Chushkin, Y.,

and Grubel, G. (2008). Hard X-ray holographic diffraction imaging. *Phys. Rev. Lett.*, 100(24):245503–4. doi:10.1103/PhysRevLett.100.245503. (Cited on page 11.)

Stepanov, A. A. (1994). Fourier-coefficient method of X-ray rocking-curve interpretation. *J. Appl. Cryst.*, 27:7–12. doi:10.1107/S0021889893005618. (Cited on page 83.)

Stepanov, S. A. (2008). X-ray dynamical diffraction data on the web (http://sergey.gmca.aps.anl.gov/). Available from: http://sergey.gmca.aps.anl.gov/cgi/WWW_form.exe?template=x0h_form.htm. (Cited on pages 27, 53 and 56.)

Stevenson, A. W., Gao, D., Gureyev, T. E., Pogany, A., and Wilkins, S. W. (1999). Hard X-ray phase-contrast imaging with a microfocus source. *AIP Conf. Proc.*, pages 641–8. (Cited on page 51.)

Talbot, H. F. (1836). Facts relating to optical science. No IV. *Philos. Mag.*, 9:401–407. (Cited on page 6.)

Tanaka, T., Honda, C., Matsuo, S., Noma, K., Oohara, H., Nitta, N., Ota, S., Tsuchiya, K., Sakashita, Y., Yamada, A., Yamasaki, M., Furukawa, A., Takahashi, M., and Murata, K. (2005). The first trial of phase contrast imaging for digital full-field mammography using a practical molybdenum X-ray tube. *Invest Radiol*, 40(7):385–96. Available from: http://www.ncbi.nlm.nih.gov/entrez/query.fcgi?cmd=Retrieve&db=PubMed&dopt=Citation&list_uids=15973129. (Cited on pages 13 and 20.)

Teague, M. R. (1983). Deterministic phase retrieval: a Green's function solution. *J. Opt. Soc. Am. A*, 73(11):1434–41. Available from: http://www.opticsinfobase.org/abstract.cfm?URI=josa-73-11-1434. (Cited on pages 13 and 18.)

Thibault, P., Dierolf, M., Menzel, A., Bunk, O., David, C., and Pfeiffer, F. (2008). High-resolution scanning X-ray diffraction microscopy. *Science*, 321(5887):379–382. doi:10.1126/science.1158573. (Cited on page 1.)

Thurn-Albrecht, T., Steffen, W., Patkowski, A., Meier, G., Fischer, E. W., GrÃijbel, G., and Abernathy, D. L. (1996). Photon correlation spectroscopy of colloidal palladium using a coherent X-ray beam. *Phys. Rev. Lett.*, 77(27):5437. doi:10.1103/PhysRevLett.77.5437. (Cited on page 1.)

Toth, R., Fourmaux, S., Ozaki, T., Servol, M., Kieffer, J. C., Kincaid, R. E., and Krol, A. (2007). Evaluation of ultrafast laser-based hard X-ray sources for phase-contrast

imaging. *Phys. Plasmas*, 14(5):053506. doi:10.1063/1.2730778. (Cited on page 50.)

Toth, R., Kieffer, J. C., Fourmaux, S., Ozaki, T., and Krol, A. (2005). In-line phase-contrast imaging with a laser-based hard X-ray source. *Rev. Sci. Instrum.*, 76(8):83701–1. doi:10.1063/1.1989407. (Cited on page 50.)

van Cittert, P. H. (1934). Die Wahrscheinliche Schwingungsverteilung in Einer von Einer Lichtquelle Direkt Oder Mittels Einer Linse Beleuchteten Ebene. *Physica*, 1(1-6):201–210. doi:10.1016/S0031-8914(34)90026-4. (Cited on page 28.)

van der Veen, F. and Pfeiffer, F. (2004). Coherent X-ray scattering. *J. Phys.- Condens. Mat.*, 16(28):5003–30. doi:10.1088/0953-8984/16/28/020. (Cited on page 26.)

van Tiggelen, B. A. (2003). Green function retrieval and time reversal in a disordered world. *Phys. Rev. Lett.*, 91(24):243904–1. doi:10.1103/PhysRevLett.91.243904. (Cited on page 75.)

Vartanyants, I. A., Koval'chuk, M. V., Kon, V. G., Nikolaenko, A. M., and Kharitonov, I. Y. (1989). Direct determination of the phase of the reflection amplitude by means of standing X-ray waves. *JETP Lett.*, 49(11):726–30. (Cited on page 83.)

Vartanyants, I. A., Robinson, I. K., Onken, J. D., Pfeifer, M. A., Williams, G. J., Pfeiffer, F., Metzger, H., Zhong, Z., and Bauer, G. (2005). Coherent X-ray diffraction from quantum dots. *Phys. Rev. B*, 71(24):245302–1. doi:10.1103/PhysRevB.71.245302. (Cited on page 10.)

Vine, D. J., Paganin, D. M., Pavlov, K. M., Kräußlich, J., Wehrhan, O., Uschmann, I., and Förster, E. (2007a). Analyzer-based phase contrast and phase retrieval using a rotating anode X-ray source. *Appl. Phys. Lett.*, 91:254110. doi:10.1063/1.2825426. (Cited on page 49.)

Vine, D. J., Paganin, D. M., Pavlov, K. M., and Podorov, S. G. (2007b). Unambiguous reconstruction of the complex amplitude reflection coefficient of a laterally homogeneous crystal using analyser-based phase contrast imaging. *J. Appl. Cryst.*, 40:650–657. doi:10.1107/S0021889807021097. (Cited on page 73.)

Volkov, V. V., Zhu, Y., and De Graef, M. (2002). A new symmetrized solution for phase retrieval using the transport of intensity equation. *Micron*, 33(5):411–416. doi:10.1016/S0968-4328(02)00017-3. (Cited on page 102.)

von Laue, M. (1931). Die dynamische Theorie der Röntgenstrahlinterferenzen in neuer Form. *Ergreb. Exakt. Naturwiss.*, 10:133–158. (Cited on page 36.)

von Laue, M. (1960). *Röntgenstrahl-Interferenzen*. Akademische Verlagsgesellschaft, Frankfurt am Main. (Cited on page 36.)

Wachtman, J. B. (1993). *Characterization of Materials*. Butterworth-Heinemann, Boston. (Cited on page 2.)

Walther, A. (1963). The question of phase retrieval in optics. *Opt. Acta*, 10(1):41–49. doi:10.1080/713817747. (Cited on page 10.)

Wapenaar, K. (2004). Retrieving the elastodynamic Green's function of an arbitrary inhomogeneous medium by cross correlation. *Phys. Rev. Lett.*, 93(25):254301–1. doi:10.1103/PhysRevLett.93.254301. (Cited on page 75.)

Wapenaar, K., Slob, E., and Snieder, R. (2006). Unified Green's function retrieval by cross correlation. *Phys. Rev. Lett.*, 97(23):234301–1. doi:10.1103/PhysRevLett.97.234301. (Cited on page 75.)

Weierstall, U., Chen, Q., Spence, J., Howells, M., Isaacson, M., and Panepucci, R. (2002). Image reconstruction from electron and x-ray diffraction patternsusing iterative algorithms: Theory and experiment. *Ultramicroscopy*, 90(2):171–195. doi:10.1016/S0304-3991(01)00134-6. (Cited on page 10.)

Weitkamp, T., Diaz, A., Nohammer, B., Pfeiffer, F., Rohbeck, T., Cloetens, P., Stampanoni, M., and David, C. (2004). Hard X-ray phase imaging and tomography with a grating interferometer. *Proc. SPIE*, 5535:137–42. doi:10.1117/12.569643. (Cited on pages 6 and 51.)

Wernick, M. N., Wirjadi, O., Chapman, D., Zhong, Z., Galatsanos, N. P., Yongyi, Y., Brankov, J. G., Oltulu, O., Anastasio, M. A., and Muehleman, C. (2003). Multiple-image radiography. *Phys. Med. Biol.*, 48(23):3875–95. doi:10.1088/0031-9155/48/23/006. (Cited on page 19.)

Wilkins, S. W. (1995). Simplified conditions and configurations for phase contrast imaging with hard X-rays. Australian Patent Application PN 2112/95; PCT Patent Application PCT/AU96/00178. (Cited on page 20.)

Wilkins, S. W., Gureyev, T. E., Gao, D., Pogany, A., and Stevenson, A. W. (1996). Phase-contrast imaging using polychromatic hard X-rays. *Nature*, 384(6607):335–8. doi:10.1038/384335a0. (Cited on pages 13 and 51.)

Wilkins, S. W., Gureyev, T. E., Mayo, S. C., Nesterets, Y. I., Paganin, D. M., Pogany, A., and Stevenson, A. W. (2007). Hard X-ray phase-contrast imaging for medical applications - physicist's dream or radiologist's mainstream? *AIP Conf. Proc.*, 902:33–6. doi:10.1063/1.2723616. (Cited on page 15.)

Williams, G. J., Quiney, H. M., Dahl, B. B., Tran, C. Q., Peele, A. G., Nugent, K. A., De Jonge, M. D., and Paterson, D. (2007). Curved beam coherent diffractive imaging. *Thin Solid Films*, 515(14):5553–6. doi:10.1016/j.tsf.2006.12.132. (Cited on page 10.)

Williams, G. J., Quiney, H. M., Dhal, B. B., Tran, C. Q., Nugent, K. A., Peele, A. G., Paterson, D., and de Jonge, M. D. (2006). Fresnel coherent diffractive imaging. *Phys. Rev. Lett.*, 97(2):025506–1. doi:10.1103/PhysRevLett.97.025506. (Cited on page 10.)

Wolf, E. (2007). *Introduction to the Theory of Coherence and Polarization of Light*. Cambridge University Press, Cambridge. (Cited on pages 25, 27, 28 and 29.)

Yale, P. B. (1988). *Geometry and Symmetry*. Dover Publications Inc., New York. (Cited on page 107.)

Yamada, H. (2003). Novel X-ray source based on a tabletop synchrotron and its unique features. *Nucl. Inst. Meth. Phys. B*, 199:509–516. doi:10.1016/S0168-583X(02)01593-8. (Cited on page 50.)

Yamada, H., Kitazawa, Y., Kanai, Y., Tohyama, I., Ozaki, T., Sakai, Y., Sak, K., Kleev, A. I., and Bogomolov, G. D. (2001). Development of the hard X-ray source based on a tabletop electron storage ring. *Nucl. Inst. Meth. Phys. A*, 467:122–125. doi:10.1016/S0168-9002(01)00238-8. (Cited on page 50.)

Zachariasen, W. H. (1968). *Theory of X-ray Diffraction in Crystals*. John Wiley & Sons, Inc., New York. (Cited on page 34.)

Zaus, R. (1992). *PhD Thesis*. PhD thesis, Munich University. (Cited on page 27.)

Zernike, F. (1934). Diffraction theory of the knife-edge test and its improved form, the phase-contrast method. *Roy. Astro. Soc. Monthly Notices*, 94:377–384. doi:10.1117/1.1488608. (Cited on page 8.)

Zernike, F. (1938). The concept of degree of coherence and its application to optical problems. *Physica*, 5(8):785–795. doi:10.1016/S0031-8914(38)80203-2. (Cited on page 28.)

Zernike, F. (1942). Phase contrast, a new method for the microscopic observation of transparent objects. I-II. *Physica*, 9:686–698. doi:10.1016/S0031-8914(42)80035-X. (Cited on page 14.)

# Appendix A

## A relationship between reciprocal space ARC and direct space Green's function for thick perfect crystal

The amplitude reflection coefficient of a thick perfect crystal is an important quantity in ABI and this thesis. In Chapters 4 and 5 we compare the reconstructions of this function to its known theoretical form.

In this appendix we present a derivation of the link between the reciprocal and real space representations.

We first begin with some house keeping to get the form of r as presented by Afanas'ev and Kohn (1971)[Eq. 3.24, p.425] into a more manageable form. The ARC for the thick perfect crystal Bragg reflection is (cf. (2.60)),

$$r(\eta') = \frac{1}{2\chi_{\bar{g}}C}[-\eta' + \sqrt{\eta'^2 + \zeta^2}] \tag{1}$$

where $\eta' = \alpha_g\gamma + \chi_0(1-\gamma)$, $\zeta^2 = 4\gamma C^2\chi_g\chi_{\bar{g}}$, $\alpha_g$ is the resonant error associated with the angular deviation from the Bragg angle, $\gamma = \gamma_0/\gamma_g$ is the ratio of the sines of the angles of incident to diffracted waves, C is the polarisation constant, $\chi_g$ and $\chi_{\bar{g}}$ are the Fourier coefficients of the crystal polarisability.

We will introduce the same parameters as Afanas'ev and Kohn (1971),

$$\eta' = \tau A, \tag{2}$$

$$\zeta = -i\tau B, \tag{3}$$

$$\tau = \frac{2\sin 2\theta_B}{k|\gamma_g|} \tag{4}$$

where A and B are,

$$A = k\chi_0\frac{\gamma_0 + |\gamma_g|}{2\sin 2\theta_B} - k\alpha_g\frac{\gamma_0}{2\sin 2\theta_B}, \tag{5}$$

$$B = \frac{kC\sqrt{\chi_g\chi_{\bar{g}}\gamma_0|\gamma_g|}}{\sin 2\theta_B}. \tag{6}$$

We make explicit use of the fact that $\gamma_g < 0$ for Bragg geometry so that now $\gamma = \gamma_0/|\gamma_g|$ and (1) becomes,

$$r(A) = \frac{-\sin 2\theta_B}{k|\gamma_g|\chi_{\bar{g}}C}(A - \sqrt{A^2 - B^2}). \tag{7}$$

Physically A describes the deviation from the Bragg angle such as occurs from rocking the crystal so that $\alpha = 2\omega \sin 2\theta_B$ where $\omega$ is the the small deviation from the Bragg angle (Gureyev and Wilkins, 1997). We expect the argument of r to also have a term which allows for the spatial frequency $\eta = k_x/k$ so that $r = r(A - \eta)$. We choose to work with $\eta$ during the following derivation and we add A in at the end using the Fourier shift theorem (Bracewell, 1986).

Our goal is to solve the following integral (Gureyev and Wilkins, 1997),

$$G(x) = \frac{-\sin 2\theta_B}{k|\gamma_g|\chi_{\bar{g}}C} \int_{-\infty}^{\infty} \left[\eta - \mathrm{sgn}(1+\eta/B)\sqrt{\eta^2 - B^2}\right] \exp(i\eta x) d\eta. \tag{8}$$

We first divide by B and rescale $\eta \to \eta/B$ and $x' = -Bx$ to give[1],

$$G(x') = -\frac{k\chi_g\gamma_0 C}{\sin 2\theta_B} \int_{-\infty}^{\infty} \left[\eta - \mathrm{sgn}(1+\eta)\sqrt{\eta^2 - 1}\right] \exp(-i\eta x') d\eta. \tag{9}$$

We now have the integral into the desired form and we will ignore multiplicative factors until we have solved the integral. To that end we break the integral into three parts,

$$\begin{aligned} I(x') \quad = \quad & \int_{-\infty}^{\infty} \left[\eta - \mathrm{sgn}(1+\eta)\sqrt{\eta^2 - 1}\right] \exp(-i\eta x') d\eta = \\ & \int_{1}^{\infty} \left(\eta - \sqrt{\eta^2 - 1}\right) \exp(-i\eta x') d\eta + \\ & \int_{-1}^{1} \left(\eta - \sqrt{\eta^2 - 1}\right) \exp(-i\eta x') d\eta + \\ & \int_{-\infty}^{-1} \left(\eta + \sqrt{\eta^2 - 1}\right) \exp(-i\eta x') d\eta \end{aligned} \tag{10}$$

and labelling them top down $I_1$, $I_2$ and $I_3$ we consider each in turn.
Beginning with the third integral we substitute $\eta = -\cosh\theta$ to give,

$$I_3(x') = \int_{-\infty}^{-1} \left(\eta + \sqrt{\eta^2 - 1}\right) \exp(-i\eta x') d\eta \tag{11}$$

$$= -\frac{1}{2} \int_{0}^{\infty} \left(1 - e^{-2\theta}\right) \exp(ix' \cosh\theta) d\theta. \tag{12}$$

From (12) we make the further substitution $t = ie^{\theta}$ to give,

$$I_3(x') = -\frac{1}{2} \int_{i}^{i\infty} \left(t^{-1} + t^{-3}\right) \exp\left[\frac{x'}{2}\left(t - t^{-1}\right)\right] dt. \tag{13}$$

[1]We introduce the negative sign in $x'$ because it saves us carrying the negative in the exponent throughout the calculation. Our final result is the sum of two even order Bessel functions of the first kind which, being even, are invariant to the negative sign and so we will eventually ignore it. If we were to continue with the negative sign the contour integral in Figure 1 would need to be reflected about the imaginary axis.

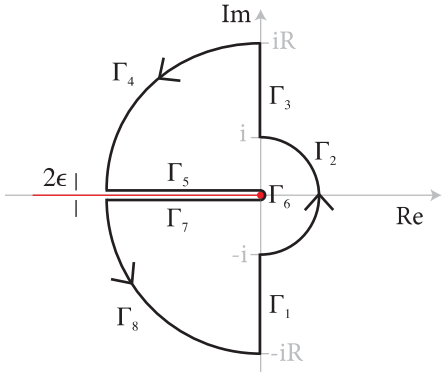


Figure 1: Bessel function contour integral. Direction is as given and the branch cut is indicated in red.

Likewise for $I_1$ we make the substitutions $\eta = \cosh\theta$ then $t = ie^{\theta}$ to give,

$$I_1(x') = -\frac{1}{2}\int_{-i\infty}^{-1} \left(t^{-1} + t^{-3}\right) \exp\left[\frac{x'}{2}\left(t - t^{-1}\right)\right] dt. \tag{14}$$

Finally for $I_2$ we substitute $\eta = \cos\theta$ and $t = ie^{i\theta}$,

$$I_2(x') = -\frac{1}{2}\int_{-i}^{i} \left(t^{-1} + t^{-3}\right) \exp\left[\frac{x'}{2}\left(t - t^{-1}\right)\right] d\theta. \tag{15}$$

We may now reassemble I to give,

$$I(x') = -\frac{1}{2}\int_{-i\infty}^{i\infty} \left(t^{-1} + t^{-3}\right) \exp\left[\frac{x'}{2}\left(t - t^{-1}\right)\right] dt. \tag{16}$$

We would like to make use of the identity,

$$J_n(x') = \frac{1}{2\pi i}\oint \left(t^{-n-1}\right) \exp\left[\frac{x'}{2}\left(t + t^{-1}\right)\right] dt, \tag{17}$$

where $J_n$ is Bessel function of the first kind and order $n$, to rewrite (16) as a sum of Bessel functions. To this end we represent (16) as a contour integral in the complex plane along the path $\Gamma$ in Figure 1. We note that, for this contour integral, in the following we must assume that $x'$ is a positive real quantity[2] and this will be included explicitly in the final result.

Noting that (16) can be expressed as,

$$I(x') = \sum_{i=1}^{3} \int_{\Gamma_i} \left(t^{-1} + t^{-3}\right) \exp\left[\frac{x'}{2}\left(t - t^{-1}\right)\right] dt \tag{18}$$

we now show that

$$\lim_{R\to\infty,\epsilon\to 0} \sum_{i=4}^{8} \int_{\Gamma_i} \left(t^{-1} + t^{-3}\right) \exp\left[\frac{x'}{2}\left(t - t^{-1}\right)\right] dt = 0. \tag{19}$$

[2]The parameter B will be complex, in general. In the following we must assume the imaginary part of B is negligible relative to the real part.

Take the integral,

$$I_4(x') = \int_{\Gamma_4} \left(t^{-1} + t^{-3}\right) \exp\left[\frac{x'}{2}\left(t - t^{-1}\right)\right] dt \tag{20}$$

and parameterise the curve $\Gamma_4$ using $t = R\exp(i\theta)$ so that,

$$I_4(x') = i \lim_{R\to\infty,\epsilon\to 0} \int_{\frac{\pi}{2}}^{\pi-\epsilon} \left(1 - R^{-2}e^{-2i\theta}\right) \exp\left(\frac{x'}{2}\left[Re^{i\theta} - \frac{1}{R}e^{-i\theta}\right]\right) d\theta. \tag{21}$$

As $R \to \infty$ the real term proportional to $R$ in the exponent will dominate however in this quadrant $\cos\theta$ is negative and this integral will vanish. A similar argument applies to $I_8(x')$.

We will now show that $I_5(x') = -I_7(x')$ by introducing the parameterisations $t = \theta \pm i\epsilon$,

$$I_5(x') = \lim_{R\to\infty,\epsilon\to 0} \int_{-R}^{0} \left((\theta + i\epsilon)^{-1} + (\theta + i\epsilon)^{-3}\right) \exp\left(\frac{x'}{z}\left[\theta + i\epsilon - \frac{1}{\theta + i\epsilon}\right]\right), \tag{22}$$

$$I_7(x') = -\lim_{R\to\infty,\epsilon\to 0} \int_{-R}^{0} \left((\theta - i\epsilon)^{-1} + (\theta - i\epsilon)^{-3}\right) \exp\left(\frac{x'}{z}\left[\theta - i\epsilon - \frac{1}{\theta - i\epsilon}\right]\right) \tag{23}$$

where the minus multiplying $I_7$ comes from swapping the limits. We can see that in the limit $\epsilon \to 0$ these integrals will cancel each other.

For $I_6$ we use $t = \epsilon\exp(i\theta)$,

$$I_6(x') = i \lim_{\epsilon\to 0} \int_{\frac{\pi}{2}}^{-\frac{\pi}{2}} \left(1 + (\epsilon e^{i\theta})^{-2}\right) \exp\left(\frac{x'}{2}\left[\epsilon e^{i\theta} - \epsilon^{-1}e^{-i\theta}\right]\right) d\theta. \tag{24}$$

Now, in $I_6$ the term in the exponent inversely proportional to $\epsilon$ will dominate but in the right half-plane $\cos\theta$ is positive and so this integral vanishes in the limit.

These results allow us to express (16) as,

$$I(x') = -i\pi\left(J_0(x') + J_2(x')\right) \tag{25}$$

If we substitute $x' \to Bx$ and include multiplicative factors (cf. (9)) we have,

$$G(x) = i\pi\frac{kC\chi_g\gamma_0}{\sin 2\theta_B}\left(J_0(Bx) + J_2(Bx)\right) H(x) \tag{26}$$

where $H(x)$ is the Heaviside step function which ensures $x$ is positive. Finally, we can include $A$ using the Fourier shift theorem and we have the desired result (cf. Afanas'ev and Kohn (1971)[Eq. 3.22, p. 425]),

$$G(x) = i\pi\frac{kC\chi_g\gamma_0}{\sin 2\theta_B}\left(J_0(Bx) + J_2(Bx)\right) H(x)\exp(iAx) \tag{27}$$

# Appendix B

## Analyser-based phase contrast imaging and phase retrieval using a rotating anode X-ray source.

This appendix presents a reprint of the paper

> "Analyzer-base phase contrast imaging and phase retrieval using a rotating anode X-ray source"
> D. J. Vine, D. M. Paganin, K. M. Pavlov, J. Kraeußlich, O. Wehrhan, I. Uschmann and E. Förster
> *Applied Physics Letters* **91**, 254110 (2007)

This paper presents the results of an experiment conducted at the Institute of Optics and Quantum Electronics, Friedrich-Schiller University, Jena Germany in late 2006. A rotating anode X-ray source is used to create quantitative phase contrast images of a plastic phantom.

The experiment was conceived between myself, Dr David Paganin, Dr Konstantin Pavlov and the experimental design was largely contributed by myself. The collaboration with our German colleagues was initiated through the head of the Institute Professor Eckhardt Förster. Dr Kraeußlich manages the X-ray diffractometers and trained me in their use and together with Mr Frank Perner trained me in the use of the Labview code which I modified to run the shutter and motor controls. Dr Wehrhan trained me in the use and development of the X-ray film and Dr Uschmann built the sample and detector translation stages and the shutter.

I designed and conducted all other aspects of the experiment myself. The post-measurement image processing was my own work and the phase retrieval was performed by myself in collaboration with Drs Paganin and Pavlov. I wrote and produced the article presented in this appendix.

Overall, I estimate my contribution to this paper as 90%.

APPLIED PHYSICS LETTERS **91**, 254110 (2007)

# Analyzer-based phase contrast imaging and phase retrieval using a rotating anode x-ray source

D. J. Vine[a] and D. M. Paganin
*School of Physics, Monash University, Victoria 3800, Australia*

K. M. Pavlov
*School of Physics, Monash University, Victoria 3800, Australia, Monash Centre for Synchrotron Science, Monash University, Victoria 3800, Australia, and School of Science and Technology, University of New England, New South Wales 2350, Australia*

J. Kräußlich, O. Wehrhan, I. Uschmann, and E. Förster
*Institute for Optics and Quantum Electronics, Friedrich-Schiller University, Jena 07743, Germany*

(Received 14 September 2007; accepted 27 November 2007; published online 19 December 2007)

We have performed an analyzer crystal based phase contrast imaging (ABI) experiment using a rotating anode x-ray source. The use of such an incoherent source demonstrates the potential of ABI as a quantitative characterization tool for the laboratory environment. A phase contrast image of a plastic phantom was recorded on high resolution x-ray film and the projected thickness was retrieved from a single image. The projected thickness recovered from the phase contrast image was shown to quantitatively agree with a reference optical microscope measurement. © *2007 American Institute of Physics*. [DOI: 10.1063/1.2825426]

Analyzer-based phase contrast imaging (ABI) is a sensitive method for imaging and quantitative measurement of the internal composition of samples that weakly diffract hard x-rays.[1–21] ABI utilizes diffraction from a perfect crystal to convert small distortions in the wavefront incident on the analyzer into measurable intensity variations of the corresponding diffracted wavefront. ABI experiments using synchrotron x-ray sources are capable of producing high quality images due to the high coherence and large flux of such sources. The use of an incoherent x-ray source with relatively low flux is also capable of producing good quality ABI images.[1–5] In this letter, we show that such images can be analyzed using phase retrieval to yield quantitative measurements of a sample's projected thickness in many practical situations where synchrotron radiation is not available or, as we shall show, necessary.

Recently, there has been considerable interest in developing phase contrast imaging systems that can be implemented in a laboratory using either "tabletop synchrotrons,"[22–24] conventional sealed tube and rotating anode x-ray sources with propagation-based phase contrast,[25] and ABI.[1,2,4,8] The grating interferometer[26,27] has similar source requirements to the ABI method presented here; both are suitable for imaging large areas, and both are sensitive to the one-dimensional transverse phase gradient. The methods use different optical elements: mutually aligned gratings and a single near-perfect crystal, respectively. One of the principal drivers of all of the above work is the potential usefulness of phase contrast techniques and ABI, in particular,[28] for medical applications and, thus, the need for a device that can operate in a clinical environment. The drawback of conventional sources for use in phase contrast experiments is that the radiation they produce is often of insufficient coherence.

The formation of ABI contrast depends critically on the temporal and spatial coherence of the wavefield incident on the sample. In terms of the spatial and temporal coherence, synchrotron radiation is measurably more coherent than a rotating anode with the optical elements described in this letter. The dependence of image contrast on temporal coherence can be understood in relation to the sensitivity of the analyzer crystal on wavelength. If we compare the analyzer crystal's rocking curve measured with monochromatic radiation to that measured with quasimonochromatic radiation, the latter will be broader. Since ABI contrast is proportional to the rocking curve gradient, a broader rocking curve will mean lower contrast. A similar effect is true for fully and partially spatially coherent radiation which implies that a divergent beam will also reduce ABI image contrast. The monochromator crystals increase the spatial coherence of the source by extracting a pseudoplane wave component from the spherical wave produced by a pointlike radiator in the source[29–31] resulting in very low divergence beams. This is equivalent to moving the source to a large distance from the object. The use of Cu $K\alpha 1$ radiation means that the source is quasimonochromatic [$\Delta\lambda/\lambda \approx 3.2 \times 10^{-4}$ (Ref. 32)] and the monochromator essentially collimates the beam. This can be compared to the synchrotron storage ring which is a chaotic, polychromatic source and requires a monochromator and a large source to object distance to provide both spatial and temporal coherence.

In this letter, we demonstrate the implementation of a simple ABI system using a rotating anode source and x-ray film that is used to measure the projected thickness of a plastic phantom. The measured projected thickness is compared to a reference measurement of the phantom found by calculating the projected thickness from an optical microscope image of the phantom's cross section. These independent measurements were found to be in quantitative agreement.

The principles of analyzer-based phase contrast imaging are as follows. Let a planar, monochromated x-ray wavefield illuminate an area of a sample such that the field exiting the sample is a function of the sample's three-dimensional com-

[a]Electronic mail: david.vine@sci.monash.edu.au.

 

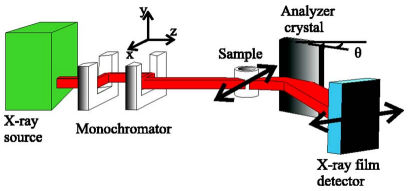


FIG. 1. (Color online) Experimental setup to record an analyzer-based phase contrast image using a rotating anode x-ray source.

plex refractive index,[33] as in Fig. 1. The analyzer crystal is oriented so that the beam in the absence of the sample is incident on the crystal close to the Bragg angle of some suitable reflection. With the sample in the beam, the wavefield will be refracted and, thus, differentially reflected as a function of the refraction angle.[1,2,18,34]

The finite source size will effectively blur the image, meaning that higher resolution images could be obtained by focusing the electron beam to a small spot on the anode; however, for this application, a focal spot of the order of a square millimeter is satisfactory.

The experiment was conducted using a Siemens D5000 x-ray diffractometer and $K\alpha 1$ radiation from a copper rotating anode x-ray source operating at 30 kV/100 mA with focal spot of 0.5 (horizontal) $\times$ 1.0 (vertical) $mm^2$. The monochromator-sample, sample-analyzer crystal, and analyzer-detector distances were 10, 15, and 25 cm, respectively. Two channel-cut crystals forming a four-reflection Ge(220) Bartels-type monochromator were used to collimate the beam, the analyzer crystal used was Ge(220) and the longitudinal and transverse coherence lengths[35,36] of the field after the monochromator $[\Delta\lambda/\lambda \approx 1.5\times 10^{-4}$ (Ref. 37)] were calculated to be $l_l=\lambda^2/\Delta\lambda=1$ $\mu$m and $l_t=\lambda/\Delta\alpha=2.5$ $\mu$m, respectively, where $\Delta\alpha$ is the angular width of the monochromator crystal.

Our sample was the interlocking strip from a resealable plastic bag. The strip cross section is shown in Fig. 2(a) and the corresponding ABI image in Fig. 2(b). The beam size at the sample was approximately $0.2\times 1.5$ $mm^2$ so the image in Fig. 2(b) is a composite of multiple overlayed exposures. The data were acquired over approximately 4 h. The ambient temperature over this time varied within ±0.5 K and was responsible for thermal drift in the analyzer crystal of approximately 1.2 arc sec. The thermal drift (and to a lesser extent, mechanical drift) is evident in the background intensity variation in Fig. 2(b) because it changes the point of the zero-deviation beam on the rocking curve.

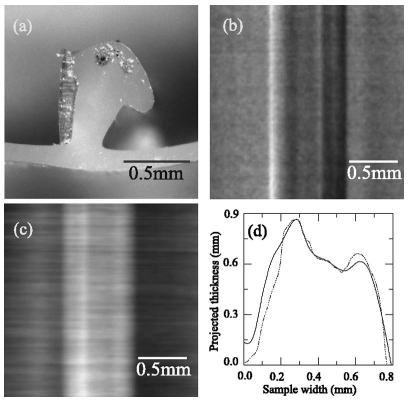


FIG. 2. (a) Optical microscopy image of cross section of plastic test phantom, (b) recorded ABI image of sample in (a), (c) the retrieved projected thickness of (b), and (d) a line profile showing the average projected thickness retrieved from the x-ray data (solid line) and the projected thickness calculated from the cross section shown in (a) (dotted line).

The projected thickness in Fig. 2(c) was retrieved from the ABI image in Fig. 2(b) using a single image phase retrieval algorithm.[14,38] This single image phase retrieval is valid if the following assumptions are satisfied: (i) the object is composed of a single material, (ii) the projection approximation for the object is valid, (iii) the crystal is laterally homogeneous, (iv) imaging can be described using the transfer function formalism, and (v) the refraction angles are small. Under these assumptions, the sample's projected thickness $T(x,y)$ is related to the measured phase contrast intensity image $I_D(x,y)$ in the following way:[14]

$$T(x,y) = -\gamma \log_e \mathbf{F}^{-1}\left[\frac{\mathbf{F}I_D(x,y)}{1+ik_x\tau}\right]. \quad (1)$$

Here, $\mathbf{F}$ is the two-dimensional Fourier transform $\mathbf{F}f(x,y) = 1/2\pi\int\int_{-\infty}^{\infty} f(x,y)\exp -i(xk_x+yk_y)dxdy$, $\gamma$ is a proportionality constant discussed below, and $\tau$ is a real parameter that encompasses the refractive index of the sample and the state of the imaging system. The value for $\tau$ is chosen by inspection when the first derivative contrast evident at the sharp edges of the reconstructed image [Fig. 2(c)] just disappears (see, e.g., Refs. 14 and 38). The use of the "tunable" parameter $\tau$ greatly simplifies the process of retrieving the projected thickness because it makes knowledge of the exact chemical composition, complex refractive index, and state of the imaging system redundant. It is particularly suitable for this experiment because, due to the thermal drift of the analyzer crystal described previously, the state of the imaging system was not constant over the duration of the experiment.

The scale of the retrieved projected thickness is calibrated using the parameter $\gamma$ against an *a priori* known feature size of the object. In this case, we used an independent measurement of the maximum projected thickness and scaled the retrieved projected thickness measurement so that both measurements had the same maximum thickness. The requirement of imaging a single material object may be removed if additional images are collected with the imaging system in a different state (change of wavelength, varying the analyzer crystal rocking angle).[10,14] The quality of the reconstruction could be improved by allowing for Fresnel diffraction in the sample-detector propagation distance.[15,17,39] However, the projected thickness retrieved under the assumption of a negligible propagation distance is evidently suitable for the analysis given here.

The retrieved projected thickness image is shown in Fig. 2(c), and Fig. 2(d) shows a line profile comparison of the projected thickness using x-ray data against a calculated projected thickness using an optical microscopy image of a cross section of the sample. The two measurements quantitatively agree and the discrepancy between the measurements can be attributed to two factors. The first is the lack of temperature control during the experiment which caused the background intensity to vary throughout the experiment. The

second is the destructive testing of the sample that was necessary to record the optical image. The optical measurement process requires a cross section of the sample which must irrevocably damage it, and we are forced to assume that the profile that was measured is a good approximation to that used in the experiment.

In conclusion, we have implemented a simple and accessible method for quantitative analyzer-based phase contrast imaging using a laboratory source. The resulting images demonstrate that, depending on the accuracy and resolution of the required measurement, it is not necessary to have a highly coherent synchrotron source to perform quantitative analyzer-based phase contrast.

D.J.V. acknowledges the German Academic Exchange Service (DAAD) and Frau R. Eberlein, the Australian Research Network for Advanced Materials (ARNAM), Mr. Frank Perner (IOQ), Professor R. Lewis for use of PCDetPak, and the Australian Postgraduate Award. D.J.V., D.M.P., and K.M.P. acknowledge funding from the Australian Research Council (ARC).

[1]E. Förster, K. Goetz, and P. Zaumseil, Krist. Tech. **15**, 937 (1980).
[2]V. N. Ingal and E. A. Beliaevskaya, J. Phys. D **28**, 2314 (1995).
[3]T. J. Davis, D. Gao, T. E. Gureyev, A. W. Stevenson, and S. W. Wilkins, Nature (London) **373**, 595 (1995).
[4]T. J. Davis, T. E. Gureyev, D. Gao, A. W. Stevenson, and S. W. Wilkins, Phys. Rev. Lett. **74**, 3173 (1995).
[5]T. J. Davis, J. X-Ray Sci. Technol. **6**, 317 (1996).
[6]D. Chapman, W. Thomlinson, R. E. Johnston, D. Washburn, E. Pisano, N. Gmur, Z. Zhong, R. Menk, F. Arfelli, and D. Sayers, Phys. Med. Biol. **42**, 2015 (1997).
[7]T. E. Gureyev and S. W. Wilkins, Nuovo Cimento D **19D**, 545 (1997).
[8]V. A. Bushuev, E. A. Beliaevskaya, and V. N. Ingal, Nuovo Cimento D **19D**, 513 (1997).
[9]A. Bravin, J. Phys. D **36**, 424 (2003).
[10]E. Pagot, P. Cloetens, S. Fiedler, A. Bravin, P. Coan, J. Baruchel, J. Hartwig, and W. Thomlinson, Appl. Phys. Lett. **82**, 3421 (2003).
[11]M. N. Wernick, O. Wirjadi, D. Chapman, Z. Zhong, N. P. Galatsanos, Y. Yongyi, J. G. Brankov, O. Oltulu, M. A. Anastasio, and C. Muehleman, Phys. Med. Biol. **48**, 3875 (2003).
[12]L. Rigon, H.-J. Besch, F. Arfelli, R.-H. Menk, G. Heitner, and H. Plothow-Besch, J. Phys. D **36**, A107 (2003).
[13]Ya. I. Nesterets, T. E. Gureyev, D. Paganin, K. M. Pavlov, and S. W. Wilkins, J. Phys. D **37**, 1262 (2004).
[14]D. Paganin, T. E. Gureyev, K. M. Pavlov, R. A. Lewis, and M. Kitchen, Opt. Commun. **234**, 87 (2004).
[15]K. M. Pavlov, T. E. Gureyev, D. Paganin, Ya. I. Nesterets, M. J. Morgan, and R. A. Lewis, J. Phys. D **37**, 2746 (2004).
[16]Ya. I. Nesterets, T. E. Gureyev, and S. W. Wilkins, J. Phys. D **38**, 4259 (2005).
[17]K. M. Pavlov, T. E. Gureyev, D. Paganin, Ya. I. Nesterets, M. Kitchen, K. K. W. Siu, J. E. Gillam, K. Uesugi, N. Yagi, M. J. Morgan, and R. A. Lewis, Nucl. Instrum. Methods Phys. Res. A **548**, 163 (2005).
[18]D. M. Paganin, *Coherent X-ray Optics* (Oxford University Press, New York, 2006), p. 270.
[19]Ya. I. Nesterets, K. Pavlov, D. Paganin, and S. W. Wilkins, Opt. Commun. **259**, 19 (2006).
[20]Ya. I. Nesterets, P. Coan, T. E. Gureyev, A. Bravin, P. Cloetens, and S. W. Wilkins, Acta Crystallogr., Sect. A: Found. Crystallogr. **A62**, 296 (2006).
[21]L. Rigon, F. Arfelli, and R. H. Menk, Appl. Phys. Lett. **90**, 114102 (2007).
[22]H. Yamada, Y. Kitazawa, Y. Kanai, I. Tohyama, T. Ozaki, Y. Sakai, K. Sak, A. I. Kleev, and G. D. Bogomolov, Nucl. Instrum. Methods Phys. Res. A **467**, 122 (2001).
[23]H. Yamada, Nucl. Instrum. Methods Phys. Res. B **199**, 509 (2003).
[24]T. Hirai, H. Yamada, M. Sasaki, D. Hasegawa, M. Morita, Y. Oda, J. Takaku, T. Hanashima, N. Nitta, M. Takahashi, and K. Murata, J. Synchrotron Radiat. **13**, 397 (2006).
[25]C. Honda, H. Ohara, and T. Gido, in *Digital Mammography: Eighth International Workshop, IWDM 2006, Manchester, UK June 18–21, 2006, Proceedings* (Springer, New York, 2006), Vol. 4046, pp. 281–288.
[26]F. Pfeiffer, T. Weitkamp, O. Bunk, and C. David, Nat. Phys. **2**, 258 (2006).
[27]F. Pfeiffer, C. Kottler, O. Bunk, and C. David, Phys. Rev. Lett. **98**, 108105 (2007).
[28]R. A. Lewis, K. D. Rogers, C. J. Hall, A. P. Hufton, S. Evans, R. Menk, G. Tromba, F. Arfelli, L. Rigon, A. Olivo, A. Evans, S. E. Pinder, E. Jacobs, I. O. Ellis, and D. R. Dance, Proc. SPIE **4682**, 286 (2002).
[29]V. Mocella, J. P. Guigay, Y. Epelboin, J. Hartwig, J. Baruchel, and S. Mazuelas, J. Phys. D **32**, 88 (1999).
[30]V. Mocella, Y. Epelboin, and J. P. Guigay, Acta Crystallogr., Sect. A: Found. Crystallogr. **A56**, 308 (2000).
[31]V. Mocella, Y. Epelboin, J. P. Guigay, and J. Hartwig, Acta Crystallogr., Sect. A: Found. Crystallogr. **A57**, 526 (2001).
[32]M. Deutsch and M. Hart, Phys. Rev. B **26**, 5558 (1982).
[33]M. Born and E. Wolf, *Principles of Optics*, 7th ed. (Cambridge University Press, Cambridge, 1999), p. 98.
[34]A. Authier, *Dynamical Theory of X-ray Diffraction* (Oxford University Press, Oxford, 2005), p. 491.
[35]J. Als-Nielsen and D. McMorrow, *Elements of Modern X-ray Physics* (Wiley, Chichester, 2000), p. 24.
[36]U. Pietsch, V. Holý, and T. Baumbach, *High-Resolution X-ray Scattering*, 2nd ed. (Springer, New York, 2004), p. 44.
[37]R. Zaus, Ph.D. thesis, Munich University, 1992, p. 56.
[38]D. Briedis, K. K. W. Siu, D. M. Paganin, K. M. Pavlov, and R. A. Lewis, Phys. Med. Biol. **50**, 3599 (2005).
[39]P. Coan, E. Pagot, S. Fiedler, P. Cloetens, J. Baruchel, and A. Bravin, J. Synchrotron Radiat. **12**, 241 (2005).

# Appendix C

## Unambiguous reconstruction of the amplitude reflection coefficient of a laterally homogeneous crystal using analyzer-based phase contrast imaging

This appendix presents a reprint of the paper

> "Unambiguous reconstruction of the amplitude reflection coefficient of a laterally homogeneous crystal using analyzer-based phase-contrast imaging"
> D. J. Vine, D. M. Paganin, K. M. Pavlov and S. G. Podorov
> *Journal of Applied Crystallography* **40**, 650 (2007)

This paper contains a theoretical development which allows an analyser-based phase contrast image of a known weak object to be inverted to reconstruct the complex amplitude reflection coefficient of the analyser crystal. The reconstruction algorithm is applied to reconstruct the kinematic diffraction ARC for a linearly strained crystal and it is then shown how the crystalline structure may be inferred unambiguously from the experimental data.

The kernel of the idea was conceived during discussions between myself, Dr David Paganin and Dr Konstantin Pavlov. The theory was developed by myself using the formalism developed Dr Nesterets in (Nesterets et al., 2004). The numerical simulations were coded and run by myself. The use of logarithmic derivatives in arriving at Eq. 18 was suggested by Dr Sergey Podorov who also participated in fruitful discussions throughout the research. I also wrote and produced the paper presented in this appendix.

Overall, I estimate my contribution to the work presented in this paper as 90%.

### Errata

Figure 5(c) abscissa largest value should read 10 and not 1.0.
On the RHS of Equation 13 all of the $x$ in the argument of $\Delta E_{in}^2(x, y)$ should be

primed.

Journal of
**Applied Crystallography**
ISSN 0021-8898
Editor: **Gernot Kostorz**

# Unambiguous reconstruction of the complex amplitude reflection coefficient of a laterally homogeneous crystal using analyser-based phase-contrast imaging

**D. J. Vine, D. M. Paganin, K. M. Pavlov and S. G. Podorov**

## research papers

Journal of
**Applied Crystallography**
ISSN 0021-8898

Received 18 January 2007
Accepted 27 April 2007



# Unambiguous reconstruction of the complex amplitude reflection coefficient of a laterally homogeneous crystal using analyser-based phase-contrast imaging

**D. J. Vine,[a]* D. M. Paganin,[a] K. M. Pavlov[a,b] and S. G. Podorov[a]**

[a]School of Physics, Monash University, Victoria 3800, Australia, and [b]Monash Centre for Synchrotron Science, Monash University, Victoria 3800, Australia. Correspondence e-mail: david.vine@sci.monash.edu.au

A theoretical approach is developed to invert analytically a hard X-ray analyser-based phase-contrast image of a known weak object to recover the complex amplitude reflection coefficient (ARC) of a laterally homogeneous crystal. Numerical simulations test the method to recover the ARC from two systems of interest: a thick perfect crystal and a linearly strained thin film. For the latter model, a kinematical diffraction approximation was used to recover the one-dimensional deformation profile from the ARC.

## 1. Introduction

The problem of unambiguously determining the deformation field and chemical composition of layered crystals and thin films from diffraction data is of significant practical importance (Pietsch *et al.*, 2004; Fewster, 2003; Birkholz *et al.*, 2006). X-ray diffraction (XRD) is a standard tool for investigating crystals to determine these properties, but in general both the intensity and the phase variations imparted by the crystal on the diffracted X-ray wavefield must be known to arrive at an unambiguous solution.

In this paper we propose an analytical solution to the problem of recovering the crystal's complex amplitude reflection coefficient (ARC) using an analyser-based X-ray phase-contrast image (Förster *et al.*, 1980; Somenkov *et al.*, 1991; Ingal & Beliaevskaya, 1995; Davis, Gao *et al.*, 1995; Davis, Gureyev *et al.*, 1995; Paganin, 2006). We then derive (within the framework of the kinematical diffraction theory) an unambiguous, analytic solution to the problem of determining the interplanar spacing of a layered crystal from a single two-dimensional intensity measurement using the recovered complex ARC. We present numerical simulations that show the implementation of our method and how the interplanar spacing may be recovered once the complex ARC has been retrieved using our technique.

Before proceeding, let us illustrate the essence of our method by way of a simple example. With reference to Fig. 1(*a*), consider an idealized standard XRD scenario in which a single plane wave $A$ is incident at an angle $\theta$ upon the surface of a laterally homogeneous crystal $C$. The intensity of the reflected plane wave $B$ is then registered using the detector $D$, which need not be position sensitive. The phase of the reflected plane wave is lost, with one performing a series of experiments for a sequence of angles $\theta$, so as to build up the rocking curve of the crystal. Compare this with the 'parallelized' scenario in Fig. 1(*b*), where an incident plane wave $E$ passes through a known weak phase-amplitude screen $F$, to yield a known coherent superposition of plane waves $G_n$ for $n = 1, 2$ *etc.* This coherent superposition of plane waves is then reflected from the surface of the same crystal $C$, with the reflected waves $H_m$ for $m = 1, 2$ *etc.* then mutually interfering to form the two-dimensional analyser-based phase-contrast image that is registered over the surface of the position-sensitive detector $I$. This phase-contrast image evidently contains information regarding both the amplitude and the phase of the complex ARC of the crystal, since (i) the mutual interference of the reflected plane waves is governed by both of these quantities, and (ii) a continuum of incident angles $\theta$ is contained within the field at the exit surface of $F$. The method illustrated in this paper shows how one may solve the inverse problem of determining the complex ARC of the crystal, given a known weak phase-amplitude object $F$, together with the

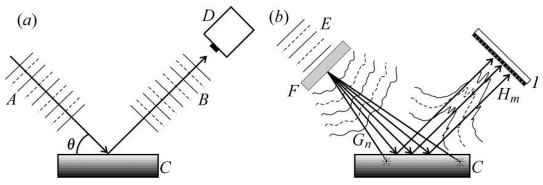


**Figure 1**
(*a*) In an idealized X-ray diffraction experiment a plane wave is diffracted from a laterally homogeneous crystal that is then incident on a point detector, which detects the reflected intensity at a series of angular space points separately. (*b*) Our method illuminates the crystal with a known coherent superposition of plane waves $G_n$. After reflection from the crystal, an area detector records the interference pattern from contributions of each plane wave component $H_m$ (equivalent to measuring the reflectivity of a continuum of angular space points in parallel), thereby recording both phase and intensity modulations imparted by the crystal.

analyser-based phase contrast image of this object registered by the detector.

We now give a brief overview of what has been achieved to solve the problem of determining the interplanar spacing of layered crystals from X-ray diffraction data (Goncharskii *et al.*, 1992). The deformation profile of such crystals can be obtained directly from the rocking curve using fitting procedures (Speriosu *et al.*, 1979; Petrashen', 1975; Kyutt *et al.*, 1980). This method cannot guarantee a unique solution because of the existence of so-called 'crystal analogues', namely crystals of differing structure that have the same reflectivity (Afanas'ev & Fanchenko, 1986, 1988; Afanas'ev *et al.*, 1990). The method of integral characteristics gives the average strain for thin layers (Afanas'ev *et al.*, 1977, 1990; Kohn *et al.*, 1981). The strain profile may be obtained directly from the rocking curve using a discrete form of the kinematic ARC (Stepanov, 1994). Iterative schemes using Fourier analysis of the rocking curve have been proposed for the kinematic (Podorov *et al.*, 1994, 1999), semi-dynamical (Podorov *et al.*, 1998) and dynamical diffraction regimes (Podorov & Punegov, 1999). These schemes are often computationally intensive, slow and prone to stagnation without necessarily achieving the correct solution. Phase retrieval can be implemented using the Hilbert transform (Petrashen' & Chukhovskii, 1989), but the solution is ambiguous and an appropriate algorithm is required to choose the unique solution (Nikulin, 1998; Dilanian *et al.*, 2006). Measuring the distribution of photoemission electrons due to X-ray standing waves in dynamical diffraction may be used to infer the phase (Afanas'ev & Kohn, 1978; Koval'chuk & Kohn, 1986; Koval'chuk *et al.*, 1986). The reliance of standing wave methods on the detection of photoelectrons means that they are limited to investigating near-surface layers where there is an appreciable probability of an electron escaping the crystal. A variant of the standing wave approach measures the distribution of both secondary photoelectrons and the scattered X-rays to find the deformation field in surface layers much smaller than the extinction length (Vartanyants *et al.*, 1989). Alternatively, the phase can be retrieved in multiple-beam diffraction by considering the interference of the diffracted waves in a crystal (Hart & Lang, 1961; Authier, 2005). Neutron reflectometry can recover phase information if the sample is mounted on a known reference layer (Majkrzak & Berk, 1995; Majkrzak *et al.*, 2000).

In contrast to the limitations of the techniques just outlined, the method that we propose gives a non-iterative, analytic solution for the ARC that requires no special sample preparation, is valid for both kinematical and dynamical diffraction regimes, and works with symmetric and asymmetric reflection, and with Bragg and Laue diffraction geometries. Our method also determines the ARC over a wide range of angular space simultaneously and is not susceptible to the problem of crystal analogues; futhermore, the inversion algorithm is fast and robust in the presence of realistic levels of experimental noise.

We require only that (i) the sample crystal be locally laterally homogeneous over the area of X-ray illumination, and (ii) the action of the crystal on the incident X-rays may be modelled using the transfer-function formalism (Paganin, 2006). Notwithstanding the X-ray illumination coherence requirements, our experimental setup is very similar to standard XRD; the only differences are the use of an area detector and the addition of an optical element between source and sample crystal (the details of which are further described in the following section).

Although we exemplify the method by uniquely reconstructing the complex amplitude reflection coefficient for X-rays diffracted from a laterally homogeneous crystal, we note that it is applicable to single-measurement reconstruction of any two-dimensional linear shift-invariant transfer function. As such, our technique is applicable to the characterization of a wide variety of shift-invariant linear imaging systems that exhibit phase contrast, such as Zernike phase contrast, differential interference contrast and Schlieren imaging (Paganin, 2006).

## 2. Theory

Our method employs the experimental setup presented in Fig. 2. In addition to the source, detector and beam optics, there are two principal X-ray optical elements: a known weak

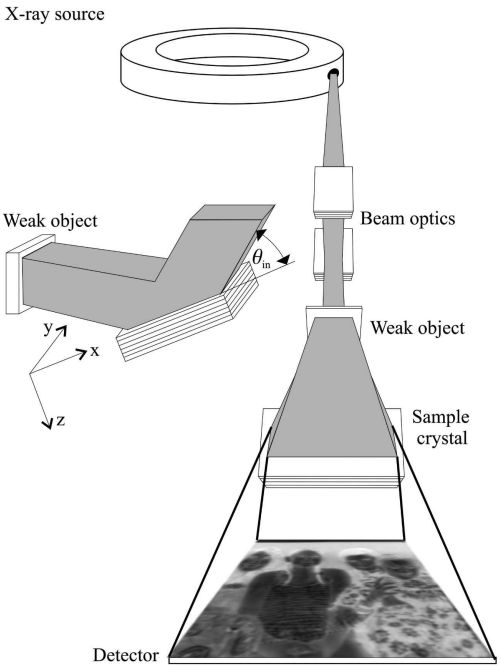


**Figure 2**
Experimental setup to record an image for ARC reconstruction. X-rays are produced at a source and monochromated/collimated before illuminating an *a priori* known weak object. The wavefield diffracted from the weak object is Bragg reflected from a sample crystal before being registered using a two-dimensional position-sensitive detector.

object (see Fig. 3 and §2.1) and a laterally homogeneous but otherwise unknown sample crystal.

The weak object is assumed to have a known projected structure (see §2.1). Since the weak-object structure is known, the phase shifts and attenuation (caused by the object) imparted on the beam are also known, the projection approximation being assumed. After transmission through the weak object, the beam's transverse spatial frequency spectrum is composed of a distribution of known frequencies whose magnitude is small in comparison with the incident beam's spatial frequency (Cowley, 1975). Illuminating the crystal with a range of Fourier frequencies, as provided by the weak object, is equivalent to rocking the crystal and means, as we shall see, that the entire ARC can be reconstructed from a single image.

The resulting two-dimensional analyser-based phase-contrast image can be analytically inverted to extract the amplitude and phase of the ARC. We emphasize the importance of being able to reconstruct the ARC from a single image. Indeed, over and above the ability to reconstruct the ARC's phase, our method can measure the reflectivity in a manner that avoids data acquisition at each reciprocal-space coordinate (Pietsch *et al.*, 2004). The range and resolution of reciprocal space that can be examined with this technique is Nyquist limited by the detector characteristics and is comparable to high-resolution XRD. The serial nature of the data acquisition at all reciprocal-space points simultaneously makes the technique suitable for high-speed measurements. Methods for single-exposure measurement of an entire rocking curve exist (Fewster, 2005); however, our method is capable of measuring the ARC modulus (positive square root of the rocking curve) and phase at a spatial resolution that is at least equal to those methods.

We now present the theoretical formalism that describes the forward problem of recording an image. A planar monochromatic X-ray beam of unit intensity is transmitted through a known weak object before being Bragg diffracted from the sample crystal and detected as in Fig. 2. In the following we consider the case of a symmetric Bragg reflection, although we note that the theory is applicable to asymmetric diffraction and Laue geometries. Let the $xy$ plane be coincident with the crystal surface and the positive $z$ axis be directed normally into the crystal. The wavefields incident, $E_{\rm in}(x, y)$, and diffracted, $E_{\rm out}(x, y; \theta_{\rm in})$, from the crystal surface $z = 0$ are related *via* a convolution integral under the assumption of a linear shift-invariant system (Afanas'ev & Kohn, 1971)

$$E_{\rm out}(-x, y; \theta_{\rm in}) = \int_{-\infty}^{+\infty} G(x - x'; \theta_{\rm in})\, E_{\rm in}(x', y)\, {\rm d}x', \qquad (1)$$

where $G(x; \theta_{\rm in})$ is the unknown point spread function (the ARC's real-space dual) which depends on the crystal properties, $E_{\rm in}(x, y)$ is an *a priori* known function, and $\theta_{\rm in}$ is the angle of incidence of the unperturbed X-ray beam. $G(x; \theta_{\rm in})$ is related to the amplitude reflection coefficient, $r(k_x, \theta_{\rm in})$, *via* the Fourier transform $\hat{f}(k_x) = \hat{\boldsymbol{F}} f(x) = (2\pi)^{-1/2} \int_{-\infty}^{\infty} f(x) \times \exp(-ik_x x)\, {\rm d}x$, $\hat{\boldsymbol{F}} G(x; \theta_{\rm in}) = r(k_x, \theta_{\rm in})$, $k_x = (2\pi/\lambda)\cos\theta_{\rm in}$, and $\lambda$ is the incident radiation's wavelength in vacuum. In this formalism, varying $k_x$ is equivalent to rocking the crystal, $\Delta k_x \propto \Delta\theta$, where $\Delta\theta$ is the variation from the Bragg position. Although in general the angle of incidence is arbitrary, it is fixed for the duration of the experiment and this will be reflected in the text by dropping the functional dependence on $\theta_{\rm in}$ where there is also a dependence on $x$ or $k_x$ and replacement by a subscript $\theta$ where there is not.

### 2.1. Weak-object approximation

Under the projection approximation, the complex amplitude $E_{\rm in}(x, y)$ is linearly related to the known weak object's projected phase $\varphi(x)$ and attenuation $\mu(x)$ *via* (Nesterets *et al.*, 2004)

$$\begin{aligned} E_{\rm in}(x, y) &\equiv \exp[i\varphi(x, y) - \mu(x, y)] \\ &= \exp(i\overline{\varphi} - \overline{\mu}) \exp[i\Delta\varphi(x, y) - \Delta\mu(x, y)] \\ &\simeq \overline{E}_{\rm in}[1 + \Delta E(x, y)]. \end{aligned} \qquad (2)$$

The overline denotes an average value, $\overline{E}_{\rm in} = \exp(i\overline{\varphi} - \overline{\mu})$; $\Delta E_{\rm in}(x, y) = i\Delta\varphi(x, y) - \Delta\mu(x, y)$ are deviations from the mean such that $|\Delta\varphi|, |\Delta\mu| \ll 1$ and $\overline{\Delta\varphi} = \overline{\Delta\mu} = 0$.

The utility of our method depends critically on whether an object that satisfies the above-mentioned criteria can be fabricated, and to that end we now state explicitly the physical parameters demanded of such an object. The weak object described here is with reference to the objects shown in Fig. 3 that are used in our numerical simulations. We note that greyscale photographs are used because they have the requisite spread of spatial frequencies.

Specifically, the object we now describe has the following four properties: (i) it is well characterized, (ii) it is weakly phase shifting ($\Delta\varphi \simeq 0.1$) with a depth profile as in Fig. 3(*a*), (iii) it is weakly attenuating ($\Delta\mu \simeq 0.1$) with a depth profile as given in Fig. 3(*b*), and (iv) the weak phase variations and weak attenuation are linearly independent. The first requirement of being well characterized can be addressed using advanced lithography techniques where a critical dimension tolerance of tens of nanometres is standard (Anderson, 2006) and continuous depth profiling (or greyscaling) such as is shown in Fig. 3 is possible (Kley, 1997; Daschner *et al.*, 1997; Geissler & Xia, 2004). We also note that the more common binary lithography object can be used for this application.

The surface topography can be precisely measured using X-ray diffraction (Paganin *et al.*, 2002; Pavlov *et al.*, 2004) or

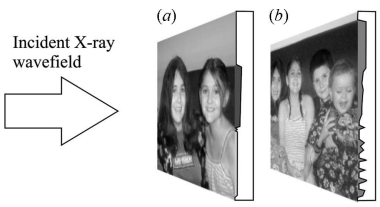


**Figure 3**
The weak phase (*a*) and amplitude (*b*) objects used in the numerical simulations (see §2.1). The greyscale level corresponds to an etching depth in the physical realization of the object. Unless otherwise stated the object is 0.5 × 0.5 mm (256 × 256 pixels).

atomic force microscopy (Foster & Hofer, 2006) given that the object is homogeneous and we need only know the surface profile.

Linear independence of $\Delta\varphi$ and $\Delta\mu$ is assured through the use of separate objects to provide the weak phase shift (the weak phase object) and weak attenuation (weak amplitude object). The weak phase object introduces a 0.1 radian phase shift and has negligible absorption. The weak amplitude object has a maximum ten percent attenuation and a $2\pi$ phase shift. The requirement that the weakly attenuating object introduce an exact $2\pi$ phase shift may seem difficult to realize but the use of refraction matching techniques makes it quite rudimentary (Hasnah *et al.*, 2005) using the following methodology. The object etching pattern must be binary so that the thickness variation corresponds to a 0 or $2\pi$ phase shift for a particular refractive index and wavelength. Any measurable deviation from this phase shift is compensated for by immersing the object in a refractive index matching fluid whose composition is varied until the position-sensitive detector, which captures an X-ray phase contrast image of the index-matched sample, records no phase contrast due to that object. The spatial frequency spectrum of a binary structure differs from a continuous depth profile in that there will be discrete diffraction orders; however, for a small enough lateral pixel size the spectrum is continuous to within the resolution of the detector. Whilst a continuous depth profile has been used for the weak amplitude object in the numerical simulations, a binary depth object will not degrade the quality of the reconstructions. Finally, an example weak phase object whose physical realization corresponds to the inset photograph of Fig. 3(*a*) is an amorphous silicon oxide (a-$SiO_2$) substrate continuously etched so that the maximum thickness variation is 0.4 µm and the lateral pixel size is 20 nm for a 20:1 aspect ratio. For 10 keV X-rays this corresponds to a phase shift of 0.1 and $|\Delta\mu| \simeq 0.001$. The weak amplitude object may be realized, for example, using an amorphous silicon (a-Si) substrate with a binary pattern similar to Fig. 3(*b*) etched into it with a thickness variation of 25.4 µm and a pixel size of 0.8 µm. At 10 keV this corresponds to $\sim 2\pi$ phase shift and $\Delta\mu \simeq 0.1$, which clearly satisfies the weak object criteria.

### 2.2. Inverse problem of reconstructing the complex ARC. I. The weak-object approximation

Substituting equation (2) into equation (1) gives for the diffracted amplitude and intensity (Nesterets *et al.*, 2004):

$$E_{\rm out}(-x,y) = \overline{E}_{\rm in} r_\theta + \overline{E}_{\rm in} \int_{-\infty}^{+\infty} G(x-x')\Delta E_{\rm in}(x',y)\,{\rm d}x', \quad (3)$$

$$I_{\rm out}(-x,y) = \overline{I}_{\rm in}\left\{R_\theta + 2{\rm Re}\left[r_\theta^* \int_{-\infty}^{+\infty} G(x-x')\Delta E_{in}(x',y)\,{\rm d}x'\right]\right\}, \quad (4)$$

where the superscript * denotes the complex conjugate, $I_{\rm out}$ is the detected intensity, $\overline{I}_{\rm in} = |\overline{E}_{\rm in}|^2$, $r_\theta = \int_{-\infty}^{+\infty} G(x;\theta_{\rm in})\,{\rm d}x$ is a single, known complex number [see the discussion following equation (11)], $R_\theta = |r_\theta|^2$ is also known and the quadratic term in $\Delta E_{\rm in}$ has been neglected.

We now show how to invert the expression in equation (4) to obtain a closed form expression for the complex ARC, as a function of a single phase-contrast image of a known weak object obtained using a laterally homogeneous analyser crystal. We begin by introducing the (known) contrast function

$$C(x,y) = I_{\rm out}(x,y)/(R_\theta \overline{I}_{\rm in}) - 1, \quad (5)$$

together with the unknown function

$$t(x) = G(x)/r_\theta. \quad (6)$$

This latter expression is the unknown function $G(x)$ divided by a single, known complex number $r_\theta$. Substituting equation (5) and equation (6) into equation (4) yields

$$-\frac{1}{2}C(-x,y) = \int_{-\infty}^{+\infty} t_{\rm I}(x-x')\Delta\varphi(x')\,{\rm d}x' + \int_{-\infty}^{+\infty} t_{\rm R}(x-x')\Delta\mu(x')\,{\rm d}x'. \quad (7)$$

The subscripts R and I refer to the real and imaginary parts of $t(x)$, respectively, so that

$$t_{\rm R}(x) = \frac{1}{2}\left[\frac{G(x)}{r_\theta} + \frac{G^*(x)}{r_\theta^*}\right], \qquad t_{\rm I}(x) = \frac{i}{2}\left[\frac{G^*(x)}{r_\theta^*} - \frac{G(x)}{r_\theta}\right]. \quad (8)$$

To proceed further we Fourier transform equation (7), giving

$$-\widehat{C}(k_x;y) = [\widehat{\Delta\mu}(k_x;y) - i\widehat{\Delta\varphi}(k_x;y)]\hat{t}(k_x) + [\widehat{\Delta\mu}(k_x;y) + i\widehat{\Delta\varphi}(k_x;y)]\hat{t}^*(-k_x). \quad (9)$$

Equation (9) may be solved using any two linearly independent lines $y_i$ of a single image. The solution, with functional dependence on $k_x$ suppressed for clarity, is given by

$$\begin{pmatrix} \hat{t}_{\rm R}^{\rm e} \\ \hat{t}_{\rm R}^{\rm o} \\ \hat{t}_{\rm I}^{\rm e} \\ \hat{t}_{\rm I}^{\rm o} \end{pmatrix} = -\frac{1}{2}\begin{pmatrix} \widehat{\Delta\mu}_{{\rm R},y_1} & \widehat{\Delta\varphi}_{{\rm I},y_1} & \widehat{\Delta\varphi}_{{\rm R},y_1} & -\widehat{\Delta\mu}_{{\rm I},y_1} \\ \widehat{\Delta\mu}_{{\rm I},y_1} & -\widehat{\Delta\varphi}_{{\rm R},y_1} & \widehat{\Delta\varphi}_{{\rm I},y_1} & \widehat{\Delta\mu}_{{\rm R},y_1} \\ \widehat{\Delta\mu}_{{\rm R},y_2} & \widehat{\Delta\varphi}_{{\rm I},y_2} & \widehat{\Delta\varphi}_{{\rm R},y_2} & -\widehat{\Delta\mu}_{{\rm I},y_2} \\ \widehat{\Delta\mu}_{{\rm I},y_2} & -\widehat{\Delta\varphi}_{{\rm R},y_2} & \widehat{\Delta\varphi}_{{\rm I},y_2} & \hat{\Delta\mu}_{{\rm R},y_2} \end{pmatrix}^{-1} \times \begin{pmatrix} \widehat{C}_{{\rm R},y_1} \\ \widehat{C}_{{\rm I},y_1} \\ \widehat{C}_{{\rm R},y_2} \\ \widehat{C}_{{\rm I},y_2} \end{pmatrix}. \quad (10)$$

The superscripts e and o refer to the even and odd parts of $\hat{t}(x)$, respectively, and the subscripts $y_1$ and $y_2$ refer to two different lines of the image.

Solution of equation (10) for $\hat{t}(k_x)$ determines $r(k_x)$,

$$r(k_x) = r_\theta \hat{t}(k_x), \quad (11)$$

which is unique up to an arbitrary additive constant phase shift given that $|r_\theta| = R_\theta^{1/2}$. Note that $|r_\theta|$ may be found from the

image by ensuring that a small portion of the beam incident on the crystal is not transmitted though the weak object and is thus a plane wave whose diffracted intensity will depend only on $\theta_{\rm in}$.

The arbitrary phase shift may be deduced by imposing suitable boundary conditions, such as requiring the phase far from a reflection to approach 0 or $\pi$.

Equation (10) requires two linearly independent lines in a single image; a typical image will have several hundred such lines so that the resulting solution is largely over-determined. The data redundancy means that noise corruption can be greatly reduced using a suitable average over each independent data set.

We make two remarks. (i) We note that the determinant of the square matrix in equation (10) is only nonzero if $\Delta\varphi$ and $\Delta\mu$ are linearly independent. This condition can be met using a weak object made from at least two materials that have differing complex refractive indices or from two single-material objects (Paganin *et al.*, 2002) with differing projected thicknesses. (ii) The effects of finite size and divergence of a polychromatic source and the detector point spread function are explored by Nesterets *et al.* (2005). These effects do not significantly affect the form of the equations presented here, although we expect that these factors will deleteriously affect the ARC's reconstruction.

### 2.3. Inverse problem of reconstructing the complex ARC. II. The relaxed weak-object approximation

The weak-object approximation allowed us to derive a closed-form expression for the complex ARC in terms of the detected intensity and known weak object. Under the weak-object approximation, all nonlinear terms, which would otherwise be present in equation (4), can be legitimately neglected. In practice, this approximation has two consequences that it is desirable to overcome. Firstly, the ability to compensate for larger phase shifts and attenuations provides some leeway to use weak objects with larger thickness variations. Secondly, there is an optimization problem between satisfying the weak-object criteria and the signal to noise in an image. Obviously a larger phase shift will result in greater contrast at the cost of invalidating the weak-object criteria. Ideally we would like to use a more strongly scattering object and to that end we present a modification to the theory of §2.2 that allows for an order of magnitude increase in the object's scattering strength ($|\Delta\varphi|, |\Delta\mu| < 1$). We refer to this as the 'relaxed weak-object approximation'.

To incorporate a relaxed weak-object approximation we must include the nonlinear terms previously neglected from equation (4). This can be achieved using an iterative procedure analogous to the Born series (Born & Wolf, 1999). To this end, we rewrite equation (10) schematically as

$$\mathbf{t}_1 = -\mathbf{\Delta}^{-1}\mathbf{C}_0/2. \tag{12}$$

Here, boldface letters denote matrices, obtained from equation (10) as follows: $\mathbf{t}$ corresponds to the column matrix on the left side, $\mathbf{\Delta}$ is the square matrix on the right side and $\mathbf{C}$ is the column vector on the right side. Subscripts 0 and 1 indicate the iteration order. As suggested by this notation, we will use equation (10) as the first-order step in an iterative procedure.

Up to second order in the known function $\Delta E_{\rm in}(x, y)$ (*cf.* §2.1) the squared modulus of equation (1) becomes

$$\begin{aligned} I_{\rm out}(-x/b, y)/\bar{I}_{\rm in} = R_\theta &+ 2{\rm Re}\left\{r_\theta^* \int_{-\infty}^{+\infty} G(x-x')\Delta E_{\rm in}(x', y)\,{\rm d}x'\right\} \\ &+ {\rm Re}\left\{r_\theta^* \int_{-\infty}^{+\infty} G(x-x')\Delta E_{\rm in}^2(x, y)\,{\rm d}x'\right\} \\ &+ \left|\int_{-\infty}^{+\infty} G(x-x')\Delta E_{\rm in}(x', y)\,{\rm d}x'\right|^2 \\ &+ \frac{1}{4}\left|\int_{-\infty}^{+\infty} G(x-x')\Delta E_{\rm in}^2(x, y)\,{\rm d}x'\right| \\ &+ {\rm Re}\left\{\left[\int_{-\infty}^{+\infty} G(x-x')\Delta E_{\rm in}(x', y)\,{\rm d}x'\right]^* \right. \\ &\left. \times \int_{-\infty}^{+\infty} G(x-x')\Delta E_{\rm in}^2(x, y)\,{\rm d}x'\right\}. \end{aligned} \tag{13}$$

All quantities are as previously defined. We now define a functional $I_{\rm neg.}[x, y, G(x)]$ containing all nonlinear terms in the right-hand side of equation (13) [*i.e.* it contains all the terms that were previously neglected in equation (4)]. The explicit dependence on the unknown function $G(x)$ is used to clarify the iterative scheme.

Successive iterations now include the nonlinear terms, $I_{\rm neg.}[x, y, G(x)]$, using the recursive formula

$$\mathbf{t}_{n+1} = -\mathbf{\Delta}^{-1}(\mathbf{C}_n)/2. \tag{14}$$

Here $\mathbf{t}_{n+1}$ is the $(n+1)$th iterative solution for the complex ARC, is as previously defined and, to define $\mathbf{C}_n$, we redefine equation (5) as follows:

$$\widehat{C}_n(k_x; y) = \hat{F}\left\{\frac{1}{R_\theta}\left[\frac{I_{\rm out}(x, y)}{\bar{I}_{\rm in}} - R_\theta - \frac{I_{\rm neg.}[x, y, G_n(x)]}{\bar{I}_{\rm in}}\right]\right\}, \tag{15}$$

so that

$$\mathbf{C}_n = \begin{Bmatrix} {\rm Re}\,[\widehat{C}_n(k_x; y_1)] \\ {\rm Imag}\,[\widehat{C}_n(k_x; y_1)] \\ {\rm Re}\,[\widehat{C}_n(k_x; y_2)] \\ {\rm Imag}\,[\widehat{C}_n(k_x; y_2)] \end{Bmatrix}. \tag{16}$$

Note the dependence of $I_{\rm neg.}[x, y, G_n(x)]$ on $n$, the current iteration of $G(x)$. Equation (14) together with equation (16) defines the iterative scheme which allows the relaxed weak-object approximation $|\Delta\varphi|, |\Delta\mu| < 1$.

## 3. Modelling

Here we numerically simulate the reconstruction of the complex ARC for two crystals of particular research interest. In §3.1 we demonstrate the reconstruction of the ARC for a semi-infinite perfect crystal. In §3.2 we reconstruct the ARC of a thin crystal with a linear deformation gradient and then use it to reconstruct the interplanar spacing.

### 3.1. Reconstructing the ARC of a semi-infinite perfect crystal

In this section we apply the iterative algorithm of §2.3 to reconstruct the ARC of a semi-infinite perfect crystal. The reconstruction quality of $r(k_x)$ is quantified by calculating the r.m.s. normalized error [r.m.s. error between reconstruction and input functions divided by the r.m.s. error between the input and its mean (Herman, 1980; Nesterets *et al.*, 2004)] against the input function.

The known weak object was simulated using the phase and amplitude maps of Figs. 3(*a*) and 3(*b*), respectively. The 'weakness' of the weak object was varied by changing the maximum values of $|\Delta\varphi|$ and $|\Delta\mu|$. Poisson noise was simulated in the detected intensity by adding Poisson-distributed random numbers whose standard deviation is a specified percentage of the maximum intensity registered in the two-dimensional image. Thus, for example, 1% Poisson noise means the noise varies locally in the image from 1% at the highest signal-to-noise regions to much larger values at the lowest signal-to-noise regions. As a result of this noise model a 1% Poisson noise level will not, in general, correspond to 1% r.m.s. error in the image. To allow for this we will quote the reconstruction error in the ARC's phase and amplitude with the error introduced into the detected intensity by the addition of noise.

The amplitude and phase (divided by $\pi$) of $r(k_x)$ for a symmetric Bragg reflection from Si(111) at 25 keV are shown in Fig. 4(*a*) and 4(*b*). Three traces are shown offset from each other for clarity and the roman numerals refer to (i) input, reconstructed with (ii) $|\Delta\varphi|, |\Delta\mu| \leq 0.1$ with no noise and (iii) $|\Delta\varphi|, |\Delta\mu| \leq 0.78$ with 1% Poisson noise (r.m.s. error: 4% amplitude, 20% phase, 4% detected intensity).

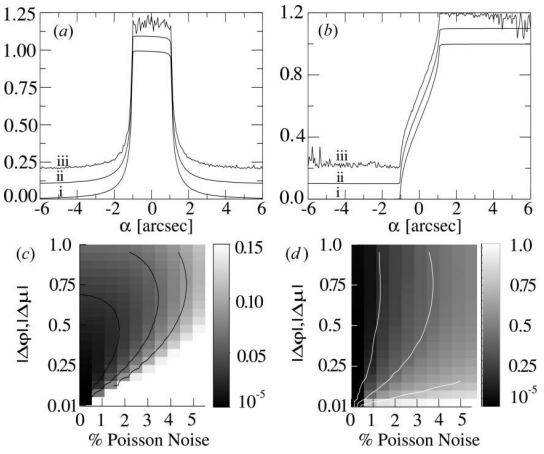


**Figure 4**
Simulated reconstruction of the semi-infinite perfect crystal ARC using equation (14). (*a*) and (*b*) show the amplitude and phase (divided by $\pi$) with three traces (offset for clarity) representing (i) input, reconstructed with (ii) $|\Delta\varphi|, |\Delta\mu| \leq 0.1$ with no noise (r.m.s. error negligible) and (iii) $|\Delta\varphi|, |\Delta\mu| \leq 0.78$ with 1% Poisson noise (r.m.s. error: 4% amplitude, 20% phase, 4% detected intensity). (*c*) and (*d*) present the r.m.s. error in the amplitude and phase, respectively, for $|\Delta\varphi|, |\Delta\mu|$ against noise. The r.m.s. errors in (*c*) have been capped at 15% to facilitate visualization of the contour details.

To gauge the success of the iterative algorithm in §2.3, consider the top-left corner of Figs. 4(*c*) and 4(*d*) for $|\Delta\varphi|, |\Delta\mu| = 1$ and no noise. Clearly, the approximation of equation (2) is not valid, but with iteration the reconstruction shows r.m.s. error of only 4 and 2% in the amplitude and phase, respectively.

All simulations used 15 iterations and a single iteration took less than 1 s using a 2 GHz Pentium M machine. One important consideration for the practical utility of this method is its robustness with respect to experimental noise. To some extent a smaller signal-to-noise can be compensated by using a more strongly scattering object at the expense of invalidating the weak-object approximation. The tradeoff between those two quantities is plotted in Figs. 4(*c*) and 4(*d*), which show that there exists an optimum level of object weakness for a given noise level.

### 3.2. Reconstructing the depth-dependent interplanar spacing

We now consider the problem of determining the layer structure of a crystal given a single two-dimensional intensity measurement using our method. A complete investigation of the inverse problem of reconstructing the layer structure where dynamical diffraction effects cannot be neglected is beyond the scope of this paper and will be given in a future publication. However, we will briefly describe the reconstruction of an arbitrary, depth dependent strain profile in a crystal for which a kinematical scattering approximation is valid.

The kinematical scattering approximation to the ARC for a symmetrical Bragg geometry in the limit of small deformation takes the form (Petrashen', 1974)

$$r(\eta) = \frac{i\pi\chi_h}{\lambda \sin\theta_B} \int_{-\infty}^{\infty} \Omega(z) \exp[i(\eta z - \mathbf{h}\cdot\mathbf{u})]\, \mathrm{d}z. \qquad (17)$$

Let $\omega$ describe the angular deviation from the exact Bragg angle, then $\eta = (4\pi\omega/\lambda)\cos\theta_B$ when $\chi_0 \simeq 0$, $\chi_h$ is the Fourier component of the susceptibility in the direction of a Bragg reflection from the substrate, $\lambda$ is the wavelength of the incident radiation, $\Omega(z)$ is the shape function equal to unity inside the crystal and zero elsewhere, and $\mathbf{h}$ and $\mathbf{u}$ are the diffraction vector and displacement of atoms from their position in the 'ideal' lattice, respectively. Setting $\chi_0 = 0$ amounts to ignoring attenuation and refraction within the thin layer. Here we investigate the case of a linear variation in the lattice parameter (Kolpakov *et al.*, 1977). The linearly strained crystal is an example of a simple crystal analogue because the sign of the strain gradient cannot be determined unambiguously from the reflectivity within the framework of the kinematical approximation (Afanas'ev & Fanchenko, 1988). The interplanar spacing can be solved explicitly when the complex

ARC is known; in that case the solution is given by (Podorov *et al.*, 1994)

$$\frac{2\pi\Delta d(z)}{d_0^2} = -\mathrm{Re}\left[\frac{\int_{-\infty}^{\infty} \eta r(\eta)\exp(-i\eta z)\,\mathrm{d}\eta}{\int_{-\infty}^{\infty} r(\eta)\exp(-i\eta z)\,\mathrm{d}\eta}\right], \qquad (18)$$

where $\Delta d(z)$ is the variation in the interplanar spacing of the film and $d_0$ is the substrate interplanar spacing. A logarithmic derivative is used to solve for the interplanar spacing because it is more stable numerically than a logarithm. As an example consider diffraction from a GaAs(004) film of 1 μm thickness with a 0.5% strain and 8.74 keV X-rays (Cu $K\alpha_1$) as in Figs. 5(*a*) and 5(*b*), trace (i). We note briefly that the characteristically asymmetric reflectivity of a thin strained layer is not observed here because absorption has been neglected and scattering from the thin layer is kinematic (Kolpakov & Punegov, 1985). The amplitude and phase maps of the known weak object are as in Figs. 3(*a*) and 3(*b*) (3.6 × 3.6 μm). The ARC's amplitude and phase (divided by $\pi$) is shown in Figs. 5(*a*) and 5(*b*), respectively, and Fig. 5(*c*) shows the variation in the interplanar spacing. The three traces refer to (i) input, reconstructed using (ii) $|\Delta\varphi|, |\Delta\mu| \leq 0.1$ with no noise (r.m.s. error negligible) and (iii) $|\Delta\varphi|, |\Delta\mu| \leq 0.5$ with 1% Poisson noise (r.m.s. error: 0.2% amplitude, 41% phase, 7% detected intensity). The oscillation in the reconstructed lattice variation Fig. 5(*c*) (ii) is caused by the step-function-like model for the film thickness and was responsible for the error not dropping below 10%. The r.m.s. error increased to 16% in Fig. 5(*c*) (iii) but the lattice parameter's linear variation is still evident.

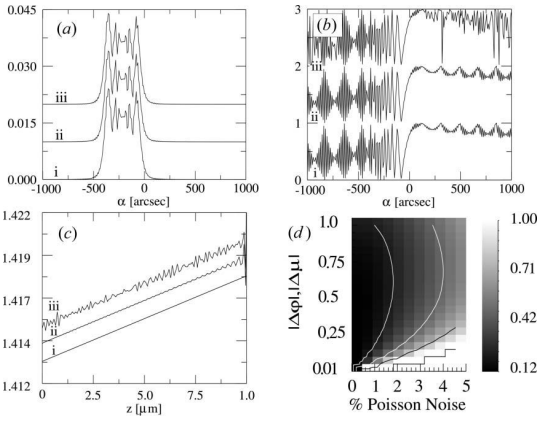


**Figure 5**
Input and reconstructed ARC and variation in the interplanar lattice spacing for a thin GaAs(004) film with 0.5% strain using equation (14). (*a*) and (*b*) show the ARC's amplitude and phase (divided by $\pi$) and (*c*) the interplanar spacing variation (Å) and $d_0$ = 1.413 Å with traces (offset by a constant) showing (i) input, and reconstruction using (ii) $|\Delta\varphi|, |\Delta\mu| \leq 0.01$ with no noise (r.m.s. error: negligible) and (iii) $|\Delta\varphi|, |\Delta\mu| \leq 0.5$ 1% Poisson noise (r.m.s. error: 0.2% amplitude, 41% phase, 6%, detected intensity). (*d*) shows the r.m.s. error in the reconstructed lattice spacing for $|\Delta\varphi|, |\Delta\mu|$.

## 4. Conclusions and further work

In summary, we have outlined a single-shot method to reconstruct unambiguously the entire complex ARC of laterally homogeneous crystals, given a two-dimensional analyser-based phase-contrast image of a known weak phase-amplitude mask. An *a priori* characterized weak object was used to introduce small perturbations on a plane wave incident on the sample crystal to render the inverse problem tractable. We have obtained closed-form expressions for the complex ARC and depth-dependent interplanar spacing in terms of a single analyser-based phase-contrast intensity image. Numerical simulations demonstrated the theory's validity and its robustness in the presence of experimental noise. This method unambiguously determines the crystal layer structure and is not susceptible to the problem of crystal analogues. Our technique enables experimental determination of the ARC phase, as predicted by X-ray dynamical diffraction theory for ideal crystals (Authier, 2005). The experimental implementation of this work is planned and will be reported in a future publication.

DJV gratefully acknowledges helpful discussions with J. E. Gillam, N. A. Zatsepin and J. E. Daniels, together with support from the APA and J. L. William Bequest. The authors acknowledge funding from the Australian Research Council.

## References

Afanas'ev, A. M. & Fanchenko, S. S. (1986). *Sov. Phys. Dokl.* **31**, 280–282.
Afanas'ev, A. M. & Fanchenko, S. S. (1988). *Acta Cryst.* A**44**, 25–33.
Afanas'ev, A. M., Fanchenko, S. S. & Maslov, A. V. (1990). *Phys. Status Solidi A*, **117**, 341–350.
Afanas'ev, A. M. & Kohn, V. G. (1971). *Acta Cryst.* A**27**, 421–430.
Afanas'ev, A. M. & Kohn, V. G. (1978). *Sov. Phys. JETP*, **47**, 154–161.
Afanas'ev, A. M., Kovalchuk, M. V., Kovev, E. K. & Kohn, V. G. (1977). *Phys. Status Solidi A*, **42**, 415–422.
Anderson, E. H. (2006). *Quantum Electron.* **42**, 27–35.
Authier, A. (2005). *Dynamical Theory of X-ray Diffraction*, revised ed. Oxford University Press.
Birkholz, M., Fewster, P. F. & Genzel, C. (2006). *Thin Film Analysis by X-ray Scattering*. Weinheim: Wiley VCH.
Born, M. & Wolf, E. (1999). *Principles of Optics*, 7th ed. Cambridge University Press.
Cowley, J. M. (1975). *Diffraction Physics*, 1st ed. Amsterdam: North-Holland Publishing.
Daschner, W., Long, P., Stein, R., Wu, C. & Lee, S. H. (1997). *Appl. Opt.* **36**, 4675–4680.
Davis, T. J., Gao, D., Gureyev, T. E., Stevenson, A. W. & Wilkins, S. W.(1995). *Nature* (*London*), **373**, 595–598.
Davis, T. J., Gureyev, T. E., Gao, D., Stevenson, A. W. & Wilkins, S. W. (1995). *Phys. Rev. Lett.* **74**, 3173–3176.
Dilanian, R. A., Nikulin, A. Y., Darahanau, A. V., Hester, J. & Zaumseil, P. (2006). *J. Appl. Phys.* **99**, 113526-1.
Fewster, P. F. (2003). *X-ray Scattering from Semiconductors*, 2nd ed. London: Imperial College Press.
Fewster, P. F. (2005). *J. Appl. Cryst.* **38**, 62–68.
Foster, A. & Hofer, W. (2006). *Scanning Probe Microscopy*. New York: Springer.

Förster, E., Goetz, K. & Zaumseil, P. (1980). *Krist. Tech.* **15**, 937–945.
Geissler, M. S. & Xia, Y. (2004). *Adv. Mater.* **16**, 1249–1269.
Goncharskii, A. V., Kolpakov, A. V. & Stepanov, A. A. (1992). *Inverse Problems in X-ray Diffraction*. Riga: Latvian University. (In Russian.)
Hart, M. & Lang, A. R. (1961). *Phys. Rev. Lett.* **7**, 120–121.
Hasnah, M. O., Parham, C., Pisano, E. D., Zhong, Z., Oltulu, O. & Chapman, D. (2005). *Med. Phys.* **32**, 549–552.
Herman, G. T. (1980). *Image Reconstruction from Projections*. New York: Acacdemic Press.
Ingal, V. N. & Beliaevskaya, E. A. (1995). *J. Phys. D*, **28**, 2314–2317.
Kley, E. B. (1997). *Microelectron. Eng.* **34**, 261–298.
Kohn, V. G., Kovalchuk, M. V., Imamov, R. M. & Lobanovich, E. F. (1981). *Phys. Status Solidi A*, **64**, 435–442.
Kolpakov, A. V., Khapachev, Y. P., Kuznetsov, G. F. & Kuz'Min, R. N. (1977). *Kristallografiya*, **22**, 473–480.
Kolpakov, A. V. & Punegov, V. I. (1985). *Solid State Commun.* **54**, 573–578.
Koval'chuk, M. V. & Kohn, V. G. (1986). *Sov. Phys. Usp.* **29**, 426–446.
Koval'chuk, M. V., Liljequist, D. & Kohn, V. G. (1986). *Sov. Phys. Solid State*, **28**, 1918–1922.
Kyutt, R. N., Petrashen', P. V. & Sorokin, L. M. (1980). *Phys. Status Solidi A*, **60**, 381–389.
Majkrzak, C. F. & Berk, N. F. (1995). *Phys. Rev. B*, **52**, 10827–10830.
Majkrzak, C. F., Berk, N. F., Silin, V. & Meuse, C. W. (2000). *Physica B*, **283**, 248–252.
Nesterets, Ya. I., Gureyev, T. E., Paganin, D., Pavlov, K. M. & Wilkins, S. W. (2004). *J. Phys. D*, **37**, 1262–1274.
Nesterets, Ya. I., Gureyev, T. E. & Wilkins, S. W. (2005). *J. Phys. D*, **38**, 4259–4271.
Nikulin, A. Y. (1998). *Phys. Rev. B*, **57**, 11178–11183.
Paganin, D. M. (2006). *Coherent X-ray Optics*. New York: Oxford University Press.
Paganin, D., Mayo, S. C., Gureyev, T. E., Miller, P. R. & Wilkins, S. W. (2002). *J. Microsc.* **206**, 33–40.
Pavlov, K. M., Gureyev, T. E., Paganin, D., Nesterets, Ya. I., Morgan, M. J. & Lewis, R. A. (2004). *J. Phys. D*, **37**, 2746–2750.
Petrashen', P. V. (1974). *Sov. Phys. Solid State*, **15**, 2096–2097.
Petrashen', P. V. (1975). *Sov. Phys. Solid State*, **17**, 1882–1883.
Petrashen', P. V. & Chukhovskii, F. N. (1989). *Sov. Phys. Dokl.* **34**, 957–959.
Pietsch, U., Holý, V. & Baumbach, T. (2004). *High-Resolution X-ray Scattering*, 2nd ed. New York: Springer-Verlag.
Podorov, S. G., Holzer, G., Forster, E. & Faleev, N. N. (1998). *Phys. Status Solidi A*, **169**, 9–16.
Podorov, S. G., Holzer, G., Forster, E. & Faleev, N. N. (1999). *Phys. Status Solidi B*, **213**, 317–324.
Podorov, S. G. & Punegov, V. I. (1999). *Tech. Phys.* **44**, 257–260.
Podorov, S. G., Punegov, V. I. & Kusikov, V. A. (1994). *Phys. Solid State*, **36**, 454–458.
Somenkov, V. A., Tkalich, A. K. & Shil'shtein, S. S. (1991). *Zh. Tekh. Fiz.* **61**, 197–201.
Speriosu, V. S., Glass, H. L. & Kobayashi, T. (1979). *Appl. Phys. Lett.* **34**, 539–542.
Stepanov, A. A. (1994). *J. Appl. Cryst.* **27**, 7–12.
Vartanyants, I. A., Koval'chuk, M. V., Kohn, V. G., Nikolaenko, A. M. & Kharitonov, I. Y. (1989). *JETP Lett.* **49**, 726–730.

# Appendix D

## Deterministic Green's function retrieval using hard X-rays

This appendix presents a preprint of the paper

> "Deterministic Green's function retrieval using hard X-rays"
> D. J. Vine, D. M. Paganin, K. M. Pavlov, K. Uesugi, A. Takeuchi, Y. Suzuki,
> N. Yagi, T. Kämpfe, E.-B. Kley and E. Förster.
> (submitted)

This paper presents the result of an experiment conducted at SPring-8 BL20XU, Japan in May 2007. In it the amplitude reflection coefficient of a thick perfect silicon 111 reflection is reconstructed using a single analyser-based phase contrast image of a known weak object.

The experimental design is largely my own with helpful discussions from Dr David Paganin and Dr Konstantin Pavlov. I designed the weak object with helpful discussions with Professor Erst-Bernard Kley and Professor Eckhardt Förster and it was fabricated at Professor Kley's Institute of Applied Physics. The CAD drawings were created by Mr Thomas Kämpfe from my designs who also oversaw the fabrication. Dr Kentaro Uesugi, Dr Akihasa Takeuchi, Dr Yoshio Suzuki and Dr Naoto Yagi provided invaluable help during the experimental preparation and execution. The experiment was conducted almost entirely by myself and Dr Pavlov over two days of beamtime.

The post-processing, coding and algorithm are my own work with helpful discussions with Dr Paganin and Dr Pavlov. In addition, I wrote and produced the article presented in this appendix.

Overall, I estimate my contribution to this article to be 90%.

# Deterministic Green's function retrieval using hard X-rays

D. J. Vine,* D. M. Paganin, and K. M. Pavlov†‡

*School of Physics, Monash University, VIC 3800 Australia*

† *Monash Centre for Synchrotron Science,*

*Monash University, VIC 3800 Australia and*

‡ *School of Science and Technology, University of New England, NSW 2350 Australia*

K. Uesugi, A. Takeuchi, Y. Suzuki, and N. Yagi

*Japan Synchrotron Radiation Research Institute (JASRI), SPring-8, Hyogo 679-5198, Japan*

T. Kämpfe, E.-B. Kley

*Institute of Applied Physics, Friedrich-Schiller University, Jena 07743 Germany*

E. Förster

*Institute of Optics and Quantum Electronics,*

*Friedrich-Schiller University, Jena 07743 Germany*

(Dated: August 28, 2008)

## Abstract

We have recently developed a deterministic method for reconstructing the complex Green's function for a linear, shift invariant imaging system. Green's function retrieval allows the measurement of the state of an optical system and makes it possible to reconstruct the complex propagators of classical optics and quantum mechanics. In this Letter we demonstrate the first experimental implementation of this technique to reconstruct the complex Green's function of a thick perfect silicon crystal using hard X-rays.

PACS numbers: 42.25.Fx, 42.30.Lr, 42.40.-i

Keywords: Green's function retrieval, holography, diffraction and scattering

*Electronic address: david.vine@sci.monash.edu.au

Green's functions in diffraction and scattering physics are used to describe the response of an optical system to the illuminating field incident upon it. Usually one uses Green's functions to calculate the scattered field to gain qualitative or quantitative information about the scatterer as is the case in imaging or holography. In this Letter we demonstrate how Green's functions themselves can be quantitatively reconstructed.

The Green's function is a descriptor of some of the most beautiful theories in physics such as the complex wavefield propagators of quantum mechanics [1] and classical optics [2]. What we propose here is a method for directly measuring the propagators of these fundamental physical theories. Notwithstanding the fundamental physics that Green's function retrieval can probe there is the possibility of improving solution of forward and inverse scattering problems by shifting the onus from modelling the Green's function of an optical or quantum mechanical system to measuring it. The advantages of Green's function retrieval have been recognised in other fields [3–5] where, for example, elastodynamic waves have been proposed to reconstruct the real Green's function of the earth itself [6]. The results we present here show how reconstruction may be realised using short wavelength ($>$ 8keV) electromagnetic fields for the more general case of complex Green's functions.

The essence of the idea we have implemented is illustrated in the following example. Consider the classic Green's function description of wavefield evolution [7],

$$\Psi(\mathbf{r}) = \int G(\mathbf{r}, \mathbf{r}')\psi(\mathbf{r}')d\mathbf{r}', \tag{1}$$

where $\Psi$, $\psi$ describe coherent complex scalar wavefields and $\mathbf{r}$ is a position vector. The problem is to solve Eq. (1) for $G$ given knowledge of $|\Psi|$ and $\psi$; in general this is a highly non-linear inverse problem. The problem can be linearised without compromising the generality of $G$ by choosing $\psi$ to have the property that $\psi(\mathbf{r}) = 1 + \eta(\mathbf{r})$ where $|\eta(\mathbf{r})| \ll 1$ - the so-called 'weakness' property [8]; we will refer to its optical element as a weak interaction element. Under these conditions it is possible, as we shall show, to solve Eq. (1) for $G$ in a manner which is non-iterative, unambiguous and useful for a wide class of complex Green's functions.

Evidently this method of reconstructing the Green's function is applicable to systems in which an object with the weak interaction property ascribed to $\psi$ can be readily fabricated, a question that is specific to the type of matter or radiation used.

For the remainder of this Letter we will describe how hard X-rays may be used to reconstruct the complex Green's function for a shift-invariant system where $G(\mathbf{r}, \mathbf{r}') = G(\mathbf{r} - \mathbf{r}')$. Hard X-ray

radiation was chosen because we can fabricate optical elements from Quartz using lithographic techniques, and for which partially coherent sources are available at synchrotrons and in the laboratory [9].

We now give two examples illustrating this technique where the Green's function for two fundamentally important theories of classical optics are reconstructed. Suppose we wish to reconstruct the Green's function for the Kirchhoff propagator that describes diffraction of a complex scalar wavefield through free space [2, 10]. The corresponding experiment simply involves illuminating the optical element with coherent X-rays and measuring the two-dimensional intensity of the field after it has been allowed to propagate through a specified distance. The Green's function can then be analytically recovered from a single intensity image using only the assumption that free space diffraction is isotropic, a symmetry that the Green's function must respect.

Perhaps instead we wish to reconstruct the Green's function that describes the dynamical diffraction of a wavefield from a crystal [11]. With reference to the previous example we must replace the free space diffraction with diffraction from a crystal. If the crystal is laterally homogeneous then the Green's function can be retrieved from a single image.

To make concrete that the technique does indeed work as in the last example we now present the results of an experiment in which the Green's function for a thick perfect silicon crystal is recovered from a single intensity image. This particular Green's function, the squared magnitude of which is known to crystallographers as the rocking curve, has a well known form given by the theory of dynamical diffraction [11]. A brief comment that speaks to the utility of Green's function retrieval: whilst we have chosen this system as a means for demonstrating the Green's function retrieval technique we note that in the regime of kinematic diffraction our approach unambiguously solves the famous one-dimensional phase problem addressed by the following techniques: Hilbert transform [12], methods based on the photoemission of electrons due to X-ray standing waves [13] and Fourier analysis techniques [14].

With reference to Fig. 1 we now outline the reconstruction algorithm alluded to in the above example in more detail [15]. Depicted is a planar monochromatic scalar hard X-ray wavefield illuminating the weak interaction element. The field propagates through the imaging system to the two-dimensional detector. The inset gives the specific case for symmetric Bragg reflection from a perfect crystal. The actual beam direction after reflection is not collinear with the incident beam however a simple coordinate transformation, the details of which are omitted for clarity, will make this so and considerably simplifies the proceeding analysis.

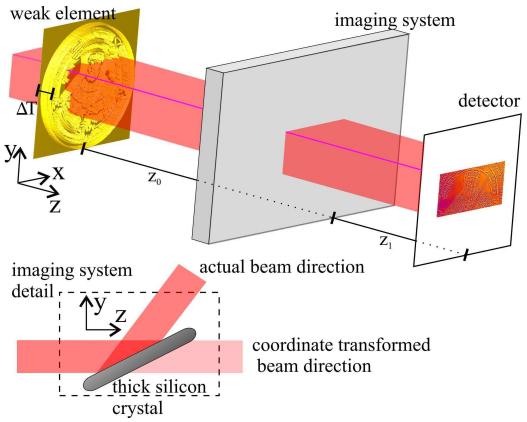


FIG. 1: (Color online). Experimental reconstruction of a generic Green's function. Inset: reconstruction of the Green's function of a thick perfect crystal. Planar X-rays illuminate the weak interaction element, the weakly perturbed field is then Bragg reflected from the crystal and recorded on a detector. This single intensity image may be deterministically inverted to recover the complex Green's function.

The exit surface complex scalar wavefield, $\psi(\mathbf{r}_\perp, z = 0)$, is the product of the incident plane wave and the complex transmission function of the weak interaction element which is composed of a single material with refractive index $n = 1 - \delta + i\beta$ and projected thickness $T(\mathbf{r}_\perp)$ [10]. We require,

$$\begin{aligned}\psi(\mathbf{r}_\perp, 0) &= \exp[ik(n-1)T(\mathbf{r}_\perp)] \\ &\approx \exp(ik(n-1)\bar{T})[1 + ik(n-1)\Delta T(\mathbf{r}_\perp)] \end{aligned} \tag{2}$$

where $\mathbf{r}_\perp = (x, y)$, $\mathbf{k}_\perp = (k_x, k_y)$ is the reciprocal space vector that is dual to $\mathbf{r}_\perp$ and $k = 2\pi/\lambda = |(\mathbf{k}_\perp, k_z)|$, $\lambda$ is the radiation wavelength, $n - 1$ gives the phase shift relative to vacuum, $\bar{T}$ and $\Delta T$ denote average thickness and deviation from the average thickness respectively. The approximation in Eq. (2) is valid when $|(n-1)k\Delta T(\mathbf{r}_\perp)| \ll 1$ and we now briefly digress from the analysis to show how this may be achieved in practice.

Splitting the arguments of Eq. (2) into real, $\mu$ - attenuation, and imaginary, $\varphi$ - phase, Eq. (2) may be written [16],

$$\psi(\mathbf{r}_\perp, 0) = \exp(i\bar{\varphi} - \bar{\mu})[1 + i\Delta\varphi(\mathbf{r}_\perp) - \Delta\mu(\mathbf{r}_\perp)]. \tag{3}$$

It is necessary that the magnitude of $\Delta\mu$ and $\Delta\varphi$ be of the same order of magnitude however for a material such as Quartz the refraction, $\delta$, is three orders of magnitude greater than the attenuation, $\beta$. We overcome the problem by allowing the wavefield to propagate before it is incident

on the crystal [10, 17–20]. The distance $z_0$ (see Fig. 1) is increased so that the curvature in the wavefront, due to the weak interaction element, causes neighbouring rays to interfere producing intensity variations that are tantamount to increasing $\beta$. For small $z$ the intensity is proportional to the transverse laplacian, $\nabla_\perp^2 = \frac{\partial^2}{\partial x^2} + \frac{\partial}{\partial y^2}$, of the phase $\Delta\varphi(\mathbf{r}_\perp, 0)$ [10] and can be considered an effective attenuation over the plane $z = z_0$.

The complex wavefield at the entrance to the imaging system that incorporates propagation contrast to bolster the effective attenuation is then given by the following angular spectrum representation [21],

$$\psi(\mathbf{r}_\perp, z_0) = \frac{1}{(2\pi)^2} \iint \exp\left(iz_0\sqrt{k^2 - |\mathbf{k}_\perp|^2}\right)\psi(\mathbf{r}'_\perp, 0) \times \exp[i\mathbf{k}_\perp \cdot (\mathbf{r}_\perp - \mathbf{r}'_\perp)]d\mathbf{r}'_\perp\mathbf{k}_\perp. \tag{4}$$

Returning to the main thread of the analysis, Eq. (2) makes clear the connection of this approach to holography: the field transmitted through the weak interaction element, $\psi(\mathbf{r}_\perp, z = 0)$, is the sum of the direct beam and a known weak perturbation. Reflection from the crystal will modulate the amplitude and phase of the field and the detector records the hologram. The hologram evidently contains the response of the imaging system to all spatial frequencies present in $\psi$ which allows a massively parallel interrogation of a wide range of reciprocal space simultaneously. We now proceed to show how to invert the hologram to recover the Green's function.

The intensity recorded on the detector is,

$$I(\mathbf{r}_\perp, z_0 + z_1; \omega) = \bar{I}\Bigg(|G(0,\omega)|^2 + 2\mathrm{Re}\left\{G^*(0,\omega)\iint G(k_y,\omega) \times [i\Delta\varphi(\mathbf{r}'_\perp, z_0) - \Delta\mu(\mathbf{r}'_\perp, z_0)]\exp[i\mathbf{k}_\perp \cdot (\mathbf{r}_\perp - \mathbf{r}'_\perp)]d\mathbf{k}_\perp d\mathbf{r}'_\perp\right\}\Bigg). \tag{5}$$

Here, $I(\mathbf{r}_\perp, z) = |\Psi(\mathbf{r}_\perp, z)|^2$, $G(k_y, \omega)$ is the Fourier transform of $G(\mathbf{r}_\perp)$, $\omega$ is the angle between the X-ray beam and crystal surface (a constant), $\mu$ and $\varphi$ now refer to attenuation and phase of Eq. (4), * denotes complex conjugation and $\bar{I} = \exp(-2\bar{\mu})$. Terms quadratic in the small quantities $\Delta\mu$, $\Delta\varphi$ are discarded as negligible, together with a phase factor due to propagation distance $z_1$ - valid for Fresnel numbers [10] of at least unity. $G(0, \omega)$ is a single complex number (given that $\omega$ was held constant throughout the experiment) which represents the ratio of DC values of $\Psi$ to $\psi$—a known quantity.

With a view to deriving an expression for $G(k_y, \omega)$ we introduce the known contrast function $C(\mathbf{r}_\perp, z; \omega) = I(\mathbf{r}_\perp, z)/\bar{I} - |G(0,\omega)|^2$ and scale the Green's function $\tilde{G}(k_y, \omega) = G(k_y, \omega) \times G^*(0, \omega)$

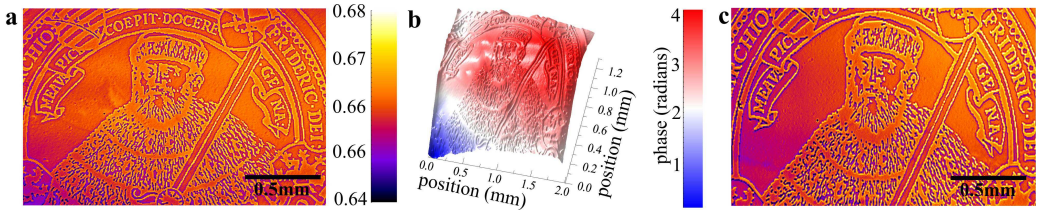


FIG. 2: (Color online). (a) Intensity measurement prior to reflection from the crystal showing only propagation phase contrast; (b) calculated phase corresponding to (a); (c) measured intensity image showing the image of the linear element after reflection from a thick perfect silicon crystal (111) reflection. The crystal was slightly detuned from the Bragg condition so that it reflects 70% of the direct beam.

so that Eq. 5 becomes, after a one-dimensional Fourier transform,

$$-C(x, z_0 + z_1; k_y, \omega) = [\Delta\mu(x; k_y) - i\Delta\varphi(x; k_y)]\tilde{G}(k_y, \omega) + [\Delta\mu(x; k_y) + i\Delta\varphi(x; k_y)]\tilde{G}^*(-k_y, \omega). \quad (6)$$

Eq. (6) is linear in the unknown complex function $\tilde{G}(k_y, \omega)$ which can be solved for using any two discrete lines $(i, j)$ of the image.

$$\begin{pmatrix} \tilde{G}^e_R \\ \tilde{G}^o_R \\ \tilde{G}^e_I \\ \tilde{G}^o_I \end{pmatrix} = -\frac{1}{2} \begin{pmatrix} \Delta\mu^i_R & \Delta\varphi^i_I & \Delta\varphi^i_R & -\Delta\mu^i_I \\ \Delta\mu^i_I & -\Delta\varphi^i_R & \Delta\varphi^i_I & \Delta\mu^i_R \\ \Delta\mu^j_R & \Delta\varphi^j_I & \Delta\varphi^j_R & -\Delta\mu^j_I \\ \Delta\mu^j_I & -\Delta\varphi^j_R & \Delta\varphi^j_I & \Delta\mu^j_R \end{pmatrix}^{-1} \begin{pmatrix} C^i_R \\ C^i_I \\ C^j_R \\ C^j_I \end{pmatrix} \quad (7)$$

where *R, I, e, o* refer to the real, imaginary, even and odd parts of the relevant function. The solution makes use of an *a priori* known symmetry that in the case of a laterally homogeneous crystal the Green's function is one-dimensional. In this case each discrete line of the image contains all the information we seek to retrieve; since there are many such lines in the output of a conventional two-dimensional detector we may perform a suitable average to greatly reduce noise artifacts. Eq. (7) is the unambiguous deterministic solution for the complex Green's function we were seeking and we now present the experimental reconstruction applied to a thick perfect silicon crystal.

The problem, as stated previously and solved by Eq. (7), is to reconstruct $G$ given $\psi(\mathbf{r}_\perp, z = z_0)$ and $|\Psi(\mathbf{r}_\perp, z = z_0 + z_1)|$ and so we must now account for how the two latter *known* quantities are measured. Clearly $|\Psi(\mathbf{r}_\perp, z_0 + z_1)|$ can be measured by recording the intensity in the manner spec-

ified by Fig. 1 but $\psi(\mathbf{r}_\perp, z = z_0)$ is a complex quantity, the phase of which cannot be measured directly. The magnitude $|\psi(\mathbf{r}_\perp, z_0)|$ is easily measured by placing the detector at the plane $z_0$ - this was done and Fig. 2(a) is the result. The phase of $\psi(\mathbf{r}_\perp, z_0)$ was calculated from Fig. 2(a) using the transport-of-intensity phase retrieval algorithm [22] and the result is shown in Fig 2(b). The remaining input $|\Psi(\mathbf{r}_\perp, z_0 + z_1)|$ discussed previously is shown in Fig 2(c).

The weak interaction element was fabricated by etching a binary, non-periodic pattern [23] of 0.8$\mu$m depth (400 nm lateral resolution) into a 0.8mm thick $SiO_2$ substrate using electron beam lithography. The pattern is approximately 2.5mm in diameter. We ensure that the wavefield transmitted through the weak interaction element will have a continuous spatial Fourier spectrum by choosing an aperiodic pattern. The experiments were conducted at the BL20XU undulator beamline at SPring-8 using 20keV X-rays from a double Si (111) monochromator. The X-ray beam size was approximately 4(hor) $\times$ 2(ver) mm at 245 m from the source, $z_0$ = 1.2m and $z_1$ = 0.06m. Images were recorded using a Hamamatsu CCD detector coupled to an optical lens and phosphor screen with a 0.9 $\mu$m effective pixel size and 2(hor) $\times$ 1.3(ver) mm field of view.

Fig. 2(c) was measured with the crystal slightly detuned from the (111) Bragg reflection so that 70% of the direct beam was reflected. The magnification of Fig. 2(c) indicates the crystal was cut asymmetrically by 0.8° to the (111) plane - the demagnification of which can be accounted for in the reconstruction algorithm. Fig. 2 represents all of the inputs to the algorithm of Eq. (7) that allows reconstruction of $G$.

The results of the reconstruction are presented in Fig. 3(a) and (b) which show the reconstructed squared modulus and phase of the Green's function of the thick perfect silicon analyzer crystal using Eq. (7) and the classic prediction of dynamical diffraction [11]. The causes of the discrepancy between the predicted Green's function and the reconstruction merits further discussion which we turn to now.

The grey shaded regions show the condition number of the inverse matrix in Eq. (7) and represents the region of validity of the reconstruction. A large condition number indicates that the output of Eq. (7) varies significantly upon a small change in the input and so at this point the solution is numerically unstable. At high spatial frequencies the large condition number is due to the low power scattered into these frequencies. The large condition number in the vicinity of the DC frequency is due to the increased susceptibility to noise at this point because the odd components of $\tilde{G}$ in Eq. (7) must be zero at this point meaning that all information is carried in only the two even components.

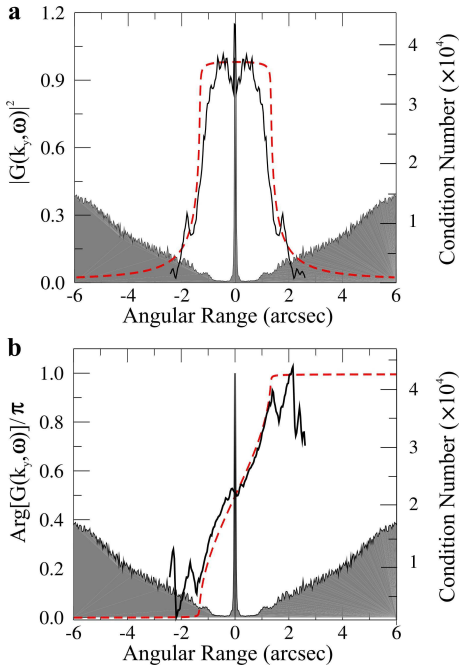


FIG. 3: (Color online). (a) $|G(k_y,\omega)|^2$ - squared magnitude of the reconstructed Green's function for the silicon analyzer crystal (solid black line) and theoretical prediction (broken red line), (b) Arg$[G(k_y,\omega)]$ - phase corresponding to (a). The condition number of the solution is shown for each angular space point.

The angular range of the single image reconstruction is Nyquist limited by the detector pixel size however in practice it is less than that limit. The resolution of the reconstruction is inversely proportional to the number of pixels used in the image. The reconstructions in Fig. 3 were calculated using a 512 square pixel sub-image of Fig. 2 yielding a angular resolution at least equal high resolution X-ray diffraction. The major problem in the analysis was the alignment of the images which must be achieved to single pixel accuracy.

In conclusion we have demonstrated the reconstruction of the complex Green's function for a perfect single crystal of silicon. The wavefield transmitted through the weak interaction element was measured after introducing some phase contrast to increase the effective attenuation at the entrance surface of the imaging system and its phase over this plane was inferred. The measurements relating to the weak object need be conducted once only and can be used to reconstruct a wide variety of complex Green's functions. The reconstruction quantitatively agrees with the prediction of the

dynamical theory of X-ray diffraction for perfect crystals.

Whilst the experiment we have presented is specifically related to crystallography we note that the technique is applicable to a very wide class of complex Green's functions. The technique as demonstrated here uses only a single intensity image or probability density, after the weak interaction element has been characterised, and as such is suitable to tomographic and real-time applications. The technique is an unambiguous, analytic approach for reconstructing complex Green's functions.

DJV acknowledges the German Academic Exchange Service (DAAD) and Frau R Eberlein, and the Australian Postgraduate Award. DJV, DMP and KMP acknowledge funding from the Australian Research Council (ARC) and Access to Major Research Facilities (AMRF). The synchrotron radiation experiments were performed at the BL20XU in SPring-8 with the approval of the Japan Synchrotron Radiation Research Institute (JASRI) (Proposal No.2007A1173-NL-np). DJV acknowledges useful discussions with Dr John Gillam.

---

[1] J. J. Sakurai, *Advanced Quantum Mechanics* (Addison-Wesley, New York, 1967).

[2] M. Born and E. Wolf, *Principles of Optics* (Cambridge University Press, Cambridge, 1999), seventh (expanded) ed.

[3] K. Wapenaar, Phys. Rev. Lett. **93**, 254301 (2004).

[4] K. Wapenaar, E. Slob, and R. Snieder, Phys. Rev. Lett. **97**, 234301 (2006).

[5] B. A. van Tiggelen, Phys. Rev. Lett. **91**, 243904 (2003).

[6] M. Campillo and A. Paul, Science **299**, 547 (2003).

[7] J. D. Jackson, *Classical Electrodynamics* (Wiley, New York, 1998), 3rd ed.

[8] J. M. Cowley, *Diffraction Physics* (North-Holland Publishing Company, Amsterdam, 1995), 3rd ed.

[9] D. J. Vine, D. M. Paganin, K. M. Pavlov, J. Kräußlich, O. Wehrhan, I. Uschmann, and E. Förster, Appl. Phys. Lett. **91**, 254110 (2007).

[10] D. M. Paganin, *Coherent X-Ray Optics* (Oxford University Press, New York, 2006).

[11] A. Authier, *Dynamical Theory of X-Ray Diffraction* (Oxford University Press, Oxford, 2005), revised ed.

[12] P. V. Petrashen' and F. N. Chukhovskii, Sov. Phys. Dokl. **34**, 957 (1989).

[13] A. M. Afanas'ev and V. G. Kon, Sov. Phys. JETP **47**, 154 (1978).

[14] S. G. Podorov, V. I. Punegov, and V. A. Kusikov, Phys. Solid State **36**, 454 (1994).

[15] D. J. Vine, D. M. Paganin, K. M. Pavlov, and S. G. Podorov, J. Appl. Cryst. **40**, 650 (2007).

[16] Ya. I. Nesterets, T. E. Gureyev, D. Paganin, K. M. Pavlov, and S. W. Wilkins, J. Phys. D **37**, 1262 (2004).

[17] A. A. Snigirev, I. I. Snigreva, V. G. Kohn, S. Kuznetsov, and I. A. Schelokov, Rev. Sci. Instrum. **66**, 5486 (1995).

[18] K. A. Nugent, T. E. Gureyev, D. F. Cookson, D. Paganin, and Z. Barnea, Phys. Rev. Lett. **77**, 2961 (1996).

[19] S. W. Wilkins, T. E. Gureyev, D. Gao, A. Pogany, and A. W. Stevenson, Nature **384**, 335 (1996).

[20] D. Paganin and K. A. Nugent, Phys. Rev. Lett. **80**, 2586 (1998).

[21] L. Mandel and E. Wolf, *Optical Coherence and Quantum Optics* (Cambridge University Press, Cambridge, 1995).

[22] D. M. Paganin, S. C. Mayo, T. E. Gureyev, P. R. Miller, and S. W. Wilkins, J. Microsc. **206**, 33 (2002).

[23] Johann Frederick (der Grossmuetige), founder of Friedrich-Schiller University.

# Appendix E

## Wide angle dynamical diffraction by deformed crystals: recurrence relations

This appendix presents a reprint of the paper

> "Wide angle dynamical diffraction by deformed crystals: recurrence relations"
> K. M. Pavlov, D. M. Paganin, D. J. Vine and L. Kirste
> *Physica status solidi A*, **8**, 2613 (2007)

This paper describes a new theoretical development in the two beam approximation of dynamical diffraction from deformed crystals. The linearised dispersion surface in the usual Takagi formulation is true only for a limited range about the Laue point. This paper introduces a new angular parameter which is valid over a larger angular range than the planar approximation to the dispersion surface.

The bulk of this paper was presented by Dr Konstantin Pavlov at the XTOP2006 conference on high resolution X-ray diffraction and imaging in Baden-Baden, Germany in late 2006. The theoretical developments were developed by Dr Pavlov in conjunction with Dr Sergey Podorov and Dr David Paganin. The numerical simulations were implemented by Dr Pavlov. This research was conducted as I was just beginning to study dynamical diffraction and as such my input was limited to group discussions providing feedback on drafts.

Overall, I estimate my contribution to this paper to be approximately 5%.

physica status solidi pss a
www.pss-a.com
applications and materials science

# Wide angle X-ray dynamical diffraction by deformed crystals: recurrence relations

**K. M. Pavlov**[1, 2], **D. M. Paganin**[2], **D. J. Vine**[2], and **L. Kirste**[3]

[1] Monash Centre for Synchrotron Science, Monash University, Victoria 3800, Australia
[2] School of Physics, Monash University, Victoria 3800, Australia
[3] Fraunhofer Institut für Angewandte Festkörperphysik (FhG-IAF), 79108 Freiburg, Germany

Received 20 September 2006, revised 10 January 2007, accepted 20 February 2007
Published online 1 August 2007

**PACS** 61.10.Dp, 61.10.Nz

Dynamical wide-angle multiwave X-ray diffraction from a deformed crystal was considered, for the special case when no more than one strong reflection occurs at a time. The obtained set of equations can be transformed to the Takagi two-beam approximation if the scattering vector is close to a vector of the reciprocal lattice. The new formalism was employed to obtain recurrence relations for the amplitude reflection coefficient corresponding to laterally homogeneous multilayer structures for the case of coplanar Bragg diffraction.

phys. stat. sol. (a) **204**, No. 8, 2613–2619 (2007) / **DOI** 10.1002/pssa.200675663

Original Paper

phys. stat. sol. (a) **204**, No. 8, 2613–2619 (2007) / **DOI** 10.1002/pssa.200675663

# Wide angle X-ray dynamical diffraction by deformed crystals: recurrence relations

**K. M. Pavlov**[*, 1, 2], **D. M. Paganin**[2], **D. J. Vine**[2], and **L. Kirste**[3]

[1] Monash Centre for Synchrotron Science, Monash University, Victoria 3800, Australia
[2] School of Physics, Monash University, Victoria 3800, Australia
[3] Fraunhofer Institut für Angewandte Festkörperphysik (FhG-IAF), 79108 Freiburg, Germany

Received 20 September 2006, revised 10 January 2007, accepted 20 February 2007
Published online 1 August 2007

**PACS** 61.10.Dp, 61.10.Nz

Dynamical wide-angle multiwave X-ray diffraction from a deformed crystal was considered, for the special case when no more than one strong reflection occurs at a time. The obtained set of equations can be transformed to the Takagi two-beam approximation if the scattering vector is close to a vector of the reciprocal lattice. The new formalism was employed to obtain recurrence relations for the amplitude reflection coefficient corresponding to laterally homogeneous multilayer structures for the case of coplanar Bragg diffraction.



## 1 Introduction

High-resolution X-ray diffraction (HRXRD) is a well-developed non-destructive characterisation technique [1, 2] for the investigation of complex multilayer structures. The standard variant of the Takagi–Taupin equations [3–5], usually employed for the simulation of HRXRD, has two well-known deficiencies (see e.g., [6]): a) the use of two-beam approximations in which only one strong reflection is taken into account, and b) the assumption that the angular deviation from the Bragg position, $\theta_B$, is small: $|\theta - \theta_B| \ll 1$. Several approaches were proposed to address these problems, some of them employing multiwave diffraction. However these approaches attack either one or the other of the two problems [7–11]. In [12] three-beam dynamical diffraction was considered, using a two-dimensional Bloch wave approach. To the best of our knowledge, dynamical diffraction theory in arbitrary deformed crystals in the case of large deviations from the Bragg conditions has not been developed, despite such situations routinely occurring in HRXRD experiments with highly deformed multilayer structures. Note, also, that to overcome the previously-mentioned problems some authors use a kinematical approach based on direct summation of waves, scattered by individual atomic planes [13, 14]. Recently, we suggested a new approach [15] to X-ray dynamical diffraction theory in distorted crystals. This approach allows one to perform simulations between Bragg peaks for non-ideal crystals, using an approach in a simple form of two distorted waves, similar to that used by Caticha [16].

Here we have reformulated the approach presented in [15], using a multiwave representation for the registered wavefields. We apply our new approach to modify the recurrence relations [17, 18] for a wide angular deviation range in the case of laterally homogeneous multilayer structures.

This article considers coplanar diffraction in the case of dynamical multiwave wide-angle diffraction in the absence of several simultaneously-strong diffracted waves. Such conditions imply that each of the

[*] Corresponding author: e-mail: Konstantin.Pavlov@sci.monash.edu.au

physica status solidi a



diffracted waves interacts dynamically with the incident beam and itself, and kinematically with the other diffracted waves.

## 2 Theory

Consider X-ray diffraction by a crystal in terms of dynamical diffraction theory. From the microscopic (non-averaged) Maxwell equations (see e.g., [19]) one can obtain, for a monochromatic wave, the following equation for the electric field $\boldsymbol{E}$ (see e.g., [20, 21]):

$$\nabla\times[\nabla\times\boldsymbol{E}]-k^2(1+\chi(\boldsymbol{r}))\,\boldsymbol{E}=0\,, \tag{1}$$

where $\chi(\boldsymbol{r})$ is the polarisability, $k=2\pi/\lambda$, and $\lambda$ is the X-ray wavelength in vacuum.

We seek the solution of Eq. (1) in the case of coplanar diffraction as a composition of the incident (wavevector $\boldsymbol{k}_0$) and registered (wavevector $\boldsymbol{k}_s$) waves [15]:

$$\boldsymbol{E}(\boldsymbol{r},\boldsymbol{s})=\boldsymbol{E}_0(\boldsymbol{r},\boldsymbol{s})\exp(i\boldsymbol{k}_0\boldsymbol{r})+\boldsymbol{E}_s(\boldsymbol{r},\boldsymbol{s})\exp(i\boldsymbol{k}_s\boldsymbol{r})\,. \tag{2}$$

Here, $\boldsymbol{E}_0(\boldsymbol{r},\boldsymbol{s})$ is assumed to be a slowly varying function, and $|\boldsymbol{k}_0|=|\boldsymbol{k}_s|=k$. Note that the propagation direction $\boldsymbol{k}_s$, of the second wave in Eq. (2), is determined by the registration system. The vectors $\boldsymbol{k}_{0,s}$ and the scattering vector $\boldsymbol{s}=\boldsymbol{k}_s-\boldsymbol{k}_0$ are determined by the experimental setup. It should also be noted that in our approach we do not introduce the wave vector of the registered wave as a sum of the wavevector of the incident wave, $\boldsymbol{k}_0$, and the appropriate vector of the reciprocal lattice, $\boldsymbol{g}$. Such a choice of the wavevector $\boldsymbol{k}_s$ has an obvious advantage of direct connection to the particular experimental setup. However, this definition of the vector $\boldsymbol{k}_s$ may cause fast variations of the function $\boldsymbol{E}_s(\boldsymbol{r},\boldsymbol{s})$. For instance, if the scattering vector $\boldsymbol{s}$ is close to the particular reciprocal lattice vector $\boldsymbol{g}$, the function $\boldsymbol{E}_s(\boldsymbol{r},\boldsymbol{s})$ can be represented, to a first approximation, as a product of a slowly varying function and the exponential term $\exp(i(\boldsymbol{g}-\boldsymbol{s})\,\boldsymbol{r})$. Later in the paper we show that this problem can be solved by representing the function $\boldsymbol{E}_s(\boldsymbol{r},\boldsymbol{s})$ as a sum, over the reciprocal lattice vectors $\boldsymbol{g}$, of products of certain slowly varying functions and exponential terms $\exp(i(\boldsymbol{g}-\boldsymbol{s})\,\boldsymbol{r})$. This implies that, despite the fact that Eq. (2) is similar in form to the standard two-beam diffraction solution, it intrinsically contains multiwave diffraction. A similar approach was used in [22], where we employed (in the two-beam approximation) external boundary conditions to connect the internal wavefield with the wavevectors $\boldsymbol{k}_g=\boldsymbol{k}_0+\boldsymbol{g}$, together with the particular external propagation direction determined by the vector $\boldsymbol{k}_s$.

After substitution of Eq. (2) into Eq. (1), and omitting functional arguments for clarity, we obtain:

$$[2i(\boldsymbol{k}_0\cdot\nabla)\,\boldsymbol{E}_0+k^2\chi\boldsymbol{E}_0]\exp(i\boldsymbol{k}_0\boldsymbol{r})+[2i(\boldsymbol{k}_s\cdot\nabla)\,\boldsymbol{E}_s+k^2\chi\boldsymbol{E}_s]\exp(i\boldsymbol{k}_s\boldsymbol{r})=0\,. \tag{3}$$

Herewith, we neglect the second derivatives of functions $\boldsymbol{E}_{0,s}(\boldsymbol{r},\boldsymbol{s})$ and assume, as usual, that $\nabla\cdot\boldsymbol{E}\approx 0$ [20]. We assume that neglecting the second derivatives of $\boldsymbol{E}_s(\boldsymbol{r})$ in our case (when only one strong reflection occurs at a time) is valid, despite the existence of rapidly oscillating terms $\exp(i(\boldsymbol{g}-\boldsymbol{s})\,\boldsymbol{r})$, because the term with second derivatives of $\boldsymbol{E}_s(\boldsymbol{r})$ is sufficiently smaller than other terms including the function $\boldsymbol{E}_s(\boldsymbol{r})$ and its first derivative, with increasing difference between $\boldsymbol{g}$ and $\boldsymbol{s}$. Another argument in support of the validity of such an operation is that our final results, in the limit of small differences between $\boldsymbol{g}$ and $\boldsymbol{s}$, transform to the well-known results of the Takagi and Taupin equations [3–5]. Note that we do not consider the case of grazing incidence, where one cannot neglect the second derivatives of $\boldsymbol{E}_{0,s}(\boldsymbol{r})$ (see [23] and references therein).

To describe the polarisability of the crystal we employ the standard Takagi-type [3, 4] representation:

$$\chi_m(\boldsymbol{r})=\sum_{\boldsymbol{g}}\hat{\chi}_{g,m}\,\mathrm{e}^{i\boldsymbol{g}(\boldsymbol{r}-\boldsymbol{u}(\boldsymbol{r}))}\,, \tag{4}$$

where the index $m$ corresponds to a particular area of chemical homogeneity. In other words, the Fourier coefficients $\hat{\chi}_{g,m}$ are functions of the coordinates. The sum in Eq. (4) is over all reciprocal lattice vectors.

 

Original Paper



To proceed further with Eq. (3), we need to implement averaging over a suitable volume. In the literature there are at least two variants on how to choose such a volume. One variant is to use a volume $V$ with linear dimensions $\tilde{L}$, where $a \ll \tilde{L} \ll \Lambda_{\text{ext}}$, $a$ is the lattice parameter, and $\Lambda_{\text{ext}}$ is the extinction length (see e.g., [20]). The second variant, of averaging over a unit cell, was employed e.g. in Takagi's paper [4]. In the current paper we average over the volume $V$, and use a special form (Eq. (5)) for the function $E_s$, to avoid problems with rapidly-oscillating terms.

To proceed with the integration we represent the wavefield, $E_s$ in the following form:

$$E_s(\boldsymbol{r},\boldsymbol{s}) = \exp(-i\boldsymbol{s}\boldsymbol{r}) \sum_g E_g(\boldsymbol{r},\boldsymbol{s}) \exp(i\boldsymbol{g}(\boldsymbol{r}-\boldsymbol{u}(\boldsymbol{r}))), \tag{5}$$

where $E_g(\boldsymbol{r},\boldsymbol{s})$ are slowly varying functions, and the sum (as in Eq. (4)) is over the reciprocal lattice vectors. Note that we have explicitly separated out the oscillating exponential terms, and made use of the fact that a general solution of the diffraction problem within a crystal [21, 24] can be represented as a product of a certain function by a sum of waves, the wavevectors of which are vectors of the reciprocal lattice.

First we substitute Eqs. (4) and (5) into Eq. (3), then multiply by the factor $\exp(-i\boldsymbol{k}_0\boldsymbol{r})$, and, after averaging over $V$, we obtain the following expression:

$$2i(\boldsymbol{k}_0 \cdot \nabla)\, \boldsymbol{E}_0 + k^2 \hat{\chi}_{0,m} \boldsymbol{E}_0 + k^2 \hat{\chi}_{-g,m} \boldsymbol{E}_g + \psi_1(\boldsymbol{s},\boldsymbol{g},\boldsymbol{r}) = 0. \tag{6}$$

The same procedure with multiplicative factor $\exp(-i\boldsymbol{k}_s\boldsymbol{r})$ gives

$$\sum_g \left[ \left\{ \int_V \mathrm{e}^{-i\boldsymbol{g}\boldsymbol{u}(\boldsymbol{r})}\, \mathrm{e}^{i(\boldsymbol{g}-\boldsymbol{s})\boldsymbol{r}} \right\} \times \left\{ 2i(\boldsymbol{k}_s \cdot \nabla)\, \boldsymbol{E}_g - 2\boldsymbol{k}_s(\boldsymbol{g}-\boldsymbol{s}-\nabla(\boldsymbol{g}\boldsymbol{u}(\boldsymbol{r})))\, \boldsymbol{E}_g + k^2 \hat{\chi}_{0,m} \boldsymbol{E}_g + k^2 \hat{\chi}_{g,m} \boldsymbol{E}_0 \right\} + \psi_2(\boldsymbol{s},\boldsymbol{g},\boldsymbol{r}) \right] = 0, \tag{7}$$

where the terms

$$\psi_1(\boldsymbol{s},\boldsymbol{g},\boldsymbol{r}) = k^2 \sum_{g' \neq g} [\hat{\chi}_{-g',m} \boldsymbol{E}_{g'}], \tag{8}$$

and

$$\psi_2(\boldsymbol{s},\boldsymbol{g},\boldsymbol{r}) = k^2 \boldsymbol{E}_g \sum_{g' \neq 0} \hat{\chi}_{g',m} \int_V \exp(i\boldsymbol{g}'\boldsymbol{r} - i\boldsymbol{g}'\boldsymbol{u}(\boldsymbol{r})) \exp(i(\boldsymbol{g}-\boldsymbol{s})\,\boldsymbol{r} - i\boldsymbol{g}\boldsymbol{u}(\boldsymbol{r})) + k^2 \boldsymbol{E}_0 \sum_{g' \neq g} \hat{\chi}_{g',m} \int_V \exp(i(\boldsymbol{g}'-\boldsymbol{s})\,\boldsymbol{r} - i\boldsymbol{g}'\boldsymbol{u}(\boldsymbol{r})), \tag{9}$$

are responsible for the dynamical interaction between waves related to different reflections. Thus Eqs. (6) and (7), which can be solved numerically, completely describe the wide-angle multiwave dynamical diffraction. The angular parameters in Eq. (7), $2\boldsymbol{k}_s \cdot (\boldsymbol{g}-\boldsymbol{s}-\nabla(\boldsymbol{g}\boldsymbol{u}(\boldsymbol{r})))$, do not suffer from the restriction of small angular deviations from the Bragg position, employed in the Takagi treatment [4]. Thus the formalism, described by Eqs. (6) and (7), allows us to overcome both deficiencies mentioned in the Introduction, namely (a) the use of a two-beam approximation; (b) the assumption that the angular deviation from the Bragg position is small. However, later in our article we consider only a special case, often occurring in HRXRD experiments, when no more than one strong reflection occurs at a time. Then the terms $\psi_{1,2}(\boldsymbol{s},\boldsymbol{g},\boldsymbol{r})$ can be neglected and analytical solutions can be obtained. To illustrate the validity of such a simplification we consider three cases. (i) First assume that $\boldsymbol{g} \sim \boldsymbol{s}$. In this case the exponential term $\exp(i(\boldsymbol{g}-\boldsymbol{s})\,\boldsymbol{r} - i\boldsymbol{g}\boldsymbol{u}(\boldsymbol{r}) - i\boldsymbol{g}'\boldsymbol{u}(\boldsymbol{r}))$ can be taken out of the integral, because it varies more slowly than the term $\exp(i\boldsymbol{g}'\boldsymbol{r})$. As a result we obtain a sum of delta functions, which is practically zero. (ii) As a

physica status solidi a



second (intermediate) case, we assume that there is a large difference between $\boldsymbol{g}$ and $\boldsymbol{s}$, but $\boldsymbol{s}$ is still far from any other reciprocal lattice vector $\hat{\boldsymbol{g}}$. Thus $\psi_2(\boldsymbol{s},\boldsymbol{g},\boldsymbol{r}) \approx k^2 \boldsymbol{E}_g \hat{\chi}_{s-g,m}$. However, since all other terms in Eq. (7) will be practically zero due to $\int_V \mathrm{e}^{-i\boldsymbol{g}\boldsymbol{u}(\boldsymbol{r})}\, \mathrm{e}^{i(\boldsymbol{g}-\boldsymbol{s})\boldsymbol{r}} \approx 0$, this implies that $\boldsymbol{E}_g \approx 0$, and so this harmonic can be neglected. (iii) If, finally, $\boldsymbol{s}$ is getting close to anothers vector $\hat{\boldsymbol{g}}$ the function $\psi_2(\boldsymbol{s},\boldsymbol{g},\boldsymbol{r}) \approx k^2 \boldsymbol{E}_0 \hat{\chi}_{\hat{g},m}\, \mathrm{e}^{-i\hat{\boldsymbol{g}}\boldsymbol{u}(\boldsymbol{r})}$, but all other components in Eq. (7) related to $\boldsymbol{E}_g$ are again very small because $\int_V \mathrm{e}^{-i\boldsymbol{g}\boldsymbol{u}(\boldsymbol{r})}\, \mathrm{e}^{i(\boldsymbol{g}-\boldsymbol{s})\boldsymbol{r}} \approx 0$.

Equation (7) is a sum which must always equal zero. This is possible only if each term of the sum is equal to zero. Thus we obtain a system of N pairs of linear differential equations, where N is the number of reciprocal-lattice vectors. These pairs are independent of one another. However, the functions $\boldsymbol{E}_{0,g}$ must satisfy the boundary conditions at the top and bottom surfaces of the crystal. For instance, at the top surface $E_0(\boldsymbol{r}_{\mathrm{top}},\boldsymbol{s}) = \tilde{E}_0$, while at the bottom surface $E_s(\boldsymbol{r}_b,\boldsymbol{s}) = \exp(-i\boldsymbol{s}\boldsymbol{r}_b) \times \sum_g E_g(\boldsymbol{r}_b,\boldsymbol{s}) \exp(i\boldsymbol{g}(\boldsymbol{r}_b - \boldsymbol{u}(\boldsymbol{r}_b))) = 0$, if there are no sources below this latter surface. Notwithstanding the fact that each of these pairs describes the entire dynamical interaction between the $\boldsymbol{E}_g$and $\boldsymbol{E}_0$ waves, there are no direct interactions between waves with different $\boldsymbol{g}$ after we neglected the terms $\psi_{1,2}(\boldsymbol{s},\boldsymbol{g},\boldsymbol{r})$ in Eqs. (6) and (7). The system of Eqs. (6) and (7) can be transformed to the case of multiwave kinematical diffraction by assuming that multiple-scattering effects, within each pair, are negligible. This is equivalent to setting $\hat{\chi}_{-g,m} \equiv 0$ in Eqs. (6) and (7). The Takagi-type Eqs. (6) and (7) describe the case of dynamical diffraction by a deformed crystal, without the restrictions of small angular deviation from a Bragg condition. If the scattering vector, $\boldsymbol{s}$, is close to only one reciprocal vector $\boldsymbol{g}'$, one can consider only one pair of the differential equations, corresponding to this particular vector $\boldsymbol{g}'$; this is the two-beam approximation of the Takagi equations [4, 5].

## 3 Examples

We now consider several important limit cases of our approach. For simplicity we assume that the incident beam has sigma polarization and that the crystal is laterally homogeneous. As a consequence of this restriction all functions $E_g$ and $E_s$ (see Eq. (5)) should be functions of the $z$ coordinate only. This can be realized if each exponential term obeys the equation $\exp(-i(s_x - g_x - \partial(\boldsymbol{g}\boldsymbol{u}(z))/\partial x)) \equiv 1$, implying delta-like functions in the diffracted intensity distribution in the direction perpendicular to the surface.

### 3.1 Laterally infinite and laterally homogeneous crystal

We can rewrite Eqs. (6) and (7) in the following (scalar) form, for each pair $E_{0,g}$:

$$\frac{\mathrm{d}E_0}{\mathrm{d}z} = i\sigma_0(z)\, E_0 + i\sigma_{-g}(z)\, E_g\,, \qquad \frac{\mathrm{d}E_g}{\mathrm{d}z} = -i\sigma_g(z)\, E_0 - i(\eta_g(z) - \sigma_0(z))\, E_g\,. \tag{10}$$

Here $\eta_g(z) = (1+b)\,\sigma_0(z) + g_z - s_z - \frac{\partial}{\partial z}\boldsymbol{g}\boldsymbol{u}(z)$, $\sigma_0(z) = \frac{k\hat{\chi}_{0,m}(z)}{2\gamma_0}$, $\sigma_g(z) = \frac{k\hat{\chi}_{g,m}(z)}{2\gamma_s}$, $\sigma_{-g}(z) = \frac{k\hat{\chi}_{-g,m}(z)}{2\gamma_0}$, $b = \gamma_0/\gamma_s$, $\gamma_0 = \sin\theta_1$, $\gamma_s = \sin\theta_2$, and $\theta_{1,2}$ are the angles between the surface and the vectors $\boldsymbol{k}_{0,s}$, respectively. After introducing the partial reflection coefficient $R_g = E_g/(E_0\sqrt{b})$, we can combine Eq. (10) in one Taupin-type [5] equation for the function $R_g$:

$$\frac{\mathrm{d}R_g}{\mathrm{d}z} = -i\sigma_{-g}(z)\, R_g^2\sqrt{b} - i\eta_g(z)\, R_g - i\sigma_g(z)\frac{1}{\sqrt{b}}\,. \tag{11}$$

 

Original Paper



This equation can be solved using the boundary condition at the bottom surface, assuming there to be no sources below this surface. To obtain the appropriate boundary condition we take into account that $E_s(\boldsymbol{r}_b, \boldsymbol{s}) = \exp(-i\boldsymbol{s}\boldsymbol{r}_b) \sum_g E_g(\boldsymbol{r}_b, \boldsymbol{s}) \exp(i\boldsymbol{g}\boldsymbol{r}_b) = 0$ only if each term of this sum is equal to zero. This yields the required boundary condition: $R_g(z_b, \boldsymbol{s}) = 0$.

The total reflection coefficient at the top of the crystal is then:

$$R = \frac{1}{\sqrt{b}} \frac{E_s(0, \boldsymbol{s})}{E_0(0, \boldsymbol{s})} = \frac{1}{\sqrt{b}} \frac{\sum_g E_g(0, \boldsymbol{s})}{E_0(0, \boldsymbol{s})} = \frac{\sum_g R_g(0, \boldsymbol{s})\, E_0(0, \boldsymbol{s})}{E_0(0, \boldsymbol{s})} = \sum_g R_g(0, \boldsymbol{s}) \,. \tag{12}$$

### 3.2 Laterally infinite planparallel homogeneous slab with thickness $L_z$

Note that the function $\boldsymbol{u}(z) \equiv 0$ for this type of sample. Thus we can easily obtain the solution for the functions $E_{0,g}$ from Eq. (10), because for such a model $\eta_g$ and all coefficients $\sigma_{0,g,-g}$ are independent of $z$:

$$\begin{aligned} E_0 &= A_{1,g} \exp\left[\frac{i}{2}(\xi_{0,g} + \xi_g) z\right] + A_{2,g} \exp\left[\frac{i}{2}(\xi_{0,g} - \xi_g) z\right], \\ E_g &= B_{1,g} \exp\left[\frac{i}{2}(\xi_{0,g} + \xi_g) z\right] + B_{2,g} \exp\left[\frac{i}{2}(\xi_{0,g} - \xi_g) z\right]. \end{aligned} \tag{13}$$

Here, $\xi_g = \sqrt{\eta_g^2 - 4\sigma_g \sigma_{-g}}$ and $\xi_{0,g} = 2\sigma_{0,g} - \eta_g$. The constants $A_i$ and $B_i$ are connected as $B_i = p_i A_i$, where:

$$p_{1,g} = \frac{-\eta_g + \xi_g}{2\sigma_{-g}}, \qquad p_{2,g} = \frac{-\eta_g - \xi_g}{2\sigma_{-g}}. \tag{14}$$

Using the boundary conditions $E_0(0, \boldsymbol{s}) = \tilde{E}_0$ and $E_g(L_z, \boldsymbol{s}) = 0$, we obtain the coefficients $A_{1,2}$:

$$A_{1,g} = \tilde{E}_0 \frac{p_{2,g}}{p_{2,g} - p_{1,g} \exp(iL_z \xi_g)}, \qquad A_{2,g} = \tilde{E}_0 \frac{p_{1,g} \exp(iL_z \xi_g)}{p_{1,g} \exp(iL_z \xi_g) - p_{2,g}}. \tag{15}$$

Finally we can obtain the partial reflection coefficient $R_g$ at the top surface ($z = 0$):

$$R_g = \frac{1}{\sqrt{b}} \frac{E_g(0, \boldsymbol{s})}{E_0(0, \boldsymbol{s})} = \frac{1}{\sqrt{b}} \frac{\sigma_g}{\sigma_{-g}} \frac{1 - \exp(iL_z \xi_g)}{p_{2,g} - p_{1,g} \exp(iL_z \xi_g)} \,. \tag{16}$$

To obtain the total reflection coefficient for this crystal one can use Eq. (12).

### 3.3 Laterally infinite planparallel homogeneous slab with thickness $L_z$, on a thick ideal substrate

A difference to the previous case is in the boundary condition at the bottom surface:

$$R_g(L_z, \boldsymbol{s}) = \frac{1}{\sqrt{b}} \frac{E_g(L_z, \boldsymbol{s})}{E_0(L_z, \boldsymbol{s})} = R_{g,\mathrm{sub}}(\boldsymbol{s}), \tag{17}$$

where $R_{g,\mathrm{sub}}$ is the partial reflection coefficient of the substrate for the $g^{\mathrm{th}}$ reflection.

physica status solidi a



Using Eq. (13)–(16) we obtain the partial reflection coefficient of such a double-layer system:

$$R_g\sqrt{b} = \frac{p_{1,g}\left(R_{g,\mathrm{sub}}\sqrt{b} - p_{2,g}\right) + p_{2,g}\left(p_{1,g} - R_{g,\mathrm{sub}}\sqrt{b}\right)\exp\left(i\xi_g L_m\right)}{R_{g,\mathrm{sub}}\sqrt{b} - p_{2,g} + \left(p_{1,g} - R_{g,\mathrm{sub}}\sqrt{b}\right)\exp\left(i\xi_g L_m\right)}. \tag{18}$$

The calculation of the partial reflection coefficient Eq. (18) requires only knowledge about the partial reflection coefficient of the underlying system and the characteristics of the particular layer defined in Eqs. (13)–(15). Thus Eq. (18) can be used to calculate the partial reflection coefficient of the laterally infinite stack of planparallel homogeneous slabs. However, in the multilayer system we have to take into account that each slab could have a different lattice constant. Therefore the function $\boldsymbol{g}\cdot\boldsymbol{u}(z)$ and its derivatives should be calculated (see e.g., [25]). The total reflection coefficient of such a multilayer system can be obtained using Eq. (12). In the limit case of small angular deviations from a Bragg reflection, this reflection coefficient formula transforms to the two-beam approximation [17, 18].

### 3.4 Semi-infinite ideal crystal (substrate)

For a semi-infinite crystal we can say that $\mathrm{d}R_g/\mathrm{d}z \equiv 0$ for Eq. (11). Then the solution of the appropriate quadratic equation with constant coefficients, for the appropriate partial reflection coefficient, is:

$$\sqrt{b}R_{g,\mathrm{sub}} = \frac{-\eta_g \pm \xi_g}{2\sigma_{-g}}\,. \tag{19}$$

To choose the sign in Eq. (19) one has to check which of the two waves in Eq. (13) will be evanescent, this being equivalent to $\mathrm{Im}\,(\xi_0 \pm \xi)$ being positive.

## 4 Conclusions

We have developed a multiwave dynamical-diffraction formalism in a deformed crystal for a special case when there is only one strong reflection at a time. We have shown how initial solution sought in the form of a two-beam approximation can be transformed to the multiwave diffraction case for large angular deviations from the Bragg positions. The proposed formalism was used for the simulation of coplanar dynamical X-ray diffraction between strong Bragg reflections in a deformed crystal. Figure 1 shows

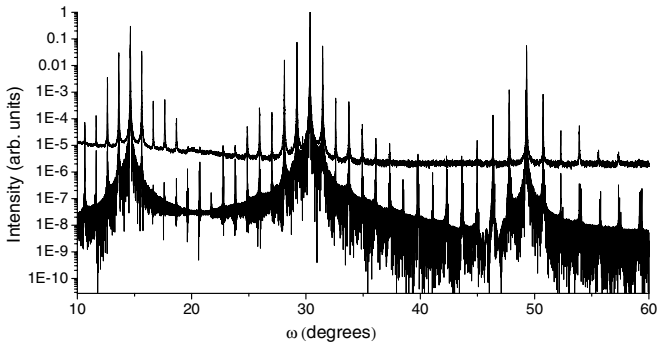


**Fig. 1** Experimental (upper) and simulated (lower) rocking curves for an InAs/GaInSb superlattice on a GaSb(001) substrate (the symmetrical coplanar diffraction case).

 

Original Paper



good agreement between the experimental and simulated rocking curves for an InAS/GaInSb superlattice grown on a GaSb substrate, in particular for the positions of the satellite peaks. The solution obtained for dynamical multiwave diffraction transforms to the two-beam approximation of the Takagi dynamical diffraction equations, if the scattering vector $\boldsymbol{s}$ is close to a vector of the reciprocal lattice. Several practically important models of crystals were considered and recurrence relations for the amplitude reflection coefficient in a wide angular range were developed for laterally homogeneous crystals.

**Acknowledgements** The authors acknowledge funding from the Australian Research Council. D. J. Vine gratefully acknowledges support from an Australian Postgraduate Award, together with the J. L. William Bequest. The authors also acknowledge discussions with Drs. V. Kaganer, I. Vartanyants and S. Podorov.

## References

[1] U. Pietsch, V. Holý, and T. Baumbach, High resolution X-ray scattering: from thin films to lateral nanostructures, 2nd edition (Springer-Verlag, New York, 2004).
[2] P. F. Fewster, X-ray scattering from semiconductors, 2nd edition (Imperial College Press, London, 2003).
[3] S. Takagi, Acta Crystallogr. **15**, 1311 (1962).
[4] S. Takagi, J. Phys. Soc. Jpn. **26**(5), 1239 (1969).
[5] D. Taupin, Bull. Soc. Fr. Mineral. Cristallogr. **87**, 469 (1964).
[6] M. Grundmann and A. Krost, phys. stat. sol. (b) **218**, 417 (2000).
[7] V. G. Kohn, J. Mosc. Phys. Soc. **1**, 425 (1991).
[8] R. Zaus, J. Appl. Cryst. **26**, 801 (1993).
[9] L. De Caro, C. Giannini, and L. Tapfer, Phys. Rev. B **56**, 9744 (1997).
[10] K. Okitsu, Acta Cryst. A **59**, 235 (2003).
[11] A. Souvorov, T. Ishikawa, A. Y. Nikulin, Y. P. Stetsko, S. L. Chang, and P. Zaumseil, Phys. Rev. B **70**, 224109 (2004).
[12] V. Holý and P. F. Fewster, J. Phys. D, Appl. Phys. **36**, A5 (2003).
[13] S. Zamir, O. Steinberg, U. Tisch, J. Salzman, and E. Zolotoyabko, J. Phys. D, Appl. Phys. **38**, A239 (2005).
[14] E. Zolotoyabko, J. Appl. Cryst. **31**, 241 (1998).
[15] S. G. Podorov, N. N. Faleev, K. M. Pavlov, D. M. Paganin, S. A. Stepanov, and E. Förster, J. Appl. Cryst. **39**, 652 (2006).
[16] A. Caticha, Phys. Rev. B **49**, 33 (1994).
[17] Yu. N. Belyaev and A. V. Kolpakov, phys. stat. sol. (a) **76**, 641 (1983).
[18] W. J. Bartels, J. Hornstra, and D. J. W. Lobeek, Acta Cryst. A **42**, 539 (1986).
[19] Z. G. Pinsker, Dynamical scattering of X-rays in crystals (Springer-Verlag, Berlin, 1978).
[20] A. M. Afanas'ev and V. G. Kohn, Acta Cryst. A **27**, 421 (1971).
[21] A. Authier, Dynamical theory of X-ray diffraction (revised edition, Oxford University Press, New York, 2005).
[22] L. Kirste, K. M. Pavlov, S. T. Mudie, V. I. Punegov, and N. Herres, J. Appl. Cryst. **38**, 183 (2005).
[23] S. A. Stepanov, E. A. Kondrashkina, R. Köhler, D. V. Novikov, G. Materlik, and S. M. Durbin, Phys. Rev. B **57**, 4829 (1998).
[24] P. P. Ewald, Ann. Physik **49**, 1 (1916); Ann. Physik **49**, 117 (1916); Ann. Physik **54**, 519 (1917).
[25] L. De Caro, C. Giannini, and L. Tapfer, J. Appl. Phys. **79**(8), 4101 (1996).

# Appendix F

## Simultaneous acquisition of dual analyser-based phase contrast X-ray images for small animal imaging

This appendix presents a reprint of the paper

> "Simultaneous acquisition of dual analyser-based phase contrast X-ray images for small animal imaging"
> M. J. Kitchen, K. M. Pavlov, S. B. Hooper, D. J. Vine, K. K. W. Siu, M. J. Wallace, M. L. L. Siew, N. Yagi, K. Uesugi and R. Lewis.
> *European Journal of Radiology* (in press), doi:10.1016/j.ejrad.2008.04.028

This paper describes experimental results where a thin silicon 111 Laue crystal was used to record diffracted and transmitted ABI images simultaneously. The simultaneous measurement of two ABI images is particularly useful for the DEI algorithm and its variants which require two measurements at different rocking curve positions to perform phase retrieval.

Dr Marcus Kitchen and Dr Konstantin Pavlov conceived the idea for the experiment and Dr Pavlov designed the analyser crystal. The experimental images related to physiological studies of Dr Stuart Hooper and Dr Megan Wallace. Dr Wallace and Ms Melissa Siew prepared the animals for imaging. Dr Karen Siu, Dr Kentaro Uesugi and I assisted with the execution of the experiment.

Overall, I estimate my contribution to this paper to be less than 5%.

+Model
EURR-3896; No. of Pages 5
ARTICLE IN PRESS

ELSEVIER

European Journal of Radiology xxx (2008) xxx–xxx

EJR
EUROPEAN JOURNAL OF RADIOLOGY

www.elsevier.com/locate/ejrad

# Simultaneous acquisition of dual analyser-based phase contrast X-ray images for small animal imaging

Marcus J. Kitchen [a,*], Konstantin M. Pavlov [a,b,c], Stuart B. Hooper [d], David J. Vine [a], Karen K.W. Siu [a,b], Megan J. Wallace [d], Melissa L.L. Siew [d], Naoto Yagi [e], Kentaro Uesugi [e], Rob A. Lewis [a,b]

[a] *School of Physics, Monash University, Victoria 3800, Australia*
[b] *Monash Centre for Synchrotron Science, Monash University, Victoria 3800, Australia*
[c] *Physics and Electronics, School of Science and Technology, University of New England, NSW 2351, Australia*
[d] *Department of Physiology, Monash University, Victoria 3800, Australia*
[e] *SPring-8/JASRI, Sayo, Japan*

Received 15 April 2008; accepted 25 April 2008

**Abstract**

Analyser-based phase contrast X-ray imaging can provide high-contrast images of biological tissues with exquisite sensitivity to the boundaries between tissues. The phase and absorption information can be extracted by processing multiple images acquired at different analyser orientations. Recording both the transmitted and diffracted beams from a thin Laue analyser crystal can make phase retrieval possible for dynamic systems by allowing full field imaging. This technique was used to image the thorax of a mechanically ventilated newborn rabbit pup using a 25 keV beam from the SPring-8 synchrotron radiation facility. The diffracted image was produced from the (1 1 1) planes of a 50 mm × 40 mm, 100 μm thick Si analyser crystal in the Laue geometry. The beam and analyser were large enough to image the entire chest, making it possible to observe changes in anatomy with high contrast and spatial resolution.


*Keywords:* Phase contrast; Animal imaging; Dynamic systems; Phase retrieval

## 1. Introduction

For more than a decade researchers have exploited the exceptional image contrast achieved when a monochromatic X-ray beam is passed through an object and then reflected from a near-perfect analyser crystal aligned near to a Bragg condition. The additional 'phase contrast' results from the analyser's reflectivity being sensitive to the small phase changes imparted to the X-ray wavefield upon transmission through the object. This contrast enhancement is particularly beneficial when imaging biological tissues that only produce weak absorption contrast between adjacent tissues [1,2].

It can be useful to separate the absorption component of the contrast from the phase component to ascertain how X-rays interact with the object's macroscopic structure. This 'phase retrieval' procedure requires at least two images of the object to be acquired with the analyser aligned at different orientations with respect to the incident beam (see, e.g., [3] and references therein). Numerous phase retrieval methods have been proposed but most require the analyser to be realigned between exposures. This prevents dynamic processes from being recorded, yet phase retrieval is possible for stationary objects. However, by simultaneously recording the beams diffracted and transmitted by the crystal, two images can be obtained that provide differing phase contrast [4,5]. Chapman et al. demonstrated that phase retrieval can be performed using these images alone [5], but the use of a narrow beam prevented that system from imaging

* Corresponding author. Tel.: +61 0 3 99058063; fax: +61 0 3 99053637.
*E-mail addresses:* Marcus.Kitchen@sci.monash.edu.au (M.J. Kitchen), Konstantin.Pavlov@sci.monash.edu.au (K.M. Pavlov), Stuart.Hooper@med.monash.edu.au (S.B. Hooper), David.Vine@sci.monash.edu.au (D.J. Vine), Karen.Siu@sci.monash.edu.au (K.K.W. Siu), Megan.Wallace@med.monash.edu.au (M.J. Wallace), Melissa.Siew@med.monash.edu.au (M.L.L. Siew), yagi@spring8.or.jp (N. Yagi), ueken@spring8.or.jp (K. Uesugi), Rob.Lewis@sync.monash.edu.au (R.A. Lewis).

0720-048X/$ – see front matter © 2008 Elsevier Ireland Ltd. All rights reserved.
doi:10.1016/j.ejrad.2008.04.028

Please cite this article in press as: Kitchen MJ, et al., Simultaneous acquisition of dual analyser-based phase contrast X-ray images for small animal imaging, Eur J Radiol (2008), doi:10.1016/j.ejrad.2008.04.028

+Model
EURR-3896; No. of Pages 5
ARTICLE IN PRESS



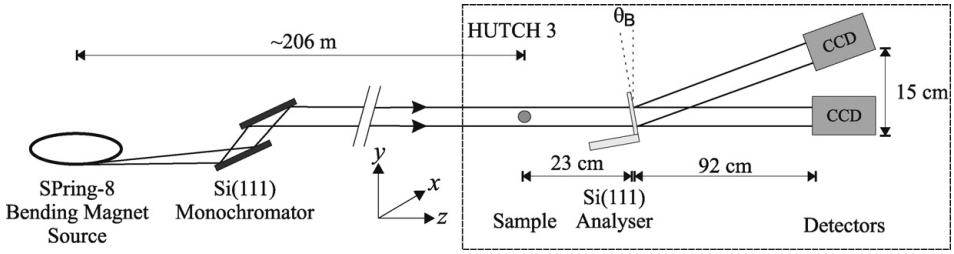


Fig. 1. Schematic of the dual-imaging Laue ABI geometry.

dynamic processes in macroscopic biological objects. Tomographic reconstructions using simulated images for the Laue geometry were also performed within the geometrical optics approximation by Bushuev and Guskova [6]. Moreover, we have shown that, in principal, it is possible to simultaneously acquire two phase contrast images of small animals in motion using a large synchrotron beam combined with an equally large analyser crystal and area detector using the Bragg geometry [7]. Here we successfully demonstrate the feasibility of using a Laue analyser crystal to image dynamic structural changes occurring within the body of a rabbit pup in near real-time with the ability to separate phase and absorption information. Furthermore, a new phase retrieval algorithm is presented for this imaging modality.

## 2. Materials and methods

For the analyser crystal we employed a 100 μm thick silicon wafer that was part of a monolithic silicon slab, connected at the base and sides, to minimise warping of the atomic planes. The thickness was chosen to provide a strong diffracted beam at the Bragg peak with minimal transmittance at 25 keV, which is a suitable energy for phase contrast imaging of small animals [8], for the Si(1 1 1) Bragg reflection. The (1 $\bar{1}$ 0) face of the wafer had an area of 50 mm × 40 mm, which is large enough to image small animals without scanning. Fig. 1 illustrates the experimental setup.

Experiments were performed at SPring-8, Japan, with images acquired in Hutch 3 of beamline 20B2 in the Biomedical Imaging Centre. 25 keV X-rays were selected from the bending magnet radiation using a Si(1 1 1) double-bounce monochromator in a non-dispersive setup with the analyser. Two optically coupled Hamamatsu CCD cameras (C4742-95HR and C4880-41S) with 10 μm thick phosphor screens were placed as shown in Fig. 1 to simultaneously capture the transmitted and diffracted images. Each CCD had 4000 × 2624 pixels with an effective pixel size of 5.9 μm, providing an active area of 23.6 mm × 15.5 mm. The CCDs were configured in 2 × 2 binning mode to improve the signal-to-noise ratio.

The rocking curves of the transmitted and diffracted beams were measured by averaging the intensity recorded in a 50 × 50 pixel square at the centre of each beam using the two CCDs whilst rotating the analyser through the Bragg condition (Fig. 2). The detector dark current offset was first subtracted from each image, as was also done for each image of the object. Fig. 2 reveals that the diffracted beam was typically less than one quarter of the transmitted intensity, making the signal-to-noise ratio significantly higher for the transmitted images. The low intensity of the diffracted beam at the Bragg peak was due partially to beam divergence, polychromaticity and imperfections within the crystal (including strain), and as a result of the average crystal thickness being a few microns less than the intended 100 μm thickness.

To test the image system and phase retrieval algorithm (outlined below), a PMMA cylinder of 3.25 mm diameter was imaged. Images were acquired at multiple analyser orientations with an exposure time of 0.3 s.

As a model for studying biological structures in motion, the fluid filled lungs of a fetal rabbit pup were mechanically inflated using an air-filled syringe pump. The rabbit was first killed by an overdose of nembutal in accordance with regulations set by Monash University and the SPring-8 Animal Care and Use Committee. The exposure time of each image was 0.3 s with a frame rate of 1.7 Hz.

### 2.1. Phase retrieval

Under the limits of the geometrical optics approximation (see, e.g., [1,3] and references therein) the intensity incident on the detector is given by

$$I_{D,T} = I_R R_{D,T}(\theta + \Delta\theta_Y), \quad (1)$$

where $I_R$ is the intensity of the beam after passing through the object, which reduces to $I_O$ with no sample in the beam. $\theta$ is

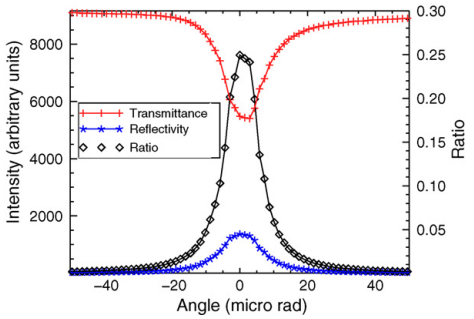


Fig. 2. Measured diffracted and transmitted rocking curves and their ratio $R_D(q)/R_T(q)$ for the 100 μm thick Si(1 1 1) Laue wafer at 25 keV.

Please cite this article in press as: Kitchen MJ, et al., Simultaneous acquisition of dual analyser-based phase contrast X-ray images for small animal imaging, Eur J Radiol (2008), doi:10.1016/j.ejrad.2008.04.028

+Model
EURR-3896; No. of Pages 5
ARTICLE IN PRESS
M.J. Kitchen et al. / European Journal of Radiology xxx (2008) xxx–xxx 3

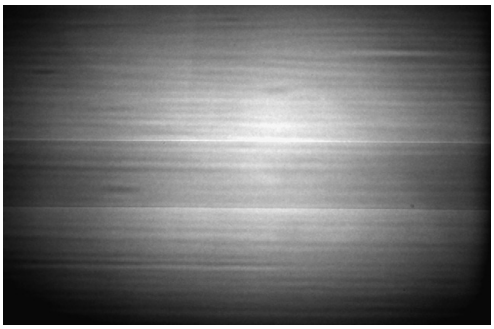

Fig. 3. Transmitted image of the PMMA cylinder.

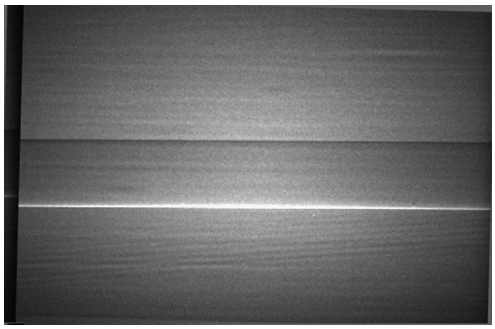

Fig. 4. Diffracted image of the PMMA cylinder.

the angle of incidence of the beam on the crystal with no object present, $\Delta\theta_Y$ is the change in angle imposed by the object in the $y$-direction parallel to the diffraction axis (Fig. 1) and $R(\theta)$ is the rocking curve of the diffracted ($D$) and transmitted beams ($T$) [9,10]. Early attempts to retrieve phase information from this type of system approximated the rocking curves as linear functions and solved (1) for the apparent absorption image ($I_R$) and the refraction angle image ($\Delta\theta_Y$); however, they met with limited success [5]. Since the rocking curve for our transmitted beam was comparatively symmetric about the Bragg peak, we exploited (1) further by equating the ratio of intensities in the images to the rocking curve ratio, at a given angle, for either all negative or all positive angles with respect to the peak. That is, the incident angle was calculated from the intensity ratio between equivalent pixels in the diffracted and transmitted images with no object present ($I_R = I_O$, $\Delta\theta_Y = 0$):

$$\frac{I_D}{I_T} = \frac{I_O R_D(\theta)}{I_O R_T(\theta)} = \frac{R_D(\theta)}{R_T(\theta)}. \tag{2}$$

A look-up table of the discretely sampled ratio of the two rocking curves (Fig. 2) was used to find the closest match to the intensity ratio, whence a linear fit between the rocking curve ratio points was then assumed to calculate the incidence angle $\theta$ for every pixel. The same process was then followed to determine the final incidence angle ($\theta_f = \theta + \Delta\theta_Y$) with the object present:

$$\frac{I_D}{I_T} = \frac{I_R R_D(\theta + \Delta\theta_Y)}{I_R R_T(\theta + \Delta\theta_Y)} = \frac{R_D(\theta_f)}{R_T(\theta_f)}. \tag{3}$$

The difference between the incidence angle with and without the object yields the net refraction angle $\Delta\theta_Y$ caused by the object. $I_R$ was then determined upon substitution of $\Delta\theta_Y$ into (1).

## 3. Results

Fig. 3 shows the image of the PMMA cylinder created by the X-ray beam that transmitted through the analyser crystal. Fig. 4 displays the diffracted image of the cylinder after correcting for offsets between the images. Note that the bright/dark upper edge of the cylinder of the transmitted image appears dark/bright in the diffracted image, respectively. Profiles of the reconstructed refraction angle and apparent absorption using (3) across the cylinder are provided in Figs. 5 and 6, respectively. Theoretical refraction and absorption curves reveal that the reconstructions closely match the expected functions except at the very edges of the cylinder where the refraction is underestimated and the intensity is highly oscillatory, thus, the geometrical optics approximation Eq. (1) is not satisfied at all points. For the theoretical curves a refractive index decrement of $\delta = 4.4 \times 10^{-6}$ and a linear attenuation coefficient of $\mu_l = 37.4\ \mathrm{m}^{-1}$ were used (see [3] for details of this calculation).

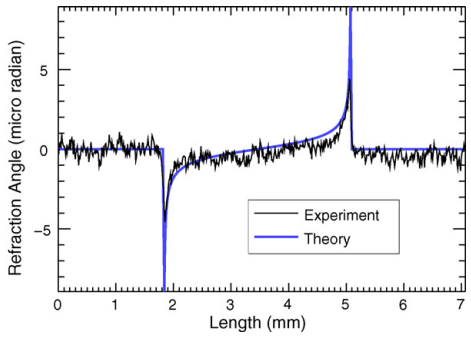


Fig. 5. Profile of the refraction angle across the PMMA cylinder.

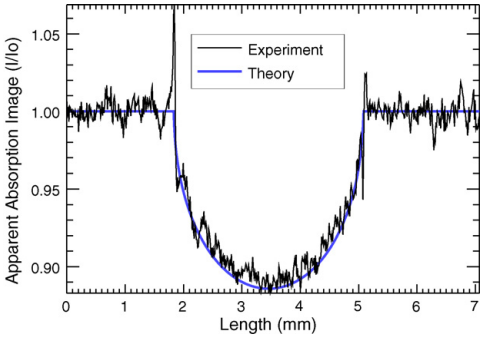


Fig. 6. Profile of the apparent absorption across the PMMA cylinder.

Please cite this article in press as: Kitchen MJ, et al., Simultaneous acquisition of dual analyser-based phase contrast X-ray images for small animal imaging, Eur J Radiol (2008), doi:10.1016/j.ejrad.2008.04.028

+Model
EURR-3896; No. of Pages 5
ARTICLE IN PRESS



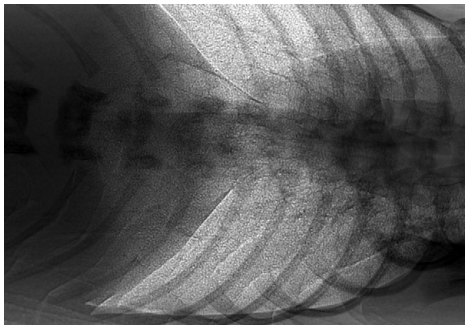

Fig. 7. Transmission image of the rabbit pup thorax.

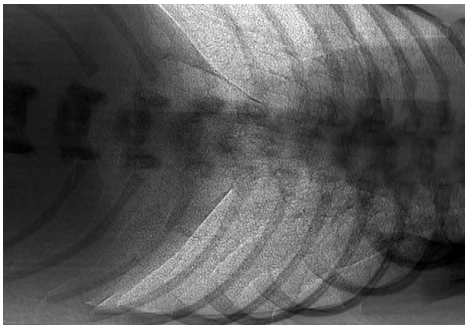

Fig. 10. Apparent absorption image reconstructed using Figs. 7 and 9.

Figs. 7 and 8 respectively show the transmitted and distortion-corrected diffracted images of the rabbit pup thorax at full inflation. Phase contrast reveals the boundaries of the major airways, lung lobes and diaphragm. The reconstructed refraction angle and apparent absorption images are shown in Figs. 9 and 10, respectively. These images reveal that much of the contrast arises from phase gradients within the airways. The airway boundaries are essentially invisible in the absorption image, yet a speckled pattern is still evident across the image of the lung tissue. All rabbit images are 20.9 mm × 14.8 mm.

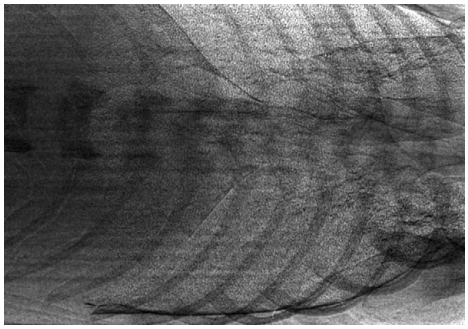

Fig. 8. Diffracted image of the rabbit pup thorax.

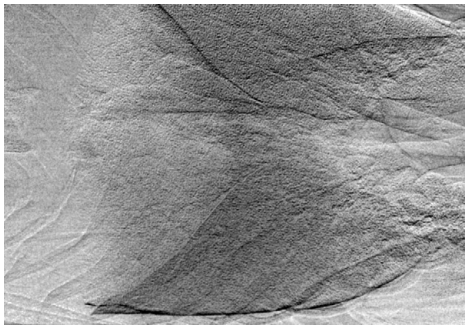

Fig. 9. Refraction angle image reconstructed using Figs. 7 and 8.

## 4. Discussion

The breakdown of the phase retrieval at the boundaries of the PMMA cylinder results from the failure of the geometrical optics approximation in the vicinity of large phase gradients; this results in an underestimation of the refraction angle, which subsequently creates troughs in the absorption image at the inner edge of the cylinder [3]. However, the outer edge of the absorption image shows unexpected sharp peaks. These are attributed to a Fresnel diffraction fringe, which arises from the high coherence of the X-ray wavefield and the large propagation distance of over 1 m between the object and detectors. Fresnel diffraction effects are also responsible for the speckled intensity pattern remaining in the apparent absorption image of the lung, as seen in Fig. 10 (see [2]). This effect should either be accounted for in the image reconstruction, or alternatively the propagation distance should be reduced [11–13].

Future experiments will improve upon the signal-to-noise ratio of the diffracted image by optimising the X-ray energy for the maximum reflected intensity at the Bragg angle. Fiducial markers will also be employed to improve the image alignment.

Work is continuing to improve the image reconstruction technique. Cubic-spline interpolation of the rocking curves and their ratio will ameliorate the scheme used to interpolate discretely sampled points. Furthermore, if suitable analytic functions can be fitted to both the transmitted and diffracted rocking curves, it may be possible to find an analytic solution for the phase retrieval that is not restricted to either side of the rocking curve.

## 5. Conclusion

A thin Laue analyser crystal can simultaneously provide two high-contrast images, which can successfully be combined to enable the separation of phase and absorption information. Together with a large, monochromatic X-ray beam, our crystal was sufficiently large and flat to enable the chest of a rabbit pup to be observed in a single exposure. This allowed us to perform phase retrieval on a dynamically recorded image sequence of lung inflation. Future work is planned for optimising the experimental setup and image reconstruction technique.

Please cite this article in press as: Kitchen MJ, et al., Simultaneous acquisition of dual analyser-based phase contrast X-ray images for small animal imaging, Eur J Radiol (2008), doi:10.1016/j.ejrad.2008.04.028

+Model
EURR-3896; No. of Pages 5
ARTICLE IN PRESS



**Acknowledgements**

The authors acknowledge funding from the Australian Research Council. This work was supported in part by the Commonwealth of Australia under the Access to Major Research Facilities Program. MJK acknowledges insightful discussions with Michael J. Morgan. KMP acknowledges funding from the Monash Centre for Synchrotron Science.

**References**

[1] Paganin DM. Coherent X-ray optics. Oxford, UK: Clarendon Press; 2005.
[2] Kitchen MJ, Lewis RA, Yagi N, et al. Phase contrast X-ray imaging of mice and rabbit lungs: a comparative study. Br J Radiol 2005;78:1018–27.
[3] Kitchen MJ, Pavlov KM, Siu KKW, Menk RH, Tromba G, Lewis RA. Analyser-based phase contrast image reconstruction using geometrical optics. Phys Med Biol 2007;52:4171–87.
[4] Ingal VN, Beliaevskaya EA. X-ray plane-wave topography observation of the phase contrast from a non-crystalline object. J Phys D: Appl Phys 1995;28:2314–7.
[5] Chapman D, Thomlinson W, Arfelli F, et al. Mammography imaging studies using a Laue crystal analyzer. Rev Sci Instrum 1996;67:1–5.
[6] Bushuev VA, Guskova MA. Image reconstruction in X-ray phase contrast method with crystal analyser in Laue geometry. Bull Russ Acad Sci 2005;69:253–9.
[7] Siu KKW, Kitchen MJ, Pavlov KM, et al. An improvement to the diffraction enhanced imaging method that permits imaging of dynamic systems. Nucl Instrum Methods A 2005;548:169–74.
[8] Lewis RA, Yagi N, Kitchen MJ, et al. Dynamic imaging of the lungs using X-ray phase contrast. Phys Med Biol 2005;50:5031–40.
[9] Gureyev TE, Wilkins SW. Regimes of X-ray phase-contrast imaging with perfect crystals. Nuovo Cimento D 1997;19:545–52.
[10] Bushuev VA, Ingal VN, Belyaevskaya EA. Dynamical theory of images generated by noncrystalline objects for the method of phase-dispersive introscopy. Crystallogr Rep 1996;41:766–74.
[11] Pavlov KM, Gureyev TE, Paganin D, Nesterets YI, Morgan MJ, Lewis RA. Linear systems with slowly varying transfer functions and their application to X-ray phase-contrast imaging. J Phys D: Appl Phys 2004;37:2746–50.
[12] Pavlov KM, Gureyev TE, Paganin D, et al. Unification of analyser-based and propagation-based X-ray phase contrast imaging. Nucl Intrum Methods A 2005;548:163–8.
[13] Coan P, Pagot E, Fiedler S, Cloetens P, Baruchel J, Bravin A. Phase-contrast X-ray imaging combining free space propagation and Bragg diffraction. J Synchrotron Rad 2005;12:241–5.

Please cite this article in press as: Kitchen MJ, et al., Simultaneous acquisition of dual analyser-based phase contrast X-ray images for small animal imaging, Eur J Radiol (2008), doi:10.1016/j.ejrad.2008.04.028